Electronic Thesis and Dissertation Repository

12-1-2014 12:00 AM

Performance of Micropiled Raft in Sand and Clay-Centrifuge and Numerical Studies

Ahmed M. Alnuaim, *The University of Western Ontario*

Supervisor: Dr. M. Hesham El Naggar, *The University of Western Ontario*
A thesis submitted in partial fulfillment of the requirements for the Doctor of Philosophy degree in Civil and Environmental Engineering
© Ahmed M. Alnuaim 2014

Follow this and additional works at: https://ir.lib.uwo.ca/etd

Part of the Geotechnical Engineering Commons

Recommended Citation

PERFORMANCE OF MICROPILED RAFT IN SAND AND CLAY–CENTRIFUGE AND NUMERICAL STUDIES

(Thesis format: Integrated-Article)

by

Ahmed Mohamed <u>Alnuaim</u>

Graduate Program in
Engineering Science
Department of Civil and Environmental Engineering

A thesis submitted in partial fulfillment
of the requirements for the degree of
Doctor of Philosophy

The School of Graduate and Postdoctoral Studies
The University of Western Ontario
London, Ontario, Canada

ABSTRACT

A micropile is a small diameter "cast-in-place" pile, which was initially used to repair deficient foundations. The overall performance of a micropiled raft (MPR) foundation system is similar to a piled raft foundation where the load is transmitted through both the raft and the micropiles. This thesis explores using micropiled rafts (MPR) as a new highly efficient foundation system that combines the advantages of the piled raft system and the efficient installation of micropiles and associated ground improvement. Currently, there is no guidance available regarding the performance of MPR foundations. Therefore, the main objectives of this research are to evaluate the behaviour of MPRs in sand and clay soils and examine the effects of different parameters on their performance.

The research methodology comprised of three primary aspects: performing a series of geotechnical centrifuge tests on MPRs and comprehensive soil characterization in order to obtain experimental results and necessary soil parameters for numerical modeling, developing, calibrating and verifying a three-dimensional finite element model (3D FEM); and conducting a comprehensive parametric study on the behaviour of MPRs in sand and clay soils using the FEM. Four MPRs centrifuge tests were conducted: three tests in sandy soil and one test in clay soil. In addition, single micropile and isolated raft foundation centrifuge tests were carried out in both sand and clay soils.

The results of the centrifuge tests were used to calibrate and verify the non-linear three-dimensional finite element models for both the sand and clay soils. Subsequently, the verified models were employed to conduct a comprehensive parametric study. The

parametric study focused on providing additional insights regarding the performance of micropiled raft system that should be helpful for the design engineers. The physical dimensions of MPR structural components and parameters considered in the parametric study are within the range used in the current practice. The results of the centrifuge tests and numerical parametric study were analyzed to establish design guidelines for micropiled rafts.

It was found that the tolerable bearing pressure of MPRs increased by as much as 191% and 101% compared to isolated rafts in sand and clay, respectively. In addition, the load carried by the raft in a MPR depends primarily on the micropile spacing and ranges between 20% and 80% of the applied load. Equations are proposed to evaluate the percentage increase in tolerable bearing pressure (PIBP) and the load carried by the components of MPR for different types of soils due to change in the micropile spacing and raft thickness. The Poulos-Davis-Randolph (PDR) method was found to be able to evaluate the performance of a MPR system with relatively stiff rafts. However, the error margin increases up to 28% for a MPR with a flexible raft. An adjustment factor is proposed to account for the raft flexibility in the PDR method, which reduces the error in estimating the axial stiffness of MPRs with a flexible raft to only 3%.

Keywords

CO-AUTHORSHIP STATEMENT

This thesis is prepared in accordance with the regulation for Integrated-Article format thesis stipulated by the school of graduate and post graduate studies at Western University, London, Ontario, Canada. All the centrifuge testing, numerical modeling, interpretation of results and writing of the draft and the final thesis were carried out by the candidate himself, under the supervision of Dr. M. Hesham El Naggar and Dr. Hany El Naggar. The supervisors' contribution consisted of providing advice throughout the research program, and reviewing the draft and the final thesis and publications results from this research. The results of the centrifuge tests, and numerical modeling presented will be used in journals and conferences publications, which will be coauthored with Dr. M.H. El Naggar and Dr. Hany El Naggar.

.

ACKNOWLEDGMENT

TABLE OF CONTENTS

LIST OF FIGURES

xvi

LIST OF TABLES

LIST OF ABBREVATIONS and SYMBOLS

Symbol	Definition
AASHTO	The American Association of State Highway and Transportation Officials
A_g	Area of grout in micropile cross section
a_g	Acceleration amplitude
A_{mp}	Cross-sectional area of micropile
a_{rp}	Raft pile interaction factor
A_s	Cross sectional area of the steel casing and steel reinforcement bar
ASD	Allowable stress design methods
ASTM	The American Society For Testing And Materials
BEM	Boundary Element Method
B_{mp}	Micropile width
B_r	Raft width
c_1 and c_2	Coefficients
C_c	Coefficient of curvature,
C_c	Compression index
C_{mp}	Circumference of micropile
CPT	Cone penetration test
C_r	Rebound index
C_u	Uniformity coefficient
CU	Consolidated Undrained Triaxial Test
c_u	Undrained cohesion
c_v	Coefficients of consolidation
c'	Effective cohesion

D_{10}	The grain diameter for which 10% of the sample is finer
D_{30}	The grain diameter for which 30% of the sample is finer
D_{50}	Average soil particle size
D_{60}	The grain diameter for which 60% of the sample is finer
DAQ	Data acquisition system
D_b	Diameter of the drill hole
D_c	The cone diameter for CPT
D_{mp}	Diameter of micropile
D_p	Pile diameter
D_r	Relative density of sand
$D_{T\text{-bar}}$	Diameter of T-bar cylinder
e	Void ratio
e_f	efficiency exponent
E_{inc}	the rate of the increase in modulus of elasticity
E_m	Modulus of elasticity of the model
$E_m A_m$	Axial rigidity for the model
$E_m I_m$	Flexural rigidity for the model
e_o	Initial void ratio
E_o	Initial modulus of elasticity
E_p	Pile material Young's modulus
$E_p A_p$	Axial rigidity for the prototype
$E_p I_p$	Flexural rigidity for the prototype
E_r	Raft elastic modulus
E_s	Soil elastic modulus
E_{sav}	Average soil Young's modulus along pile shaft

E_{sc}	Modulus of elasticity of the steel casing
E_{st}	Soil Young's modulus at pile tip
E_{sul}	Lateral reaction modulus of the soil surrounding the micropile at the unsupported length.
E_u	Undrained modulus of elasticity
FDM	Finite Difference Method
FEA	Finite Element Analysis
FEM	Finite Element Method
FHWA	The Federal Highway Administration
FOREVER	The French National Project on Micropiles
FS	Factor of safety
f_s	Skin friction
f_{si}	Skin friction corresponding for each segment
f_y	Yield stress of steel
f'_c	Unconfined compressive strength of the grout
g	Earth's gravity
G_b	Shear modulus for the soil beneath the pile
G_s	Average soil shear modulus
G_{sl}	Soil shear modulus at the pile toe
G_{sr}	Shear modulus
G_u	Undrained shear modulus
H_f	Final height
h_m	Height of the model
h_{si}	Height of each segment
I	Influence factor

i	Segment number
IBC	The International Building Code
I_{mp}	Moment of inertia of the micropile
K	modulus number
K_{PG}	Pile group stiffness
K_{pr}	Piled raft stiffness
K_r	Raft stiffness
KRF	Kaolin and silica rock flour
K_{rs}	Raft-soil stiffness ratio
K_s	Lateral earth pressure coefficient
K-S	Kaolin-silt mixture
KSS	Kaolin-silt-sand
L_b	Bond length.
LDT	Linear displacement transducer
L_{mp}	Length of micropile
L_p	Pile length
L_r	Raft length
L_{us}	Unsupported length of the micropile
LVDT	Linear Variable Differential Transducer
m	Mass
M_{center}	Bending moment at the raft center
M_{cl}	Bending moment for column loading
M_{edge}	Bending moment at the raft edge
MP	Micropile
MPR	Micropiled Raft

M_u	Bending moment for uniform loading
n	Scale factor
N_b	Bar factor
n_e	exponent varies between 0.45 and 0.6 for sand
N_k	Empirical factor
n_{mp}	Number of micropile in group
n_p	Number of piles
n_s	Number of segments
O.D	Outer diameter
OCR	Consolidation ratio
P_a	Atmospheric pressure
$P_{c\text{-}allow}$	Allowable compression force
P_{cr}	The critical buckling load
PDR	Poulos-Davis-Randolph method
$P_{g\text{-}allow}$	The allowable capacity
PI	Plasticity Index
PIBP	Percentage Increase in Tolerable Bearing Pressure
P_m	P-multiplier for p-y curve for any pile in pile group
PPT	Pore Pressure Transducers
P_r	Load carried by the raft
P_s	Axial force carried by shaft of micropiles
P_t	Total applied load
$P_{t\text{-}allow}$	Allowable tension force
$P_{T\text{-}bar}$	Force per unit length acting on the T-bar cylinder
P_{tmp}	Axial load on the pile top

P_{up}	The ultimate capacity of piles in the piled raft
PVC	Polyvinyl Chloride
Q	Total applied load
q	Applied pressure
q_c	Cone tip resistant
QD	Quasi Displacement
Q_g	The allowable capacity of a micropile group
QND	Quasi Non-Displacement
Q_{pile}	Load carried by a single pile
Q_{pr}	Total load carried by pile raft
r	Radius
r_e	Effective radius
R_{int}	Interface reduction factor
r_m	Radius of influence $= 2.5\rho L_p(1-v)+2.5D_p$
r_o	Radius of pile
r_r	Average radius of raft
r_t	Radius at top of the model
S/B_{mp}	Spacing ratio based on micropile width
S/D_{mp}	Spacing ratio based on micropile diameter
S/D_p	Spacing ratio based on pile diameter
S_B	Spacing between micropiles along width of MPR
S_d	Differential settlement
S_L	Spacing between micropiles along length of MPR
SSI	Soil-Structure-Interaction
s_u	Undrained shear strength

t_r	Raft thickness
UU	Unconsolidated Undrained Triaxial Test
v	Steady speed
w_L	Liquid Limit
w_p	Plastic Limit
X	The proportion of the total applied load transmitted by the raft
z	Depth of interest
Z_{ref}	Reference depth
α_{bond}	Grout-to-ground ultimate bond strength
α	Coefficient for α method
α_i	Micropile inclination angle
α_o	The optimal value for Raft-soil stiffness ratio
α'_p	Percentage of load carried by the piles
α_{pr}	Piled raft coefficient
α_{rp}	Raft pile interaction factor
β	Coefficient for β method
γ	Unit weight
γ_d	Dry unit weight at certain relative density
γ_{max}	Maximum unit weight
γ_{min}	Minimum unit weight
δ	Tolerable settlement
ζ	Coefficient $= \ln(r_m/r_o)$
η	Group efficiency factor
θ	Angular distortion

θ_r	Angular distortion for isolated raft
κ and μ	Coefficients to calculate ω_{pr}
ν_m	Poisson's ratio of the model
ν_r	Poisson's ratio of the raft
ν_s	Poisson's ratio of the soil
ρ	Degree of homogeneity
ρ_s	Density
σ_1	Initial stress
σ_2	Second stress
σ'_h	Horizontal effective stress
σ'_m	Mean effective stress,
σ_v	Total vertical stress
σ'_v	Effective vertical stress
σ_z	Contact pressure
σ_{zt}	Axial stress at top of micropile
ϕ	The angle of internal friction
ϕ_t	Total friction angle
ϕ'	The effective friction angle
ϕ'_c	The critical friction angle
ϕ'_r	Residual friction angle
ψ	Dilation angle
ω	Angular speed
ω_{PR}	Adjustment factor

CHAPTER ONE: INTRODUCTION

1.1. Background

A micropile is a small diameter "cast-in-place" pile. Micropiles were initially used to repair historic buildings that were damaged during World War II, which entailed installing micropiles by drilling through the existing foundation and filling the holes with cement grout and a steel bar (Lizzi, 1982). Nowadays, different types of micropiles are used to provide the load carrying capacity of new foundation systems (FHWA, 2005). In current practice, the diameter of a micropile is typically less than 300 mm. Micropiles were introduced to North America in the mid 1980's and their use has been rapidly growing ever since. Their construction methods have been improved and new construction techniques have been developed. The advancements in drilling equipment have resulted in the ability to drill through almost any ground condition to install micropiles at any angle with minimum noise, vibration and disturbance. In addition, the relatively small size of the equipment has allowed the underpinning of existing foundations even in restricted access situations (Bruce et al., 1995). Micropiles are used in a variety of applications, including: (1) to serve as a main foundation system for static and dynamic loading; (2) to upgrade an existing foundation system; and (3) to stabilize slopes and reinforce the soil (Bruce et al., 1995). Micropiles installation methods have a significant contribution to the enhancement of the grout-ground bond strength along the shaft of a micropile. Using pressurized grout as one of the installation methods has some advantages such as densifying the surrounding soil (especially for granular soil), increasing the shear strength of the soil along the grout-ground interface and due to the

high applied pressure, the grout will penetrate into the soil, which will increase the micropile cross-section and extend the grout influential zone.

1.2. Micropiled Raft Systems (MPR)

The concept of underpinning foundation systems using micropiles is similar to the concept of the piled raft, which is a composite structure with three components: subsoil, raft and piles. These components interact through a complex soil-structure interaction scheme, including the pile-soil interaction, pile-soil-pile interaction, raft-soil interaction, and finally the piles-raft interaction. The piled raft foundation system offers some advantages over pile group design in terms of serviceability and efficient utilization of materials. For a piled raft, the piles will provide sufficient stiffness to control the settlement and differential settlement at serviceability loads, while the raft will provide additional capacity at ultimate load. The raft in a piled raft transmits approximately 30% to 50% of the applied load to the soil depending on the spacing between the piles (Clancy and Randolph, 1993). Normally, a piled raft will require fewer piles in comparison to a pile group to satisfy the same capacity and settlement requirements (Poulos et al. 2011). These advantages of piled raft foundations need to be examined for micropiled raft foundation systems as limited studies have been conducted to evaluate the performance of MPRs. Only limited studies focused on MPR performance. For example, Han and Ye (2006) performed one micropile load test using a 1.5 m by 1.5 m square raft with four micropiles 150 mm in diameter and spaced at 750 mm. It is recommended to use micropiled rafts (MPR) as a new foundation system to take advantage of the combined benefits the piled raft system and the efficient installation of micropiles and associated ground improvement.

Poulos (2001) has formulated the findings of several studies into an analytical approach, widely known as Poulos-Davis-Randolph (PDR), to evaluate the axial stiffness of piled rafts for preliminary design purposes. However, the ability of the PDR method to evaluate the axial stiffness of MPR has to be confirmed in order to be used in preliminary design stage. In addition, the effect of raft flexibility is neglected in the PDR method, which can lead to overestimating the axial stiffness of the piled raft or micropiled raft foundation systems.

1.3. Geotechnical Centrifuge Technology

Geotechnical centrifuge technology has proven to be a powerful and affordable tool to examine the behaviour of complex systems such as dams, soil-structure interaction, culverts and caissons. A large and complex structure can be modeled using a suitable scaling factor under centrifugal acceleration to simulate the performance of this structure at prototype scale for design verification or research purposes. Several research programs were carried out using the geotechnical centrifuge to study the behaviour of pile groups, piled raft, micropile groups subjected to different loading conditions (e.g. Horikoshi et al. (2002, 2003a, b); Juran et al. (2001); and Horikoshi and Randolph (1996)) and to provide experimental data to calibrate and verify finite element models (FEM). Performing full scale testing for micropile-raft foundations is expensive as it may require testing a number of full scale foundations with different configurations in order to fully understand the performance of this type of system. Moreover, the complexity involved in measuring the localized stresses in the field adds another challenge in performing full scale tests. Therefore, using centrifuge testing on a smaller scale model compared to the prototype is preferable because it provides approximately the same results of a full scale test.

Moreover, it has a significant advantage over 1-g models in that the stress level in the centrifuge modelling is equal to the stress level in the prototype, which is very important to achieve accurate soil stiffness and strength. This advantage is due to increasing the acceleration of the centrifuge model.

1.4. Research Objective

This study is focused on investigating the overall performance of micropiled rafts (MPR) in cohesionless and cohesive soils. The primary objectives of this research are:

1. Conduct geotechnical centrifuge tests to investigate the performance of MPRs in sand soil and assess their axial stiffness. In addition, to examine the effect of raft flexibility on load sharing between micropiles and raft, raft bending moment, and differential settlement.

2. To conduct triaxial tests to establish a design guideline for kaolin-silt clay (K-S), which can be used to estimate the undrained shear strength and modulus of elasticity for K-S clay for future geotechnical centrifuge applications. In addition these tests are very important in order to evaluate the necessary parameter for the finite element constitutive model.

3. To conduct geotechnical centrifuge tests to investigate the performance of MPRs in K-S clay soil and assess their axial stiffness and compare it with the isolated raft foundation.

4. To evaluate the ability of the Poulos-Davis-Randolph (PDR) method to estimate the axial stiffness of MPRs, and revise as necessary to account for the raft flexibility.

5. To develop 3D finite element models (3D FEM) to simulate the performance of typical raft sizes in current practice in sand and clay soils with different number of micropiles. The numerical model was calibrated and verified using the centrifuge tests results.

6. To investigate the effect of different factors such as number of micropiles, raft thickness, load type and soil condition on the axial stiffness of MPRs, differential settlement, load sharing and raft bending moment.

7. To develop a set of equations, tables and graphs which will help in the preliminary design for MPRs in sand and clay soils.

1.5. Research Methodology

The research methodology comprised of three primary aspects: 1) performing a series of geotechnical centrifuge tests on MPR and comprehensive soil characterization to obtain experimental results and necessary soil parameters for numerical modeling, 2) developing, calibrating and verifying three-dimensional finite element models (3D FEMs), and 3) conducting a comprehensive parametric study on the behaviour of MPRs in sand and clay soils using the FEM. Four MPR centrifuge tests were conducted: three tests in sandy soil and one test in clay soil. In addition single micropile and isolated raft foundation centrifuge tests were carried out in both sand and clay soils.

The results of the centrifuge test were used to calibrate and verify the non-linear three dimensional finite element models for both the sand and clay soils. Subsequently, the verified models were employed to conduct a comprehensive parametric study. The parametric study provides insights regarding the performance of micropiled raft system, which will be helpful for the design engineers. The physical dimensions of structure

components and parameters considered in the parametric study are within the range considered in the current practice. The results of the centrifuge tests and numerical parametric study were analyzed to establish a design guideline for micropiles as retrofitting elements for isolated rafts or as a main foundation system.

1.6. Organization of the Thesis

This thesis is divided into eight chapters. The first chapter introduces the concept of micropiles and micropile rafts under investigation. In addition, the importance of geotechnical centrifuge technology is introduced as well as the objective and methodology of this research.

Chapter two presents a comprehensive review regarding micropiles, piled raft and geotechnical centrifuge technology. In this review, different types of micropiles, design requirements and classification are introduced; in addition, a number of previous studies are discussed. For piled rafts, a brief description of design methods is presented along with a brief description of the previous studies conducted to investigate the performance of piled rafts under different types of loading. A brief description of the concept of geotechnical centrifuge testing is presented including the scaling laws and issues associated with the centrifuge, followed by a short description of the previous work conducted to investigate the performance of micropile and micropile group using centrifuge technology.

Chapter three introduces the centrifuge testing program, including details of the design of the micropiled raft models. In addition, the results of laboratory tests conducted on the soil used in the centrifuge tests are presented. Furthermore, the calibration data for

the instrumentation used throughout the testing program are introduced. The design of the different test beds and centrifuge package head works setup for different tests are described in detail.

Chapter four reports on the behaviour of micropiled raft foundation in sand soil using the geotechnical centrifuge technology. The study investigated the effects of the raft flexibility on the important design parameters using geotechnical centrifuge testing. The effects of raft flexibility on the raft differential settlement, contact pressure, and load sharing between the raft and micropiles were evaluated. In addition, using micropiles as a method to reduce differential settlement is considered.

Chapter five presents the behaviour of micropiled raft foundations in clay soil using the geotechnical centrifuge technology. The study investigates performance of MPRs using geotechnical centrifuge testing. The effects of the presence of micropiles on the raft differential settlement, contact pressure, and load sharing between the raft and micropiles were evaluated.

Chapter six and Chapter seven introduce the results of the comprehensive parametric study of MPRs in sand and clay, respectively, using the 3D FEM. A detailed description of the 3D FEM is provided, as well as the calibration and verification process using the results obtained from geotechnical centrifuge tests. The effect of different parameters such as the number of micropiles (MPs), the spacing to micropile diameter (S/D_{mp}) and the raft thickness on the MPR axial stiffness; differential settlement; load sharing between the micropiles and the raft; and the raft bending moment have been investigated. In addition, the FEA examined the ability of PDR method to evaluate the

axial stiffness of MPR for preliminary design stage. Furthermore, an adjustment factor (ω_{PR}) is introduced to account for the raft flexibility in the PDR method.

Chapter eight comprises of the summary, conclusions and recommendations for future research.

REFERENCES

Bruce, D. A., DiMillio, A. F. and Juran, I. (1995). Introduction to Micropiles: An International Perspective. Foundation Upgrading and Repair for Infrastructure Improvement, ASCE, Geotechnical Special Publication, (50): 1-26.

Clancy, P. and Randolph, M. F. (1993). An Approximate Analysis Procedure for Piled Raft foundations. International Journal for Numerical and Analytical Methods in Geomechanics, **17**(12): 849-869.

FHWA. (2005). Micropile Design and Construction Guidelines, Implementation Manual. National Highway Institute.

Han, J. and Ye, S. (2006). A Field Study on the Behaviour of a Foundation Underpinned by Micropiles. Canadian Geotechnical Journal, **43**(1): 30-42.

Horikoshi, K. and Randolph, M.F. (1996). Centrifuge Modelling of Piled Raft Foundations on Clay. Géotechnique, **46**(4):741-752.

Horikoshi, K., Matsumoto, T., Hashizume, Y. and Watanabe, T. (2003a). Performance of Piled Raft Foundations Subjected to Dynamic Loading. International Journal of Physical Modelling in Geotechnics, **3**(2):51-62.

Horikoshi, K., Matsumoto, T., Hashizume, Y., Watanabe, T. and Fukuyama, H. (2003b). Performance of Piled Raft Foundations Subjected to Static Horizontal Loads. International Journal of Physical Modelling in Geotechnics, **3**(2):37-50.

Horikoshi, K., Watanabe, T., Fukuyama, H. and Matsumoto, T. (2002). Behaviour of Piled Raft Foundations Subjected to Horizontal Loads. *In* Proceeding of the International conference of Physical Modelling in Geotechnics. St John's, Newfoundland, Canada.

Juran, I., Benslimane, A. and Hanna, S. (2001). Engineering Analysis of Dynamic Behaviour of Micropile Systems. Transportation Research Record: Journal of the Transportation Research Board, Vol. 1772, pp. 91-106.

Lizzi, F. (1982). The Static Restoration of Monuments: Basic Criteria-Case Histories, Strengthening of Buildings Damaged by Earthquakes . Genova: Sagep Editrice.

Poulos, H. G. (2001). Piled Raft Foundations: Design and Applications. Géotechnique, **51**(2): 95-113.

Poulos, H. G., Small, J. C. and Chow, H. (2011). Piled Raft Foundations for Tall Buildings. Geotechnical Engineering Journal of the SEAGS and AGSSEA, **42**(2): 78-84.

CHAPTER TWO: LITERATURE REVIEW

2.1. INTRODUCTION

Micropiles have been successfully used to retrofit historical buildings since the 1950s (Lizzi, 1982). Over the last few decades, numerous studies have been carried out to evaluate their performance in different soils through field testing, physical modeling and finite element analysis (FEA). From structural and geotechnical points of view, the performance of a foundation retrofitted with micropiles is similar to that of a group of piles connected to a pile cap, commonly known as a piled raft. While the performance of piled rafts is widely investigated, the performance of micropiles and the retrofitted foundation as one unit, i.e. a micropiled raft, is scarcely investigated. Due to the notable differences between piles and micropiles in terms of their geometrical, capacity and performance characteristics, the methods developed for the analysis and design of piled rafts may not be directly applicable to micropiled rafts. However, knowledge of micropile performance characteristics as well as those of piled rafts provides valuable insights towards the understanding of the performance of micropiled rafts.

In this chapter, a comprehensive literature review is presented for the subjects related to the scope of this research. It provides a detailed description of the geotechnical and structural design, bearing capacity and behaviour of micropiles. It reviews some of the studies that have been conducted to evaluate the performance of micropiles installed in different soil conditions and under various loading types (vertical, horizontal and dynamic). In addition, a discussion of the piled raft foundation concept is provided and the previous studies that have been conducted in this area have been reviewed. Finally,

some relevant information about geotechnical centrifuge testing is provided along with a description of some of the piled raft centrifuge studies reported in the literature.

2.2. MICROPILES

2.2.1. Introduction

A micropile is a cast-in-place pile that has a small diameter. The micropile (initially termed a root pile) system was invented in the early 1950s by Dr. Fernando Lizzi. Micropiles were initially used to repair historic buildings that were damaged during World War II, but were later used for different purposes. The philosophy of this technique was to underpin the existing foundation system with minimal disturbance. This was achieved by installing micropiles with a small diameter (about 100 mm) and varying lengths (between 6m and 30m) through holes drilled in the existing foundations using rotary drilling; the holes were filled with cement grout and a steel bar. In most cases, the micropiles were installed in inclined groups (Lizzi, 1982). The addition of micropiles increases the bearing capacity of the support system so that it can resist static and seismic loading, as well as improve the soil's shearing resistance (FHWA, 2005).

In current practice, the diameter of a micropile is 300 mm or less, and it transfers the load primarily through skin friction with the soil in the bonded area between the grout and the soil. Micropiles were introduced into North America in the mid 1980s and since then, a rapid growth of their use was recorded. In addition, the construction methods for micropiles were improved and new techniques were developed. The applications in which micropiles are used include: (1) serving as a main foundation system for static and

dynamic loading, (2) upgrading an existing foundation system and, (3) stabilizing slopes and reinforcing the soil (Bruce et al., 1995).

2.2.2. Construction of Micropiles

The recent development of powerful drilling equipment facilitates drilling through almost any ground condition to install micropiles at different angles with minimum noise, vibration and disturbance. Moreover, this powerful equipment allows constructing micropiles up to 300 mm in diameter and up to 60 m deep. In addition, the relatively small size of the equipment allows the underpinning of the existing foundation even with restricted access to the foundation (Bruce et al., 1995).

Typical micropiles are constructed by drilling the pile shaft (the bore hole) to the desired depth using one of many drilling methods; the selected drilling method depends on the depth and size of micropiles and the sensitivity of the site to disturbances. During drilling, a steel casing is installed simultaneously to support the shaft wall. After the drilling is finished, a steel reinforcement element, which is usually steel bars, steel rods or steel pipes, is placed which occupies about 5% to 8% of the whole volume. Subsequently, grout is placed in the micropile shaft, usually using pressure after removing the temporary casing to increase the diameter of the bonded length and to increase the friction with the adjacent soil. The temporary casing may not be fully removed in order to increase the lateral stiffness of the micropiles (Shong and Chung, 2003).

2.2.3.   Classification of Micropiles

According to the Federal Highway Administration (FHWA, 2005), the micropile system is classified based on two criteria: (1) the behaviour or purpose of the micropile system, which is symbolized by a number, and (2) the method of grouting, which defines the grout-soil bond capacity, and is denoted by a letter. These two classifications are integrated to fully describe the micropile from the criteria of purpose and construction method of the micropile system. The following sections briefly describe the two classifications.

2.2.3.1. Classification of the purpose of the micropile system

In this classification, micropiles are divided into two categories: (1) CASE 1 micropile and (2) CASE 2 micropile. The CASE 1 micropile is loaded directly as the main foundation system and the pile reinforcement resists the majority of the applied load and transfers it to the ground through the grout-soil bond (skin friction). This type of micropile might be designed to perform individually or in groups. CASE 2 micropiles are used to reinforce the soil in order to increase the bearing capacity for an existing foundation system, to stabilize slopes or to reduce the settlement; this type is also known as a reticulated pile network. Moreover, the reinforcement in CASE 2 micropiles is light since their purpose is to enhance the soil and not to sustain the applied load directly.

2.2.3.2. Classification of the method of grouting

This classification system describes the method in which the grouting is placed. The grouting method depends on the soil type and controls the grout-soil bond capacity. Therefore, it is very important for the designer to recognize the different types of grouting

in order to achieve the desired bond capacity. The FHWA (2005) classifies grouting into four categories, designated by letters from A to D, based on the placement method of the grouting. The following list briefly describes each type of grouting:

Type A: Grout is simply placed solely under gravity action. This method was common in the past, but is less common in the present. Neat cement grout or sand-cement mortars can be used. The behaviour of this type is similar to the bored pile system, which is characterized by lower shaft friction compared to other pressurized grouting types.

Type B: Neat cement grout is placed into the micropile shaft by applying injection pressure, which is normally about 0.5 to 1 MPa. During this process, the temporary steel casing is withdrawn to allow maximum bonding between grout and soil, which will increase the shaft capacity. In this type, the shaft friction is high due to the penetration of the grout into the soil pores under the pressure effect.

Type C: This type is common some parts of Europe and consists of two steps: (1) similar to Type A, neat cement grout is placed under gravity head and, (2) before the cement grout is hardened (about 15 to 25 minutes), a sleeved grout pipe is used to inject similar grout at minimum 1 MPa pressure without using packers at the bond zone. Similar to Type B, the shaft friction is high due to penetration of grout into adjacent soil.

Type D: This type is similar to Type C except some alterations to step 2. Before the hardening of the neat cement grout from step 1, the additional grout is injected at a pressure of 2 to 8 MPa using a sleeved pipe similar to the one used in Type C. In order to increase the friction capacity of the bond, a packer may be used at desirable locations inside the sleeved pipe. This type is very common worldwide. In this type the side

friction is even higher than Type B and Type C due to the high pressure at multiple locations. The grout-to-ground bond is about 63% higher than Type A (FHWA, 2005).

A new generation of micropiles was devised in 1983, and involves a threaded hollow bar connected to a drill bit advanced into the soil using air, water, or grout. The grout is then injected, typically at 1.0 to 1.5 MPa through the centre of the hollow bar, passing through the nozzles in the drill bit while the system is rotated. In some published literature, hollow bar micropiles are categorized as Type B. On the other hand, Timothy et al. (2012) denoted this type as Type E micropile (i.e. supplementary to the original four types A to D indicated by the FHWA). In addition, the American Association of State Highway and Transportation Officials (AASHTO, 2012) includes a Type E micropile specific to hollow bars. Hollow bar micropiles can be placed in a one-step operation in which the hole is drilled, reinforced and grouted simultaneously.

Due to the injection pressure, the diameter of the grout is larger than the bit diameter. Under these conditions, Type E micropiles perform well under tension and compression loading; however, because of their small diameter, their ability to resist lateral load is limited (Bruce et al., 2010). Figure 2.1 shows the different type of micropiles classified according to the types of grouting from Type A to Type D.
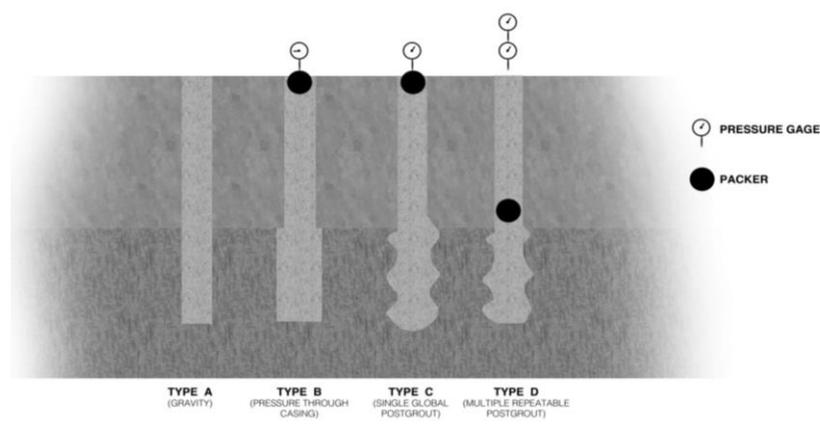
Figure 2.1. Different types of micropiles classified according to the types of grouting from Type A to Type D (after FHWA, 2005).

2.2.4. Pros and Cons of Micropiles

This section presents the advantages and disadvantages of using micropiles for different conditions and discusses the optimum applications for micropiles.

A micropile foundation can be desirable in some situations due to its small size and the versatility and mobility of its construction equipment, especially for remote sites and restricted access areas. In some cases, drilling or driving a conventional pile is difficult due to ground problems or potential vibration problems; the micropile foundation offers a favourable choice. Moreover, micropiles can be installed into an existing foundation to enhance its bearing capacity as well as to reduce time-dependant consolidation settlement. In some situations, the noise and vibration tolerance of the installation are limited due to adjacent structures; therefore, using micropiles can satisfy these limitations (Shong and Chung, 2003). For dynamic and lateral loading conditions, the high flexibility of a micropile system may be desirable in some situations. Furthermore, micropiles can

be easily installed at an inclined angle in order to enhance the performance under lateral and dynamic loading.

On the other hand, the main limitation of micropiles is their limited capacity in the lateral direction compared with conventional piles. It is possible to use micropiles for seismic retrofitting applications except for areas where the liquefaction potential is high. Due to the high slenderness ratio (length/diameter) of micropiles, liquefaction may increase the risk of buckling subsequent to lack of lateral support. Another disadvantage of the micropile system is its cost can be high compared to driven piles or bored piles (FHWA, 2005).

2.2.5. Design of Micropiles

The design guidelines for micropiles have been gaining tremendous attention and a number of codes include sections about micropiles design. Their design consists of two aspects: i) the structural design and, ii) the geotechnical design. The Federal Highway Administration published a comprehensive design approach, which consisted of 12 steps (FHWA, 2005). The International Building Code (IBC, 2009) introduced micropiles design, which governs material specifications, allowable stresses, reinforcement, seismic reinforcement and installation.

In this section, the structural design and the geotechnical design for micropiles under compression and tension loading will be presented according to the FHWA (2005) and IBC (2009) guidelines. The lateral resistance of micropiles and seismic considerations are also discussed.

2.2.5.1. Structural Design

Conventional pile foundations have high structural capacity and stiffness due to the large piles cross-section; therefore, their design is usually controlled by the geotechnical capacity (end bearing capacity and skin friction). For micropiles, both the structural and geotechnical aspects normally control the design. This is because of the relatively small cross-section of micropiles and the relatively high geotechnical load carrying capacity attributed to the high grout-to-ground resulting from pressurized grouting (FHWA, 2005).

This section presents the methods used to evaluate the allowable axial forces for both compression and tension loading conditions according to FHWA (2005) and IBC (2009). Both standards adopt the allowable stress design methods (ASD) for designing micropiles. For the compression loading condition, the axial force is calculated using the following equations:

- FHWA (2005):

$$P_{c-allow} = \left[0.4\acute{f_c} \times A_g + \ 0.47f_y \times A_s\right] \tag{2.1}$$

- IBC (2009):

$$P_{c-allow} = \left[0.33\acute{f_c} \times A_g + \ 0.4f_y \times A_s\right] \tag{2.2}$$

Where: $P_{c-allow}$ = allowable compression force; $\acute{f_c}$ = unconfined compressive strength of the grout; A_g = area of grout in micropile cross section; f_y = yield stress of steel; and A_s = cross sectional area of the steel casing and steel reinforcement bar.

According to AASHTO (2012), "the maximum usable strain at the extreme concrete compression fiber is equal to 0.003". Consequently, to maintain this level of compression strain for the grout, FHWA (2005) and IBC (2009) require that the yield stress for the reinforcing bar not to exceed 600 MPa and 550 MPa respectively (for modulus of

elasticity equal to 200GPa), at the uncased portion of the micropiles. This is to satisfy the strain compatibility between all the components of micropiles (i.e. reinforcement bar, steel casing and grout) and to protect the grout from being crushed under the compression load at an assumed strain of 0.003.

If the micropile is installed in a relatively weak or liquefiable soil, where the lateral support for the micropile is limited, it is important that the axial load not to exceed the critical buckling load. According to FHWA (2005), the critical buckling load is calculated considering the contribution only of the steel casing, i.e.:

$$P_{cr} = \frac{\pi^2 \, E_{sc} I_{mp}}{L_{us}^2} + \frac{E_{sul} I_{mp}^2}{\pi^2} \tag{2.3}$$

Where: E_{sc}= modulus of elasticity of the steel casing; I_{mp} = moment of inertia of the micropile; L_{us}= unsupported length of the micropile which is assumed to be the thickness of the weak soil or liquefiable soil; and E_{sul}= lateral reaction modulus of the soil surrounding the micropile at the unsupported length.

For the tension loading condition, the load is supported only by the steel components due to the very limited tensile strength of the grout. The tension force is calculated using the following equations based only on the steel element:

- FHWA (2005):

$$P_{t-allow} = \left[\, 0.55 f_y \times A_s \right] \tag{2.4}$$

- IBC (2009):

$$P_{t-allow} = \left[0.6 f_y \times A_s \right] \tag{2.5}$$

Where: $P_{t-allow}$ = allowable tension force; f_y = the minimum yield stress of the steel bar and casing; and A_s = cross sectional area of the steel casing and steel reinforcement bar.

2.2.5.2. Geotechnical Design

Only the allowable bond capacity ($P_{G\text{-allow}}$) along the bond length is considered when calculating the compression and tension capacities of the micropile. Because the diameter of micropiles is relatively small and hence the cross-sectional area is small, the end bearing capacity is negligible (Cadden et al., 2004). The $P_{G\text{-allow}}$ is based mainly on the grout-to-ground bond strength. The allowable capacity, $P_{G\text{-allow}}$, is then given by (FHWA, 2005):

$$P_{G-allow} = \frac{\alpha_{bond}}{FS} \times \pi \times D_b \times L_b \qquad (2.6)$$

Where: α_{bond} = grout-to-ground ultimate bond strength; FS = factor of safety (2 to 3); D_b = diameter of the drill hole; and L_b = bond length.

To determine the grout-to-ground bonding ultimate capacity, FHWA (2005) established different values of α_{bond} which depends on the type of installation and soil medium as presented in Table 2.1. These values are based on a review of published information on soil nails, tiebacks and drilled shafts. Table 2.1 reflects the influence of the grouting pressure (Type B, Type C and Type D) on α_{bond}, demonstrating that the upper bound increases significantly compared with Type A micropiles especially for granular soils. Cadden et al. (2004) state that Type C and Type D are supposed to achieve a higher bond strength value than Type B; however, due to the lack of information based on field tests and measurements, the values used in Table 2.1 are conservative for Type C and Type D.

Table 2.1. Grout-to-ground ultimate bond capacity according to FHWA (2005).

Soil	α_{bond} (kPa)			
	Micropile Types (depend on grout placing method)			
	Type A	Type B	Type C	Type D
Silt & Clay (some sand) (soft, medium plastic)	35-70	35-90	50-120	50-145
Silt & Clay (some sand) (stiff, dense to very dense)	50-120	70-190	95-190	95-190
Sand (some silt) (fine, loose-medium dense)	70-145	70-190	95-190	95-240
Sand (some silt, gravel) (fine-coarse, med.-very dense)	95-215	120-360	145-360	145-385
Gravel (some sand) (medium-very dense)	95-265	120-360	145-360	145-385
Glacial Till (silt, sand, gravel) (medium-very dense, cemented)	95-190	120-310	120-310	120-335

FHWA (2005) promotes using the conventional total stress method (α method) and effective stress method (β method), used to evaluate the ultimate capacity for conventional piles, for calculating the capacity of micropiles. However, these methods may result in a conservative design. The Canadian Foundation Engineering Manual provides an empirical equation based on the cone penetration test (CPT) to evaluate the shaft resistance for different types of piles including micropiles (CFEM, 2006). The IBC (2009) did not include any information about the geotechnical design for micropiles. It recommends using a factor of safety of 2 for calculating the allowable capacity.

2.2.5.3. Micropiles Group Geotechnical Design

In most cases, micropiles are installed in groups in order to achieve the design requirement in terms of the axial compressive capacity, uplift capacity and lateral capacity or to maintain a certain level of settlement. The load carrying capacity of a

micropile group may be evaluated using a group efficiency factor, η, similar to the approach used for evaluating the load carrying capacity of a conventional pile group. The efficiency factor depends on the spacing between the piles and the type of soil. According to the FHWA (2005), the allowable capacity of a micropile group for center-to-center spacing to diameter, $S/D_{mp} > 3$, is the sum of the capacity of the individual micropiles within the group (i.e., η = 1). For $S/D_{mp} < 3$, the following equation can be used:

$$Q_g = \left(\frac{\alpha_b \times \pi \times D_{mp} \times L_B}{FS}\right) \times \eta \times n_{mp} \tag{2.7}$$

Where: n_{mp} = number of micropile in group (for $S/D_{mp} < 3$, η < 1).

2.2.6.   Behaviour of Micropiles under Axial Load

The behaviour of a micropile varies according to the type of soil and the grouting method. This section presents some studies that evaluated the axial performance of single micropiles and micropile groups constructed in different types of soil and using different grouting methods.

Jeon and Kulhawy (2001) examined the results of 21 full scale field tests on micropiles with diameters that varied between 0.15 m and 0.19 m and shaft depths that varied between 9 m and 30 m. Eight of the micropiles were installed in cohesive soils and 13 micropiles were installed in cohesionless soils with a wide range of soil parameters. Different grout types were used including: Type B, C and D. The analysis indicated that the load-carrying capacity of the micropile is significantly different than the drilled shaft due to how the grouting pressure affects the state of stress in the soil. Moreover, the micropile load carrying capacity can be higher than larger diameter drilled shafts for shaft

depth to diameter ratio less than 100. This increase in capacity depends on the type of soil. For sand, the capacity of a micropile is 1.5 to 2.5 that of drilled shafts. In clay, the micropile capacity could be 1.5 times the capacity of drilled shaft. These capacity increases are attributed to the high pressure grout, which will enlarge the effective diameter of the micropile over the actual hole diameter.

Han and Ye (2006) conducted a field study of a micropiled raft foundation. They conducted load tests on a micropiled raft comprised of a square raft (1.5 m x 1.5 m) supported by four micropiles 150 mm in diameter and spaced at $5D_{mp}$. It was found that the load transmitted by the micropiles was about 70% to 86% of the additional load that was applied to the raft after it was underpinned by the micropiles. However, the effects of raft flexibility on the raft-soil interaction, the load sharing between raft and micropiles and differential settlement have not been investigated.

Tsukada et al. (2006) evaluated the improvement in bearing capacity of a spread footing due to reinforcement with micropiles. The tests were performed on small models that represented the footing and the micropiles. Three groups of models were made from different materials and with varying degrees of stiffness, including: (1) circular footings without micropiles, (2) circular footings with a single micropile and (3) circular footings with micropiles (n_{mp}=2-8). The soil beds were sand with different values of relative density. A wide range of micropile inclination angles ($\alpha_i = 0°$- $60°$) were used in the study. A number of observations could be made:

  (1) In dense sand, the dilation had a significant effect in increasing the bearing capacity compared to loose and medium dense sand.

(2) The bearing capacity of the spread footing reinforced with a micropile group was double the summation of the individual bearing capacity of the surface footing and the micropile load carrying capacity.

(3) The axial stiffness and skin friction of the micropiles had a significant influence on the bearing capacity of the system due to the increase in the confinement of the soil and enhanced interaction between the footing and the micropile group (Tsukada et al., 2006).

Sagara et al. (2002) performed in-situ tests of a high capacity micropile foundation on Japanese mountain ground. The micropiles were 205 mm in diameter and 8 m in length. The micropiles were reinforced using a 177.8 mm O.D with 12.7 mm wall thickness along with 51 mm diameter steel reinforcement bars. The grout-ground bonding zone was about 4 m. The ultimate capacity of 4100 kN was attained at 60 mm vertical displacement; however, the yield capacity was about 2100 kN and was reached at 12.4 mm displacement.

Thomson et al. (2007) performed a field investigation on micropiles under axial compression, axial tension and lateral loads. The purpose of the investigation was to confirm the micropile design according to FHWA (2005). Eight tests were performed as follows: 2 tests under axial compressive loading, 2 tests under axial tension loading and 4 tests under lateral loading. All micropiles consisted of 273 mm outside diameter steel casing with 13 mm wall thickness as well as an inner steel casing with 168 mm outside diameter and 9.5 mm wall thickness. In addition, each micropile contained a #20 reinforcement steel bar that was extended from the top of the micropile and along the full length of the micropile. The grout strength, $f_c^{`} = 25$ MPa after 7 days and 35 MPa after 28

days. The embedded lengths of micropiles varied between 16.8 m and 27.5 m and the cased lengths varied from 7.3 m to 12 m. Based on the micropile load tests, the following observations were made:

(1) The micropile design according to the FHWA (2005) provides a reasonable agreement with field load tests.

(2) The grout volume used in the tests was significantly higher than the geometrical volume of the hole which indicated that the grout penetrated into the ground and the micropile diameter increased.

(3) The lateral response observed from the field test was stiffer compared to the predicted behaviour.

2.2.7.   Behaviour of Micropiles under Lateral Load

2.2.7.1.   Single Micropiles

One of the major disadvantages of micropiles is their low lateral resistance due to their high slenderness ratio and small flexural rigidity (EI). To overcome this limitation in current practice, a steel casing must be installed in the top part of the micropile to increase its flexural rigidity. However, the behaviour of a micropile under lateral loads is similar to the behaviour of a driven pile or drilled shaft. The lateral load will be carried by the top part of the micropile with a length equivalent to 15 to 20 times the micropile diameter. Beyond this length (15-20 D_{mp}) the micropile will not experience any noticeable bending moments caused by lateral loads applied at the ground level. In addition, the center steel reinforcement will not contribute much to the lateral resistance

(FHWA, 2005). Therefore, it is recommended to use 20 D_{mp} as the minimum micropile cased length.

Several methods can be used to evaluate the lateral load capacity, bending moments and micropile head deflection. To evaluate the lateral capacity of the micropile, Brom's method (1964a and 1964b) and the pressuremeter method (Meyerhof and Sastry, 1987) can be used. In order to evaluate the micropile head movement and its internal forces, the elastic continuum method (Randolph, 1981) and the nonlinear analysis p-y curves approach (Reese et al., 1974 and Reese and Welch, 1975) can be used. The FHWA (2005) guidelines provide seven steps to evaluate the lateral capacity, bending moments and micropile head deflection using the LPILE software package.

Richards and Rothbauer (2004) performed 20 lateral load tests on vertical micropiles as part of eight different projects. All micropiles had length-to-diameter ratios greater than 20 and consisted of steel casing. Their diameters ranged from 197 mm to 381 mm. The yield strength of the steel casing was 552 MPa and the grout unconfined compressive strength was 34.5 MPa. The results obtained from the load tests were compared to the predictions using different analytical methods including: the LPILE program, NAVFAC method (NAVFAC, 1986) and characteristic load method (CLM) (Duncan et al., 1994). Considering the load corresponding to 6.25 mm as the ultimate load criterion, the ultimate lateral load varied between 40 kN and 120 kN. The main observation from the comparison was that the ultimate loads calculated using the different methods were conservative, and the calculated responses were larger than the observed responses during the lateral load tests.

Long et al. (2004) conducted lateral load tests on 10 micropiles that were 15.2 m long with steel casings 244 mm OD and 13.8 mm thick. The load test results were compared with the predictions made by using the LPILE software, and the two sets were in reasonable agreement with the difference being within ±10%.

Teerawut (2002) conducted lateral load tests on micropiles with different diameters installed in sand soil with different relative densities and back calculated the corresponding p-y curves. It was observed that the stiffness of the p-y curves increased as the pile diameter increased. However, this increase was marginal for micropiles installed in dense sand.

2.2.7.2. Micropile Groups

The performance of a micropile group is similar to that of other pile types, i.e. it is affected by the micropile spacing and soil type. Normally, the pile group deflection is 2 to 3 times higher than the deflection of a single pile under lateral load equal to the average load per pile within the group. Moreover, the lateral resistance of the piles in the lead row (along the load direction) is significantly higher than the resistance of piles in subsequent rows. This behaviour occurs because the soil between two subsequent piles loses some of its strength due to the movement of the lead row, which is known as the shadowing effect. To account for the group effect in the analysis using the p-y curve approach, the p-y curves for any pile in the group is based on the modified p-y curve of a single pile using the p-multiplier, P_m. The P_m depends on the position of the pile within the group to account for the pile-soil-pile interaction (Brown et al., 1988).

As part of the French National Project on Micropiles (FOREVER), many lateral load tests were conducted on micropile groups to evaluate their lateral performance using

square micropiles with width (B_{mp}) of 0.2 m (Shahrour and Ata, 2002). The results indicated that for a micropile group with $S/B_{mp} = 7$ subjected to an in-line horizontal load, will not be influenced by the group effect.

2.2.8. Cyclic Behaviour of Micropiles

Micropiles are used to enhance the seismic performance of an existing foundation system located in seismically active areas in order to withstand the seismic forces as required by the design code. In recent years, micropiles have been used increasingly for seismic retrofitting projects due to their construction advantages for underpinning situations.

The seismic response of micropiles is complex as it is affected by the soil non-linear behaviour, the gapping between the soil and micropile, and soil-micropile-structure interaction. In this section, a number of previous studies on the cyclic response of micropiles and micropile group are presented.

McManus et al. (2004) investigated the influence of cyclic loading on model micropile systems installed in loose sand ($D_r = 40\%$), considering the cyclic shear strain level. The study involved inclined single micropile and 2-micropile group (30° from vertical axis). The saturated sand was contained in a laminated box that was 2 m deep by 1.8 m long by 0.8 m wide. Both tests were subjected to two levels of shaking intensity (0.12 g and 0.16g) using a one dimensional shaking table. The study showed that a single micropile had little influence on soil deposit. On the other hand, the two inclined micropiles reduced the shear strain by 50% and the settlement by 20%. This is because the 2 micropiles possibly prevented liquefaction of the saturated sand. (McManus et al., 2004).

Shahrour et al. (2001) conducted 3D finite element analysis of a model superstructure supported by a single micropile and a micropile group to evaluate their seismic performance considering the number of micropiles and their spacing as well as the location of the micropile within the group. The FEM consisted of 5771 20-node solid elements. In order to eliminate any effect of the boundaries, the base of the model was placed at depth equal to 1.5 time the length of micropiles (L_{mp} = 10 m); furthermore, the lateral boundaries of the soil mass in the direction of the excitation was placed at 6 L_{mp} from the micropile axis. The micropiles experienced significant inertial forces at the micropile head, in particular at a loading frequency close to the fundamental frequency of the superstructure. In addition, the bending moment for the case of for S/D_{mp} = 3 was 46% higher than the case for S/D_{mp} = 7. Moreover, the center micropiles experienced bending moment 40% than that of the corner micropiles (Shahrour et al., 2001).

Sadek and Shahrour (2004) investigated the behaviour of inclined micropiles subjected to dynamic loading. A fully 3D FEA was performed to compare the behaviour of a vertical micropile group with a group of inclined micropiles (α_i = 7°, 13° and 20°) in homogenous soil. The soil was modeled using linear elastic constitutive model and consisted of 21576 8-node elements. The 10 m micropiles were modeled using 34 3D-beam elements. The lateral boundaries were placed at distance of 240 micropile diameter (D_{mp} = 0.25 m) from the central axis of micropile group. The spacing-to-diameter ratio (S/D_{mp}) for the micropile group was 5. The dynamic loading was applied as harmonic acceleration with a_g = 0.2 g. The study showed a positive influence of inclination on seismic performance of the micropile group in terms of bending moment and shearing

forces. The bending moment and shearing forces were decreased by 35% and 92% respectively, by increasing α_i from 0° to 20° (Sadek and Shahrour, 2004).

Juran et al. (2001) performed centrifuge testing on single and groups of micropiles to evaluate the influence of micropile inclination, S/D_{mp} and group configuration on both the load transfer mechanism and resisting force of the micropile systems. The number of micropiles varied between 1 and 18, arranged different configurations considering S/D_{mp} = 3 and 5, and micropile inclination angle of 0°, 10° and 30° with vertical. The micropile groups were subjected to dynamic excitation with acceleration amplitudes that varied between 0.03 g and 0.5 g. The experimental results were compared to the predictions of the computer programs LPILE and GROUP (ENSOFT, 2014). A number of conclusions were drawn from this study:

(1) A positive group effect was achieved for S/D_{mp} =3 and S/D_{mp} = 5 compared to a single pile.

(2) For the inclined micropile group, the bending moment was reduced and the axial stress increased compared to the vertical groups.

(3) The computer program GROUP predicted successfully the bending moment for the inclined micropile, but failed to predict the positive group effect as achieved in the experimental tests (Juran et al., 2001).

Wong (2004) conducted FEA on single micropile and micropile groups arranged in different configurations and subjected to input motions with different intensities, which varied between 0.1g and 0.5g. As expected, the maximum bending moment and maximum deflection increased as the input motion intensity increased for both vertical and inclined micropiles.

Shahrour and Juran (2004), as part of the FOREVER project, conducted geotechnical centrifuge model testing and 3D numerical simulations to study the effect of the kinematic interaction, the group effect, and micropile inclination on micropiles and assessed the performance of micropiles in liquefiable soil. The geotechnical centrifuge model testing part of the FOREVER project will be discussed in more detail in Section 2.4.5. The results of the experimental and numerical investigation yielded the following observations:

(1) A positive group effect for the micropile group under seismic loading as compared with the single micropile or large spacing micropile group.

(2) The stiffness of the micropile was increased and both the shear force and bending moment were reduced for the inclined micropile system.

(3) Centrifuge testing results indicated soil confinement induced by the micropiles, which led to reduction in the build up of pore water pressure; and hence reduced the liquefaction potential.

Turan et al. (2008) performed a 3D finite element analysis on a group of nine micropiles subjected to dynamic excitation to evaluate the effect of casing termination, pile cap flexibility and the existence of surface surcharge loading on the lateral behaviour of micropile groups. The micropiles were 15 m long and 250 mm in diameter and they were connected to a 3 m x 3 m reinforced concrete cap considering different level of rigidity. The micropile group was subjected to a horizontal acceleration of 0.3g applied at the base of the model. Several conclusions were drawn based on the results, including:

(1) An increase of 100 % in bending moment was observed for the cased micropile at the location of the casing termination compared to the uncased micropile.

(2) The separation between soil and micropile was 33% higher for the flexible pile cap compared to the rigid pile cap. The effect of pile cap flexibility was noticeable on the micropile shaft-soil contact pressure between 1 m and 3 m below the pile cap. However, the effect of pile cap flexibility was negligible below 3 m.

2.3. PILED RAFT FOUNDATIONS

2.3.1. Introduction

A typical piled raft foundation system consists of the following components: raft, pile and soil. The interaction between these components improves the performance of the piled raft compared to the raft or the piles separately. Similarly, installing micropiles into an existing raft renders the whole system a micropiled raft foundation system. It is anticipated that the two systems would have similar performance characteristics. However, the literature is rich with studies on piled rafts but is devoid of studies on the performance of micropiled rafts. Thus, this section presents some studies that investigated the behaviour of piled raft foundations, which will be used later to evaluate the behaviour of micropiled rafts.

2.3.1.1. Background

The construction of a piled raft foundation is similar to the current practices used to construct pile group foundations in which the cap is normally cast directly on the ground.

Although this installation method allows a significant percentage of the load to be transmitted directly from the cap to the ground, the pile group is usually designed conservatively by ignoring the bearing capacity of the raft (i.e. the pile cap). The raft alone may provide adequate bearing capacity; however, it may experience excessive settlement, both maximum and differential. Therefore, the concept of settlement reducer piles was presented by Burland et al. (1978) where the piles are used to limit the average and differential settlements.

The vertical load is transmitted to the ground by both the raft and the piles in the pile raft foundation. This fact differentiates the piled raft from the pile group. The percentage of load each element carries depends on a number of factors, such as the spacing of piles, the number of piles, subsoil type, and the raft flexibility. The piles load share, can be described using the piled raft coefficient, α_{pr}, given by:

$$\alpha_{pr} = \frac{\sum_{i=1}^{n} Q_{pile,i}}{Q_{PR}} \qquad (2.8)$$

Where: Q_{pile} = load carried by a single pile; and Q_{pr} = total load carried by pile raft foundation (Mandolini, 2003).

According to Equation 2.8, α_{pr} for is equal to 0 a raft foundation with no piles, equal to 1 for a pile group and varies between 0 and 1 for a piled raft. Figure 2.2 shows the raft foundation, pile group and piled raft configurations.
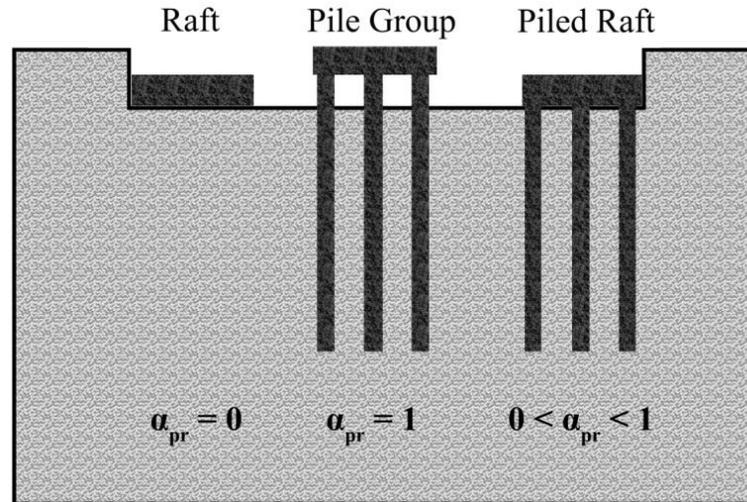
Figure 2.2. Raft, pile group and piled rafts foundation systems (after Mandolini, 2003)

Zeevaert (1957) described a successful application of a piled raft foundation to support a high rise building (the Tower Latino Americano) in Mexico City. Since then, several analytical and numerical solutions were developed to predict the load-settlement behaviour and the average and differential settlements for piled rafts. Poulos and Davis (1980) proposed an approximate analytical approach for piled rafts based on the behaviour of a single pile and suitable interaction factors along with a raft element. Randolph (1983) proposed an analytical method to evaluate the response of a piled raft foundation by combining the pile group and raft responses through a single interaction factor. Numerical solutions were also adopted to evaluate the performance of piled raft foundations using the boundary element method (BEM), finite element method (FEM) and hybrid numerical method as presented by the work of Weisner and Brown (1976); Hain and Lee (1978); Bilotta et al. (1991); Clancy and Randolph (1993) and Reul and Randolph (2003).

2.3.1.2. Advantages of a Piled Raft Foundation

The advantages of piled rafts over conventional pile groups are widely recognized. The most important advantages of piled rafts are listed here.

A piled raft foundation will require fewer piles in comparison to a pile group to satisfy the same design requirements, i.e. a more economical design. In a piled raft, the piles will provide sufficient stiffness to control the settlement at serviceability load and the raft will provide additional capacity at ultimate load. The raft can carry 30% to 50% of the applied load (Clancy and Randolph, 1993). On the other hand, the pressure applied from the raft to the subsoil may increase the lateral confining stress on the underlying piles, which can increase the pile capacity compared to a pile in a pile group (Katzenbach et al., 1998). Additionally, in case a pile in a piled raft becomes defective, the raft allows re-distribution of the load from the damaged pile to other piles (Poulos et al., 2011).

The optimum application for a piled raft foundation is when the raft can provide sufficient bearing capacity; however, the settlement and/or the differential settlements do not satisfy the serviceability design requirements. The following soil profiles are ideal for a piled raft: (i) soil profiles consisting of relatively stiff clay and (ii) soil profiles consisting of relatively dense sand. For both cases, a raft would satisfy the bearing capacity and stiffness requirements for the design while the piles would enhance the performance of the foundation system (Poulos, 2001).

2.3.2. Design of a Piled Raft

There are different design philosophies for a piled raft foundation system. The selection of the appropriate philosophy depends on the specific application of the piled

raft. For example, if the raft alone can sustain the applied load, but not the settlement. Therefore, the piles can be used to reduce the settlement. Randolph (1994) summarized the main design philosophies for a piled raft as the following:

(1) **The conventional design**: this design is similar to the pile group with similar piles spacing, but it allows the pile cap to transmit a portion of the load directly to the ground. This design will yield a pile group with reduction in the total number of piles because only 60 to 75 % of the total load is being carried by the piles.

(2) **The creep piling**: in this design, the raft alone can withstand the applied load; however, the piles are designed to reduce the settlement by reducing the net contact pressure between the raft and soil. The piles are typically operated at 70 ~ 80 % of their ultimate capacity. Moreover, an extreme version of creep piling allows the full capacity of the pile to be mobilized. This concept is based on using the pile to only reduce the settlement (Poulos, 2001).

(3) **Differential settlement control**: the previous two design approaches assume a uniform arrangement of piles underneath the raft in order to reduce the overall settlements to satisfy the design requirements. By reducing the total settlement, the differential settlements will also decrease in some case. However, this may require a large number of piles to control the differential settlements even though the average settlement is at an acceptable level. Therefore, using a limited number of piles located strategically, especially at the center of the raft, will reduce the differential settlements. These piles are known as a "central pile".

2.3.2.1. Axial Stiffness of Piled Rafts

A number of methods can be used to evaluate the bearing capacity of a piled foundation, some of which are simple and others are more complicated. The complexity is due to the interaction between different components of a piled raft foundation: pile-soil-interaction, pile-raft-interaction and raft-soil-interaction. For a preliminary design, the vertical loading capacity of a piled raft can be taken as the lesser of the following two values:

(1) The sum of the raft and all piles' ultimate capacities.

(2) The ultimate capacity of the block containing the raft and the piles in addition to the part of the raft outside the edge of the piles.

In order to estimate the load-settlement behaviour, the load sharing between the piles and raft and stiffness of piled raft, Randolph (1983 and 1994) proposed a procedure to evaluate the piled raft stiffness accounting for the stiffness of the piles and the raft and the piles-raft interaction using interaction coefficients based on an individual pile-raft unit. In this approach, the piled raft stiffness is calculated first, i.e.

$$K_{pr} = \frac{K_{PG} + K_r(1 - \alpha_{rp})}{1 - \alpha_{rp}^2 K_r K_{PG}} \qquad (2.9)$$

Where: K_{pr}= piled raft stiffness; K_{PG}= pile group stiffness can be estimated using the solution adopted by Poulos and Davis (1980); K_r= raft stiffness; α_{rp}= raft pile interaction factor. The raft-pile interaction factor is given by:

$$\alpha_{rp} = 1 - \frac{\ln(\frac{r_r}{r_o})}{\zeta} \qquad (2.10)$$

Where: r_r= average radius of raft which is equal to the area of the raft divided by the number of piles; r_o= radius of pile; $\zeta = \ln(r_m/r_o)$; r_m= $2.5\rho L_p(1-\nu_s)+2.5 D_p$; ρ= E_{sav}/E_{st}; E_{save} = average soil Young's modulus along pile shaft; E_{st} = soil Young's modulus at the pile tip; L_p= pile length; ν_s = Poisson's ratio of the soil; and D_p= pile diameter.

The proportion of the total applied load transmitted by the raft can then be estimated by:

$$\frac{P_r}{P_t} = \frac{K_r(1-\alpha_{rp})}{K_p + K_r(1-\alpha_{rp})} = X \qquad (2.11)$$

Where: P_r= load carried by the raft; P_t= total applied load; and X= the proportion of the total applied load transmitted by the raft.

Using Equations 2.9, 2.10 and 2.11, a tri-linear load-settlement curve can be obtained as illustrated in Figure 2.3. As described by Poulos (2001), the first segment of the curve between points O to A is drawn by using the stiffness of the piled raft which will remain effective until the piles are fully mobilized. The load P_1 marked on Figure 2.3 is calculated as:

$$P_1 = \frac{P_{up}}{1-X} \qquad (2.12)$$

Where: P_1= load corresponding to point A in Figure 2.3; P_{up}= the ultimate capacity of piles in the piled raft; and X= the proportion of the total applied load transmitted by the raft based on equation 2.11.

The slope of the second segment of the curve in Figure 2.3 (between points A and B) represents the stiffness of the raft alone which will remain operative until the ultimate

bearing capacity of the piled raft is reached. Moreover, the P_u can be calculated using the equation 2.11. The final segment of the load-settlement curve becomes horizontal (i.e. constant resistance).

Clancy and Randolph (1993) proposed an enhanced analysis to evaluate the raft pile interaction factor, α_{rp}, in which the raft was represented by a plate and the piles by springs. The results from this analysis demonstrated that the raft-piles interaction factor became constant at a value equal to 0.8-0.85 as the size of the pile group increased, regardless of the pile spacing, slenderness ratio or stiffness ratio.
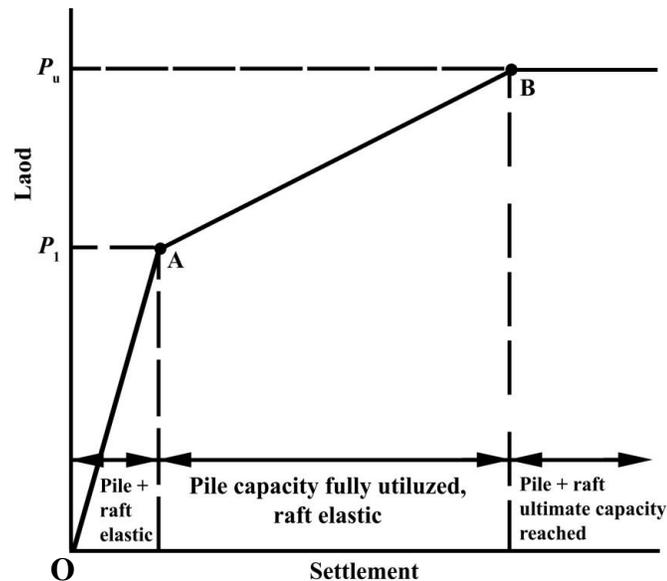
Figure 2.3. Simplified load settlement curve of piled raft (after Poulos, 2001).

Several methods are proposed conduct preliminary design of piled rafts including the evaluation of their ultimate bearing capacity and settlement. These methods include:

(1) Plate on springs method in which the raft is represented by a plate and the piles are represented by springs (Clancy and Randolph, 1993).

(2) Methods based on combining the finite element analysis for the raft and the boundary element analysis for the piles (e.g. Ta and Small, 1996).

(3) Methods based on a three-dimensional finite elements analysis (e.g. Katzenbach et al., 1998).

For the final design of piled raft foundations, it is highly recommended to perform a three-dimensional finite elements analysis taking into account the raft flexibility and the non-linearity of the raft, piles and soil.

2.3.2.2. Settlement of a Piled Raft

The average settlement of a piled raft can be estimated using the same concept of the piled raft interaction factor proposed by Randolph (1983 and 1994). With reference to Figure 2.3, the settlement of the piled raft can be calculated by using the piled raft stiffness, K_{pr}, to evaluate the settlement corresponding to any load between the points O and A. For loads between points A and B, the corresponding average settlement is calculated using the raft stiffness, K_r. However, this approach assumes that the raft is rigid. For more accurate prediction of the foundation average settlement, it is necessary to revise this approach to account for the raft flexibility.

Clancy and Randolph (1993 and 1996) analyzed the response of piled rafts by modeling them as a flexible plate and modeling the piles by rods and springs. Based on the results of the analysis, they developed charts that can be used conveniently to evaluate the average settlement for piled rafts with different pile-soil stiffness ratios, raft-soil stiffness ratios, pile slenderness ratios and spacing-to-pile diameter ratios.

2.3.2.3. Differential Settlement of a Piled Raft

The differential settlement should be evaluated carefully, especially for piled raft foundations with non-uniform loading. The differential settlement will depend mainly on the relative rigidity of the raft, the distribution of the applied load and the piles configuration (Randolph, 1994).

A number of methods can be used to evaluate the differential settlement for piled raft foundations. The equivalent piers method proposed by Poulos and Davis (1980) can be used to estimate the differential settlement within the piled raft foundation by using several piers beneath the raft (instead of modeling the whole group by a single pier).

Horikoshi and Randolph (1997) related the differential settlement and average settlement ratio to the raft-soil stiffness ratio, K_{rs}, given by:

$$K_{rs} = 5.57 \frac{E_r}{E_s} \frac{1-v_s^2}{1-v_r^2} \left(\frac{B_r}{L_r}\right)^{\alpha_o} \left(\frac{t_r}{L_r}\right)^3 \qquad (2.13)$$

Where: E_r= Raft elastic modulus; E_s= soil elastic modulus; v_s= Poisson's ratio of the soil; v_r= Poisson's ratio of the raft; B_r and L_r raft width and length; t_r= raft thickness; and α_o= the optimal value varies between -1 to 1. For convenience, the raft average settlement and differential settlement were presented in terms of charts for different K_{rs} and raft aspect ratio (B_r/L_r).

2.4. CENTRIFUGE MODELLING

2.4.1. Introduction

Performing a full scale testing program for raft-micropiled foundations could be extremely expensive if all important factors that influence their performance are to be investigated. Centrifuge testing offers an acceptable alternative for full-scale testing because it provides approximately the same stress level of the prototype case, which is important to replicate the soil stiffness and strength.

2.4.2. Concept of Centrifuge Modelling

The concept of this test is to rotate a body of certain mass (m) at a constant radius (r) with a steady speed (υ) about an axis. To maintain the circular path, the body will experience a constant radial centrifugal acceleration equal to $r\omega^2$. The body will be subjected to a radial force equal to $mr\omega^2$, where $r\omega^2 = \frac{\upsilon^2}{r}$ (ω = angular speed). This radial acceleration can be normalized by earth's gravity, g, so the body is subjected to an acceleration equal to ng where n is scale factor, which can be given by (see Figure 2.4):

$$n = \frac{r\omega^2}{g} \qquad (2.15)$$
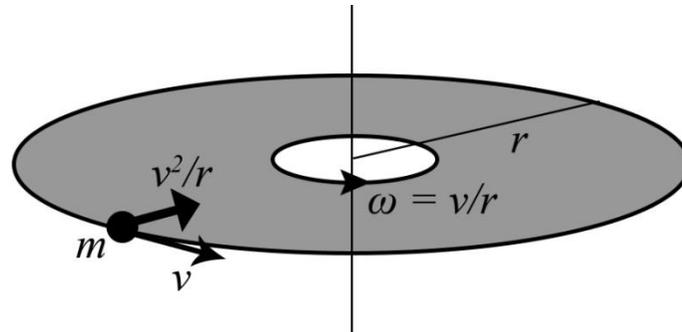
Figure 2.4. Typical movement of an object in a steady circular orbit (after Wood, 2004)

Under these conditions, the stresses in the centrifuge model will increase to maintain equilibrium and will be similar to the stresses at equivalent points on the prototype. However, the centrifuge model dimensions are scaled down by a linear scale equal to n as will be discussed later. However, the scale is not linear in all situations (Wood, 2004). Figure 2.5 shows a comparison between the soil under 1g gravity field and the soil in the centrifuge test under ng gravity field. Table 2.2 shows a comparison between the vertical stress level in 1-g model and centrifuge model to the vertical stress level in the prototype. Table 2.2 shows that the 1-g small-scale model reduces the stresses level at any equivalent point of the prototype, which can lead to some errors, especially if the model is sensitive in respect to the vertical and horizontal stresses in the soil such as the case for pile-soil interaction modelling. On the other hand, the small-scaled centrifuge model can replicate the same state of stress as the prototype case.
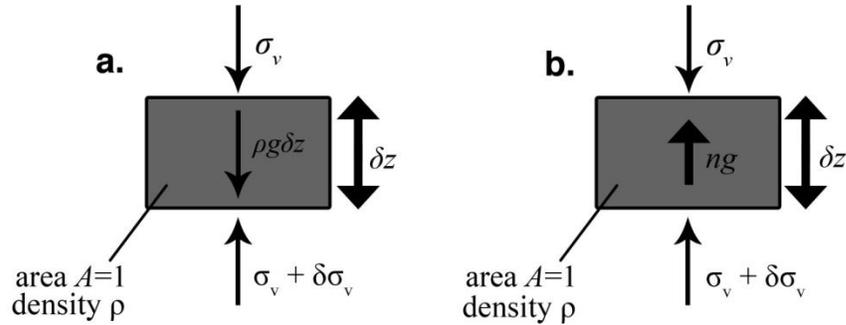
Figure 2.5. An element of soil: (a) at 1g gravity field and (b) on centrifuge test under ng gravity field (after Wood, 2004).

2.4.3. Scaling Laws of Centrifuge Modelling

The main advantage of the centrifuge testing is to model the prototype using a model with smaller dimensions while maintaining the soil state of stress unchanged between the prototype and the model. However, the scaling of the prototype has to follow certain scaling laws to simulate the real behaviour of the prototype for the problem under consideration. Garnier et al. (2007) presented a set of scaling laws necessary for accurate modeling of piled raft foundations under *ng* gravity field. Table 2.3 summarizes the scaling laws applicable to micropiled raft foundations. However, it may be difficult to use the same material in the small scale centrifuge model as the prototype because it would lead to a very small cross-section or thickness, especially at high gravity fields. In this case, using a material with lower elastic modulus (E) will lead to a reasonable (larger) cross-section. This is achieved by maintaining the proper stiffness property of the model. For example, the axial rigidity of a model pile can be simulated by:

$$\frac{E_p A_p}{E_m A_m} = n^2 \tag{2.16}$$

Where: $E_p A_p$ = axial rigidity for the prototype; and $E_m A_m$ = axial rigidity for the model.

As a result, choosing the model material is crucial and is influenced by a number of factors including: the test acceleration, the model size, the prototype size, the capacity of the centrifuge equipment and the ability to use the same material as the prototype.

Table 2.2. Scaling factors for parameters used to calculate the vertical stress in 1g testing and centrifuge testing (ng).

Quantity	1g testing		centrifuge testing (ng)	
	Prototype	Model	Prototype	Model
Depth, z (m)	h	h/n	h	h/n
Density, ρ_s (Kg/m^3)	1	1	1	1
Unit Weight, γ (kN/m^3)	$\rho_s g$	$\rho_s g$	$\rho_s g$	$\rho_s n g$
Stress = z*γ (kPa)	$h\rho_s g$	$h\rho_s g/n$	$h\rho_s g$	$h\rho_s g$

Table 2.3. Scaling laws used in centrifuge testing.

Characteristic	Model/ Prototype
Gravity	n
Density	1
Stress	1
Length	$1/n$
Acceleration	n
Dynamic Frequency	n
Velocity	1
Axial Rigidity, EA	$1/n^2$
Flexural Rigidity, EI	$1/n^4$
Force	$1/n^2$
Mass	$1/n^3$
Moment	$1/n^3$

2.4.4. Issues Related to the Centrifuge Modeling

In geotechnical centrifuge modelling, there are some issues related to the radius of rotation, the lateral acceleration, soil particles size effect and gravity switch-on. This section presents these issues and discusses their effects on the centrifuge model.

2.4.4.1. Radius of Rotation

As the model starts to accelerate, it experiences a small variation in the acceleration throughout its depth due to the variation of the radius of rotation along the sample height, which may lead to error in the stress field. This variation in the state of stress will increase with the sample depth. To overcome this error, it is recommended to use the effective radius, i.e.

$$r_e = r_t + \frac{h_m}{3} \qquad (2.17)$$

Where: r_e = effective radius; r_t = radius at top of the model; and h_m = height of the model.

The effective radius is then used in calculating the scale factor (Equation 2.15). In this case, the maximum error in the soil vertical stress would be in the range of 3% of the prototype stress (Taylor, 1995). To further reduce the error is soil stresses due to the effect of the radius of rotation, the model height should be $\leq 0.1\ r_e$ (Wood, 2004).

2.4.4.2. Scale Effect

In order to evaluate the effect of the soil particle size on the accuracy of the centrifuge model, Ovesen (1975) examined the behaviour of circular foundations resting on sand. He conducted a number of tests using different models at various centrifugal accelerations in which the models represented the same prototype. The results indicated that the behaviour was consistent in general; however, when the foundation diameter to the average grain size ratio was less than 15, the behaviour deviated compared to the common behaviour. Therefore, it is recommended to keep the foundation diameter to the average grain size ratio greater than 15. Based on these results Ovesen (1975) established guidelines for the critical ratios between the average soil particle size (D_{50}) and the model

dimensions. Additionally, Taylor (1995) demonstrated that if these guidelines are not respected, the soil particles in the geotechnical centrifuge model will affect the behaviour of the model as opposed to the soil behaving like a continuum as it is the case in the prototype.

2.4.4.3. Rotational Acceleration Field

During the centrifuge flight, the acceleration direction is towards the center of rotation. Therefore, the direction of acceleration with respect to the vertical plane along the width of the model will be altered. For instance, a model with half width = 400 mm tested in a centrifuge with an effective radius, r_e = 2 m, it will experience a maximum lateral acceleration of 0.4/2 or 0.2 times the vertical acceleration (Taylor, 1995). To minimize the effect of rotational acceleration on the results, it is suggested to place the part of the model that will experience the major event at the central section of the model.

2.4.4.4. Gravity Switch-On

Constructing the model under the prototype stress (in flight) is ideal (e.g. pile installation). However, in most case it is difficult or requires a powerful and advanced robotic system to construct the model in flight. Therefore, in many geotechnical studies, the model is constructed at 1-g. In this case, the overburden stresses will increase suddenly during in flight (gravity switch-on). To minimize the effect of the gravity switch-on, the gravity should be increased at a very slow rate, especially for soils that may be influenced by the stress history (Barchard, 2002).

2.4.4.5. Special Considerations for Deep Foundations

As mentioned earlier, it is ideal to install the model in flight (at ng) in order to form the proper stress regime in the soil. The type of installation is critical for modelling the pile because its behaviour is influenced by the state of stress in the soil. Kusakabe (1995) investigated the influence of installing the pile in flight and compared it to installing the pile at 1 g. For both cases of installations, the piles were tested at 70 g. It was found that when installed at 1 g, the pile capacity decreased by 60% compared to the case of in-flight installation.

2.4.5. Previous Small-Scale and Centrifuge Modelling of Micropiles

Several studies were conducted using small-scale (1g) and geotechnical centrifuge modeling (ng) to evaluate the performance of single micropiles or micropile groups taking into account the effect of a number of variables such as micropile diameter, number of micropiles in a group and type of loading. This section presents the details of some experimental programs and their findings.

As part of the FOREVER project, Juran et al. (2001) conducted geotechnical centrifuge tests to evaluate the effects of the micropile-soil-micropile and the micropile inclination on the behaviour of micropile groups under static and seismic loading. The micropiles were modeled using Polystyrene with similar flexural rigidity of the micropile prototype. The interface between the micropile and soil simulated the high grout-ground bonding by gluing sand particles along the entire micropile shaft. The soil bed comprised Nevada sand with D_r = 57% and D_{50} = 0.13 mm. To eliminate the influence of the grain size on the load settlement behaviour, the ratio between the diameter of the model

micropile and average grain size, D_{mp}/D_{50}, should be within 30 to 180 (Ovesen, 1975). Therefore, Juran et al. (2001) used micropile diameters of 6.5 mm and 9.5 mm to achieve ratios of 50 and 73, respectively. To reduce the side friction between the soil and the container walls, a 0.2 mm thick latex membrane was used.

Tsukada et al. (2006) investigated using a micropile group to retrofit shallow foundations that had been damaged during an earthquake event. They conducted 1g small-scale model tests in loose, medium dense and dense sands to evaluate the load-displacement behaviour of this enhanced foundation system. The mean grain size for the sand (D_{50}) was 0.18 mm. The effects of several factors were examined: the micropile length and diameter, number of micropiles in a group and type of soil. The footing was modeled using 40 mm circular stainless steel plate and two micropile models were used: stainless steel bar with $D_{mp} = 1.83$ mm and plastic bar with $D_{mp} = 2$ mm. To simulate the high grout-ground bonding, sand particles were glued along the entire micropile shaft. The sand was placed using a funnel with a nozzle at the bottom to freely place the oven dry sand. This installation procedure reduced the disturbance of the sand around the micropile and minimized locked-in stresses in the sand and micropile. The tests comprised only axial compression loading and no strain gauges were used to evaluate the skin friction of the micropile.

McManus et al. (2004) conducted 1g small scale model tests to evaluate the influence of micropiles on cyclic shear strain of loose sand. Two tests were performed: one without micropiles and the other with two inclined micropiles. The models were enclosed in a large laminar tank that was placed on a one degree of freedom shaking table was used to perform the tests. Flexible membrane linear with a thickness of 1 mm was

used to contain the soil within the container. Several instrumentations (i.e. potentiometer and accelerometers) were used to evaluate the micropile displacement and acceleration, and soil settlement. The soil bed was grade 30/60 silica sand and was placed in the container using air pluviation.

Rose et al. (2013) investigated the performance of perimeter pile groups in clays using geotechnical centrifuge testing and numerical modeling. The study considered different pile group arrangements. The pile diameter was 300 mm for all different cases. It was found that the failure mechanism for the perimeter groups consisting of 14 to 20 piles with $1.75D_p$ spacing was block failure and the group efficiency ratio was about 0.9.

2.5. SUMMARY

In this chapter a comprehensive review about micropiles, piled raft and geotechnical centrifuge technology. In this review, different types of micropiles, design requirements and classification are introduced; in addition, a number of previous studies are discussed. For piled rafts, a brief description of design methods is presented along with a brief description of the previous studies conducted to investigate the performance of piled rafts under different types of loading. A brief description of the concept of geotechnical centrifuge testing is presented including the scaling laws and issues associated with the centrifuge, followed by a short description of the previous work conducted to investigate the performance of micropile and micropile group using centrifuge technology.

REFERENCES

AASHTO. (2012). AASHTO LRFD Bridge Design Specifications. The American Association of State Highway and Transportation Officials (AASHTO), Customary U.S. Units, Section 10.

Barchard, J. (2002). Centrifuge Modeling of Piled Embankments on Soft Soils. M.Sc.E. Thesis, the University of New Brunswick.

Bilotta, E., Caputo, V. and Viggiani, C. (1991). Analysis of Soil-Structure Interaction for Piled Raft. *In* Proceeding of the 10th European Conference on Soil Mechanics and Foundation Engineering, Florence, 26-30 May 1991, Vol.1, pp. 315-318.

Broms, B. B. (1964a). Lateral Resistance of Piles in Cohesionless Soils. Journal of the Soil Mechanics and Foundations Division, **90**(3): 123-158.

Broms, B. B. (1964b). Lateral Resistance of Piles in Cohesive Soils. Journal of the Soil Mechanics and Foundations, **90**(2): 27-64.

Brown, D. A., Morrison, C. and Reese, L. C. (1988). Lateral Load Behaviour of Pile Group in Sand. ASCE Journal of Geotechnical Engineering, **114**(11):1261-1276.

Bruce, D. A., DiMillio, A. F. and Juran, I. (1995). Introduction to Micropiles: An International Perspective. Foundation Upgrading and Repair for Infrastructure Improvement, ASCE, Geotechnical Special Publication, (50): 1-26.

Bruce, D., Beam, J. and Myers, T. (2010). MiniJET: A New Type of Micropile. International Workshop on Micropiles, Washington, DC. September 22-25 .

Burland, J. B., Broms, B. B. and De Mello, V. B. (1978). Behaviour of Foundations and Structures. *In* Proceeding of the 9th International Conference on Soil Mechanics and Foundation Engineering, Tokyo, Vol. 2, pp. 496-546.

Cadden, A., Gomez, J., Bruce, D. and Armour, T. (2004). Micropiles: Recent Advances and Future Trends. ASCE Conference Proceeding: Current Practices and Future Trends in Deep Foundations (GSP 125), pp. 140-165.

CFEM. (2006). Canadian Foundation Engineering Manual. 4th edition. The Canadian Geotechnical Society.

Clancy, P. and Randolph, M. F. (1993). An Approximate Analysis Procedure for Piled Raft foundations. International Journal for Numerical and Analytical Methods in Geomechanics, **17**(12): 849-869.

Clancy, P. and Randolph, M. F. (1996). Simple Design Tools for Piled Raft Foundations. Géotechnique, **46**(2): 313-328.

Duncan, J. M., Evans, J. L. and Ooi, P. S. (1994). Lateral Load Analysis of Single Piles and Drilled Shafts. Journal of Geotechnical Engineering, **120**(6): 1018–1033.

ENSOFT. (2014). GROUP v. 2014 User Manual.

FHWA. (2005). Micropile Design and Construction Guidelines, Implementation Manual. National Highway Institute.

Garnier, J., Gaudin, C., Springman, S., Culligan, P., Goodings, D., Konig, D., Kutter, B., Phillips, R., Randolph, M. F. and Thorel, L. (2007). Catalogue of Scaling Laws and Similitude Questions in Geotechnical Centrifuge Modeling. International Journal of Physical Modelling in Geotechnics, **8**(3):1-23.

Hain, S. J. and Lee, I. K. (1978). The Analysis of Flexible Pile-Raft System. Géotechnique, **28**(1): 65-83.

Han, J. and Ye, S. (2006,). A Field Study on the Behaviour of a Foundation Underpinned by Micropiles. Canadian Geotechnical Journal, **43**(1): 30-42.

Horikoshi, K. and Randolph, M. (1997). On the Definition of Raft-Soil Stiffness Ratio for Rectangular Rafts. Géotechnique, **47**(5): 1055-1061.

IBC. (2009). International Building Code [ICC,IBC]. Country Club Hills, IL: International Code Council, Inc.

Jeon, S. S. and Kulhawy, F. H. (2001). Evaluation of Axial Compression Behaviour of Micropiles. *In* Proceedings of a specialty conference: Foundations and Ground Improvement (GSP 113) (pp. 460-471). Blacksburg, Virginia: ASCE.

Juran, I., Benslimane, A. and Hanna, S. (2001). Engineering Analysis of Dynamic Behaviour of Micropile Systems. Transportation Research Record: Journal of the Transportation Research Board, **1772** (1):91-106.

Katzenbach, R., Arslan, U., Moorman, C. and Reul, O. (1998). Piled Raft Foundation: Interaction Between Piles and Raft. Darmstadt Geotechnics, Darmstadt University of Technology, **4**(1): 279-296.

Kusakabe, O. (1995). Foundations. In R. N. Taylor (Ed.), "Geotechnical Centrifuge Technology" (pp. 120-172). London: Chapman and Hall.

Lizzi, F. (1982). The Static Restoration of Monuments: Basic Criteria-Case Histories, Strengthening of Buildings Damaged by Earthquakes . Genova: Sagep Editrice.

Long, J., Maniaci, M., Menezes, G. and Ball, R. (2004). Results of Lateral Load Tests on Micropiles. *In* Proceedings of sessions of the GeoSupport Conference: Innovation and Cooperation in the Geo-Industry, Orlando, Florida: Geo-Institute of the American Society of Civil Engineers, pp. 122-133.

Mandolini, A. (2003). Design of Piled Raft Foundation: Practice and Development. *In* Proceedings of the 4th International Geotechnical Seminar on Bored and Auger Piles Ghent, Belgium, June 2-4, 2003: Millpress, Rotterdam, pp. 59-80.

McManus, K. J., Charton, G. and Turner, J. P. (2004). Effect of Micropiles on Seismic Shear Strain. *In* Proceedings of the GeoSupport Conference: Drilled Shafts, Micropiling, Deep Mixing, Remedial Methods, and Specialty Foundation Systems, Orlando Florida, United States: American Society of Civil Engineers, pp. 134-145.

Meyerhof, G. G. and Sastry, V. V. (1987). Full-Displacement Pressuremeter Method for Rigid Piles under Lateral Loads and Moments. Canadian Geotechnical Journal, **24**(4): 471-478.

NAVFAC. (1986). Foundation and Earth Structures, Design Manual 7.02. Naval Facilities Engineering Command (NAVFAC).

Ovesen, N. K. (1975). Centrifugal Testing Applied to Bearing Capacity Problems of Footing on Sand. Géotechnique, **25**(2): 394-401.

Poulos, H. G. (2001). Piled Raft Foundations: Design and Applications. Géotechnique, **51**(2): 95-113.

Poulos, H. G. and Davis, E. H. (1980). Pile Foundation Analysis and Design. New York: Wiley.

Poulos, H. G., Small, J. C. and Chow, H. (2011). Piled Raft Foundations for Tall Buildings. Geotechnical Engineering Journal of the SEAGS and AGSSEA, **42**(2): 78-84.

Randolph, M. F. (1994). Design Methods for Piled Groups and Piled Rafts. *In* Proceeding of the 13th ICSMFE, New Delhi, India, pp. 61-82.

Randolph, M. F. (1983). Design of Piled Raft Foundations. *In* Proceeding of the International Symposium on Recent Developments in Laboratory and Field Tests and Analysis of Geotechnical Problems, 6-9 December 1983, Bangkok, pp. 525-537.

Randolph, M. F. (1981). The Response of Flexible Piles to Lateral Loading. Géotechnique, **31**(2): 247–59.

Reese, L. C., and Welch, R. C. (1975). Lateral Loading of Deep Foundations in Stiff Clay. Journal of the Geotechnical Engineering Division, **101**(7): 633-649.

Reese, L. C., Cox, W. R. and Koop, F. D. (1974). Analysis of Laterally Loaded Piles in Sand. Paper Number OTC 2080, *In* Proceeding of the Fifth annual offshore technology conference. Dallas, Texas, Vol.2, pp. 473-485.

Reul, O. and Randolph, M. F. (2003). Piled Rafts in Overconsolidated Clay: Comparison of in Situ Measurements and Numerical Analysis. Géotechnique, **53**(3): 301-315.

Richards, T. D. and Rothbauer, M. J. (2004). Lateral Loads on Pin Piles (Micropiles). *In* Proceedings of the GeoSupport Conference: Drilled Shafts, Micropiling, Deep Mixing, Remedial Methods and Specialty Foundation Systems, Orlando Florida, United States: American Society of Civil Engineers, pp. 158-174.

Rose, A. V., Taylor, R. N. and El Naggar, M. (2013). Numerical Modelling of Perimeter Pile Groups in Clay. Canadian Geotechnical Journal, **50**(3): 250-258.

Sadek, M. and Shahrour, I. (2004).Three-Dimensional Finite Element Analysis of the Seismic Behaviour of Inclined Micropiles. Soil Dynamics and Earthquake Engineering, **24**(6):473-485.

Sagara, M., Shito, K., Igase, Y., Ohashi, G., Saito, E., Sasaya, T. and Hatano, T. (2002). In-situ Load Test of High Capacity Micropile Foundation on Mountain Ground. *In* Proceedings of the 5th International Workshop on Micropile. Venice, Italy, International Society for Micropiles.

Shahrour, I. and Ata, N. (2002). Analysis of the Consolidation of Laterally Loaded Micropiles. Ground Improvement, **6**(1): 39-46.

Shahrour, I. and Juran, I. (2004). Seismic Behaviour of Micropile Systems. Ground Improvment, **8**(3): 109-120.

Shahrour, I., Sadek, M. and Ousta, R. (2001). Seismic Behaviour of Micropiles: Used as Foundation Support Elements: Three-Dimensional Finite Element Analysis. Transportation Research Record: Journal of the Transportation Research Board, **1772**(1): 84-90.

Shong, I. L. and Chung, F. C. (2003). Design and Construction of Micropiles. Geotechnical Course for Pile Foundation Design and Construction, IPOH, (29-30 September, 2003) .

Ta, L. D. and Small, J. C. (1996). Analysis of Piled Raft System in Layered Soils. International Journal for Numerical and Analytical Methods in Geomechanics, **20**(1): 57-72.

Taylor, R. N. (Ed.). (1995). Geotechnical Centrifuge Technology. 1st edition. London: Chapman and Hall.

Teerawut, J. (2002). Effect of Diameter on the Behaviour of Laterally Loaded Piles in Weakly Cemented Sand. Ph.D. Dissertation, University of California, San Diego, California.

Thomson, P., Leew, B., Zakeri, A., Becker, D., Bunce, C. and Dittrich, P. (2007). Axial Compression, Axial Tension and Lateral Load Response of Pre-Production Micropiles for the CPR Mile 62.4 Nipigon Subdivision Bridge. *In* Proceedings of the 8th International Workshop on Micropiles (IWM). Toronto, ON, Canada: IWM.

Timothy, M. J., Bean, J. J. and Bolton, M. K. (2012). MiniJET: a New Type of Micropile. *In* Proceedings of Grouting and Deep Mixing 2012. American Society of Civil Engineers (ASCE). New Orleans, Louisiana (15-18 February 2012), pp. 1095-1104.

Tsukada, Y., Miura, K., Tsubokawa, Y., Otani, Y. and You, G.-L. (2006). Mechanism of Bearing Capacity of Spread Footings Reinforced With Micropiles. Soils and Foundations, **46**(3): 367-376.

Turan, A., El Naggar, M. H. and Hinchberger, S. (2008). Lateral Behavior of Micro-Pile Groups under Static and Dynamic Loads. In Proceedings of the 4th Canadian Conference on Geohazards.

Weisner, T. J. and Brown, P. T. (1976). Behaviour of Piled Strip Footings Subject to Concentrated Loads. Australian Geomechanics Journal, **G6**(1): 1-5.

Wood, D. M. (2004). Geotechnical Modelling. 1st edition. London and New York: Spon Press.

Wong, J. C. (2004). Seismic Behavior of Micropiles. Doctoral dissertation, Washington State University.

Zeevaert, L. (1957). Foundation Design and Behaviour of Tower Latino Americana in Mexico City. Géotechnique, **7**(3): 115-133.

CHAPTER 3 CENTRIFUGE TESTING PROGRAM

3.1. INTRODUCTION

In the field of geotechnical engineering, centrifuge technology has been a valuable tool for evaluating an array of complex problems, such as soil liquefaction, soil-structure interaction and behaviour of underground structures (e.g. foundations, culverts and tunnels). Professor Schofield in the 20th Rankine lecture in 1980 described one of the first centrifuge facilities (i.e. the Cambridge Geotechnical Centrifuge) and discussed a number of projects, which emphasized the ability of the geotechnical centrifuge to model a wide range of sophisticated geotechnical problems. For example, it was used to evaluate remoulded soil behaviour, tunnels in soft ground soil, flow slides and fractures (Schofield, 1980). The results of a centrifuge test can provide excellent data for calibrating and verifying the results of numerical modeling.

A number of studies were performed to understand the performance of micropiles using centrifuge technology under different types of loading as presented in Section 2.4.5. However, more studies are needed to understand the effect of the flexibility of a raft on the overall behaviour of piled and micropiled raft foundation systems, as well as using the micropiled raft as a new foundation system. Flexible rafts tend to deform more than stiff rafts; due to this deformation of the flexible raft, the underlying soil will experience larger deformation and consequently more load will be carried by the raft. It is necessary to investigate the behaviour of a micropiled raft in both sand and clay soil to understand the behaviour of micropiled rafts comprehensively in different soil types. Furthermore, retrofitting a raft foundation with micropiles would result in a change in its overall behaviour and the raft foundation would start to perform as a micropiled raft foundation.

In addition, using micropiled rafts (MPR) system as a new highly efficient foundation system has some advantages that combines the benefit of the piled raft system and the efficient installation of micropiles and associated ground improvement. Thus, the main objective of the current research is to evaluate the overall behaviour of a micropiled raft under vertical loading in sand and clay.

This objective will be achieved using geotechnical centrifuge modeling and finite element analysis. The aim of the centrifuge testing is to provide accurate responses of different micropiled raft configurations under vertical load in both sand and clay. The results of the centrifuge tests are then used to calibrate an advanced 3D finite element model (FEM), which will be employed to perform an extensive parametric study. This chapter describes the centrifuge test facility, the preparation of the physical model, the instrumentation, the design and preparation of soils, the design and setup of the test headwork, and the test plan.

3.1.1. The C-CORE Centrifuge Center

The C-CORE Centrifuge Center at Memorial University of Newfoundland, St. John's, has an Acutronic 680-2 centrifuge. It has a maximum rotational speed of up to 189 rpm with a maximum centrifugal acceleration of 200 g at an effective radius of 5 m. The maximum payload at 100g and 200g is 2.2 tons and 0.65 tons, respectively. An HBM QuantumX MX840A 48 channel data acquisition system is used to collect electrical signals from strain gauges and transducers throughout the tests. In order to produce high quality results and accurately capture the sudden changes in acceleration, the data acquisition samples the data at high frequency. The data acquisition system has the ability

to sample data at a high rate of up to 19.2 kHz. However, for the static loading tests conducted in this study, the sampling rate was set at 5 Hz (i.e. 5 readings per second).

3.1.2. Instrumentation

Different instrumentations were used to measure strain, movement, load, excess pore pressure and contact pressure. The strain gauges were used to evaluate the axial forces acting on the micropiles due to the vertical load. The differential raft settlement due to the concentrated load was measured using a linear variable differential transducer (LVDT), which was placed on the edge of the raft. In addition, a very sensitive laser beam was used to accurately measure the axial deformation at the center of the raft. Moreover, miniature pressure transducers were used to measure the contact pressure between the raft and the soil. Pore pressure transducers (PPT) were used in the clay test to measure the excess pore pressure and its dissipation during the spinning. All the details of instrumentation used in this study will be presented along with the calibration data in a subsequent dedicated section.

3.2. MODEL DESIGN

The centrifuge testing program consisted of the following tests: (i) a single micropile installed in sand; (ii) a raft with a thickness equivalent to 0.6 m at prototype scale resting on the sand; (iii) three micropiled groups with different raft thicknesses installed in sand (i.e. 0.3 m, 0.45 m and 0.6 m on prototype scale); (iv) one test to evaluate reduction of raft differential settlement using a single micropile installed at the center of a raft 0.6 m thick resting on sand; (v) a single micropile installed in clay; (vi) a raft with a thickness equivalent to 0.6 m at prototype scale resting on clay; and (vii) a micropiled raft with a

thickness equivalent to 0.6 m at prototype scale in clay. Table 3.1 summarizes all tests performed throughout this investigation.

All tests were performed under a centrifugal acceleration of 50g. The prototype size of the micropile was 150 mm. To obtain reasonable model size to deal with using the linear scaling factor of 50, the models of the rafts and micropiles were fabricated using PVC, which has a modulus of elasticity smaller than the prototype concrete. Using the scaling laws for the axial rigidity of the micropiles and the flexural rigidity of the raft (Eqs. 3.1 and 3.2 below), the models had reasonable dimensions, facilitating the installation of strain gauges to measure the axial forces in the micropiles.

Table 3.1. Summary of the testing program.

Test	Material	Test Description	Micropile/s	Raft
1	Sand	Only micropile	Single micropile	-
2		Only raft	-	Raft only
3		Micropiled raft	4 micropiles	0.6 m equivalent thickness raft at prototype scale
4			4 micropiles	0.45 m equivalent thickness raft at prototype scale
5			4 micropiles	0.3 m equivalent thickness raft at prototype scale
6		Micropile as settlement reducer	Single micropile	0.6 m equivalent thickness raft at prototype scale
7	Clay	Micropiled raft	4 micropiles	0.6 m equivalent thickness raft at prototype scale
8[*]		Only raft	-	Raft only
9[*]		Only micropile	Single micropile	-

([*]) test 8 and 9 were conducted in the same flight.

$$\frac{E_p A_p}{E_m A_m} = n^2 \tag{3.1}$$

$$\frac{E_p I_p}{E_m I_m} = n^4 \tag{3.2}$$

Where: $E_p A_p$: axial rigidity for the prototype; $E_m A_m$: axial rigidity for the model; $E_p I_p$: flexural rigidity for the prototype; and $E_m I_m$: flexural rigidity for the model.

Eq. 3.1 and Eq. 3.2 accurately models the axial rigidity (EA) and flexural rigidity (EI) of the micropile and raft, respectively (Wood, 2004). Figure 3.1 presents the outline for the micropiled raft and the micropile as a settlement reducer and Table 3.2 provides the scaling laws and the model and prototype dimensions.
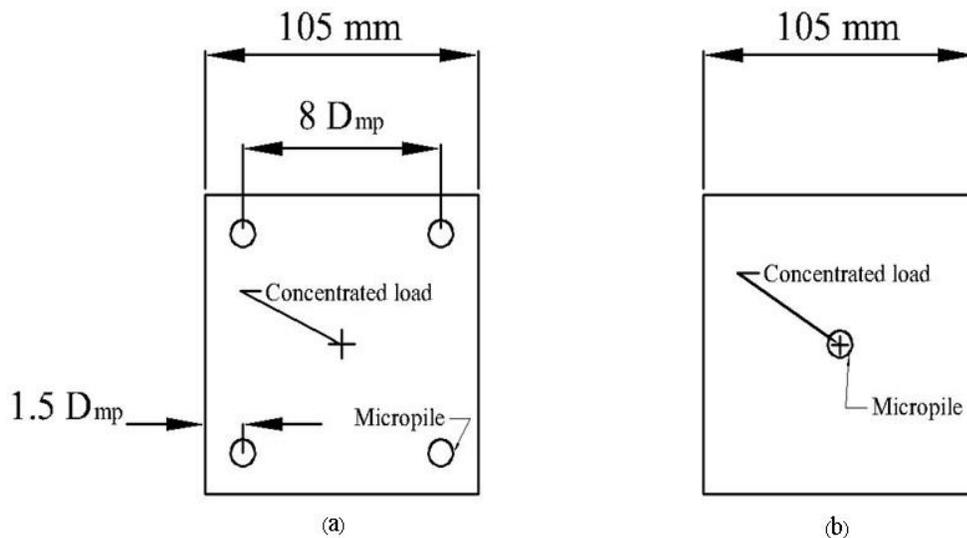
Figure 3.1. Layout for (a) a micropiled raft and (b) a micropile as a settlement reducer.

Table 3.2. Dimensions of models used throughout the testing program and equivalent prototype dimensions.

Description		Prototype size	Model size	Scaling law
Micropile Diameter		150 mm	9.53 mm	E_pA_p/n^2
Axial Rigidity (EA)		516737 kN	207 kN	
Micropile Length		10 m	200 mm	$1/n$
Raft Width and Length		5.25 m	105 mm	$1/n$
t_r=0.6 m	Raft Thickness	0.6 m	16.4 mm	E_pI_p/n^4
	Flexural Rigidity	697950 kN. m^2	0.112 kN. m^2	
t_r=0.45 m	Raft Thickness	0.45 m	12.3 mm	E_pI_p/n^4
	Flexural Rigidity	294448 kN. m^2	0.047 kN. m^2	
t_r=0.30 m	Raft Thickness	0.3 m	8.2 mm	E_pI_p/n^4
	Flexural Rigidity	87244 kN. m^2	0.014 kN. m^2	

3.3. SOIL MATERIALS AND CLASSIFICATION TESTS

This section presents a detailed description of the soils used throughout this study. Two different soil beds were considered in the investigation: (i) cohesionless soil; and (ii) cohesive soil. A number of classification tests were performed in order to determine the characteristics of the soils used in the tests. The soil properties are important consideration in the design of the centrifuge test and the calibration of the finite element model (FEM). All classification tests were performed according to the standards of the American Society for Testing and Materials (ASTM).

3.3.1. Cohesionless Soil

The sand considered in the investigation was poorly graded white dry silica sand (#00) with round to subround partials shape. The sand was supplied by Shaw Resource in 40 kg bags. The advantage of using silica sand is its ability to achieve a ratio greater than

15 between the foundation width and the average grain size (D_{50}) (Ovesen, 1975). As the raft width in this case was 105 mm and the D_{50} was equal to 0.21 mm, the ratio in this case was 500, which satisfied the condition for the test. The following tests were performed to characterize the sand: (i) a sieve analysis; (ii) maximum and minimum unit weight; (iii) a direct shear test and (iv) an in-flight cone penetration test (CPT).

3.3.1.1. Sieve Analysis

The particle size distribution was obtained by using the sieve analysis method according to ASTM D 422. Three sieve analysis samples were used to perform the test in order to obtain more representative results. Figure 3.2 shows the average results for the sieve analysis for the sand used in the centrifuge tests. According to Figure 3.2, the sand can be classified as poorly graded sand. Based on the sieve analysis, the mean grain size, D_{50}, is 0.21 mm. Table 3.3 presents the characterization values for the sand under consideration.
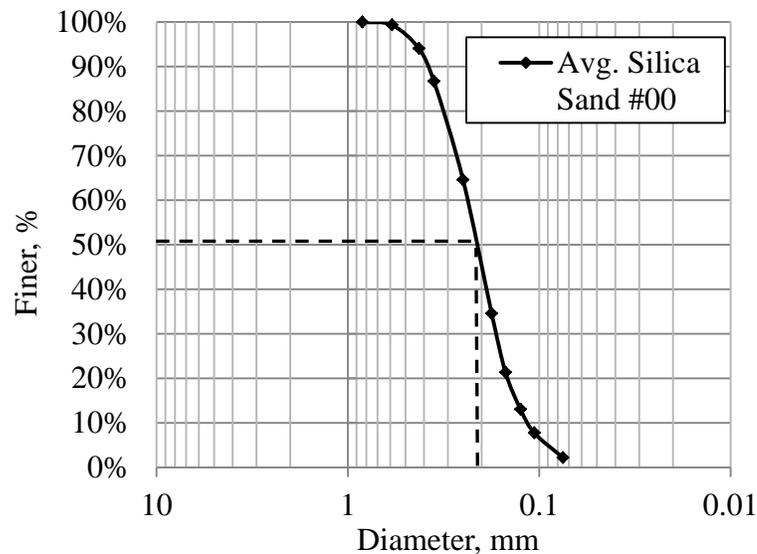
Figure 3.2. Average sieve analysis profile for the silica sand used in centrifuge tests.

Table 3.3. Results of sieve analysis for silica sand.

Mean grain size, D_{50}	0.21 mm
D_{10}	0.13 mm
D_{30}	0.17 mm
D_{60}	0.23 mm
Uniformity coefficient, C_u	1.86
Coefficient of curvature, C_c	1.11

3.3.1.2. Maximum and Minimum Unit Weight

To achieve the desired relative density, D_r, during the preparation of the sand test beds, it is required to identify the maximum unit weight, γ_{max}, and minimum unit weight, γ_{min}, for the silica sand. The tests were conducted according to ASTM D 4253 and ASTM D 4254 for the maximum and minimum unit weights, respectively. The maximum and minimum unit weights were found to be 16.39 kN/m^3 and 12.44 kN/m^3, respectively. Therefore, to achieve 70% relative density, the sand would have to be prepared at a unit weight equal to 14.97 kN/m^3, as per Equation 3.3 below.

$$\gamma_d = \frac{\gamma_{max}\,\gamma_{min}}{\gamma_{max} - D_r\gamma_{max} + D_r\gamma_{min}} \qquad (3.3)$$

Where: γ_d: unit weight at certain relative density (kN/m^3); γ_{max}: maximum unit weight (kN/m^3); γ_{min}: minimum unit weight (kN/m^3); and D_r: relative density (Budhu, 2007).

3.3.1.3. Direct Shear Test

Evaluating the shear strength for the sand is necessary for the interpretation of the load test data as well for simulating the sand behaviour in the FEM. The direct shear test was performed according to the ASTM D 3080. Five normal stresses values were applied

in the following manner: 25, 50, 75, 100, 200 and 300 kPa. The angle of internal friction, ϕ, was evaluated from the test results and was found to be 40°. Figure 3.3 shows the results of the direct shear test.
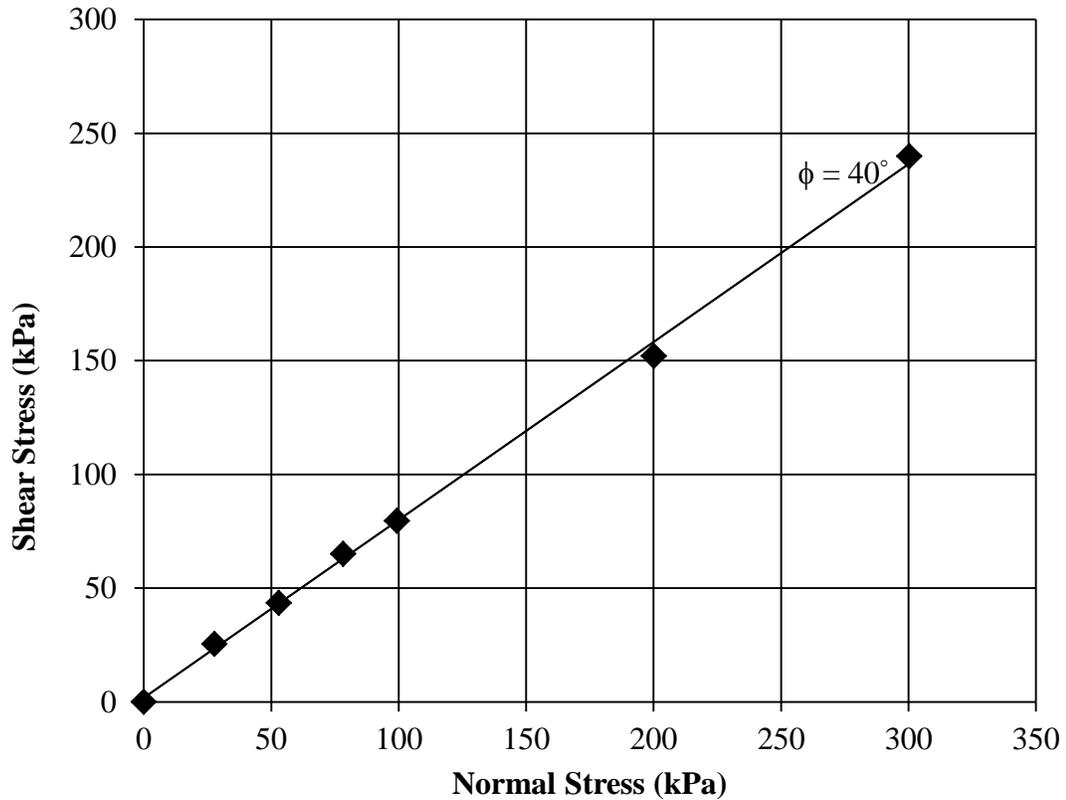
Figure 3.3. Results of direct shear test.

3.3.2. Cohesive Soil

The use of kaolin clay to simulate the behaviour of natural clay in geotechnical physical modeling has been adopted and used in many research studies due to its ability to simulate different stress histories with different undrained shear strength values to model the soil under consideration. In addition, the relatively high permeability for this type of clay reduces the laboratory and centrifuge consolidation times. However, due to

the high plasticity of kaolin clay, it is difficult to achieve a soil profile with high strength and stiffness to realistically replicate certain natural soils. The soils with high clay content tend to develop a low strength residual shearing surface with a residual friction angle (approximately 12°) smaller than the critical friction angle ($\phi'_r < \phi'_c$) (Tovey, 1970, Rossato et al., 1992, Springman, 1993). The clay fraction in kaolin clay is approximately 80%, which is very high compared to natural clay that typically contains a higher percentage of sand and silt. Therefore, it is necessary to develop a clay model that can accurately reproduce most field soils. Different attempts have been made to increase the strength and stiffness of kaolin clay by adding some granular material.

Rossato et al. (1992) studied the behaviour of kaolin and compared it with a kaolin-silt-sand (KSS) mixture. The results indicated that a more realistic clay model, in terms of undrained shear strength, can be achieved by consolidating the KSS mixture from a slurry. Meanwhile, kaolin and silica rock flour (KRF) was studied by Springman (1993). The mixture consisted of 70% kaolin and 30% silica rock flour which was prepared by one dimensionally consolidating the slurry. A series of direct shear tests were performed under various overconsolidation ratios (OCR). The conclusion drawn by Rossato et al. (1992) and Springman (1993) was that the behaviour of KSS and KRF is close to the behaviour of natural clays.

Lin (1995) and Paulin (1998) studied the performance and use of the 50% Speswhite kaolin clay and 50% Sil-Co-Sil silt (by weight) as clay model. They found that the kaolin/silt (K-S) mixture can produce undrained shear strength of 50 kPa under 95 kPa effective vertical stress and with an overconsolidation ratio of 4.2 (about 400 kPa

preconsolidation pressure) under a centrifugal acceleration 50g. The kaolin/silt clay model was adopted to study the performance of the micropiled raft in clay.

The properties of the clay model used in the centrifuge tests are presented in the following section.

3.3.2.1.   Materials and Physical Characterizations

This section provides a brief description of the kaolin clay and the silt used to manufacture the clay bed, including the physical properties and partial size distribution for the kaolin, silt and the K-S mixture. The Speswhite kaolin clay that was used in the study was supplied by IMERYS in England. Meanwhile the silt used in the K-S mixture was Sil-Co-Sil 75 which was supplied by US SILICA in the USA. The specific gravity for the kaolin and K-S are 2.63 and 2.62, respectively (Lin, 1995). A number of characterization tests were conducted in order to obtain the physical properties of the kaolin and the K-S mixture. The hydrometer method was used according to ASTM D422 to evaluate the soil particles distribution. It was found that the mean grain size, D_{50}, for the kaolin, silt and K-S mixture was approximately 0.00052, 0.017 and 0.0025, respectively, and the results are consistent with those reported by Lin (1995) and Paulin (1998). Figure 3.4 presents the particle distribution for the different materials. The Atterberg limits for the kaolin and K-S mixture were determined according to the ASTM D4318 (see Table 3.4).

Table 3.4. Properties of the Kaolin and the K-S mixture.

Soil Type	kaolin	50% kaolin and 50% silt
Liquid Limit, w_L, %	60.6	38
Plastic Limit, w_p, %	34	22.3
Plasticity Index, PI, %	26.6	15.72
Mean Particle size, D_{50}, mm	0.00052	0.0025
Clay Fraction (<2 μm), %	82	50
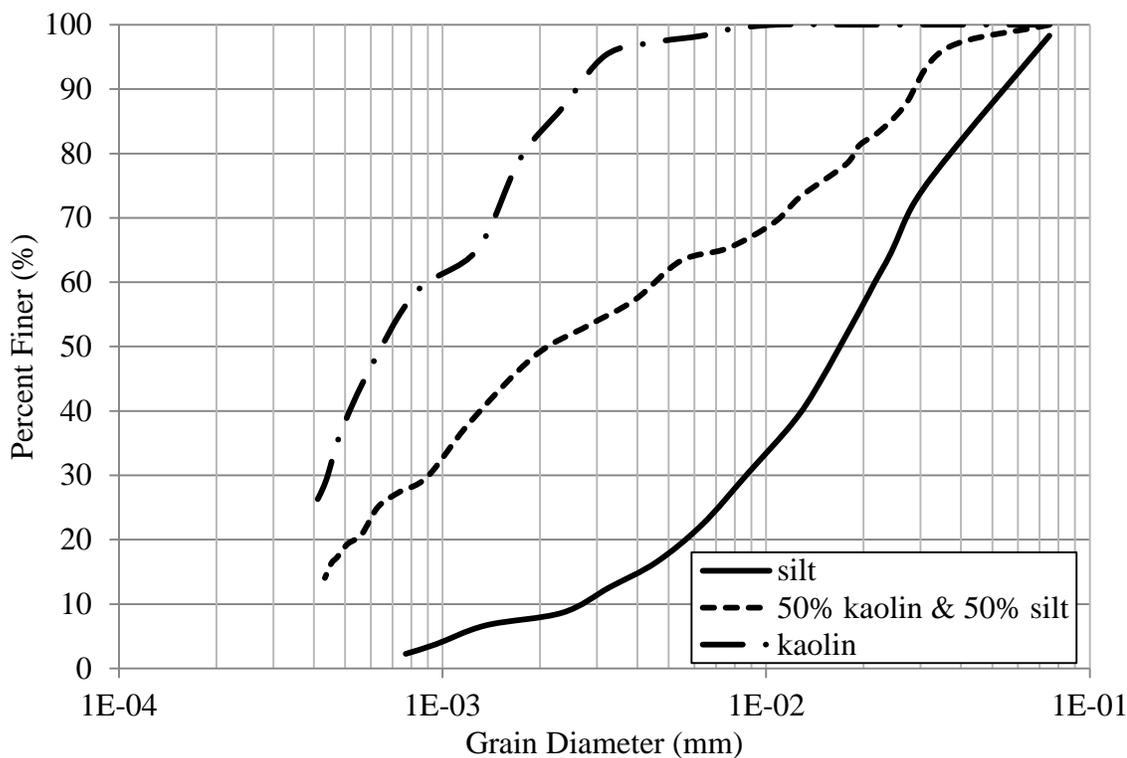
Figure 3.4. Soil particle size distribution for the different materials.

3.3.2.2. Consolidation Parameters

The consolidation parameters, including the compression index, C_c, rebound index, C_r, and coefficient of consolidation, c_v, are essential in designing the clay bed. As the final thickness of the clay layer is known based on the requirements of the testing program, the initial height of the clay slurry can be predicted using the compression

index, C_c, and rebound index, C_r. Moreover, the coefficient of consolidation, c_v, are used to estimate the required time for each load step to reach approximately 90% consolidation. The oedometer test was carried out according to ASTM D2435-11. The sample was prepared using 50% kaolin and 50% silt by weight, which was mixed with 70% of distilled water. Then the sample was spooned into the consolidation ring which was 50 mm in diameter and 14.9 mm in height. Figure 3.5 presents the void ratio and vertical stress curve for the loading and the unloading steps and Table 3.5 summarizes the different consolidation parameters at different loading increments. From Figure 3.5, the compression index, C_c, and the rebound index, C_r, are 0.28 and 0.05, respectively. These results are consistent with those reported by Lin (1995) (C_c= 0.29 and C_r= 0.04).
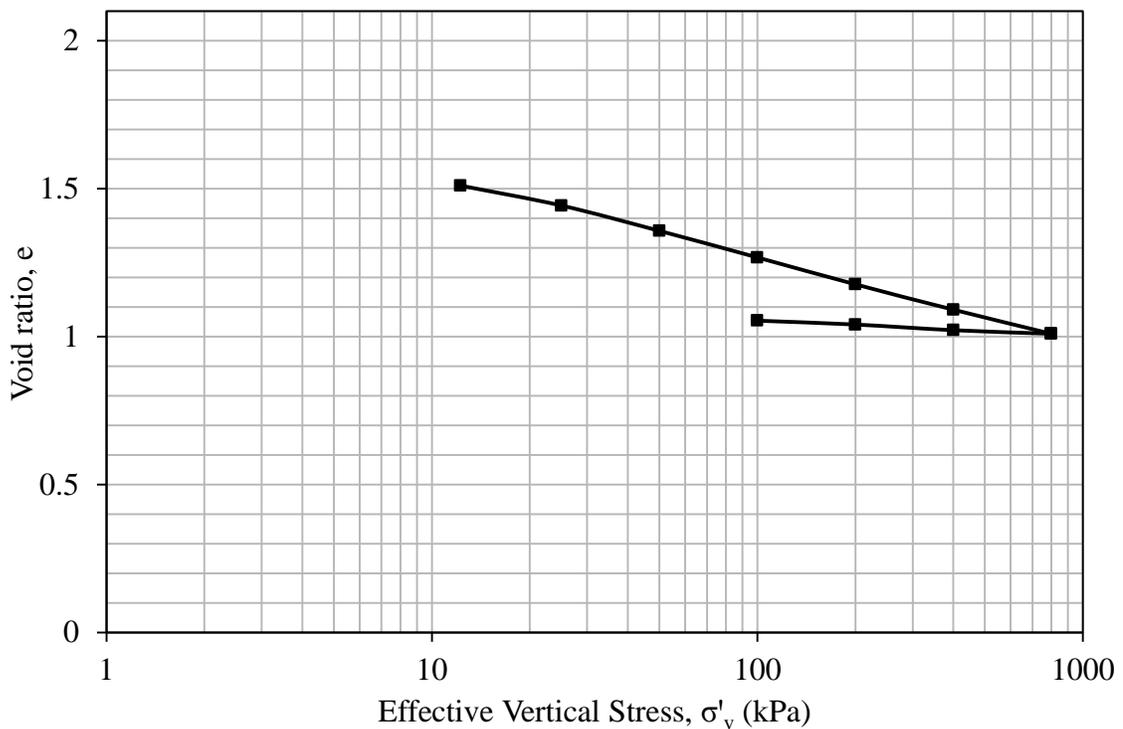
Figure 3.5. Void ratio vs. σ'_v curve for the small consolidation sample.

Table 3.5. Consolidation parameters of the K-S mixture.

σ_1 kPa	σ_2 kPa	H_f m	t_{90} min	C_v m^2/min	e	C_c
5	12.25	0.0129	3.25	1.13E-05	1.51	-
12.25	25	0.0125	3.24	1.06E-05	1.44	0.22
25	50	0.0121	2	1.61E-05	1.36	0.28
50	100	0.0116	0.81	3.69E-05	1.27	0.30
100	200	0.0112	0.41	6.73E-05	1.18	0.30
200	400	0.0107	0.25	0.000102	1.09	0.28

Four oedometer tests were performed on K-S soil undisturbed specimens, which were retrieved after the centrifuge testing program was concluded. Initial water content of the tested samples was found to be 30% and an average initial void ratio (e_o) of 0.85. These values are consistent with the values obtained during preparation of the samples from the slurry and pre-consolidated to a pressure of 300 kPa. The initial degree of saturation was found to be around 95%. Samples were inundated in the consolidometer for about 24 hours to ensure 100% saturation. To prevent samples from swelling during saturation, a seating load of 1.25 kPa was applied. Samples were tested under the vertical effective pressure (σ'_v); (including the saturation load), of 26.25, 51.25, 101.25, 201.25, 276.25, 326.25, 401.25, 451.25, and 501.25 kPa. Figure 3.6 shows the e-log σ'_v of K-S clay. Compression index (C_c) of the tested soil was found to be 0.21. The average recompression index (C_r) was found to be 0.15 and the swell index (C_s) was 0.04. The final degree of saturation after the consolidation test was found to be 100%.
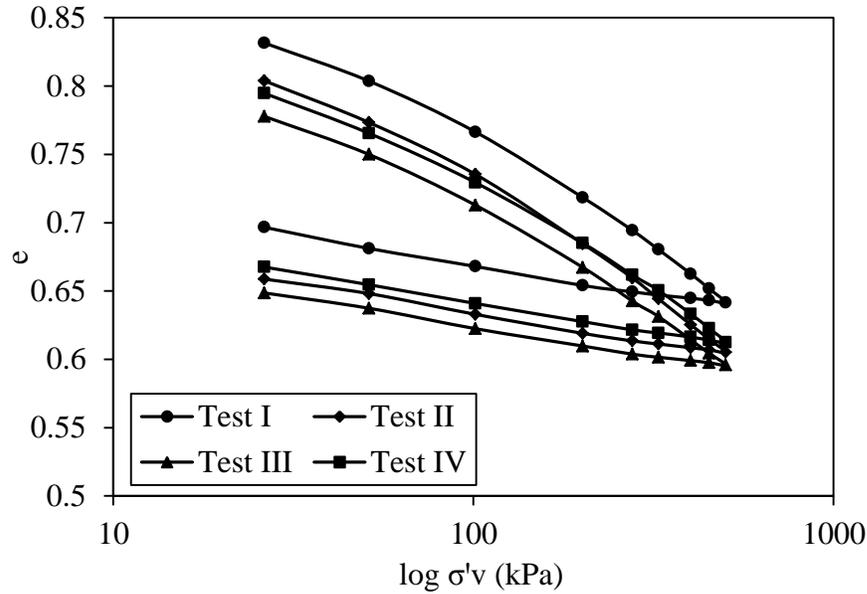
Figure 3.6. Results of 1D consolidation tests on K-S clay

3.3.2.3. Triaxial Tests

A series of triaxial tests were conducted in order to obtain the shear strength parameters as well as the undrained modulus of elasticity for the kaolin-silt mixture. In addition, the relationship between the undrained shear strength, overconsolidation ratio (OCR) and vertical effective stress was examined. These parameters are essential to simulate the behaviour of the micropiled raft installed in clay using the finite element method (FEM). Three specimens were tested under unconsolidated undrained triaxial compression conditions according to ASTM D2850. Moreover, four samples were tested under consolidated undrained triaxial test conditions employing different consolidation pressure levels according to ASTM D4767-11. The samples used throughout this testing program were retrieved after the centrifuge testing program was concluded (see section 3.6.2.2).

3.3.2.3.1. Unconsolidated Undrained Triaxial (UU) Test

Three UU tests were performed with confinement pressures of 40, 80, and 160 kPa. The test was performed at an axial strain rate of 1%/min according to ASTM D2850. Figure 3.7 presents the Mohr's circle for the UU test and the undrained shear strength, s_u, obtained from the test was 29 kPa. Because the sample was not consolidated, any effect of the different confinement pressures on the undrained shear modulus did not take place.

3.3.2.3.2. Consolidated Undrained Triaxial (CU) Test

The parameters obtained from the CU triaxial tests were not only valuable to calibrate the FEM as will be presented in Chapter 7, but also to design the clay bed based on s_u and OCR for future applications. Four CU triaxial tests were conducted using confinement pressures of 40, 80, 160 and 320 kPa. As the ASTM D4767-11 procedure for the CU test required to saturate and consolidate the sample before shearing it, the specimens were consolidated to reach effective consolidation pressures of 40, 80, 160 and 320 kPa, which corresponded to OCR values of 7.5, 3.8, 1.9 and 1, respectively. As the samples were previously consolidated from the slurry deposition to vertical effective stress of 300 kPa (see section 3.4.2.), they were at an overconsolidated state for the confinement pressures of 40, 80 and 160 kPa; however, for the 320 kPa confinement pressure, the sample was normally consolidated. The samples were sheared at an axial strain rate of 0.02 mm/min. Figure 3.8 presents the stress-strain relationships for the K-S samples under the CU condition for different confinement pressures. For the overconsolidated clay test (σ_3= 40, 80 and 160 kPa), the stress-strain behaviour yielded at approximately 1% axial strain and reached a plateau at approximately 10%, which is the plastic condition similar to the Mohr Coulomb model (elastic plastic model); similar

behaviour was reported by Bishop and Henkel (1962) for heavily overconsolidated clay (OCR=8). Figure 3.9 a and b presents the failure envelope for the K-S under total stresses and effective stresses, respectively, clay based on the Mohr-Coulomb failure criterion which yielded a total friction angle, ϕ_t, and undrained cohesion, c_u, of 12° and 32 kPa, respectively, under total stress. Moreover, under the effective stresses, the effective friction angle, ϕ', and effective cohesion, c', is 25° and 14 kPa, respectively
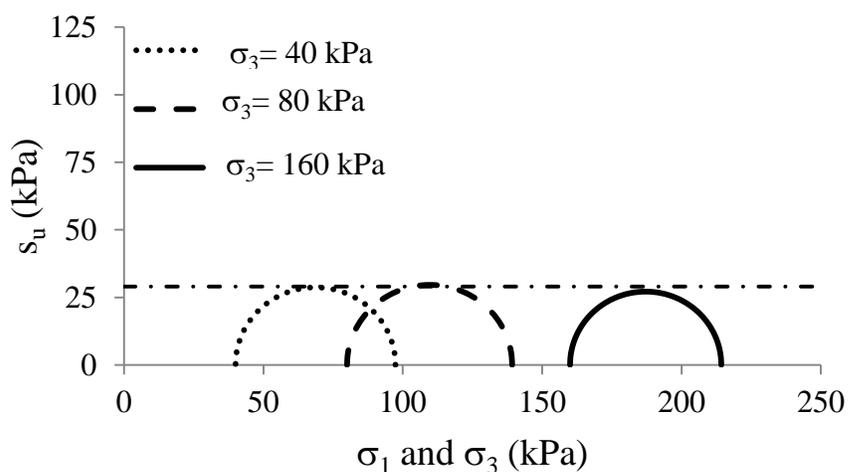
Figure 3.7. Mohr's circles for unconsolidated undrained (UU) triaxial tests results.
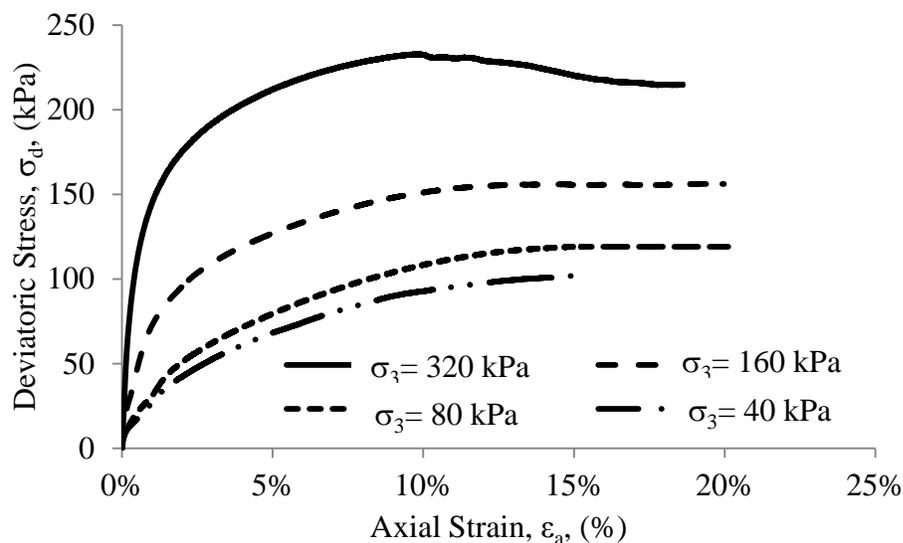
Figure 3.8. Stress-strain relationships for the K-S samples under the CU condition for different confinement pressures.

Based on the measured soil properties, two equations can be proposed. The first equation correlates the undrained modulus of elasticity, E_u, with the mean effective stress, σ'_m ($\sigma'_m = \frac{\sigma'_1 + 2\sigma'_2}{3}$), under the isotropic condition. Figure 3.10 shows the linear relationship between E_u and σ'_m which produces:

$$E_u \approx 155\, \sigma'_m \tag{3.4}$$

Another equation can be proposed relating s_u, OCR and σ'_m. Figure 3.11 shows the correlation between s_u/σ'_m and OCR, and the relationship can be written using a power function similar to Eq. 3.6, i.e.

$$s_u = 0.31\, \sigma'_m\, (OCR)^{0.51} \tag{3.5}$$

In Eq. 3.5, the parameters c_1 and c_2 are obtained from curve fitting data in Figure 3.11 as 0.31 and 0.51, respectively. The prediction of s_u based on Eq. 3.5 was compared to the results obtained from the in-flight T-bar test and they were in very good agreement as shown in Figure 3.12. Using σ'_m to estimate s_u employing Eq. 3.5 is more representative of the soil stress state than using the effective vertical stress. The ratio E_u/s_u varied between 250 and 500 with an average of 375. This value is at the lower bound of the values reported by Jaimolkowski et al. (1979) for clay with a plasticity index (PI) less than 30 and OCR between 4 and 6.
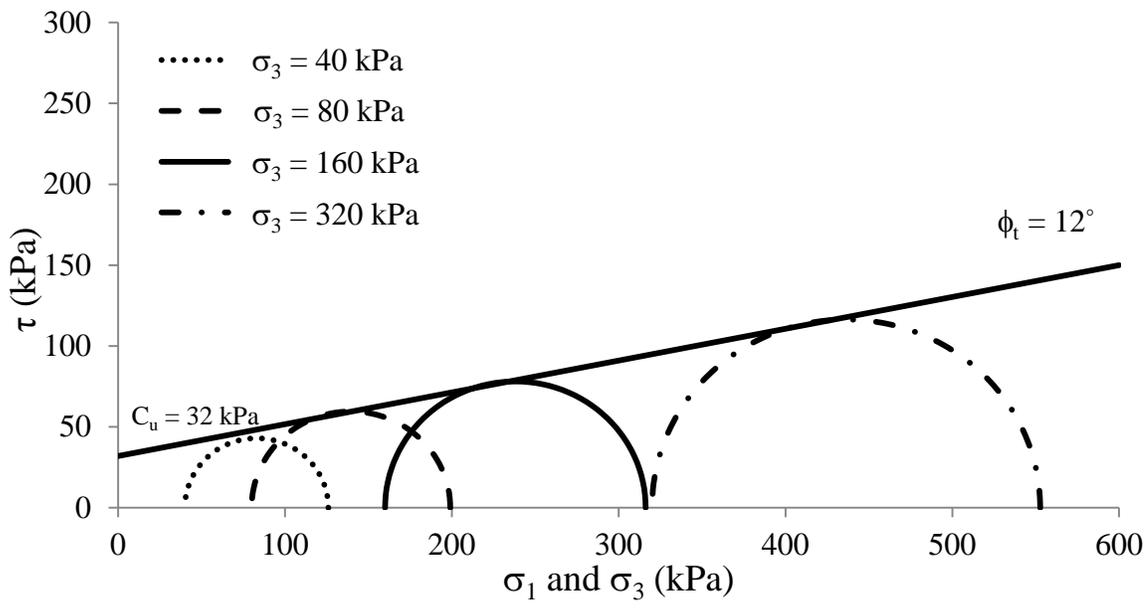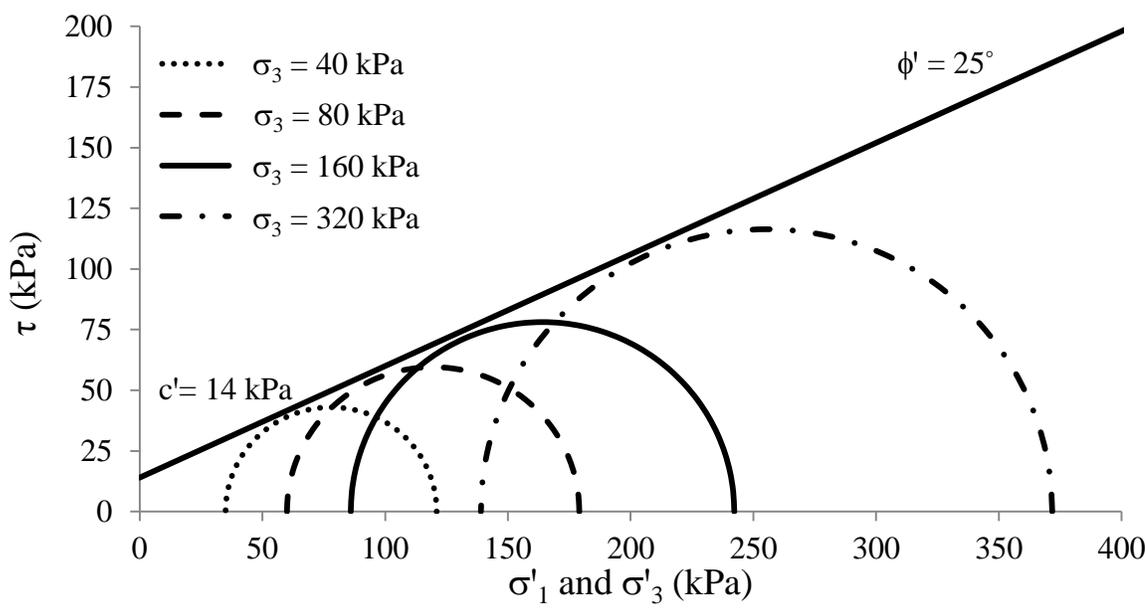
Figure 3.9. Mohr's circles and failure envelope for the consolidated undrained (CU) triaxial tests: (a) under total stresses; and (b) under effective stresses.
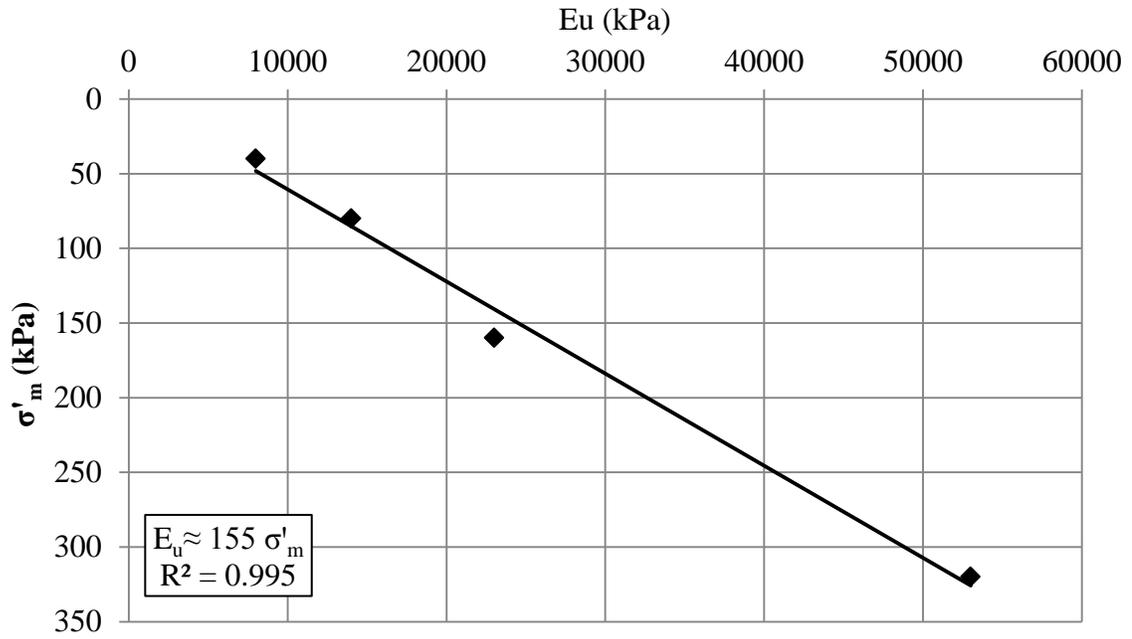
Figure 3.10. Relationship between E_u and mean effective stress.
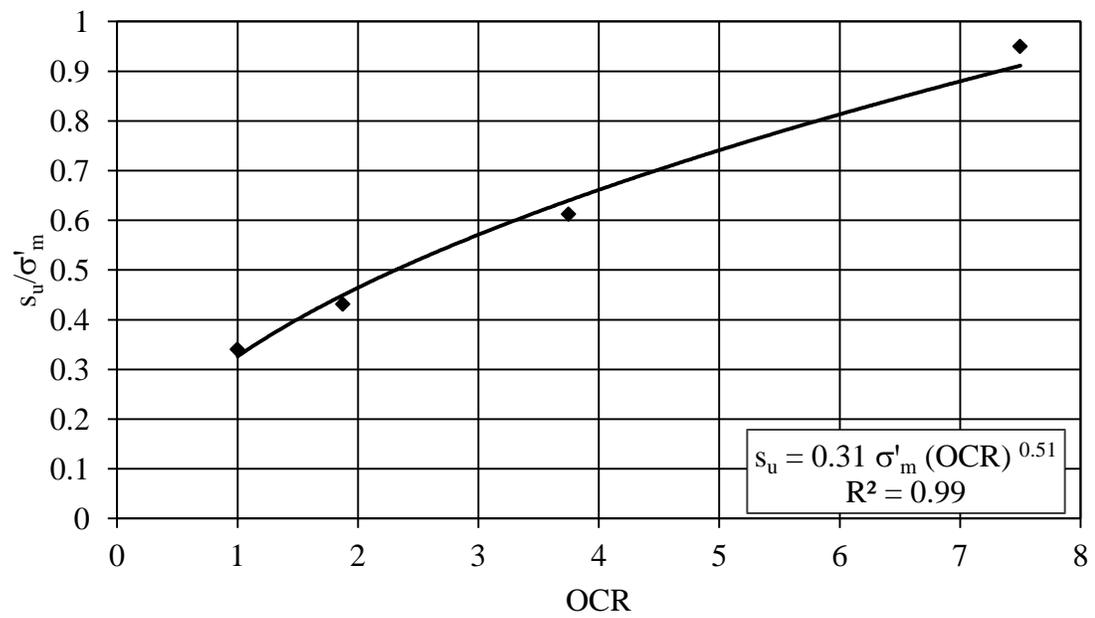
Figure 3.11. Relationship between s_u/σ'_m and OCR.
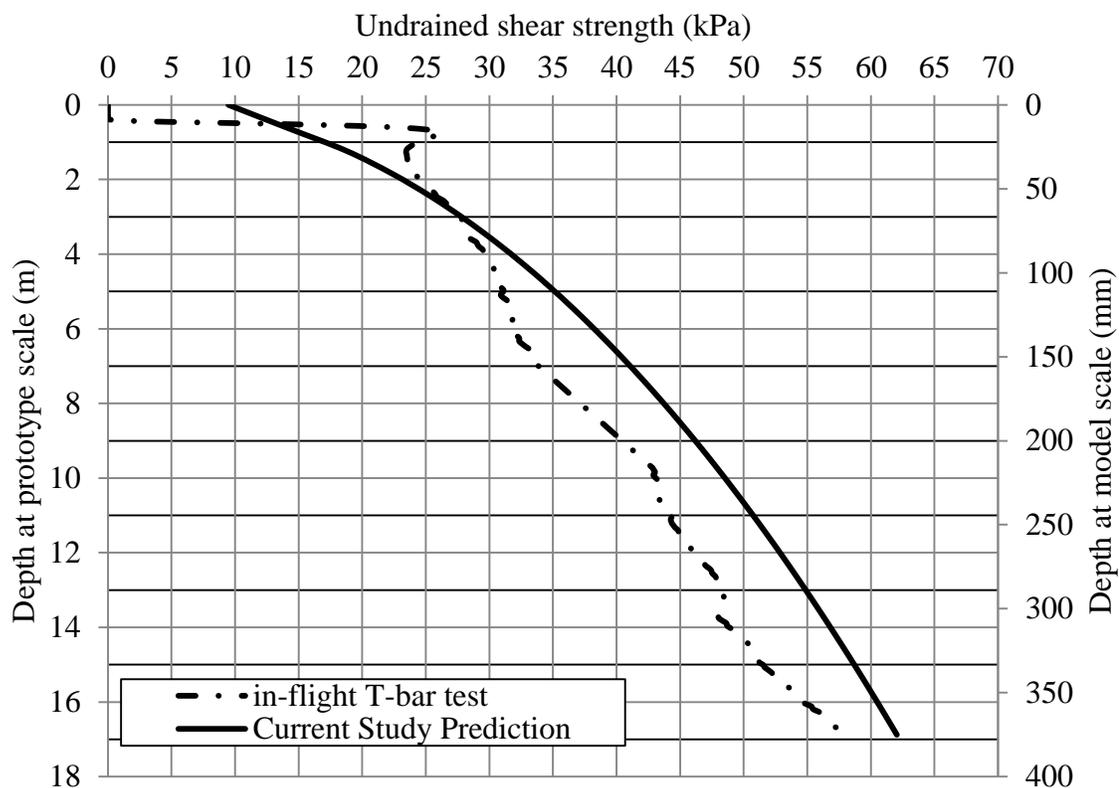
Figure 3.12. Comparison between estimated s_u and in-flight T-bar test.

3.4. DESIGN AND PREPARATION OF TEST BEDS

The processes adopted to design the sand and clay test beds are discussed herein. For the sand test bed, the process involved determining its overall relative density. For the clay test bed, the process was focused on establishing representative undrained shear strength.

3.4.1. Sand Test Bed

The targeted relative density, D_r, for the sand was 70%, which corresponded to a unit weight in the range of 14.97 kN/m³. In order to achieve this relative density, the strong box height was divided into seven layers and was marked by lines along its interior perimeter. Knowing the total weight and the volume of the sand for each sublayer, it was

possible to estimate the weight required for each sublayer to achieve the required relative density. However, the density of the soil at the bottom of the box increases as the soil height increases; therefore, a number of trial and error experiments were conducted in order to achieve the best height (which would be higher than the sublayer at the top of the box) for the sand sublayers at the bottom of the box to ensure a uniform density along the overall height of the sand. The sand was rained by using a scoop at a falling height of 150 mm from the sand surface. In addition, each sublayer was gently tamped in order to achieve the height required. The overall relative density was confirmed by the final height and weight of the sand bed. During the centrifuge spinning, the sand surface settled by an average of 2 mm. This amount was observed in all six tests conducted. Figure 3.13 presents the typical sand settlement during the spinning.
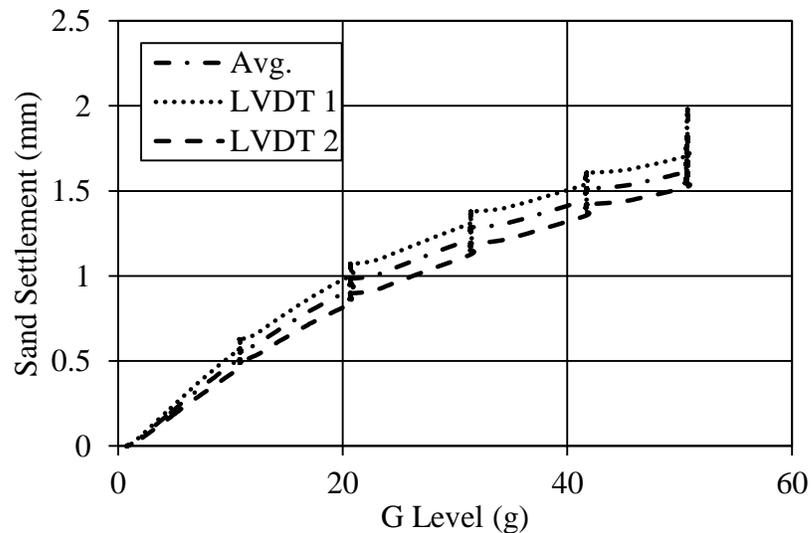
Figure 3.13. Settlement of sand during the increase in g level.

3.4.2. Clay Test Bed

A number of steps were involved in order to design and prepare the clay bed with undrained shear strength of approximately 30 kPa at a depth of 100 mm (at the middle

point of the micropile). These steps consisted of: estimating the laboratory consolidation pressure at which the required overconsolidation ratio (OCR) in the centrifuge would be attained; mixing the 50% kaolin clay with 50% silt; completing the laboratory consolidation; and finally allowing for the consolidation in the centrifuge. The following section will outline these steps in detail.

3.4.2.1. Design of the Clay Test Bed

To establish the targeted stress states for the clay during consolidation under self-weight in the centrifuge, the clay has to be consolidated first in the laboratory. Schofield and Wroth (1968) proposed a method to estimate the undrained shear strength for the overconsolidated clay i.e.

$$s_u = c_1 \sigma'_v OCR^{c_2} \tag{3.6}$$

Where: s_u: undrained shear strength; c_1 and c_2: are coefficients; σ'_v : effective vertical stress; and OCR: overconsolidation ratio.

The target OCR profile for the clay bed design can be induced by consolidating the clay in the laboratory at an effective vertical stress higher than the vertical stress in the centrifuge due to the clay weight. Based on Equation 3.6, the clay has to be consolidated at 300 kPa effective vertical stress to yield the required undrained shear strength. If the clay was consolidated only under its self-weight (normally consolidated), s_u at 100 mm would only be 8.5 kPa. Lin (1995) estimated c_1 and c_2 coefficients as 0.253 and 0.657, respectively, based on vane shear test results for the 50% kaolin clay with 50% silt. Figure 3.14 presents the changes in clay properties with depth including the undrained shear strength, water content and effective unit weight.
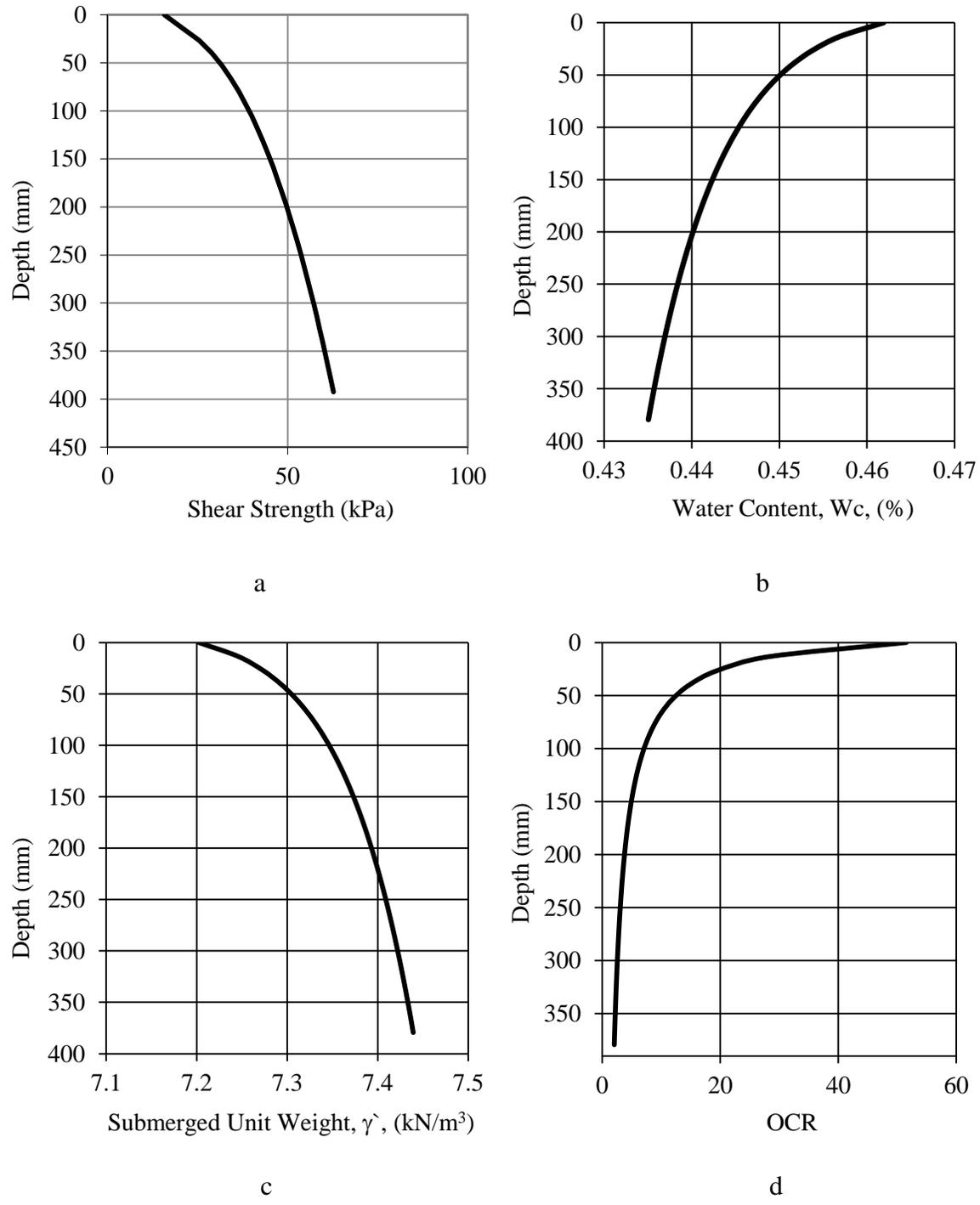
Figure 3.14. Design curves for clay test bed parameters: (a) undrained shear strength; (b) water content; (c) submerged unit weight; and (d) overconsolidation ratio.

3.4.2.2. Mixing the Clay

A 5HP Bower horizontal paste mixer (Figure 3.15a) with 200 L capacity was used to mix a total of 180 kg of kaolin clay, 180 kg of silt and 288 kg of water. The mixer uses plough type blades (see Figure 3.15b). The total weight of the material was divided into four batches with each batch weighing approximately 162 kg. The clay was mixed for 30 minutes at 14 rpm. The clay was then placed for 3 hours under vacuum of 65 kPa in order to reduce the air trapped in the slurry. This procedure produced homogenous slurry with high degree of saturation in the final consolidated clay.

(a)   (b)

Figure 3.15. Clay slurry mixer; (a) outside view and (b) inside.

3.4.2.3. Preparing the Round Tub

A cylindrical container 904 mm in diameter and 817 mm extended height was used. The extended container consisted of two parts: (i) the primary tub of 500 mm height (Figure 3.16b); and (ii) 317 mm high extinction, which was connected to the primary tub

to contain the slurry before the consolidation process. A steel extrusion plate was placed on the bottom of the tub to facilitate the post-test extraction for the clay test bed. A 40 mm saturated sand drainage layer was placed at the bottom of the tub to accelerate the consolidation process (Figure 3.16c). A layer of geotextile and filter paper were placed on top of the sand to allow drainage but retain clay particles (Figure 3.16d). To reduce the friction between the clay mixture and the container's walls during the consolidation process, the wall was coated using a thin grease layer (Figure 3.16d). The slurry was then poured into the container with extreme caution not to allow air to be trapped within the clay slurry (Figure 3.16e). A second layer of filter paper and geotextile was placed with the filter paper being on top of the clay. After the slurry was placed in the tub, it was left to consolidate under its self-weight for about one day. These steps are shown in Figure 3.16.

3.4.2.4.   Laboratory Consolidation of the Clay Slurry

A rigid steel piston weighing 233 kg was carefully placed level on top of the clay, which produced a pressure equal to 3.6 kPa. The slurry was subjected to the piston pressure until 90% degree of consolidation was achieved. The consolidation was measured using two string pots (see Section 3.5.8) and it was confirmed using manual measurement. The tub was then loaded under the consolidation frame to consolidate the clay slurry under higher pressure using a hydraulic press which can apply required pressure as shown in Figure 3.17. The water was allowed to drain from the tub top and bottom during the consolidation process. Stress increments were applied to consolidate the clay slurry until it reached the maximum consolidation stress (300 kPa) as shown in Table 3.6. The increase in the stress between each successive increment was by a factor

of 2. Each stress increment was maintained until more than a 90% degree of consolidation was reached. The total process took approximately five weeks to complete with a total consolidation settlement of about 194 mm.

After the clay sample was consolidated at the maximum stress interval, the unloading process was started by reducing the pressure by half until it was removed completely. Table 3.6 summarizes the different consolidation parameters at different stress intervals. Figure 3.18 presents the void ratio and vertical stress curve for the loading and the unloading steps during the laboratory consolidation for the clay slurry. Based on Figure 3.18, the compression index, C_c, the rebound index, C_r, are 0.3 and 0.032, respectively.

a

b

c

d

e

f

Figure 3.16. Different steps involved in preparing the steel tub and pouring the clay slurry.

a   b
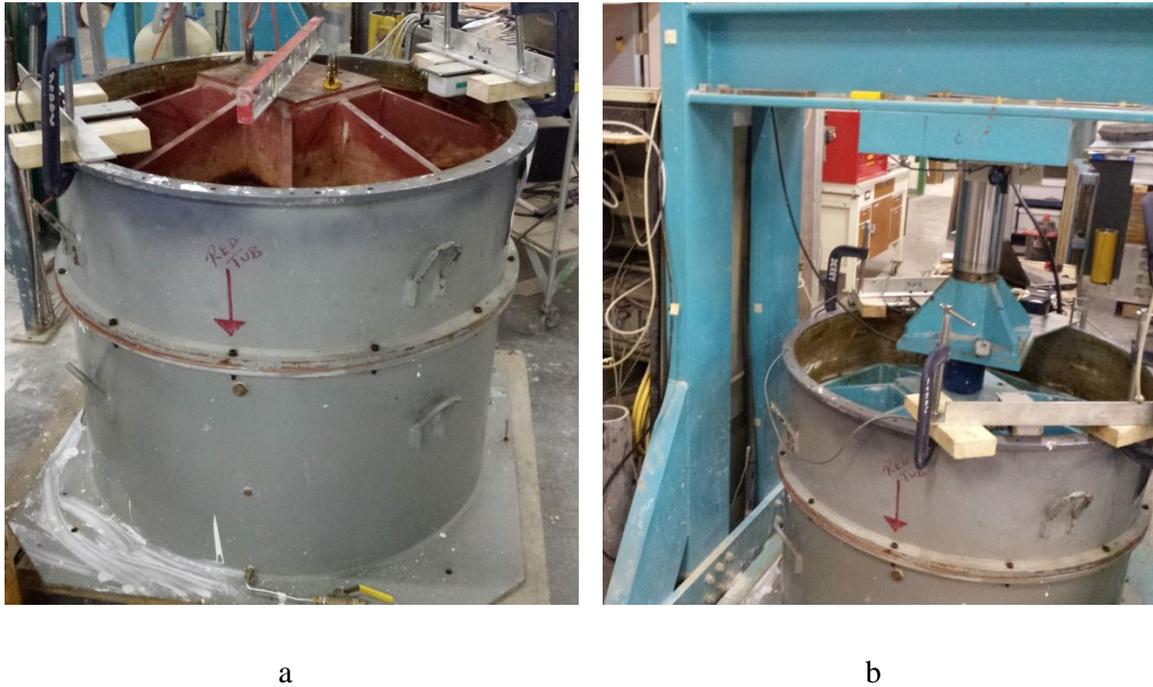
Figure 3.17. (a) Rigid steel piston and (b) the tub under the consolidation frame.

Table 3.6. Summary of consolidation parameters during laboratory consolidation for clay test bed.

σ_1	σ_2	H_f	t_{90}	C_v	e
kPa	kPa	m	min	m^2/min	
Self weight		624.0			1.99
1	3.6	560.86	5625	1.323E-05	1.68
3.6	9.55	500.0	6400	9.320E-06	1.39
9.55	18.75	475.0	4900	1.028E-05	1.27
18.75	37.5	448.0	4225	1.069E-05	1.14
37.5	75	426.5	2401	1.688E-05	1.04
75	150	405.5	2025	1.812E-05	0.94
150	300	388.3	1600	2.087E-05	0.86
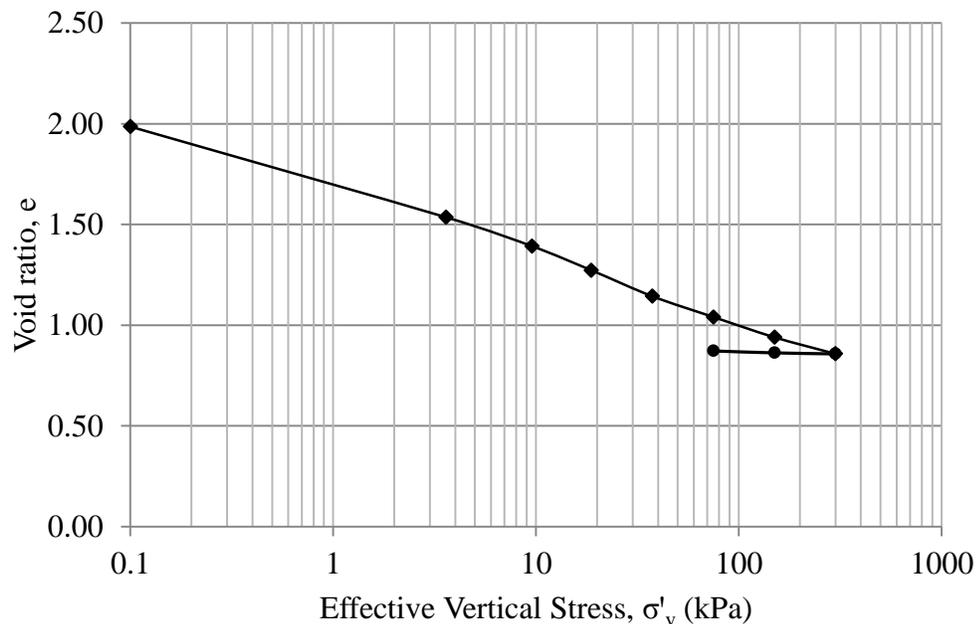
Figure 3.18. Void ratio vs. σ'_v curve for the consolidation of the clay test bed in the laboratory.

3.5. INSTRUMENTATION

Four different types of instrumentations were used to measure strain, movement, pore water pressure and contact pressure. The strain measurements were used to obtain the axial forces in the micropiles and the stress distribution at the raft base resulting from the vertical loading. Each micropile was instrumented with four strain gauges distributed along its shaft in order to evaluate the load transfer between the micropiles and the soil. In addition, two extra strain gauges were attached at the top of two micropiles in the micropiled raft to confirm the axial force carried by the micropiles. For the raft, two strain gauges were attached to the raft base in order to evaluate the bending stresses at the center and at the edge of the raft.

A linear displacement transducer (LDT) and two linear variable differential transformers (LVDT) were used to monitor settlements; two LVDTs to monitor the movement of the soil surface during the spinning of the centrifuge and one LDT to measure settlement at the edge of the raft. The vertical deflection at the center of the raft was measured using an accurate laser device. Three pressure transducers were utilized to measure the contact pressure between the raft and the soil at the center of the raft, the edge of the raft, and at the mid-way point between the center and the edge of the raft. Finally, a load cell was attached to the actuator to measure the vertical load applied to the micropiles, raft and MPR foundations.

All LVDTs, the load cell, pressure transducers, PPTs, T-bar and sand cone (for CPT) were calibrated prior to beginning the tests in order to ascertain their accuracy. Table 3.7 summarizes the instrumentations used for different tests.

Table 3.7. Summary of instrumentation used for each test.

Test	Test bead	Element	Strain Gauge	LDT and LVDTs	Pressure Transducer	Laser	Load Cell	Pore Pressure Transducer (PPT)
Test 1	Sand	1 Micropile	4 along the micropile shaft	2 for sand movement	-	1for Axial movement	1	N/A
Test 2		Raft	2 at raft base	2 for sand movement/ 1 for differential settlement	2 at raft base	1for Axial movement	1	
Test 3		4 Micropile	4 along the micropile shaft/ 2 at top of 2 more micropiles	2 for sand movement/ 1 for differential settlement	2 at raft base	1for Axial movement	1	
		Raft $t_r =$ 0.6 m	2 at raft base			1for Axial movement		
Test 4		4 Micropile	4 along the micropile shaft/ 2 at top of 2 more micropiles	2 for sand movement/ 1 for differential settlement	2 at raft base	1for Axial movement	1	
		Raft $t_r=$ 0.45 m	2 at raft base			1for Axial movement		
Test 5		4 Micropile	4 along the micropile shaft/ 2 at top of 2 more micropiles	2 for sand movement/ 1 for differential settlement	2 at raft base	1for Axial movement	1	
		Raft $t_r =$ 0.3 m	2 at raft base			1for Axial movement		
Test 6		1 Micropile	4 along the micropile shaft	2 for sand movement/ 1 for differential settlement	2 at raft base	1for Axial movement	1	
		Raft $t_r =$ 0.6 m	2 at raft base			1for Axial movement		
Test 7	Clay	1 Micropile	4 along the micropile shaft	2 for sand movement		1for Axial movement	1	2
Test 8		Raft	2 at raft base	2 for sand movement/ 1 for differential settlement	2 at raft base	1for Axial movement	1	2
Test 9		4 Micropile	4 along the micropile shaft/ 2 at top of 2 more micropiles	2 for sand movement/ 1 for differential settlement	2 at raft base	1for Axial movement	1	2
		Raft $t_r =$ 0.6 m	2 at raft base			1for Axial movement		

3.5.1. The Linear Displacement Transducer (LDT) and the Linear Variable Differential Transformers (LVDTs)

Both the LDT and the LVDTs measure the movement of the point of interest; however, they are constructed using different electrical mechanisms. The voltage range for the LDT is from 0 to 10 v while for the LVDT it is from -8 to 8 v. The physical stroke for the LDT and LVDT is approximately 45 mm. The LDT and LVDTs were calibrated using a special calibration device (see Figure 3.19). The instrument was mounted in the device and connected to the Data Acquisition System (DAQ system). Using the caliper a precise movement was applied to push the instrument core inward and the output voltage was displayed and stored along with the physical measurement using the DAQ system. This procedure was repeated for at least 5 points between the maximum and minimum measuring points for each instrument in order to obtain the correlation between the output voltage and the physical movement (see Figure 3.20). The average error between the reading from DAQ and the applied physical movement was about 0.12%.
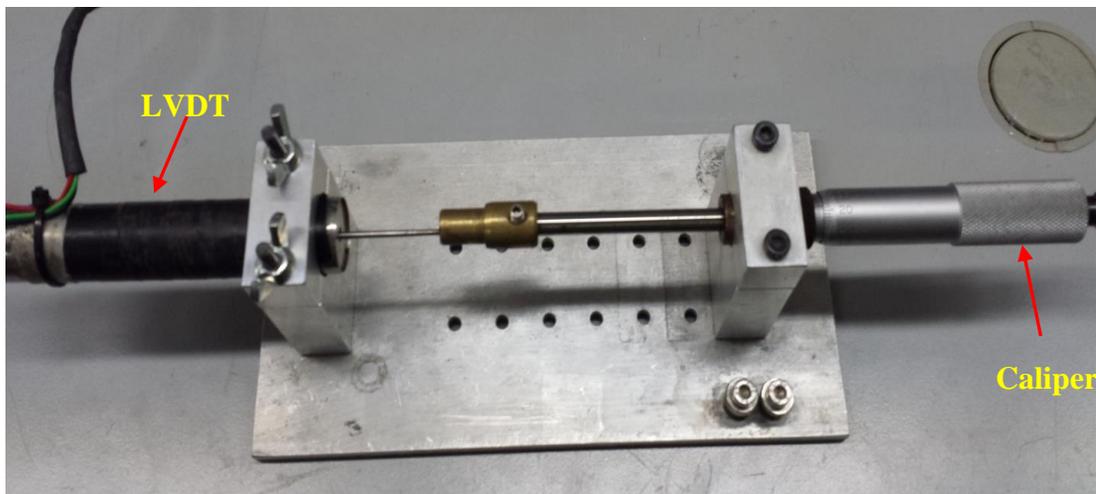
Figure 3.19. Device used to calibrate the LVDT.
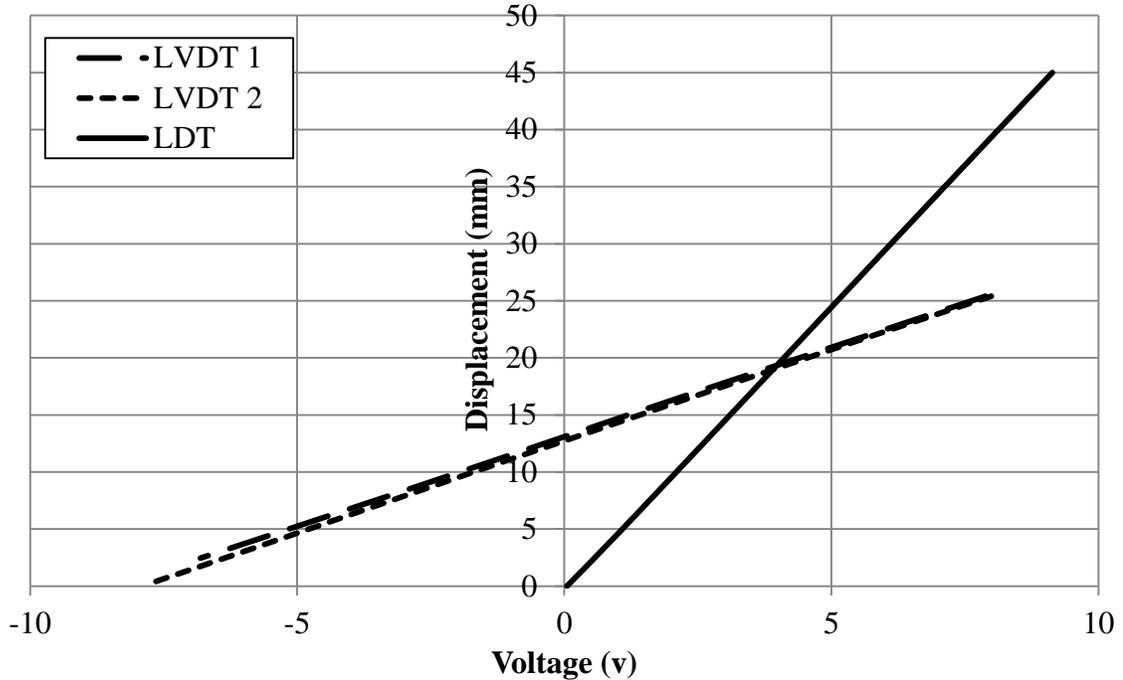
Figure 3.20. Changes in LVDTs and LDT voltage with a change in displacement.

3.5.2. Cone Penetrometer

The cone penetrometer was used to perform the cone penetration test in-flight to obtain the strength profile for the sand. It was 11.5 mm in diameter with a 60° tip angle and 1 cm^2 cross-sectional area. Its load cell was calibrated using premeasured physical loads. The probe was fixed to the calibration frame, which transferred the load to the probe. Furthermore, a small ball with the same diameter as the probe was placed between the load cell and a socket in the calibration frame in order to apply the load axially (see Figure 3.21). By adding the load to the load hanger that attached to the calibration frame, the output voltage corresponding to this particular load increment was obtained and stored into the DAQ system. Figure 3.22 presents the correlation between the output voltage and the physical load.

After the calibration process was concluded, the DAQ output was verified with the physical load and the average error was found to be less than ±3%.
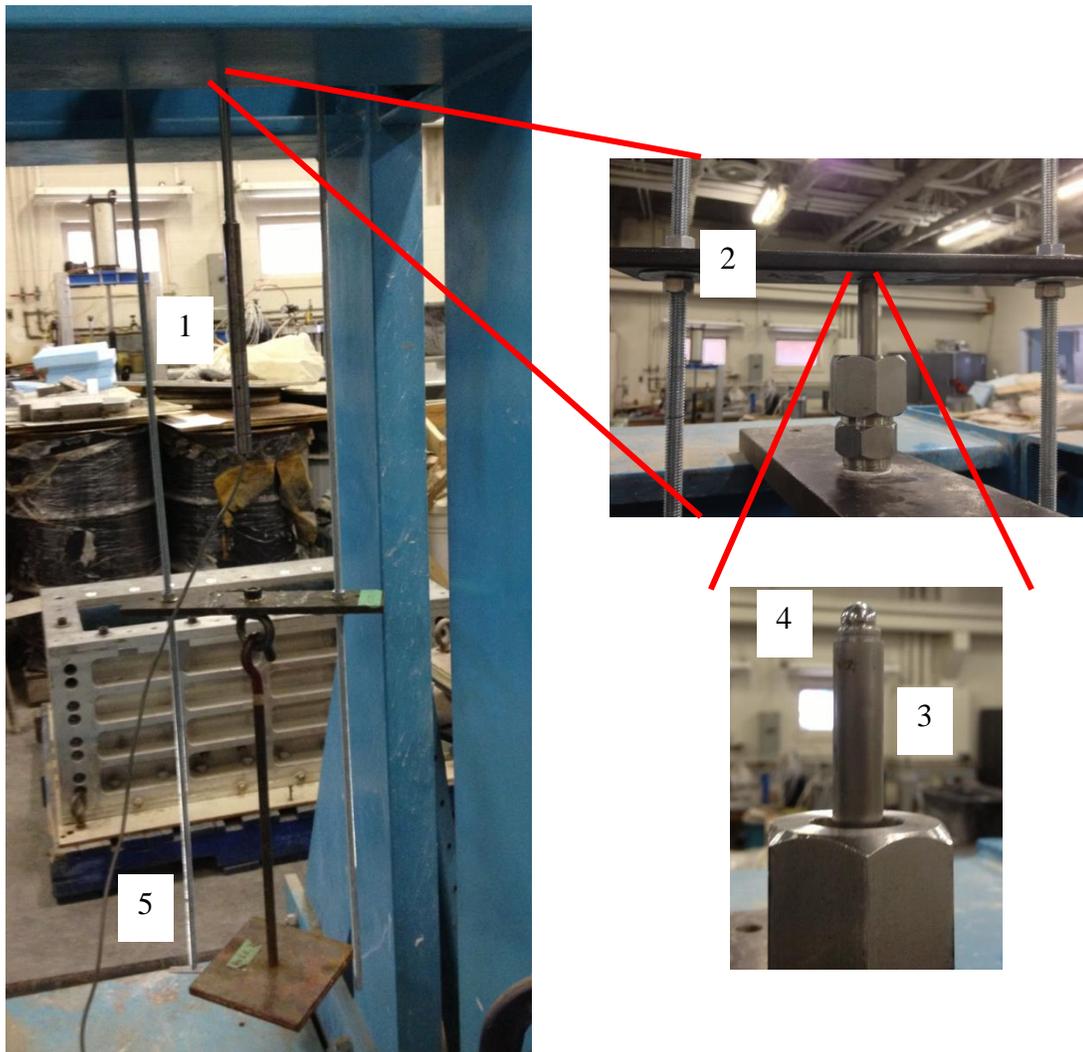
Figure 3.21. Components used for calibrating the sand cone, including: (1) sand cone probe; (2) calibration frame; (3) load cell; (4) ball on top of the load cell; and (5) load hanger.
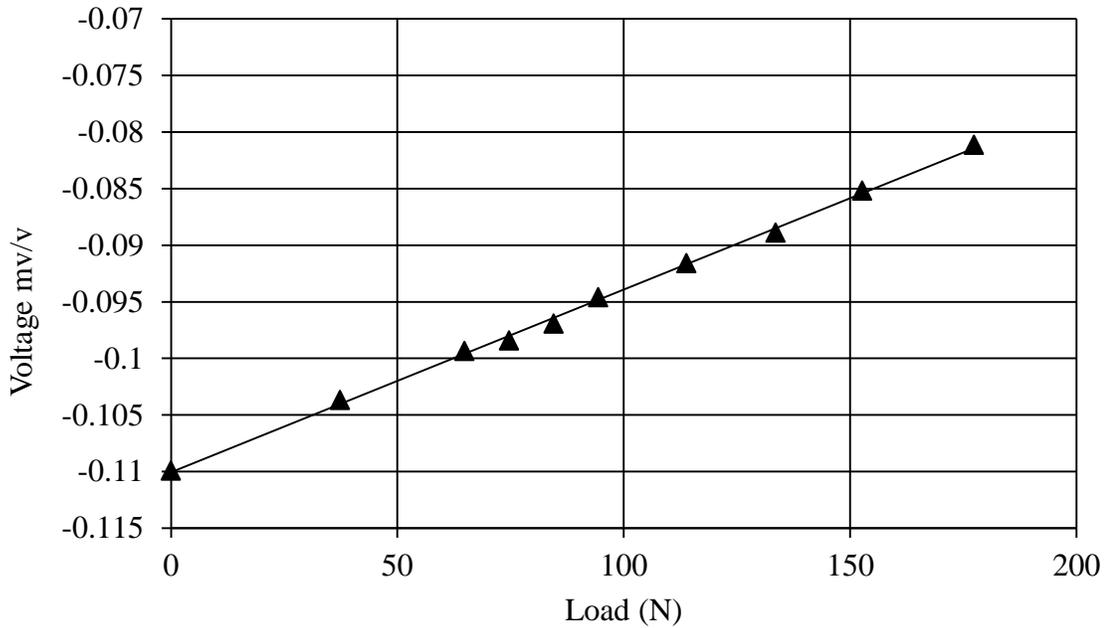
Figure 3.22. Load vs. voltage for the sand cone.

3.5.3.   Primary Load Cell

A 25 kN primary load cell was used to measure the load applied at the top of the raft. The primary load cell was calibrated using the compression test machine (see Figure 3.23). The correlation between the output voltage and the physical load is presented in Figure 3.24. The DAQ output was verified with physical load after the calibration process was completed and the average error was found to be less than ±2%.

Figure 3.23. Calibration process for the primary load cell using the compression machine.
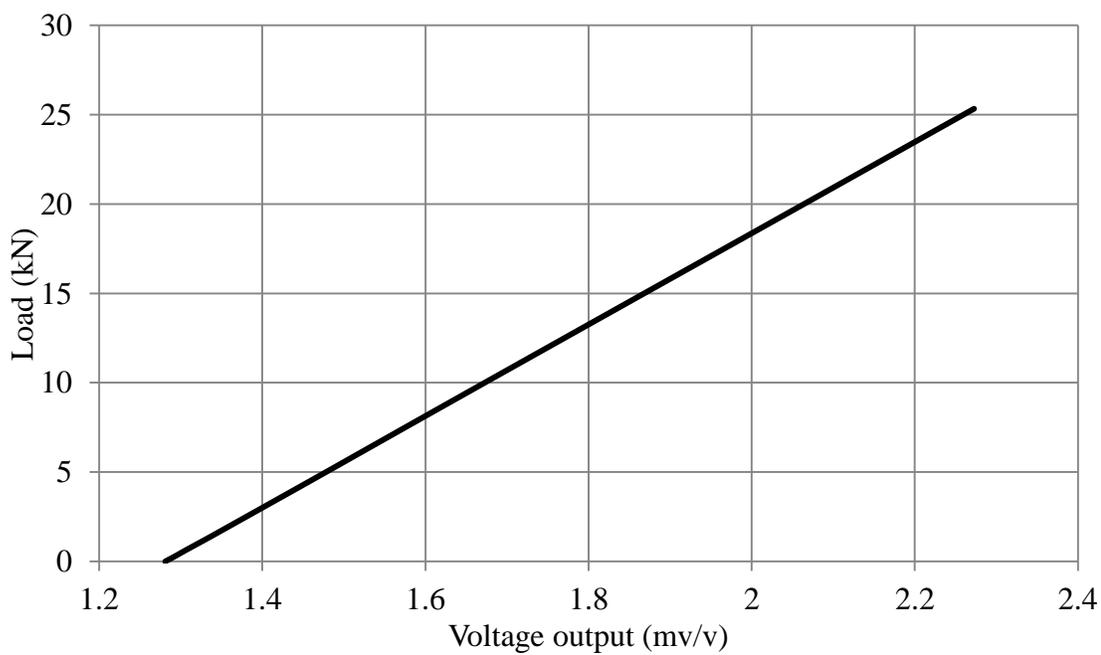
Figure 3.24. Load vs. voltage for the primary load cell.

3.5.4. Pressure Transducer

Two miniature earth pressure gauges were used to measure the contact pressure between the raft and the soil. The pressure transducer models PDA-1MPa, shown in Figure 3.25, were manufactured by Tokyo Sokki Kenkyujo Co. The calibration data supplied by the manufacturer was adopted; however, further verification process for the output pressure was conducted. An extra pressure transducer was attached to the base of an empty centrifuge box. The box was then filled with a compacted sand soil layer (0.345 m thick) with unit weight, γ = 14.97 kN/m^3. Subsequently, the box was subjected to centrifugal acceleration up to 50g. The reading of the pressure transducer at different acceleration points was recorded and a correlation between the theoretical pressures at the base of the box was plotted as can be seen in Figure 3.26. It was found that at 50g, the pressure transducer overestimates the actual pressure by approximately 14%. Therefore, the output results were corrected accordingly.
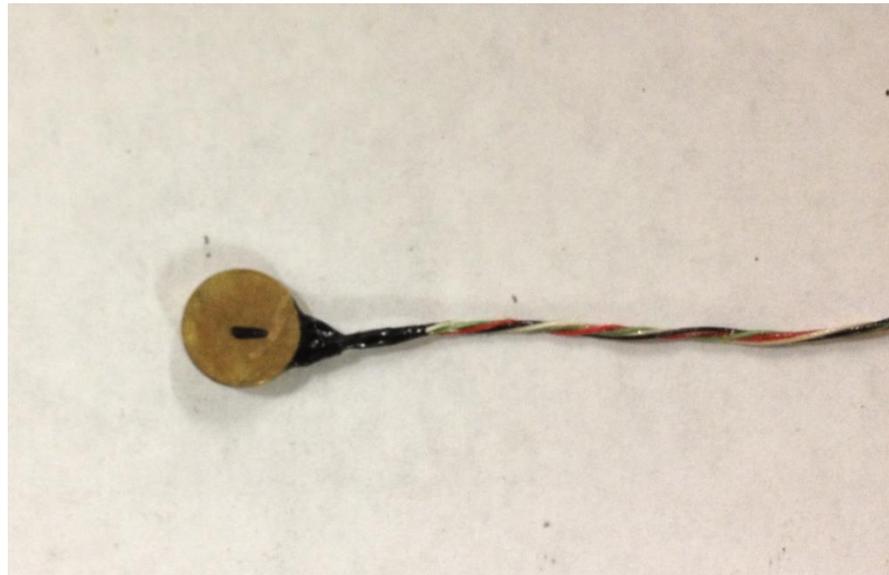
Figure 3.25. Miniature pressure gauges.
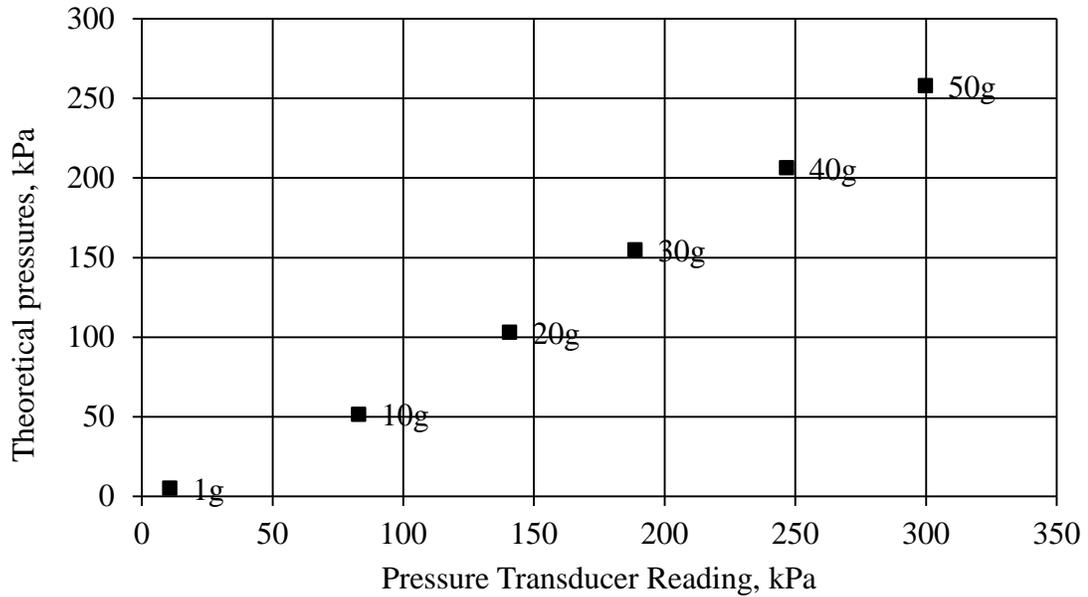
Figure 3.26. Relationship between theoretical and measured pressures using miniature pressure gauges.

3.5.5. The Laser Distance Sensor

A highly accurate laser was used to measure the settlement at the raft center. The laser was the model OADM 20I4460 manufactured by Baumer Electric Ltd. A reflection plate was placed on top of the primary load cell (used to measure the force at the raft center (see Figure 3.27). The reflection plate was required in order to reflect the laser beam so the laser sensor could obtain the corresponding distance using the triangulation measurement principle. The calibration supplied by the manufacturer was used. The accuracy for the laser was ±0.06 mm.

3.5.6. Vertical Actuators

Two vertical actuators, shown in Figure 3.28, were used in the testing program. One was used to apply the load to the test model and the second one was used to perform the CPT and T-bar tests.
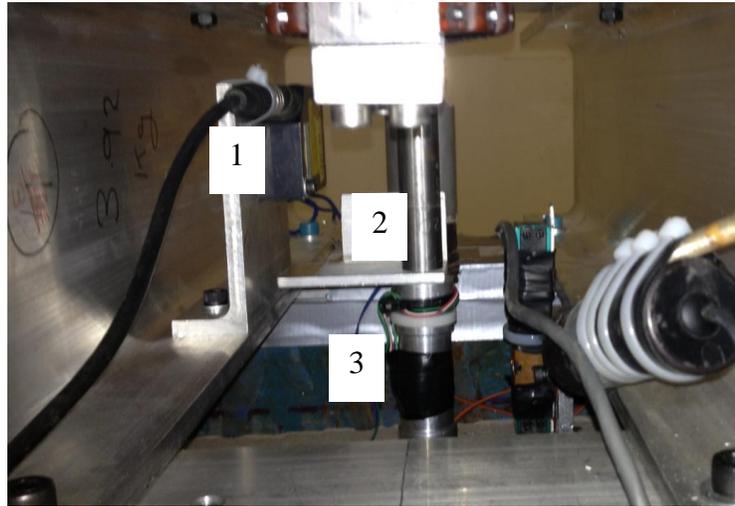
Figure 3.27. Setup for the laser sensor showing the following components: (1) laser; (2) reflection plate; and (3) primary load cell.

Figure 3.28. Two actuators used during the centrifuge testing program.

The accuracy of the vertical actuators was verified by moving the actuators a distance of 10 mm and 20 mm while monitoring the corresponding movement in the DAQ system. Moreover, physical measurements of the actual movement of the actuators were conducted using a caliper. It was found that the average error in the DAQ feedback in comparison to the caliper reading was approximately ±0.7%.

3.5.7. Strain Gauges

A total of 50 strain gauges (Micro-Measurements strain gauges models CEA-06-125UW-350) were used to evaluate the strain for the raft and micropiles. They have a resistance of 350 ohm, which significantly reduces the error produced by the variation in the input current.

Four strain gauges were distributed equally along the shaft of each micropile (one for each micropiles raft case) in order to evaluate the shaft load transfer (see Figure 3.29a). Two more strain gauges were used at the top of two micropiles (for micropiles raft cases only) to evaluate the applied axial load. For the rafts, two strain gauges were used to evaluate the bending moment at the center and edge of the raft (see Figure 3.29b).

The strain gauges were attached to the micropiles and the raft using Loctite 495 instant adhesive. Two measures were taken to protect the strain gauges during handling and testing. First, a thin layer of M-coat A was administered. Second, a thin layer of quick dry epoxy was used to prevent the strain gauges from getting damaged and to protect the lead wires. In order to simulate a micropile rough interface, fine sand particles were sprinkled on the uncured epoxy film.

a   b
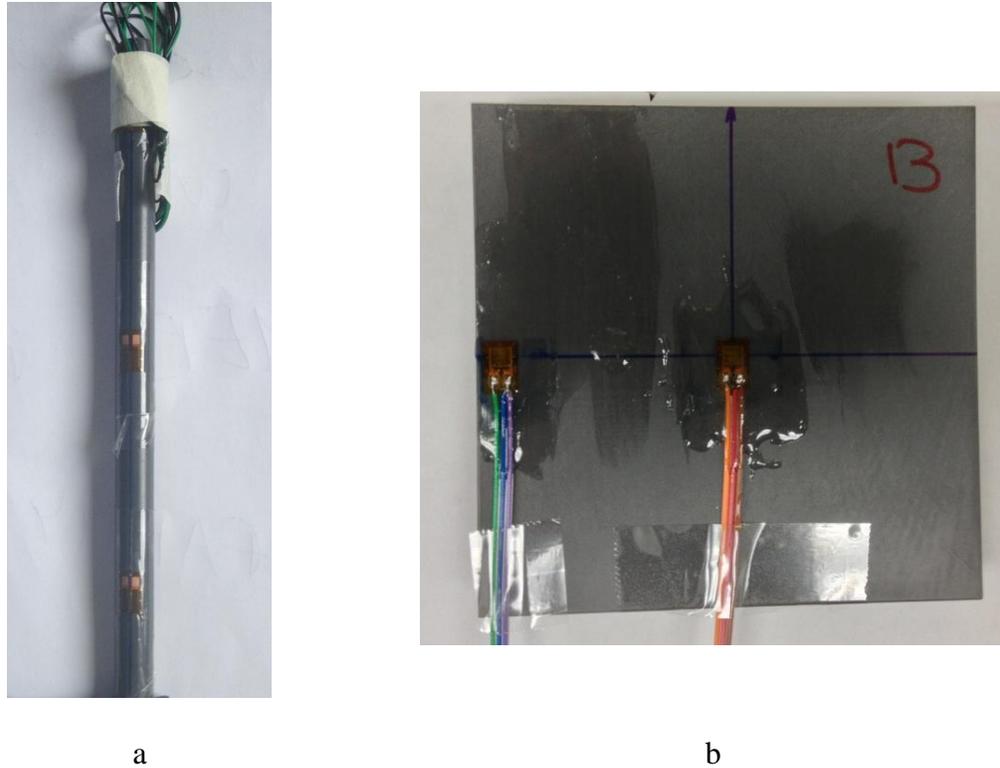
Figure 3.29. Strain gauges attached to: (a) the micropile model; and (b) the raft model.

3.5.8. The String Pot

Two string pot or string potentiometer (shown in Figure 3.30) were used to monitor the clay vertical settlement during consolidation. The string pot was calibrated by extending the string pot's cable for a predetermined length and recording the corresponding voltage from the DAQ system. This process was repeated for a number of points for both string pots (see Figure 3.31).

Figure 3.30. Typical string pot used to measure the consolidation settlement for the clay.
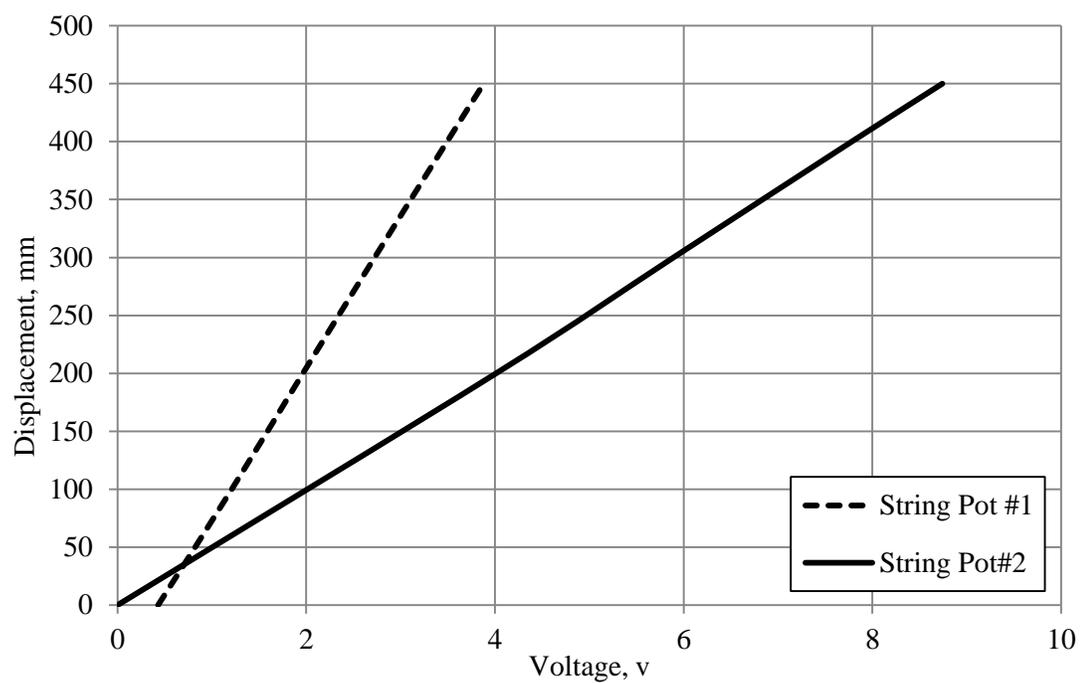
Figure 3.31. Displacement vs. voltage for both string pots.

3.5.9. Pore Pressure Transducer (PPT)

Two miniature pore pressure transducers (PPT) with a capacity of 900 kPa (manufactured by Druck Ltd., model PDCR81) were used to monitor the dissipation of excess pore water pressure to establish the degree of consolidation during the in-flight consolidation. They are only 11.4 mm in length and 6.4 mm in diameter, so they induce minimal disturbance to the test bed. The PPTs were calibrated using the PPT calibration device (see Figure 3.32b). The calibration process was conducted by inserting the PPT into the calibration device which was sealed using a rubber plug to prevent any leakage in the pressure (see Figure 3.32a). The values of the applied pressure and resulting voltage were recorded by the DAQ system. Figure 3.33 presents the calibration curve for the PPTs.

The two PPTs were installed at a depth of 125 mm and 275 mm from the top of the clay layer. The installation process was performed after the laboratory consolidation was concluded. The pore stone used to protect the sensing diaphragm was de-aired by placing it in boiling water for approximately 15 minutes. The pore stone was then attached to the PPT while the PPT was immersed in water immediately before inserting it into the sample. At the designated predrilled holes in the tub's wall (see Figure 3.32c), the PPTs were installed using the following procedure: (i) an extension part was mounted to the tub wall at a selected location to allow for a precision horizontal drilling; (ii) a small greased wall tube with a diameter of 7 mm was inserted horizontally into the clay sample to prevent the clay from collapsing during the excavation of the hole. The tube was approximately 5 mm shorter than the PPT location to allow the instrument to be in contact with an intact clay sample; (iii) an auger was used to remove the clay within the

tube; (iv) the PPT was then placed on a guide and inserted into location with the intact clay sample; (v) the tube was slowly withdrawn while injecting the gap with clay slurry; (vi) in the final step, a rubber gland seal was fitted around the PPT cable to prevent any leakage.

a

b
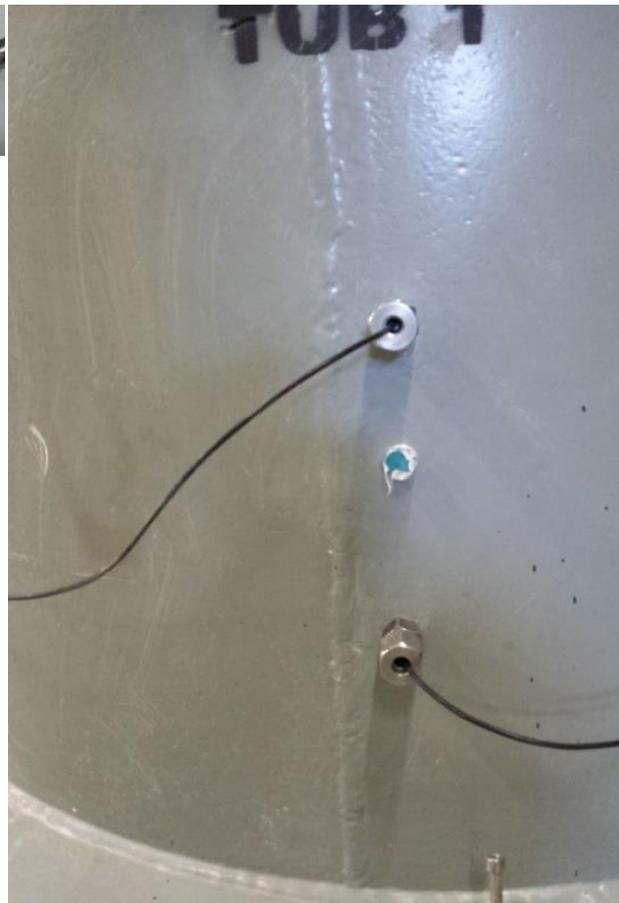
c

Figure 3.32. (a) PPT used to monitor the consolidation in the centrifuge; (b) the PPT calibration device; and (c) the PPT installed in the tub.
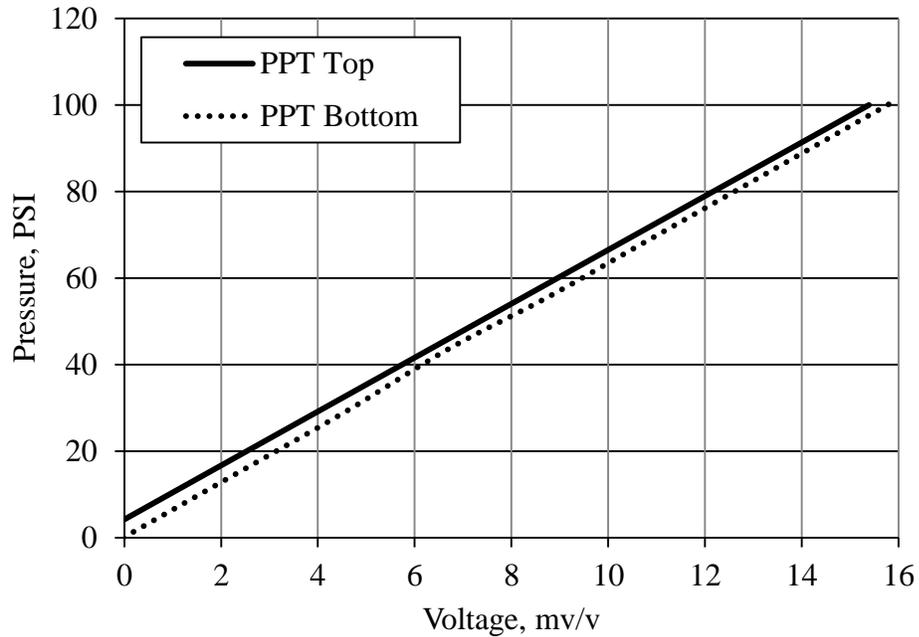
Figure 3.33. Pressure vs. voltage for the PPTs used in the testing program.

3.5.10. T-Bar

The cone penetration test (CPT) was used to evaluate the soil profile in-flight. However, the undrained shear strength, s_u, that is calculated using the CPT needs to be corrected for the ambient total vertical stress, σ_v, according, i.e.

$$s_u = \frac{(q_c - \sigma_v)}{N_k} \tag{3.7}$$

The cone empirical factor, N_k, is sensitive to the soil stress history, stiffness and stress level; consequently, a previous knowledge of the soil is required to evaluate a proper value of N_k.

Stewart and Randolph (1991) developed the T-bar test. The T-bar test provides a suitable alternative to the CPT for clay soil because it is related directly to the undrained shear strength, s_u, and does not require any corrections. The clay undrained strength is evaluated from the T-bar test as:

$$s_u = \frac{P_{t-bar}}{D_{T-bar}N_b} \tag{3.8}$$

Where: s_u: undrained shear strength; P_{T-bar}: force per unit length acting on the cylinder; D_{T-bar}: diameter of T-bar cylinder; and N_b: bar factor depends on the surface rightness of the cylinder, and varies between 9 and 12 with a recommended value of 10.5 (Stewart and Randolph, 1994).

The T-bar consists of a small cylinder attached to a conventional cone pentameter probe at a right angle (see Figure 3.34). The cylinder used in this study was 7.5 mm in diameter and 29 mm in length. The T-bar was calibrated as shown in Figure 3.35 with an error of 1.1%.

Figure 3.34. Typical apparatuses used in T-bar test.
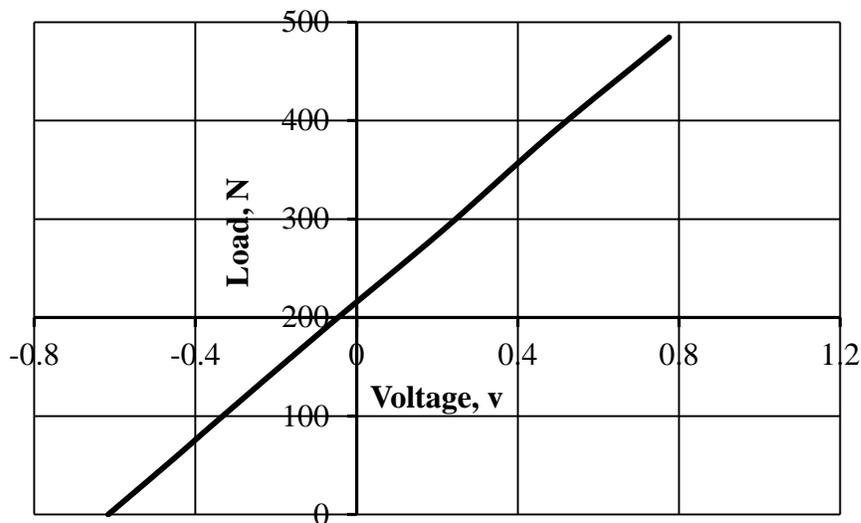
Figure 3.35. Load vs. voltage for the T-bar apparatuses.

3.6. CENTRIFUGE TESTS

A detailed description of the test setup and head works that were used to perform the centrifuge testing program in both sand and clay is presented in this section including the different actuators and instrumentations used throughout the testing program. In addition, technical information for each test group will be provided including the testing procedure.

3.6.1. Sand

3.6.1.1. Test Setup

The sand head work consisted of 2 actuators with 10 kN capacity each as shown in Figure 3.36. The first actuator with the primary load cell attached to it was used to apply the load to the model. This actuator was located at the center of the strong box to leave enough distance between the model and the strong box walls. The model displacement was measured using both the actuator's movement sensor and a laser beam to achieve high accuracy. In order to eliminate the boundary effect of the strong box's walls, smooth

plastic sheets were attached to the walls. The second actuator was used to perform the cone penetration test (CPT). Both the actuators were mounted on 3 I-beams and bolted to the strong box as shown in the 3D model in Figure 3.37. Two LVDTs were mounted on the outside I-beams to monitor the sand settlement during the flight (see Figure 3.36). An LDT was used to measure the differential settlement of the raft which was mounted on the inside I-beam.

In order to reasonably simulate the installation of the type B micropile (in which pressurized grout is used resulting in enlargement of micropile cross-section) and improvement of adjacent soil, the micropile model with a roughened surface was pushed into sand which caused densification to the surrounding soil. Figure 3.38 displays the typical final setup for the centrifuge testing in sand.
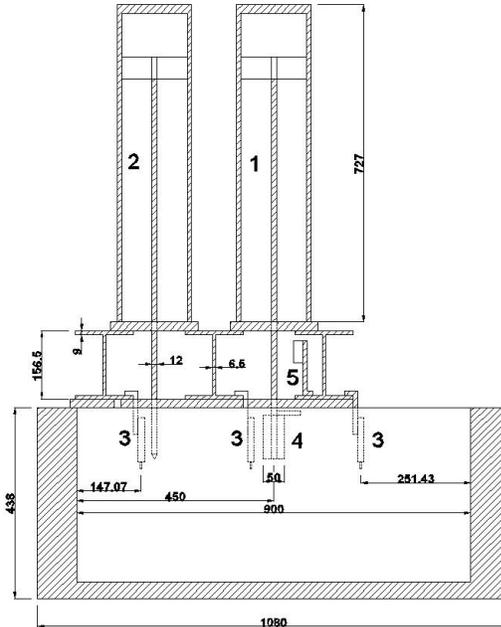
Figure 3.36. Vertical cross-section of centrifuge package, including: (1) vertical actuator for applying load; (2) sand cone for CPT; (3) LDT and LVDTs; (4) load cell; and (5) laser (all dimensions in mm).

3.6.1.2. Centrifuge Test Procedure

All six sand tests were carried out using the same testing procedure. After preparing the sand, the head work was attached to the strong box and the package was transferred to the centrifuge. Once the safety protocol was completed, the test began. The test speed was increased gradually to 93 rpm, which produced acceleration equal to 50g at the effective centrifuge radius. However, at each 10g interval, the speed was kept constant for 5 minutes in order to monitor the change in the sand level. At 50g, the test was started by loading the model at a rate of 0.1 mm/sec until failure or when it reached the capacity of the actuator (10 kN). Next, actuator#1 was raised to its original position and the CPT was performed at a rate of 2 mm/sec. Subsequently, actuator#2 (for the CPT) was raised and the centrifuge was stopped gradually.
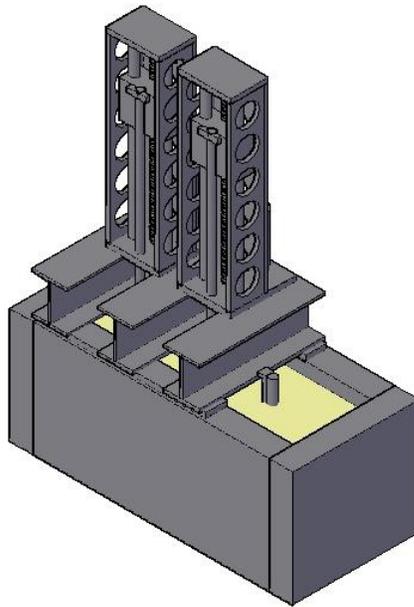
Figure 3.37. 3D model for the sand package.
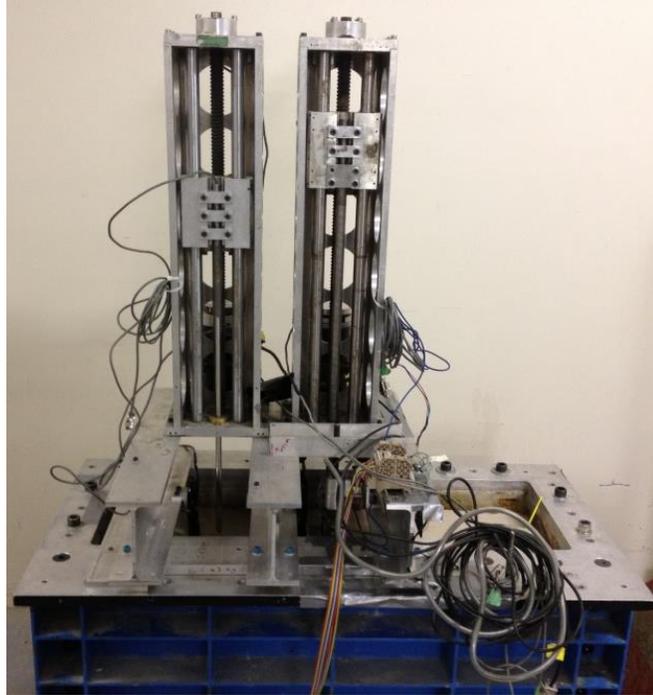
Figure 3.38. Complete centrifuge package for sand test.

3.6.1.3.   In-Flight Cone Penetration Test (CPT)

Three in-flight cone penetration tests were conducted during the centrifuge tests in the sand soil. The rate of penetration was 2 mm/sec. To eliminate any boundary effect, the minimum distance between the cone center and the container wall was kept at $15D_c$, where D_c is the cone diameter. Bolton et al. (1999) suggested that the distance between the boundaries of the container to the cone diameter (B/D_c) should be greater than 10. Figure 3.39 shows the CPT results for different centrifuge tests in sand with a final penetrating depth of approximately 190 mm. The results indicate that the density of the sand was uniform along the height of the sand due to the linear increase in the resistance of the cone tip.
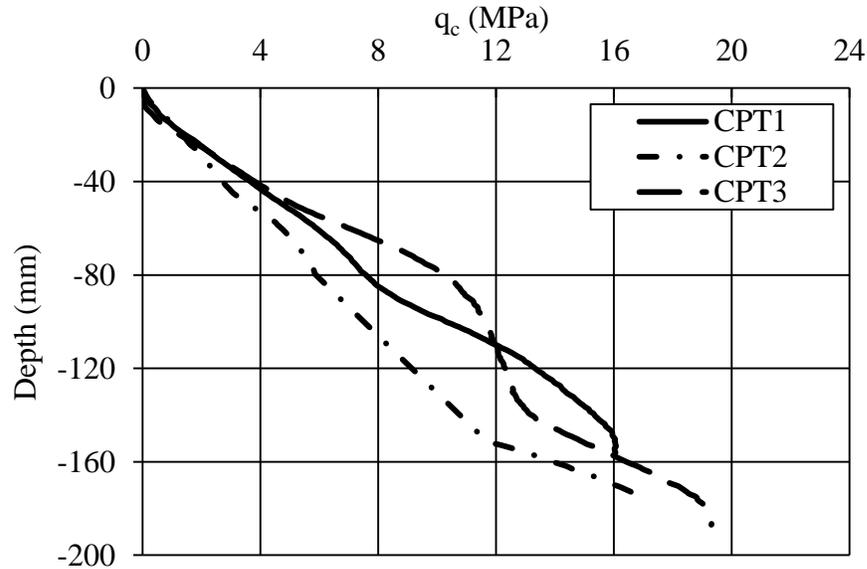
Figure 3.39. The in-flight CPT.

3.6.2. Clay

3.6.2.1. Test Setup

The headwork for clay test No. 7 consisted of 2 actuators with 10 kN capacity each as shown in Figure 3.40. Three test models were distributed across the surface of the clay with a minimum of 200 mm clearance (2 times the width of the raft) and a 90° angle between all the models and the steel tub's wall to minimize boundary effects. Two main cross I-beams were laid out along the center of the tub and bolted to the tub. A 120 mm gap between the I-beams was kept in order to allow for the movement of the actuators. The first actuator with the primary load cell attached to it was used to apply the load to the model. This actuator was located 150 mm away from the center of the tub.

The model displacement was measured using both the actuator's movement sensor and a laser beam to achieve high accuracy. In order to help eliminate the boundary effect

of the tub's walls, grease was applied before the consolidation process. The second actuator was used to perform the T-bar penetration test at the center of the tub. Both actuators were mounted on the cross I-beams as shown in Figure 3.41. Actuator#2 for the T-bar was mounted on 2 small I-beams on top of the main I-beams to allow for sufficient room for the T-bar probe.

Tests No. 8 and 9 were performed in the same flight by using actuator No. 2 to apply the load to the single micropile. This was done by moving actuator #2 and mounting it on the main cross I-beams with a distance of approximately 400 mm between the two actuators. For the second flight, the test was performed by rotating the main I-beam 90° and changing the location of the second actuator, which was done in a very short period of time to keep the clay in its original condition.

Two LVDTs were mounted on the tub's wall to monitor the in-flight consolidation (see Figure 3.41). An LDT mounted on the inside of the main I-beam was used to measure the differential settlement of the raft. In addition, two PPTs were used to monitor pore water pressure dissipation during the in-flight consolidation.

All micropiles were installed in similar fashion. A hole with a diameter smaller than the micropile was drilled vertically as shown in Figure 3.42. The purpose of the pre-drilled hole was to reduce the risk of damaging the model micropile during jacking into clay due to the relatively high undrained shear strength of the model clay (approximately 30 kPa at the depth equal to one half the micropile length, 100 mm). The micropile model with a roughened surface was pushed into the small pre-drilled hole causing it to enlarge. The complete package for test#7 and test#8 and 9 are shown in Figure 3.43a and Figure 3.43b, respectively.
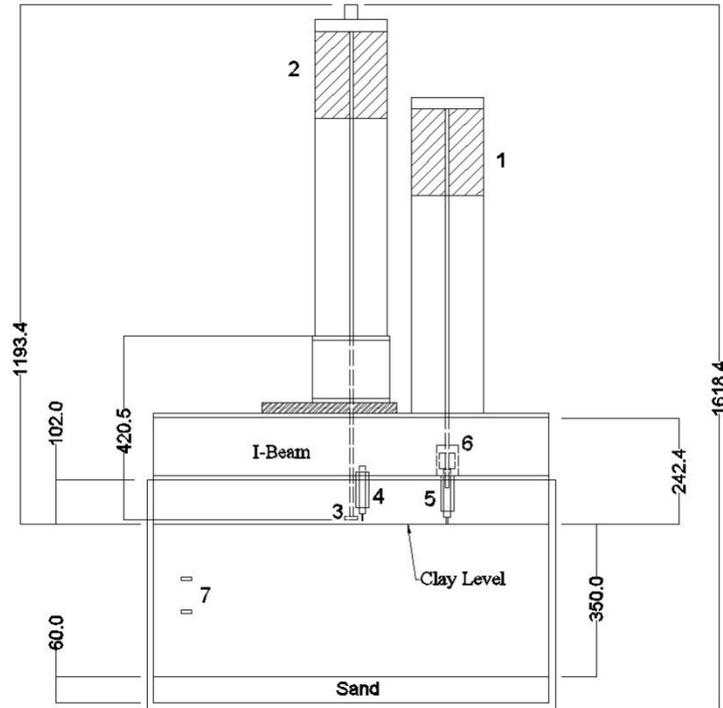
Figure 3.40. Vertical cross-section of centrifuge package including: (1) vertical actuator for applying load; (2) actuator used for T-bar; (3) T-bar; (4) LVDTs to measure clay settlement; (5) load cell; (6) laser; and (7) PPTs (all dimensions in mm).
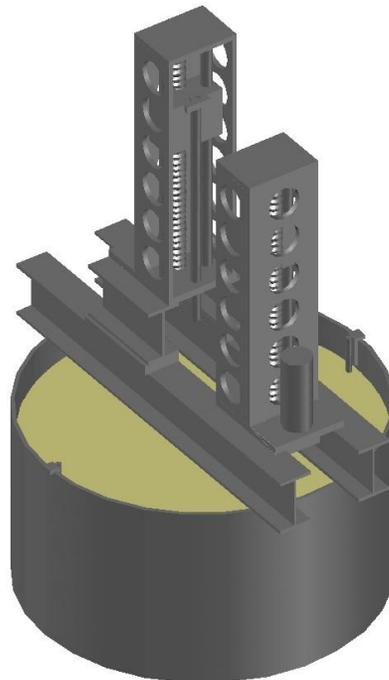
Figure 3.41. 3D model for the clay package.

Figure 3.42. Process used to install the micropile in clay.

a
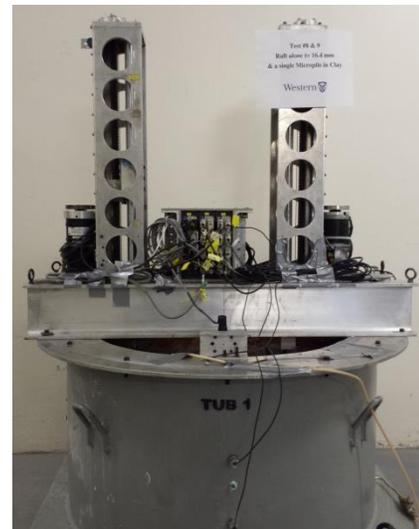
b

Figure 3.43. Complete centrifuge package for clay test: (a) for test#7; and (b) for test#8 and 9.

3.6.2.2. Centrifuge Test Procedure

Once the laboratory 1D consolidation was completed, the tub was removed from the consolidation frame, the excess water was vacuumed, and the loading piston was removed slowly. The tub extension was removed and the surface of the clay was leveled and prepared to install the model. The final height and weight of the clay was measured in order to calculate the final unit weight (18.4 kN/m^3). The models and PPTs were installed as described earlier and the surface of the clay was covered with a thin layer of grease in order to prevent the surface from drying out. Subsequently, the head work was attached, the instrumented package was loaded into the centrifuge and the base valve was opened to allow for water drainage during the in-flight consolidation. The centrifuge was accelerated in increments of 10g up to 50g and the consolidation step started. For each increment, the acceleration was kept constant for approximately five minutes to check the instruments' readings. At 50g, the clay was consolidated to 90% degree of consolidation under self-weight. The consolidation progress was monitored using two LVDTs and two PPTs. Figure 3.44 presents the consolidation progress for test No. 7 when the t_{90} was equal to 72.25 minutes. In addition, the consolidation process and results for tests No. 8 and 9 (same flight) were consistent with test No. 7. Once the consolidation process was concluded for test No. 7, actuator No. 1 was moved to apply the load at a rate of 6 mm/min. Next, the T-bar test was performed at a rate of 3 mm/sec to a depth of 330 mm. The test was concluded and the centrifuge was stopped slowly. Once the centrifuge came to a complete stop, the base valve was closed to prevent the clay from sucking the water from the sand layer. The package was then prepared for the text test.

For the second flight, the test started after the consolidation process was finished by loading the raft alone using actuator No. 1 at a rate of 6 mm/min. Subsequently, the loading of the single micropile was performed at 6 mm/min. Once the clay testing program was concluded, several undisturbed clay samples were retrieved by using PVC tubes that were 100 mm in diameter and 350 mm high. The tubes were inserted into the clay to a depth of 345 mm and the remaining 5 mm were filled with wax in order to preserve the moisture content. After the top wax was dried the tubes were dug out, the excess clay at the other end was trimmed and a 5 mm gap was created which was filled with wax.   The spacing between the tube locations was 200 center-to-center. These samples were later used to perform a number of triaxial tests.
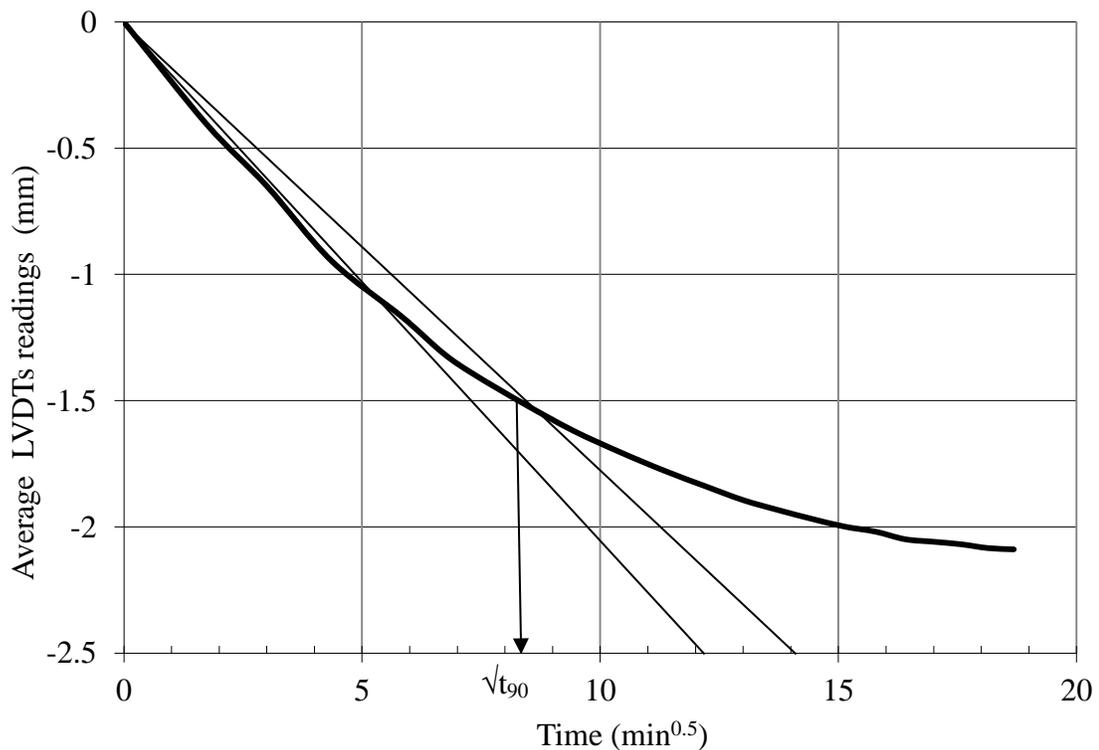
Figure 3.44. Settlement vs. $\sqrt{t}$ for the in-flight consolidation for the clay test bed showing $\sqrt{t_{90}}$

3.6.2.3. In-Flight T-bar Test

The measured undrained shear strength using the in-flight T-bar test is presented in Figure 3.45. The s_u was calculated according to Eq. 3.8 with N_b equal to 10.5. Although the profile shows sudden increases in the s_u value at the first 10 mm due to the high OCR, it starts to increase linearly afterward at a rate equal to 0.1 kPa/mm (2 kPa/m at prototype scale). These values can be used to estimate the elastic modulus as the ratio E_u/s_u varied between 250 and 500 with an average of 375 based on the CU triaxial tests. This value is at the lower bound of the values reported by Jaimolkowski et al. (1979) for clay with a plasticity index (PI) less than 30 and OCR between 4 and 6 in which the E_u= 300~1000 s_u.
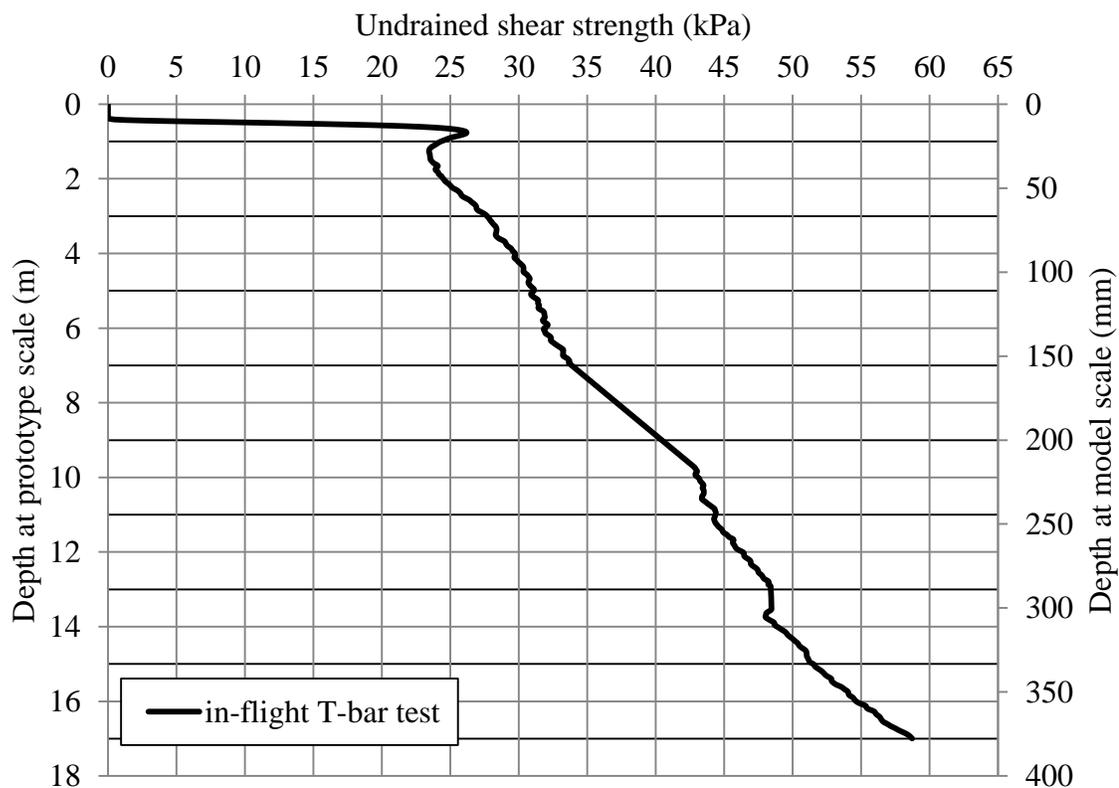
Figure 3.45. Undrained shear strength profile along the clay depth using the T-bar test results.

3.7. CONCLUSIONS

This chapter is dedicated to describe the technical details involved in designing the centrifuge testing program. A number of critical aspects were examined including the design of model parts, the properties of the soil material used for both sand and clay test beds and the steps involved in designing the test beds. In addition, all the instruments involved in this testing program were calibrated. The procedures and the steps used to prepare the sand and K-S clay test beds were thoroughly presented. Finally, the technical details regarding the centrifuge testing sequence for the different micropile, rafts and micropiled rafts were provided.

A series of UU and CU triaxial tests were performed using clay specimens retrieved from the K-S clay used in the centrifuge testing program after it was concluded. These tests yielded two equations that can be used to relate undrained shear strength to the mean effective stress for similar clay materials. It was found that the undrained modulus of elasticity, E_u, is approximately 155 times the mean effective stress. Moreover, c_1 and c_2 parameters used to evaluate the undrained shear strength, s_u, according to Eq. 3.5 were 0.31 and 0.51, respectively. By using the proposed Eq. 3.5, the estimated s_u was in good agreement with the values obtained from the in-flight T-bar test.

REFERENCES

ASTM Standard D2850. (2007). Standard Test Method for Unconsolidated-Undrained Triaxial Compression Test on Cohesive Soils. ASTM International, West Conshohocken, PA.

ASTM Standard D422-63. (2007). Standard Test Method for Particle-Size Analysis of Soils. ASTM International, West Conshohocken, PA.

ASTM Standard D4318-10. (2010). Standard Test Methods for Liquid Limit, Plastic Limit, and Plasticity Index of Soils. ASTM International, West Conshohocken, PA.

ASTM Standard D4767-11. (2011). Standard Test Method for Consolidated Undrained Triaxial Compression Test for Cohesive Soils. ASTM International, West Conshohocken, PA.

ASTM Standard D 4253-63. (2007). Standard Test Methods for Maximum Index Density and Unit Weight of Soils Using a Vibratory Table. ASTM International, West Conshohocken, PA.

ASTM Standard D 4253-63. (2006). Standard Test Methods for Minimum Index Density and Unit Weight of Soils and Calculation of Relative Density. ASTM International, West Conshohocken, PA.

ASTM Standard D 3080. (2011). Standard Test Method for Direct Shear Test of Soils Under Consolidated Drained Conditions. ASTM International, West Conshohocken, PA.

Bishop, A. W. and Henkel, D. J. (1962). The Measurement of Soil Properties in the Triaxial Test. London: Edward Arnold Publishers Ltd.

Bolton, M. D., Gui, M. W., Garnier, J., Corte, J. F., Bagge, G., Laue, J. and Renzi, R. (1999). Centrifuge Cone Penetration Tests in Sand. Géotechnique, **49**(4): 543-552.

Budhu, M. (2007). Soil Mechanics and Foundations. 2nd edition. John Wiley & Sons, Hoboken, NJ.

Jaimolkowski, M., Lancellotta, R., Pasqualini, E., Marchetti, S. and Nova, R. (1979). Design Parameters for soft clays. General Report. *In* Proceedings of the 7th European Conference on Soil Mechanics and Foundation Engineering. No. 5, pp. 27–57.

Lin, L. (1995). Strength Characteristics of a Modelling Silty Clay. M.Eng. Thesis, Memorial University of Newfoundland. St. John' s, Newfoundland. Canada.

Ovesen, N. K. (1975). Centrifugal Testing Applied to Bearing Capacity Problems of Footing on Sand. Géotechnique, **25**(2): 394-401.

Paulin, M. J. (1998). An Investigation into Pipelines Subjected to Lateral Soil Loading. PhD Thesis, Memorial University of Newfoundland. St.John's, Newfoundland, Canada.

Rossato, G., Jardine, R. J. and Ninis, N. L. (1992). Properties of Some Kaolin Based Model Clay Soils. ASTM Geotechnical Testing JournaL, **15**(2): 166-179.

Schofield, A. N. (1980). Cambridge Geotechnical Centrifuge Operations. Géotechnique, **30**(3): 227-268.

Schofield, A. N. and Wroth, C. P. (1968). Critical State Soil Mechanics. New York: McGraw-Hill.

Springman, S. M. (1993). Centrifuge Modelling in Clay: Marine Application. *In* Proceedings of the 4th Canadian Conference on Marine Geotechnical Engineering, St.John 's, Newfoundland, pp. 397-403.

Stewart, D. and Randolph, M. (1994). T-bar Penetration Testing in Soft Clay. ASCE Journal of Geotechnical Engineering, **120**(12): 2230-2235.

Tovey, N. K. (1970). Electron Microscopy of Clays. University of Cambridge PhD dissertation.

CHAPTER 4: CENTRIFUGE MODELING OF MICROPILED RAFTS IN SAND

4.1. INTRODUCTION

A micropile is a small diameter "cast-in-place" pile. Micropiles were initially used to repair historic buildings that were damaged during World War II, which entailed installing micropiles by drilling through the existing foundation and filling the holes with cement grout and a steel bar (Lizzi, 1982). Nowadays, different types of micropiles are used to provide the load carrying capacity of new foundation systems (FHWA, 2005). These types include: type A in which the grout is simply placed solely by gravity action; type B: in which neat cement grout is placed into the micropile shaft by applying injection pressure, which is normally about 0.5 to 1 MPa; type C: This type is accomplished in two steps: (1) grout is placed under gravity head and, (2) before the cement grout is hardened (about 15 to 25 minutes), a sleeved grout pipe is used to inject similar grout at minimum 1 MPa pressure without using packers at the bond zone; finally type D, which is similar to type C, but in order to increase the friction capacity of the bond, a packer may be used at desirable locations inside the sleeved pipe. In current practices, the diameter of a micropile is typically less than 300 mm. A micropile transfers its load through skin friction to the soil in the bonded area between the grout and the soil.

Micropiles were introduced into North America in the mid 1980's and their use has been rapidly growing ever since. Their construction methods have been improved and new construction techniques have been developed. The advancements in drilling equipment have resulted in the ability to drill through almost any ground condition to

install micropiles at any angle with minimum noise, vibration and disturbance. In addition, the relatively small size of the equipment has allowed the underpinning of existing foundations even in restricted access situations (Bruce et al., 1995).

In most cases, the micropiles are constructed by drilling the pile shaft (the bore hole) to the desired depth using an appropriate drilling method depending on the depth and size of the micropiles and the sensitivity of the site to disturbance. During drilling, a casing is installed simultaneously to support the shaft wall. After the drilling is completed, a steel reinforcement, (e.g. steel bars) is placed, occupying approximately 8% of the total volume. Subsequently, grout is placed in the predrilled micropile hole; in most cases the grout is pressurized after removing the temporary casing to increase the diameter of the bonded length and to increase the friction of the micropile shaft with the soil. In order to increase the lateral stiffness and capacity of the micropile, the top portion of the temporary casing can be left in ground and is not fully removed (Shong and Chung, 2003).

Micropiles are used in a variety of applications, including: (1) to serve as a main foundation system for static and dynamic loading; (2) to upgrade an existing foundation system; and (3) to stabilize slopes and reinforce the soil (Bruce et al., 1995). Several studies have been conducted in order to evaluate the performance of single micropiles and micropile groups in sand under various types of loading. Different testing techniques have been employed such as full-scale micropile load tests, 1g physical modeling, and geotechnical centrifuge modeling. Jeon and Kulhawy (2001) examined the results of 21 full scale field tests on micropiles with diameters that varied between 0.15 m and 0.19 m and shaft depths that varied between 9 m and 30 m. Eight micropiles were installed in

cohesive soils and 13 micropiles were installed in cohesionless soils with a wide range of soil parameters. Different grouting types were used including: Type B and Type C or D. The analysis of the test results indicated that the load-carrying capacity of the micropile is significantly different than the drilled shaft due to how the pressure grouting affects the state of stress in the soil. Moreover, the micropile load carrying capacity per pile volume can be higher than larger diameter drilled shafts for shaft depth to diameter ratio less than 100. This increase is in the order of 1.5 to 2.5 for micropiles installed in sand. Meanwhile, Tsukada et al. (2006) evaluated the improvement in bearing capacity of spread footings reinforced with micropiles through load testing small models that represented the footing and the micropiles. The test models were made from different materials and with varying degrees of stiffness, including: (1) circular footing without micropiles, (2) circular footing with a single micropile and (3) circular footing with a group of micropiles (n_{mp}=2-8). The test soil was constituted of sand with different densities. The micropiles inclination angle, α_i, was varied from 0° to 60°. They reported that the bearing capacity of foundations in dense sand increased significantly due to the dilation effect and that the load capacity of the spread footing reinforced with micropiles was double the summation of the individual load capacity of the surface footing and the capacity of micropiles.

The concept of underpinning foundation systems using micropiles is similar to the concept of the piled raft, which is a composite structure with three components: subsoil, raft and piles. These components interact through a complex soil-structure interaction scheme, including the pile-soil interaction, pile-soil-pile interaction, raft-soil interaction, and finally the piles-raft interaction. Several studies have been conducted in order to

evaluate the piled raft performance including Poulos and Davis (1974); Clancy and Randolph (1993 and 1996); Randolph (1994); and Poulos (2001). Poulos (2001) has formulated the findings of several studies into an analytical approach, widely known as Poulos-Davis-Randolph (PDR), in order to evaluate the axial stiffness of piled rafts for preliminary design purposes. However, the ability of the PDR method to evaluate the axial stiffness of MPR has to be confirmed in order to be used in preliminary design stage.

The effect of raft flexibility is neglected in the PDR method, which can lead to overestimating the axial stiffness of the piled raft or micropiled raft foundation systems. In addition, the piled raft foundation system offers some advantages over the pile group design in terms of serviceability and efficient utilization of materials. For a piled raft, the piles will provide sufficient stiffness to control the settlement and differential settlement at serviceability load while the raft will provide additional capacity at ultimate load. The raft in a piled raft transmits approximately 30% to 50% of the applied load to the soil depending on the spacing between the piles (Clancy and Randolph, 1993). Normally, a piled raft would require fewer piles in comparison to a pile group to satisfy the same capacity and settlement requirements (Poulos et al. 2011).

The geotechnical centrifuge testing is a useful tool to simulate soil-structure-interaction (SSI) problems. Several research programs were carried out using the geotechnical centrifuge in order to study the behaviour of pile groups, piled raft, micropile groups subjected to different loading conditions, and to provide experimental data to calibrate and verify finite element models (FEM). Horikoshi et al. (2002, 2003a, b) used this centrifuge testing to evaluate the performance of piled rafts under different

types of loading: vertical; horizontal and dynamic loading. The tests were conducted under 50g centrifugal acceleration and all the model parts were made of aluminum. The model consisted of four piles rigidly connected to the raft at spacing of 4 times the pile diameter (0.5 m at prototype scale). Toyoura sand was used as the model ground (Horikoshi et al. 2003a). From the centrifuge results, the stiffness of single pile and piled raft were 0.376 kN/mm and 2.91 kN/mm, respectively. This finding suggested that the axial stiffness of piled raft is 140% higher than of group of 4 piles (4 x 0.376 = 1.504 kN/mm).

Mahboubi and Nazari-Mehr (2010) evaluated the performance of single and micropile groups in sand under dynamic loading employing a FEM verified using centrifuge test results. Their results indicated a flexible behaviour of the soil-micropile system, which lead to small stresses introduced to the soil. Juran et al. (2001) performed centrifuge testing on a number of single and group micropile configurations in sand. They evaluated the influence of micropile inclination, spacing-to-diameter ratio and micropile configurations on both the load transfer mechanism and resisting force of the micropile systems. The micropiles were modeled using polystyrene tubes with roughened surface. The number of micropiles varied between 1 and 18 micropiles with spacing-to-diameter ratio between 3 and 5. The micropile groups were subjected to dynamic excitation with acceleration amplitudes that varied between 0.03 g and 0.5 g. The results indicated a positive group effect was achieved for spacing to pile diameter ratios (S/D_{mp}) 3 and 5 compared to a single pile; for the inclined micropile group, the bending moment was reduced and the axial stress increased compared to vertical groups, indicating improved seismic resistance for the network configuration. Furthermore, Rose et al. (2013)

investigated the performance of perimeter pile groups in clays using geotechnical centrifuge testing and numerical modeling. The study was conducted considering different pile group arrangements. The pile diameter was 300 mm for all different cases. It was found that the failure mechanism for the perimeter groups consisting of 14 to 20 piles with 1.75 D_p spacing was block failure with group efficiency ratio of about 0.9.

In addition, several micropile load tests were conducted in order to evaluate the lateral performance of micropiles (e.g. Richards and Rothbauer (2004), Long et al. (2004), Shahrour and Ata (2002), and Teerawut (2002)).

The overall behaviour of micropiles used as retrofitting elements for an existing foundation is similar to a piled raft foundation. In such cases, the load is transmitted through both the foundation and the micropiles. Therefore, it is necessary for the design engineers to better understand the behaviour of the micropiles as retrofitting option for the isolated raft foundation. In addition, it is recommended to use micropiled raft (MPR) as a new foundation system to take advantage of the combined benefits of the piled raft system and the efficient installation of micropiles and associated ground improvement. In this paper, the main focus is to evaluate the performance characteristics of the MPR as well as to examine the ability of micropiles to boost the axial stiffness of an isolated raft foundation. The effects of raft flexibility on the important design parameters of the MPR system will be evaluated, including: the axial stiffness of MPR, raft differential settlement, contact pressure, and load sharing between the raft and micropiles. Moreover, the validity of Poulos-Davis-Randolph (PDR) method to estimate the axial stiffness of MPR for different raft flexibility values will be addressed. In addition, using micropiles as a method to reduce differential settlement was considered.

4.2. EXPERIMENTAL SETUP

4.2.1. Centrifuge Facility

The C-Core centrifuge facility located at Memorial University, St. John's, Newfoundland, was used in the current study. The Acutronic 680-2 geotechnical centrifuge with a maximum centrifugal rotational speed of up to 189 rpm and a maximum acceleration of 200 g at an effective radius of 5 m was used in conducting the tests. The maximum payloads at 100g and 200g are 2.2 ton and 0.65 ton, respectively. A 48-channels data acquisition system is used to collect electrical signals from strain gauges and transducers throughout the tests.

4.2.2. Model Design and Centrifuge Package Setup

The centrifuge testing programme consisted of the following tests: (1) one test on a single micropile; (2) one test on a raft with a thickness equivalent to 0.6 m at prototype scale; (3) three tests on micropiled rafts with different raft thicknesses (i.e. 0.3 m, 0.45 m and 0.6 m at prototype scale); and (4) one test for a raft with a thickness equivalent to 0.6 m with a single micropile at its center to evaluate the use of micropiles as settlement reducers. All tests were performed on dry sand soil with a relative density (D_r) of 70% and under centrifugal acceleration of 50g. The prototype diameter of the micropile was 150 mm and its length was 10 m.

Table 4.1 provides the model and prototype dimensions along with the appropriate scaling laws. In order to work with reasonable size cross-sections, the models of the rafts and micropiles were fabricated using PVC (E_m=2900 MPa, ν_m= 0.4), which has a modulus of elasticity smaller than that of the prototype material (concrete). Equations 4.1

and 4.2 were used for evaluating the geometrical dimensions of the centrifuge models, i.e.,

$$\frac{E_p A_p}{E_m A_m} = n^2 \qquad (4.1)$$

$$\frac{E_p I_p}{E_m I_m} = n^4 \qquad (4.2)$$

Where: $E_p A_p$: axial rigidity for the prototype element; $E_m A_m$: axial rigidity for the model element; $E_p I_p$: flexural rigidity for the prototype element; $E_m I_m$: flexural rigidity for the model element; and n: scaling factor.

The size of the model micropiles facilitated the installation of strain gauges to measure their axial forces, and the size of the model raft relative to the size of the centrifuge box minimized the boundary effects. Equations 4.1 and 4.2 accurately model the axial rigidity (EA) and flexural rigidity (EI) of the micropile and raft, respectively (Wood, 2004).

Figure 4.1 presents the layout plans for the micropiled raft models and Figure 4.2 shows a schematic for the setup used during the testing program. The soil model in the strong box was 350 mm thick (i.e. 17.5 m at prototype scale). The load was applied vertically to the raft center using an electrical actuator at a constant displacement rate of 0.1 mm/sec (model scale). In order to model the rough surface of Type B micropiles, in which the grout is injected under pressure, the surface of the model micropiles was roughened by gluing sand particles to it. Furthermore, one of the factors that contribute to boosting the capacity of a micropile is the increased grout-ground bonding for the soil surrounding the micropile due to the pressurized grout used in its construction. To simulate this increased bonding condition and densification of the surrounding soil prior to conducting the test, the micropile was jacked at 1g into the soil, hence increasing the

confining pressure of the soil on the pile leading to increased micropile-soil frictional resistance. The adopted method is believed to be more appropriate to represent the actual construction method comparing to the method used by Horikoshi et al. (2003a) in which the pile was placed using a special device prior to pouring the sand.
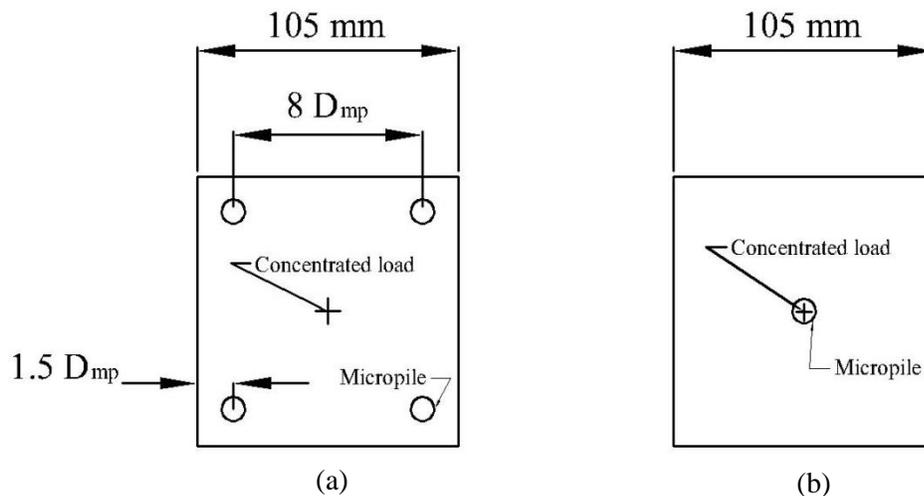
Figure 4.1. Layout for: (a) a micropiled raft and (b) a micropile as settlement reducer.

Table 4.1. Scaling laws for centrifuge modeling and models and equivalent prototype dimensions.

Description		Scaling law	Prototype	Model
Micropile Diameter		E_pA_p/n^2	150 mm	9.53 mm
Axial Rigidity (EA)			516737 kN	207 kN
Micropile Length		1/n	10 m	200 mm
Raft Width and Length		1/n	5.25 m	105 mm
t_r=0.6 m	Raft Thickness	E_pI_p/n^4	0.6 m	16.4 mm
	Flexural Rigidity		697950 kN. m^2	0.112 kN. m^2
t_r=0.45 m	Raft Thickness	E_pI_p/n^4	0.45 m	12.3 mm
	Flexural Rigidity		294448 kN. m^2	0.047 kN. m^2
t_r=0.3 m	Raft Thickness	E_pI_p/n^4	0.3 m	8.2 mm
	Flexural Rigidity		87244 kN. m^2	0.014 kN. m^2
Force (kN)		-	n^2	1
Stress (kPa)		-	1	1
Stiffness (kN/m)		-	n	1
Moment (kN.m)		-	n^3	1
Density (kg/m^3)		-	1	1
Displacement (mm)		-	n	1
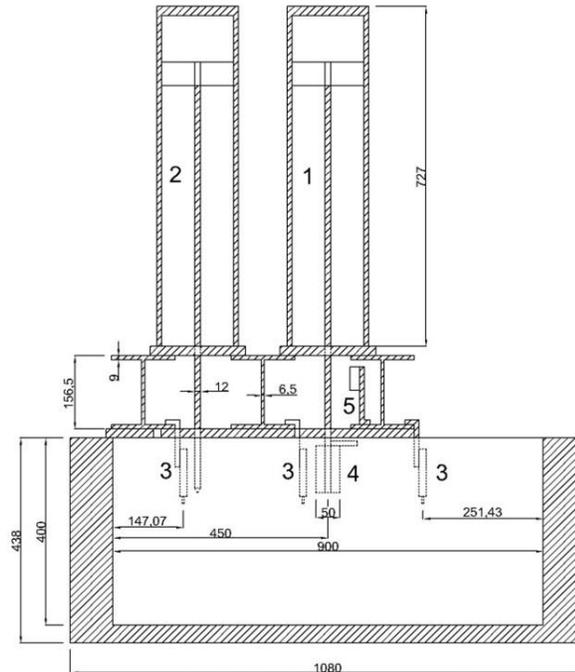
Figure 4.2. Vertical cross-section of centrifuge package including: (1) vertical actuator for applying load; (2) sand cone for CPT; (3) LVDTs; (4) load cell; and (5) laser (all dimensions in mm).

4.2.3. Soil Material

All tests were conducted on micropiles installed in cohesionless soil. The sand was poorly graded #00 white dry silica sand (see particle size distribution in Figure 4.3) with a maximum and minimum unit weight of 16.39 kN/m^3 and 12.44 kN/m^3. Table 4.2 summarizes the sand properties. The sand grain size allowed a foundation width to average grain size (D_{50}) ratio greater than 15 (Ovesen, 1975). The overall height of the sand was divided into 7 sub layers of 50 mm and the sand was compacted to achieve 70% relative density. By knowing the total weight and the volume of the sand, the relative density was confirmed to be 70%.
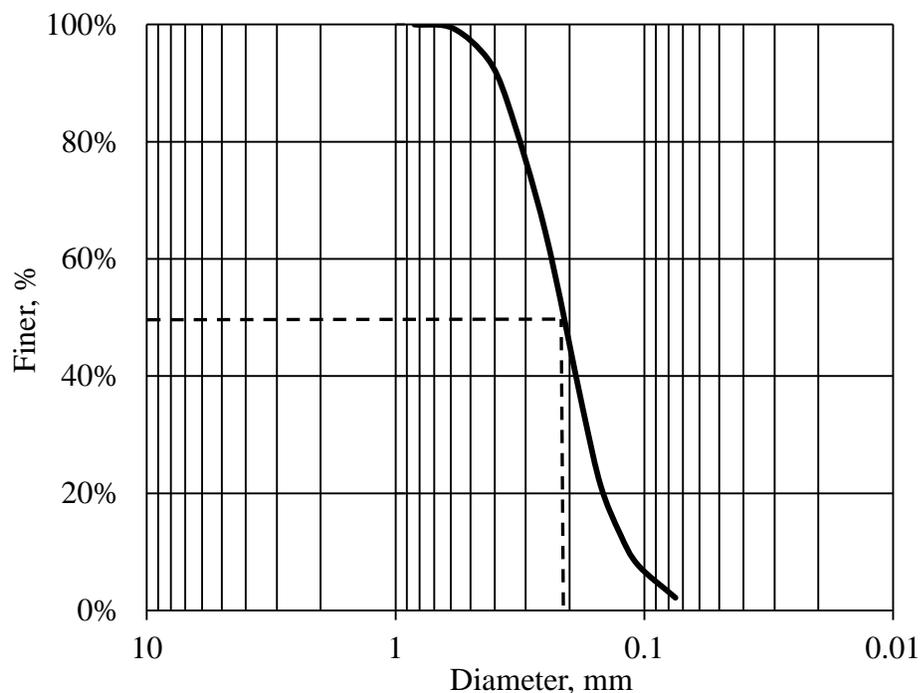
Figure 4.3. Average sieve analysis profile for sand used in the centrifuge tests.

During the centrifuge spinning, the sand surface settled by an average of 2 mm. This amount was observed in all six tests conducted. Figure 4.4 presents the typical sand settlement during the spinning.

Table 4.2. Summary of the classification tests results for the silica sand.

Test	Standard	Result
Maximum unit weight, γ_{max}	ASTM D 4253	16.39 kN/m^3
Minimum unit weight, γ_{min}	ASTM D 4254	12.44 kN/m^3
Angle of internal friction, ϕ	ASTM D 3080	40°
Mean grain size, D_{50}		0.21 mm
Effective grain size, D_{10}	ASTM D 422	0.13 mm
Uniformity coefficient, C_u		1.7
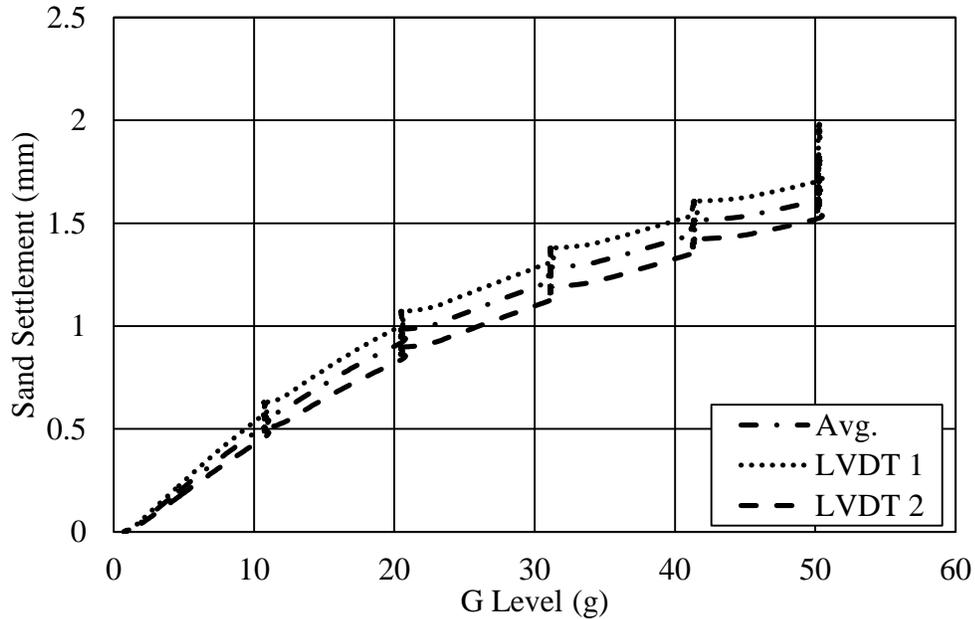
Figure 4.4. Typical settlement of sand surface during centrifuge spinning of the centrifuge

A miniature cone penetrometer was advanced in the soil bed in-flight at 50 g to evaluate the soil strength and stiffness profiles. The results of the cone penetration test (CPT) performed at 50g are presented in Figure 4.5 As can be noted from Figure 4.5, the cone tip resistance, q_c, increased almost linearly with depth. The in-flight CPT results varied by about 25%, which was considered to be reasonable due to a number of factors including: over or under compacting some parts of the layer, the change of sand density during loading the test package into the centrifuge, and the error produced by CPT's load cell; similar variation was reported by (Horikoshi et al., 2003a). The CPT measurements could be correlated to the soil modulus of elasticity, e.g. (Tomlinson, 1996):

$$E_s = 2\sim4\ q_c \tag{4.3}$$

Thus, the CPT measurements demonstrate that the stiffness of the soil increased almost linearly with depth.
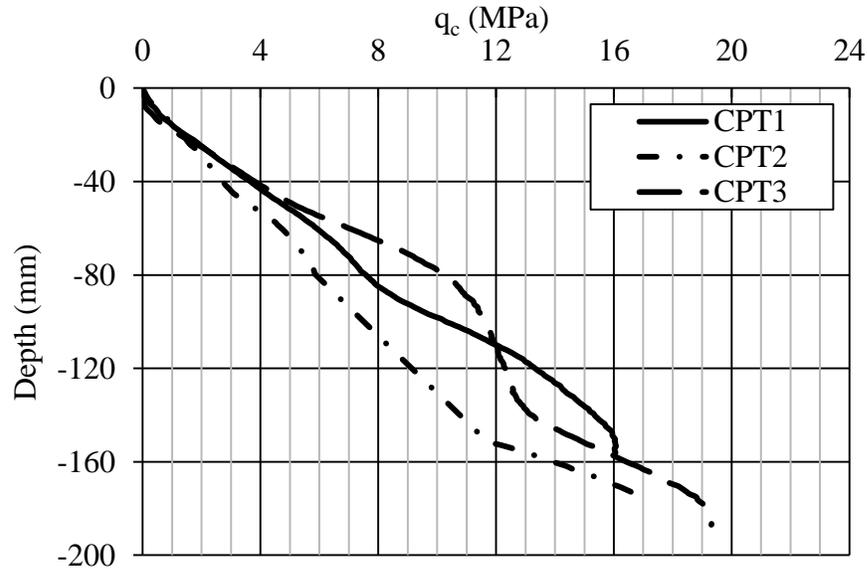
Figure 4.5. In-flight CPT results at model scale.

4.2.4. Instrumentation

Different instrumentations were used to measure different actions, which are important for understanding the behaviour of the tested foundations. Three different types of instrumentations were used to measure strain, movement and contact pressure. The strain measurements were used to obtain the axial forces in the micropiles and the stress distribution at the raft base resulting from the vertical loading. Each micropile was instrumented with four general purpose strain gauges (CEA-06-125UW-350) evenly distributed along its shaft (at spacing of 67 mm) in order to evaluate the load transfer between the micropiles and the soil. The strain gauges had strain range of ±5%. In addition, two extra strain gauges were attached at the top of two micropiles in the micropiled raft to confirm the axial force carried by the micropiles. For the raft, two strain gauges were attached to the raft base along its centerline (at the center and the edge

of the raft) in order to evaluate the bending stresses at the center and at the edge of the raft.

Three LVDTs were used to monitor settlements; two LVDTs to monitor the movement of soil surface during the spinning of the centrifuge and one LVDT to measure settlement at the edge of the raft. The vertical deflection at the center of the raft was measured using a very accurate laser device. Three pressure transducers were utilized to measure the contact pressure between the raft and the soil at the center of the raft, the edge of the raft, and at the mid-way point between the center and the edge of the raft. Figure 4.6 shows the distribution of the instruments used in micropiles and raft to measure both the strain and the contact pressure. Finally, a load cell was attached to the actuator to measure the vertical load applied to the micropiles, raft and MPR foundations. Table 4.3 summarize all the instrumentation used for each test. All LVDTs, load cell, pressure transducers and sand cone (for CPT) were calibrated prior to beginning of tests in order to ascertain their accuracy.
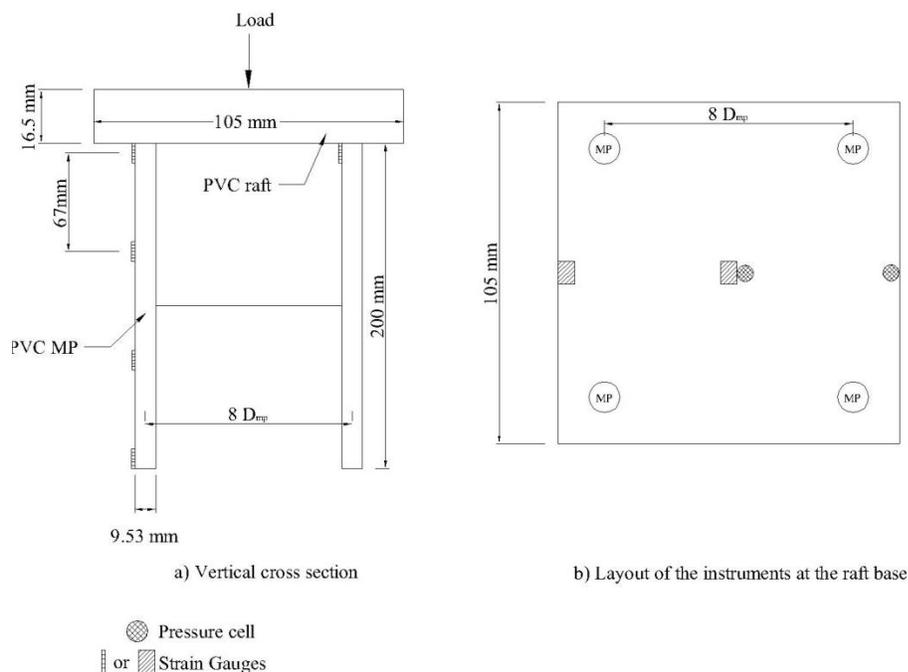
Figure 4.6. Detailed layout of the instruments used to measure the strain and contact pressure (dimensions not to scale).

Table 4.3. Summary of the instrumentations used for each test.

Test	Element	Strain Gauge	LVDTs	Pressure Transducer	Laser
Test 1	1 Micropile	4 along the micropile shaft	2 for sand movement	-	1for Axial movement
Test 2	Raft	2 at raft base	2 for sand movement/ 1 for differential settlement	2 at raft base	1for Axial movement
Test 3	4 Micropile	4 along the micropile shaft/ 2 at top of 2 more micropiles	2 for sand movement/ 1 for differential settlement	2 at raft base	1for Axial movement
	Raft t_r= 0.6 m	2 at raft base			1for Axial movement
Test 4	4 Micropile	4 along the micropile shaft/ 2 at top of 2 more micropiles	2 for sand movement/ 1 for differential settlement	2 at raft base	1for Axial movement
	Raft t_r= 0.45 m	2 at raft base			1for Axial movement
Test 5	4 Micropile	4 along the micropile shaft/ 2 at top of 2 more micropiles	2 for sand movement/ 1 for differential settlement	2 at raft base	1for Axial movement
	Raft t_r= 0.3 m	2 at raft base			1for Axial movement
Test 6	1 Micropile	4 along the micropile shaft	2 for sand movement/ 1 for differential settlement	2 at raft base	1for Axial movement
	Raft t_r= 0.6 m	2 at raft base			1for Axial movement

4.3. RESULTS AND DISCUSSION

4.3.1. Single Micropile Load Test Results

A single micropile was load tested in order to determine its performance characteristics and capacity without the interaction effects with raft. The micropiles were coated with a layer of sand to increase the surface roughness of the pile in order to simulate the actual interface conditions of prototype micropile, which has a rough surface due to the injection of grout under high pressure. This coating method was used successfully in a number of centrifuge tests such as those conducted by El Naggar and Sakr (2000), Horikoshi et al. (2002) and Horikoshi et al. (2003a, b). Furthermore, one of the factors that contribute to increasing the capacity of a micropile is the increased grout-ground bonding for the soil surrounding the micropile due to the pressurized grout used in its construction. To simulate this increased bonding condition in the centrifuge testing, the micropile was jacked into the soil after coating the micropile surface with sand, hence increasing the confining pressure of the soil on the pile leading to increased micropile-soil frictional resistance.

Figure 4.7 shows the load-settlement curve for a single micropile under in-flight axial compressive loading. Considering the interpreted ultimate load as the load corresponding to pile head displacement equal to 10% of pile diameter (Terzaghi, 1942), the ultimate load was 0.8 kN in the model scale (i.e. 2000 kN in the prototype scale). This ultimate pile capacity is close to the calculated ultimate capacity using the approach proposed by FHWA (2005) for micropile Type B in medium dense sand (1900 kN). A number of factors contributed to such high ultimate load, including the following: (i) the

rough micropile surface; (ii) the density of the sand; and (iii) the micropile installation method (jacking), which increased soil confining pressure around the micropile. The axial stiffness of the micropile was evaluated from the initial slope (the linear part) of the load-settlement curve for the single micropile and was found to be 0.96 kN/m at model scale (48 MN/m at prototype scale).
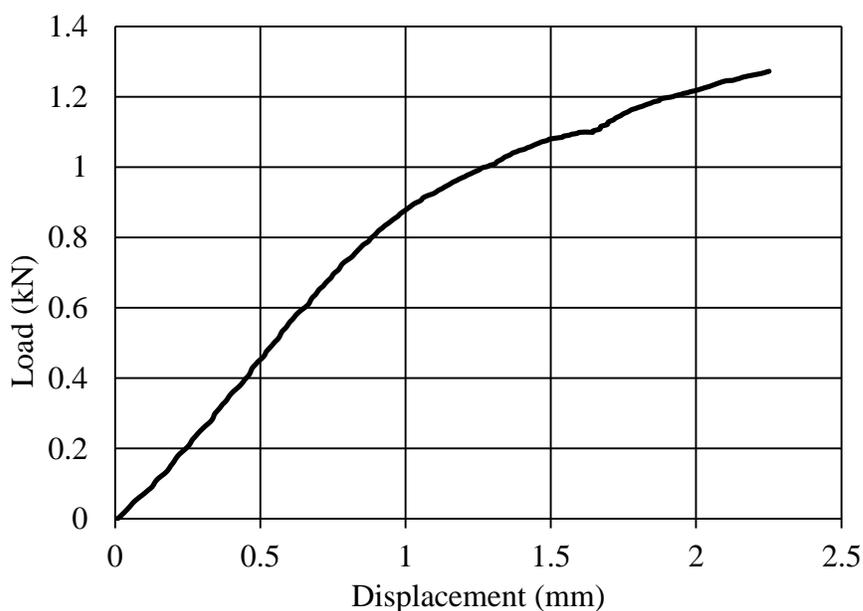
Figure 4.7. Load-settlement curve for a single micropile at model scale.

4.3.2. Raft Load Test Results

A centrifuge test was conducted on a 16.4 mm thick raft (0.6 m at prototype scale) without micropiles. The purpose of this test was to establish a reference point for evaluating the behaviours of an MPR and a raft with a single micropile used as a settlement reducer. The raft was instrumented with strain gauges to evaluate bending stresses in the raft, pressure transducers to evaluate the contact pressure of the raft and LVDTs to evaluate the settlement of the raft edge. The settlement of the raft center was

measured using a precise laser device. The results from the different instrumentation are presented in the following sections.

For raft foundations, the bearing capacity is usually evaluated from the vertical load-settlement curve as the load corresponding to a limiting settlement value divided by the raft area. The load-settlement curve is also used to establish the axial stiffness for the raft (K_r). Figure 4.8 presents the load-settlement curve for the raft during the in-flight vertical load test, which is based on the reading of the settlement under the concentrated load at the raft center. It is clear from Figure 4.8 that the load-settlement curve for the raft remained within the linear elastic range for the entire loading range. The axial stiffness for the raft (K_r) was evaluated from the initial slope of the curve and was found to be 2.29 MN/m at model scale (114 MN/m at prototype scale). Poulos and Davis (1974) developed an equation to calculate the vertical stiffness for a rectangular raft foundation, i.e.

$$K_r = I\sqrt{B_r L_r} \left(\frac{2G_{sr}}{(1-v)}\right) \text{ (kN/m)} \tag{4.4}$$

Where: K_r = axial stiffness for the raft foundation; L_r and B_r = length and width of the raft foundation; G_{sr} = shear modulus at depth = $2B_r/3$; v_s = soil Poisson's ratio = 0.3; and I = influence factor which is a function of the raft aspect ratio = 1.03 for square raft.

The raft axial stiffness obtained from the centrifuge test was used in Eq. 4.4 to back calculate the value of G_{sr} for the soil at depth of 3.5 m ($2B_r/3$), which would then be used to evaluate the correlation coefficient between CPT reading and E_s (i.e. Eq. 4.3). The calculated G_{sr} was 6730 kPa, which corresponds to E_s = 17,500 kPa. Considering the value of q_s at this depth, then E_s = 2~3 q_s. This value will be used later to calculate the axial stiffness for MPR using the PDR method.

The other results of the raft test such as contact pressure, differential settlement and stress distribution at the raft base will be presented along with the results of the MPR for comparison purposes.
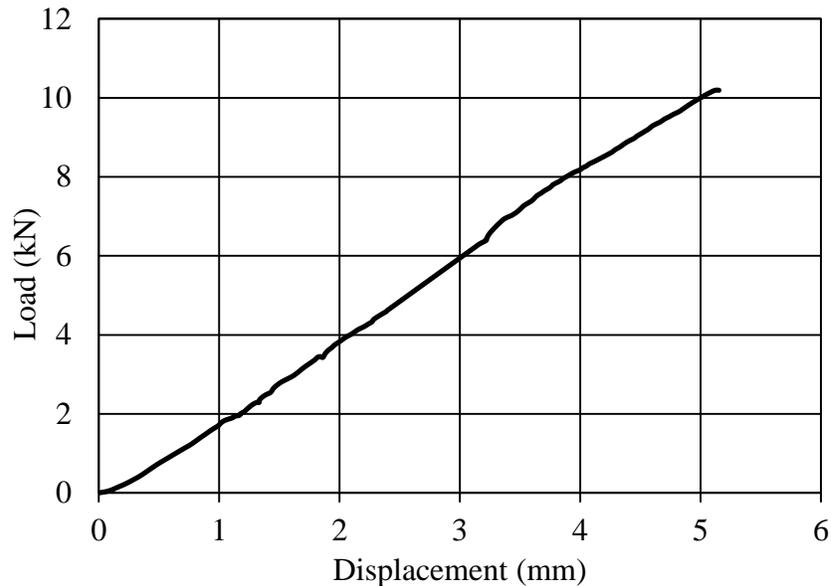
Figure 4.8. Load-displacement curve for the raft center at model scale.

4.3.3. Micropiled Raft Load Test Results

The raft flexibility, influenced primarily by its thickness, has a major impact on the overall performance of the micropiled raft. The raft flexibility affects the contact pressure, differential settlement and load sharing between the raft and the micropiles as demonstrated below. Horikoshi and Randolph (1997) evaluated the raft-soil stiffness ratio for a rectangular raft from centrifuge studies. They proposed an equation to evaluate the raft flexibility considering an earlier definition of the raft-soil stiffness ratio for a circular raft proposed Brown (1969). They proposed that the flexibility of a rectangular raft is given by:

$$K_f = 5.57 \; \frac{E_r}{E_s} \frac{(1-v_s^2)}{(1-v_r^2)} \left(\frac{B_r}{L_r}\right)^{\alpha_o} \left(\frac{t_r}{L_r}\right)^3 \qquad (4.5)$$

Where: E_r = the raft Young's modulus; v_r = raft Poisson's ratio = 0.2; t_r = raft thickness; v_s = soil Poisson's ratio = 0.3; E_s = average soil elastic modulus at depth = $2B_r/3$; and α_o = optimal value =0.5.

Although Eq. 4.5 is for a raft foundation, it was used for the micropiled raft in this study but considering the spacing between the micropiles instead of the raft width, B, and length, L i.e.

$$K_f = 5.57 \; \frac{E_r}{E_s} \frac{(1-v_s^2)}{(1-v_r^2)} \left(\frac{S_B}{S_L}\right)^{\alpha_o} \left(\frac{t_r}{S_L}\right)^3 \qquad (4.6)$$

Where S_L and S_B= spacing between micropiles along length and width of MPR.

This is justified because the spacing between the micropiles represents the unsupported span of the raft. As the pile spacing decreases, the deflections at locations between the micropiles and at the center of the raft will decrease. Thus, it is considered more representative of the micropiled raft width for the purpose of evaluating its flexibility (Alnuaim et al., 2013).

Based on the value of the raft flexibility, K_f, the raft can be characterized according to the following conditions: (i) perfectly rigid if $K_f > 1000$; (ii) perfectly flexible when $K_f < 0.001$; and (iii) intermediately flexible if K_f varies between 0.001 and 1000 (Horikoshi and Randolph, 1997). Using Eq. 4.6, K_f values for the rafts considered in the test were 783, 330 and 98 corresponding to a raft thickness of 0.6 m, 0.45 m and 0.3 m, respectively, and pile spacing of 8 D_p. These values imply that the thick raft was closer to being rigid while the thin raft was closer to being flexible. The effects of raft flexibility

on the foundation bearing capacity, load sharing between the micropiles and the raft, contact pressure and differential settlement are discussed in the following sections.

4.3.4. Axial Stiffness of Micropiled Raft

Poulos (2001) introduced the simplified Poulos-Davis-Randolph (PDR) method in order to estimate the axial stiffness of a piled raft foundation. This method combines the analytical methods proposed by Poulos and Davis (1974) and Randolph (1994), which were developed for the analysis of piled rafts. In this method, the axial stiffness of a piled raft is evaluated considering the pile group stiffness and the raft axial stiffness (Randolph, 1994), i.e.

$$K_{pr} = \frac{K_{PG} + (1 - 2a_{rp})K_r}{1 - \left(a_{rp}^2 \left(\frac{K_r}{K_{PG}}\right)\right)} \tag{4.7}$$

In Eq. 4.7, K_{PG} is the stiffness of the pile group and is calculated using the following equation:

$$K_{PG} = n_p^{1-e_f} K_p \tag{4.8}$$

Where n_p is the number of piles within the group; the efficiency exponent, e_f; and K_p is the stiffness of a single pile (Fleming et al., 2009), which can be calculated from:

$$K_p = G_{sl} * D_p * \frac{\frac{2\eta}{(1-\nu)\xi} + \frac{2\pi\rho}{\zeta} * \frac{\tanh(\mu L)}{\mu L} * \frac{L_p}{D_p}}{1 + \left[\frac{8\eta}{\pi\lambda(1-\nu_p)\xi} * \frac{\tanh(\mu L_p)}{\mu L_p} * \frac{L_p}{D_p}\right]} \tag{4.9}$$

The raft stiffness, K_r is calculated according to Eq.4.4; while a_{rp} is the raft pile interaction factor, which can be calculated from:

$$a_{rp} = 1 - \{\ln(r_r/r_o) /\zeta\} \qquad\qquad (4.10)$$

Where: r_r = average radius of raft (i.e. equivalent to an area similar to the raft area / number of piles); r_o = pile radius; D_p = pile diameter; $\zeta = \ln(r_m/r_o)$; $r_m = 2.5\rho(1-\nu)L_p$; $\xi = E_{sl}/E_{sb}$; $\rho = E_{sav}/E_{sl}$; $\mu L = (2/(\zeta\lambda))^{0.5}*(L/r_o)$; $\lambda = E_p/G_{sl}$; $\eta = r_b/r_o$; r_b = radius at pile base); L_p = pile length; E_{sl} = soil Young's modulus at the pile toe level; E_{sb} = soil Young's modulus below pile tip; E_{sav} = average soil Young's modulus along pile shaft; ν = soil Poisson's ratio; G_{sl} = soil shear modulus at the pile toe level; and E_p = pile material Young's modulus.

The suitability of these analyses for the case of a micropiled raft needs to be evaluated considering the relatively small axial stiffness of the micropile compared to that of the larger diameter piles. Therefore, the axial stiffness of the micropile raft was evaluated from the centrifuge testing results. Three centrifuge load tests were performed on MPR foundations with different raft flexibility (i.e. different thickness values: 16.4 mm, 12.3 mm and 8.2 mm) and the results are discussed herein and compared with the PDR method.

Figure 4.9 presents the load-settlement curves for all three tests at model scale. The rafts with thickness of 16.4 mm and 12.3 mm displayed similar (almost linear) behaviour, but the 16.4 mm thick raft had higher axial stiffness. On the other hand, the relatively flexible raft (8.2 mm thick (0.3 m at prototype scale) exhibited nonlinear behaviour, which is attributed to the large deflection of the flexible raft center under the concentrated load. As the flexible raft deformed, the contact pressure was high at the center of the raft, which resulted in higher deformation of the soil, and consequently, nonlinear behaviour.

This also resulted in large differential settlement between the center and the edge of the raft.

Figure 4.10 displays the relationship between the overall stiffness of the MPR foundation and the thickness of the raft. The MPR stiffness values were 159 MN/m, 134 MN/m and 71 MN/m at prototype scale for raft thicknesses of 0.6 m, 0.45 m and 0.3 m, respectively. As expected, the stiffness of the flexible raft (8.2 mm thick) was only approximately 45% of the stiffness of the stiff raft (16.4 mm thick), which is attributed to the non-uniform distribution of the contact pressure due to the excessive deflection of the flexible raft at the center and relatively small deflection at the edge. This deflection pattern resulted in high contact pressure at the center and dramatic drop in the contact pressure at edge of the raft. This finding will be addressed further in a separate section.

The axial stiffness of the MPR with 16.4 mm thick raft (159 MN/m) was 39% higher than the stiffness of the same raft but without micropiles (114 MN/m). This increase in stiffness (45 MN/m) was due to the contribution of the 4 micropiles supporting the raft. Since the load was applied at the raft center, it is reasonable to assume that each micropile contributed about 11.25 MN/m to the overall stiffness of the micropiled raft. Comparing the axial stiffness of a single micropile (48 MN/m) with that of a micropile in the MPR (11.25 MN/m), it clearly shows the effect of micropiles-raft interaction. This behaviour was attributed to the direct transfer of a significant portion of the load from the raft to the soil. Furthermore, the high soil stresses caused by the raft, overlapped with the stress along the micropile shaft, resulting in nonlinear behaviour of the micropiles. This interaction needs to be comprehensively investigated.

The PDR method was used to evaluate the axial stiffness of the MPR configurations used in the centrifuge tests. The calculated axial stiffness is 167 MN/m, which is close to the axial stiffness values evaluated from the experimental results for the MPR with raft equal to 0.6 m (159.5 MN/m) with only about 5.3% error. However, the calculated axial stiffness using the PDR method is much higher than the values obtained from the test (133.6 MN/m and 71 MN/m) for the MPR with raft thickness of 0.45 m and 0.3 m due to neglecting the effect of the raft thickness in Eqs. 4.4 and 4.7. Therefore, an adjustment factor (ω_{PR}) should be used to evaluate the axial stiffness for the MPR accounting for the raft flexibility in the PDR method. Using the adjustment factor (ω_{PR}), Eq. 4.7 can be rewritten to account for the raft flexibility, i.e.

$$K_{mpr} = \omega_{PR} \frac{K_{PG} + (1 - 2a_{rp})K_r}{1 - \left(a_{rp}^2 \left(\frac{K_r}{K_{PG}}\right)\right)} \tag{4.11}$$

The adjustment factor (ω_{PR}) was evaluated by comparing the axial stiffness obtained from the centrifuge tests for the different MPRs and the theoretical value given by the PDR method and the obtained ω_{PR} values are presented in Table 4.4. By curve fitting the relationship between ω_{PR} and K_f, the following equation is obtained:

$$\omega_{PR} = 0.26 \ln(K_f) - 0.76 \tag{4.12}$$

The errors in evaluating the MPR axial stiffness using Eq. 4.12 vary between 1% and 7% with an average of 3% as shown in Table 4.4. However, due to the limited centrifuge test data, the validity of this equation is restricted for soil of a similar density, micropile spacing, and type of loading. Further investigation is required to verify validity of Eq. 4.12 for a wide range of K_f values and for different soils.

Table 4.4. Variation of adjustment factor (ω_{PR}) with raft flexibility.

Raft flexibility, K_f (Eq.4.6)	Adjustment factor (ω_{PR})	Adjustment factor (ω_{PR}) by using Eq. 4.12	Error
98	0.42	0.43	1%
330	0.8	0.75	7%
783	0.95	0.97	2%
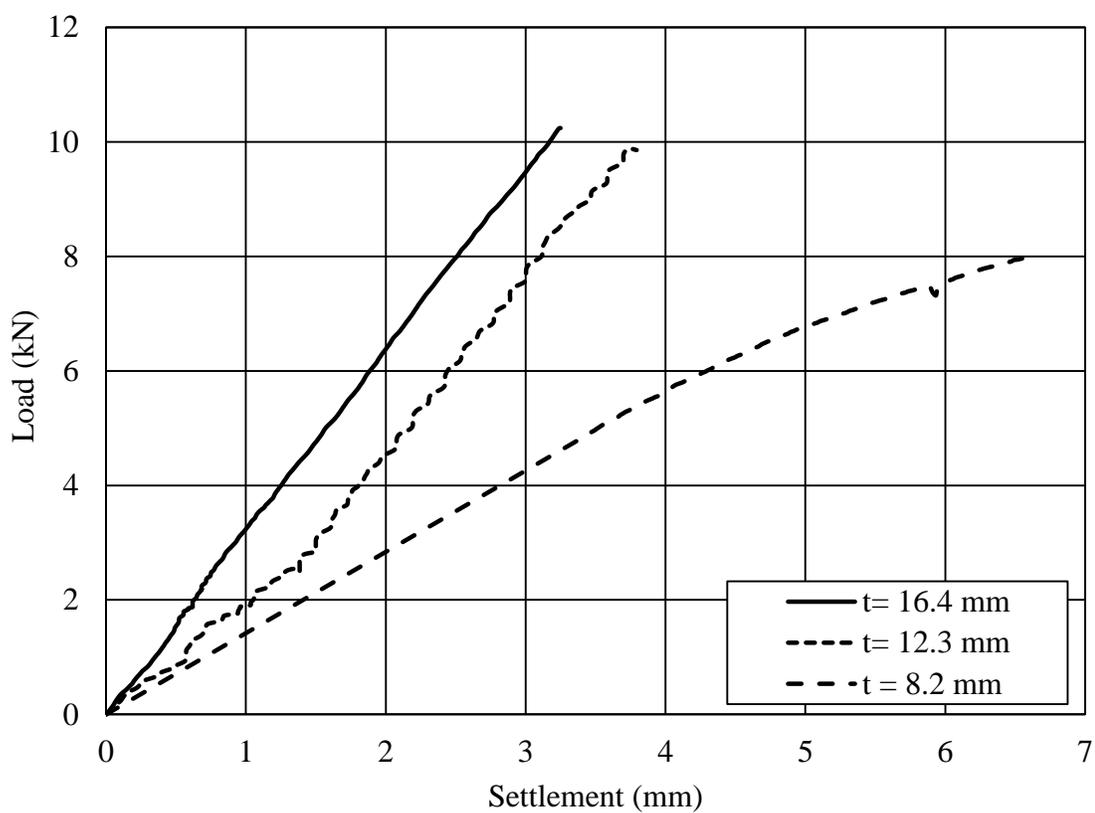
Figure 4.9. Load-settlement curve of the micropiled rafts with different raft thickness at model scale.
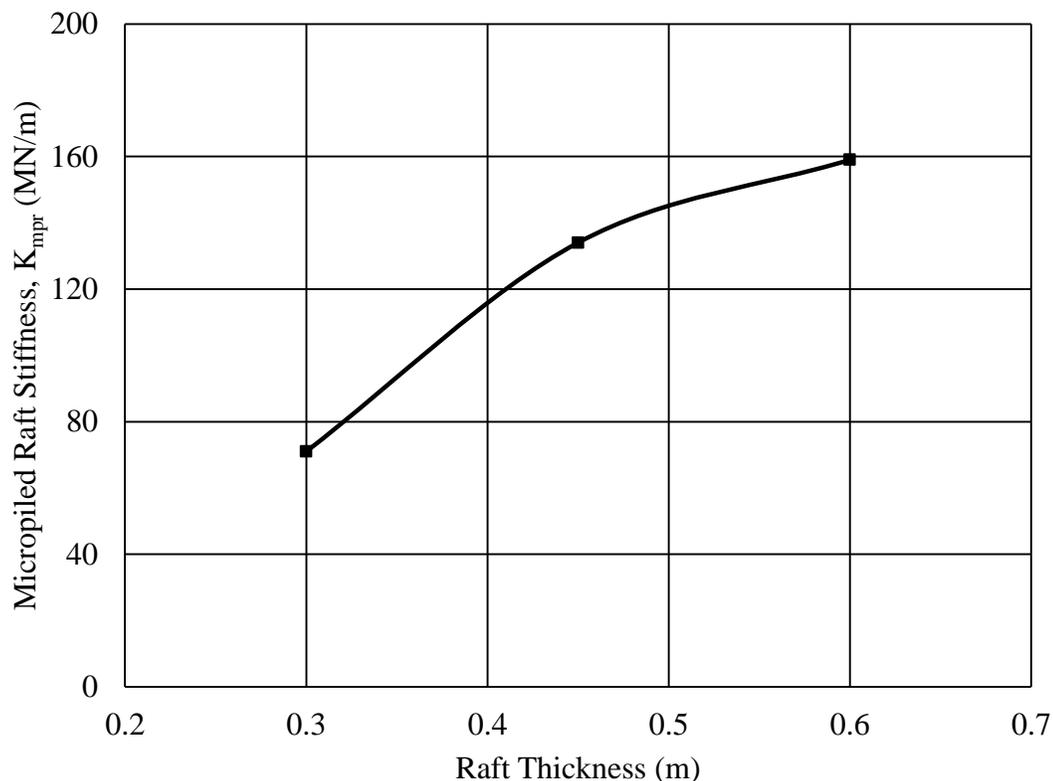
Figure 4.10. Axial stiffness of the micropiled rafts with different raft thicknesses at prototype scale.

4.3.5. Micropiled Raft Contact Pressures

The load is transferred from the micropiled raft to the soil, which led to an increase in the soil reaction (i.e. contact pressure). The magnitude and distribution of the contact pressure depend on a number of parameters such as: type of loading, type of soil, stiffness of soil, spacing of piles and flexibility of the raft. A very flexible foundation subjected to a concentrated load may have zero subgrade reaction at the edge due to the uplift of the raft edge above the ground (Terzaghi et al., 1996). Furthermore, Faber (1933) showed experimentally that the contact pressure for a shallow footing resting on cohesionless soil decreases from the maximum at the center to zero at the edge for both flexible and rigid

foundations. However, it was expected that the micropiled raft would exhibit different pressure distribution due to the presence of the micropiles, especially at locations close to the micropiles (Terzaghi et al., 1996). Thin (flexible) rafts with large spacing between the micropiles are expected to deform more than thick (rigid) rafts; due to this increased raft deformation, the flexible raft induces more deformation in the subsoil, and consequently higher contact pressure is expected; however, the contact pressure for the flexible raft would be concentrated at the center of the raft unlike the uniformly distributed contact pressure across the rigid raft. Figure 4.11 presents the contact pressure at the raft center for different values of raft thickness and varying concentrated load (2 kN, 4 kN and 8 kN) applied at the center. The average difference in contact pressure for the relatively stiff rafts (16.4 mm and 12.3 mm) was small (less than 14%) However, the contact pressure for the flexible raft (8.2 mm thick) was almost twice the contact pressure for the stiff raft, 16.4mm thick, due to the high deflection at the center of the flexible raft. Figure 4.12 presents the variation of the contact pressure with the applied load. As can be noted from Figure 4.12, there is a noticeable change in the slope at applied load level of 2 kN due to the increase in the load carried by the raft at the same load increment (as demonstrated later in Figure 4.16). This increase in the raft load transfer caused a redistribution of the contact pressure within the raft contact area.
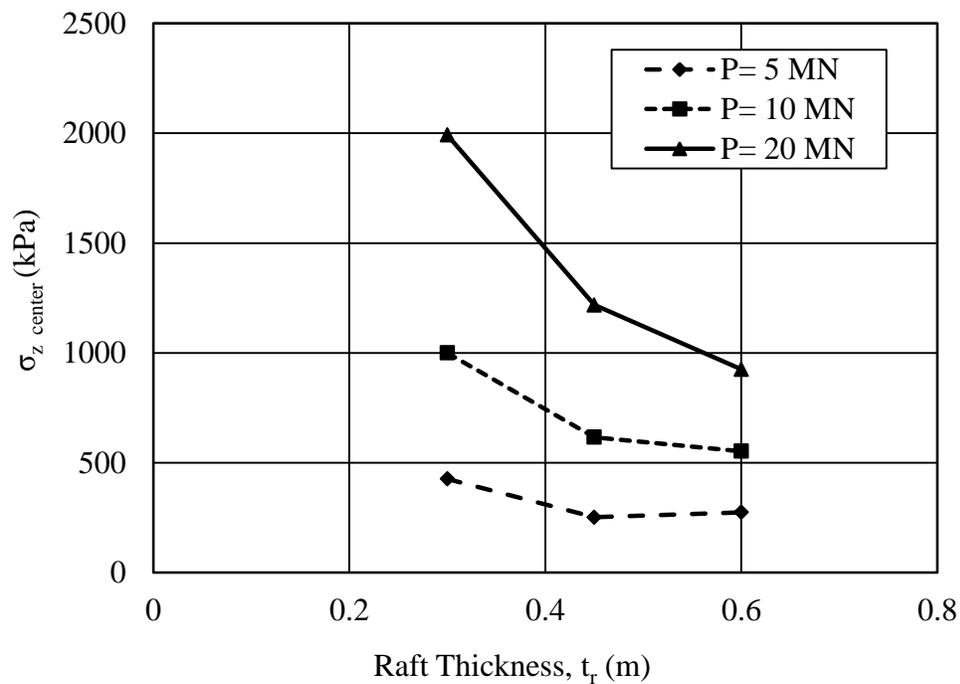
Figure 4.11. Contact pressure at the raft center for different values of raft thickness.
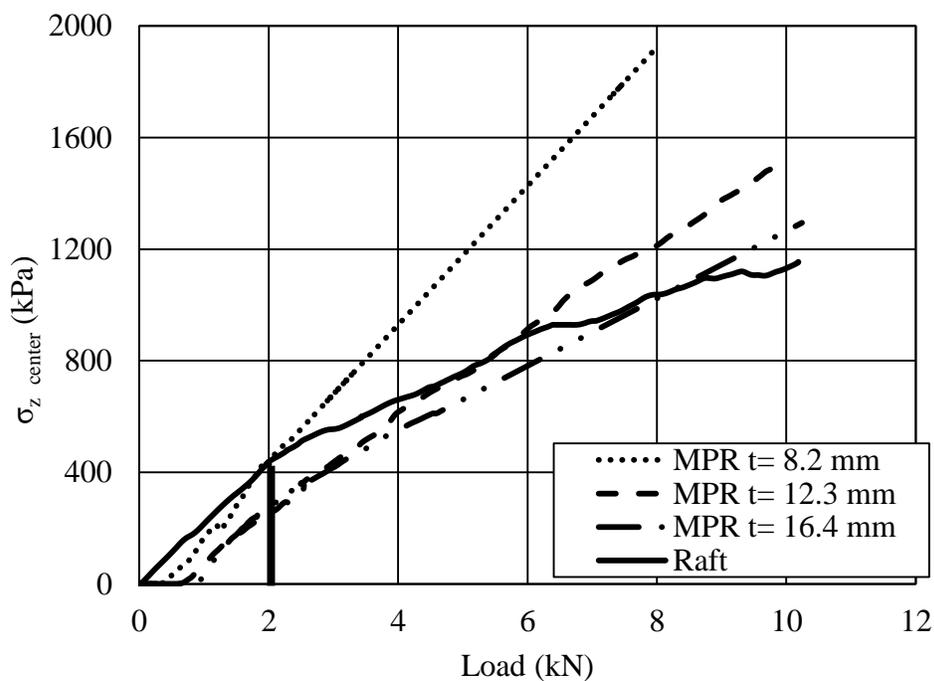
Figure 4.12. Variation of contact pressure with applied load at the raft center for different rafts.

The variation of contact pressure values between the raft center and edge influences the interaction between the micropiles and the raft in terms of load transfer to the soil. Figure 4.13 presents the ratio $\sigma_{z(center)}/ \sigma_{z(edge)}$ for the different micropiled raft cases as well as for the raft case. A number of observations can be noted from Figure 4.13. At early stage of loading, the contact pressure ratio was high for all MPR cases as a result of the micropiles decreasing the settlement at the edge of the raft, which reduced the contact pressure. As the loading progressed, the soil adjacent to the micropiles started to yield, which induced more movement at the edge of the raft; therefore, the contact pressure at the raft edge increased and the $\sigma_{z(center)}/ \sigma_{z(edge)}$ ratio decreased. However, the contact pressures ratio remained constant for the flexible raft at higher load levels. Even though the edge settlement increased, the settlement at the raft center also increased at the same rate. This also indicated that the micropiles had not yet failed completely. However, the $\sigma_{z(center)}/ \sigma_{z(edge)}$ ratio for the stiff micropiled rafts approached the same value as the raft case, which can be attributed to the fact that the micropiles loads approached their ultimate capacity and they could not sustain any additional load. At this point, the raft would take any load increment and the micropiled raft started to behave like a raft.
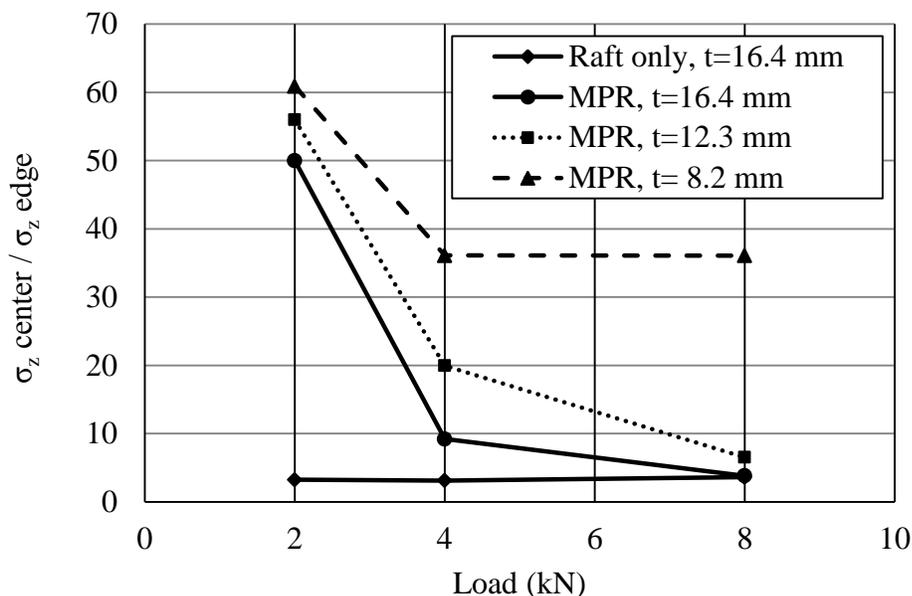
Figure 4.13. Variation of ratio of contact pressure at the center and edge of raft with its thickness.

4.3.6. Skin Friction of Micropiles as a MPR Component

Figure 4.14 shows the load-displacement curve for a micropile as a part of a MPR curve for different raft flexibility condition. The curves were based on the readings of the strain gauges at the top of the micropile with the LVDT reading at the edge of the raft for each MPR case. Based on the 0.1 D_{mp} failure criteria, the failure load for the micropiles are 1.2 kN, 0.94 kN and 0.8 kN for MPR with 8.2 mm, 12.3 mm and 16.4 mm thicknesses, respectively. As discussed earlier, the high contact pressure for the flexible MPR (8.3 mm thick) causing high confining pressure which resulting in increasing the axial capacity for the micropiles. Figure 4.15 presents the distribution of skin friction of the micropile as a component of the MPR for different raft thicknesses. The results clearly demonstrate the effect of increased soil confining pressure, due to the raft contact pressure, on the skin friction. For the flexible raft (8.2 mm thick), the contact pressure

was much higher than the other two cases, which resulted in increased confining pressure, and consequently, the load transmitted through the upper section of the micropiles (0 to 67 mm). The shear strength of sand is influenced by the confining pressure, i.e., as confining pressure increases along the micropile shaft, the sand resistance increases For MPR with rigid raft (16.4 mm), the increase in confining pressure was limited and had minor impact on the shaft resistant along the upper section of the micropile; however, the variation in the skin friction for the mid and lower sections (67 mm to 134 mm and 134 mm to 200 mm) of the micropiles depended on the overburden pressure of the sand, which increased with depth.
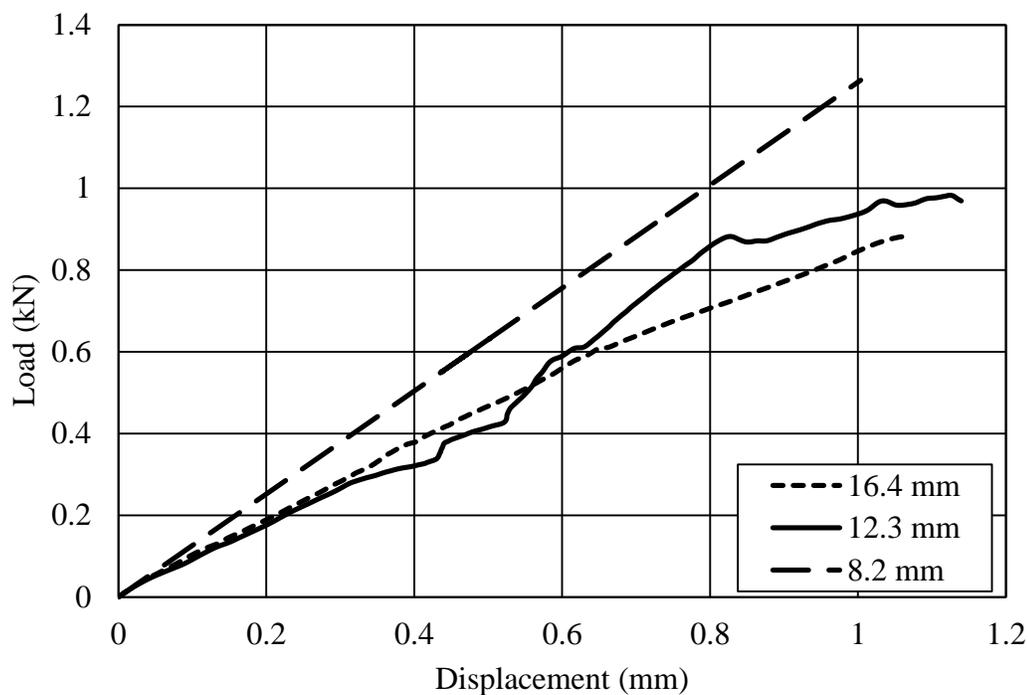
Figure 4.14. Axial load carried by a single micropile as a component of MPRs for different raft thicknesses.
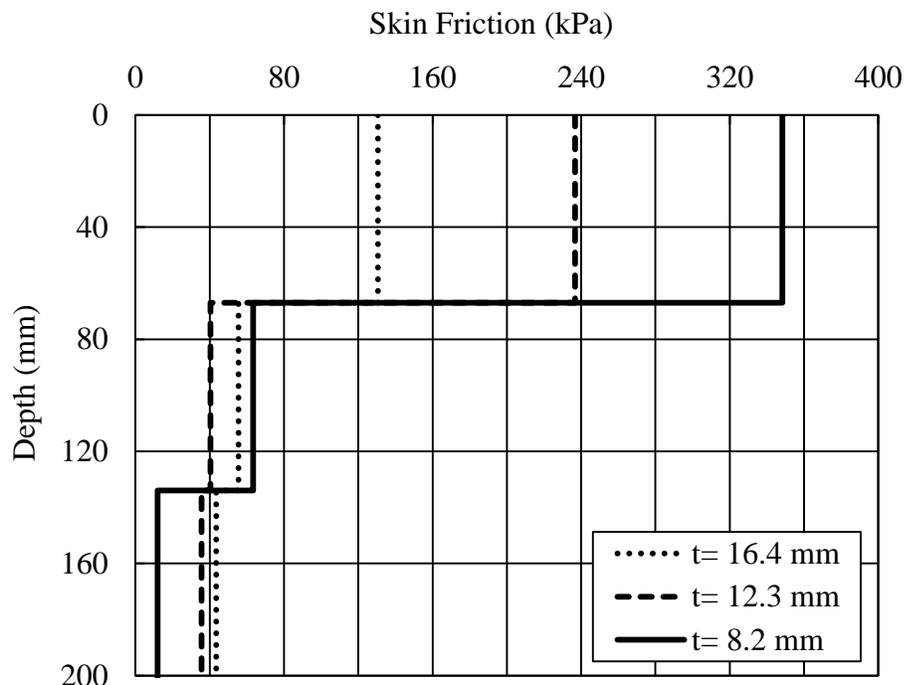
Figure 4.15. Skin friction along a micropile as a component of MPRs for different raft thicknesses at 8 kN load increment applied on the top of the MPR.

4.3.7. Load Sharing in Micropiled Rafts

The axial load carried by the micropiles in a micropiled raft system is affected by the raft flexibility, which is influenced primarily by the raft thickness and the spacing between the micropiles as shown in Eq. 4.6. Figure 4.16 presents the percentage of load carried by each component of the micropiled raft system with different values of raft thickness at different load levels. At the initial load stage, most of the load was carried by the micropiles; this is believed to be due to the lack of intimate contact between the raft and underlying soil, as the soil tends to settle and compact during the increase of g level. Similar behaviour was reported by Horikoshi and Randolph (1996). As the applied load increased, the proportion of the load carried by the micropiles dropped significantly at about 1 kN and continued to decrease gradually after that. At approximately 4 kN, the load transferred by the micropiles reached a plateau and became almost constant. At this

load level, the percentage of load carried by the raft was 41%, 49% and 58% of the total applied load for a raft thickness of 8.2 mm, 12.3 mm and 16.4 mm, respectively.

These results demonstrated that the flexible micropiled raft transferred most of the load through the micropiles due to the increased confining pressure and hence the skin friction of the micropiles. These factors lead to more load transmitted to the soil by the micropiles. The average micropile axial load at an applied load level of 8 kN was 1.18 kN, 0.98 kN and 0.8 kN for a raft thickness of 8.2 mm, 12.3 mm and 16.4 mm, respectively. The axial load carried by the micropiles for the case of flexible micropile raft system was actually higher than the ultimate capacity of the identical single micropile (0.8 kN) and the other micropiles as part of the other MPR cases tested under the same conditions. This increase in ultimate micropile capacity is attributed to the increased raft contact pressure, which increased the confining pressure for the micropiles, which in turn increased the micropile load carrying capacity. Katzenbach et al. (1998) made similar observations for piled raft foundation systems.

These results also provided further explanation for the increase of the contact pressure at the raft edge for stiff raft thicknesses of 12.3 mm and 16.4 mm. As the axial force of the micropiles approached its ultimate load, the micropiles experienced excessive settlement. Consequently, the raft deflection increased and the load transferred by the raft to the underlying soil was increased, including at the edge, hence increasing the contact pressure. It is worth mentioning that the load sharing is effected by the spacing between the piles, i.e., as the spacing decreases most of the load would be carried by the piles as in the pile group system (Katzenbach et al., 2000).
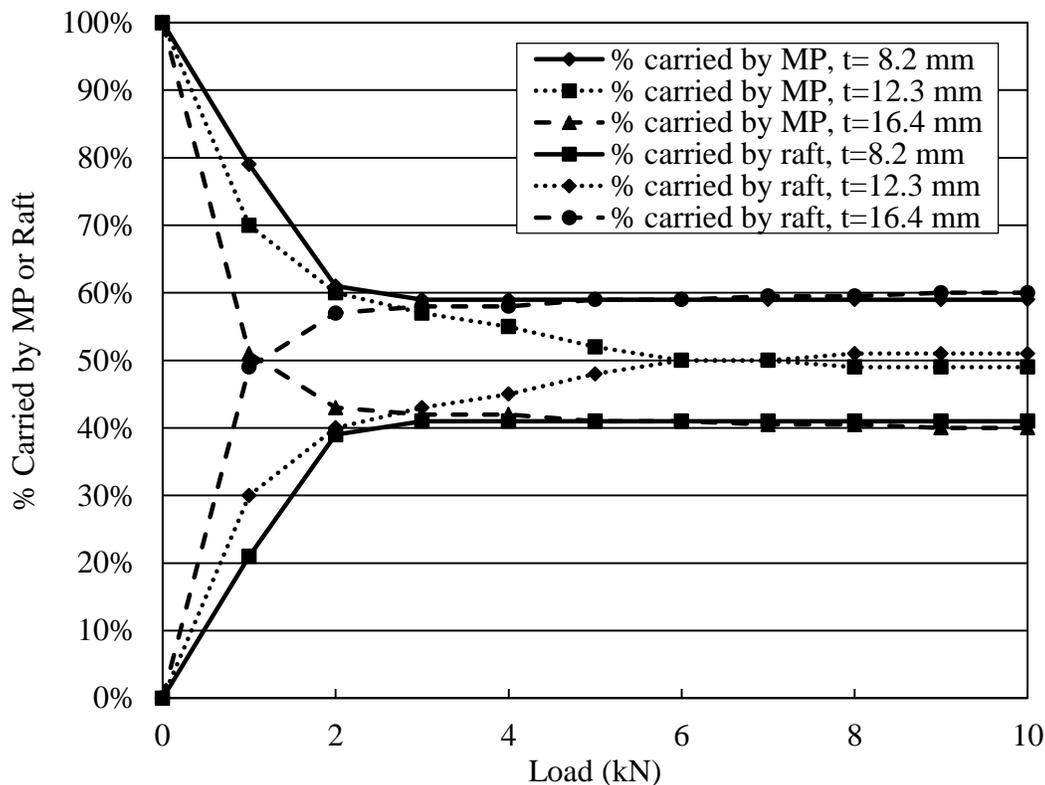
Figure 4.16. Load sharing between the micropiles and the raft for different raft thicknesses.

4.3.8. Differential Settlement of Micropiled Rafts

Figure 4.17 presents the differential settlement of the micropiled rafts evaluated as a percentage of the half width of the raft ($S_d/0.5B_r$) for different values of raft thickness at different load increments. As expected, the flexible raft produced the largest differential settlement due to its low flexural stiffness, and consequently the high percentage of the load carried by the micropiles, and the low percentage of axial load carried by the raft compared to the other cases. As the load applied at the raft center increased from 2 kN to 4kN then to 8 kN, the percentage of differential settlement increased at different rates: (i) for the MPR with t_r =8.2 mm, the rates were almost constant (at approximately 100%) for both load increments meaning the differential settlement doubled as the load doubled (ii) for the MPR with t_r =12.3 mm, the percentage increases in differential settlement were

108% and 79% for the two load increments; and (iii) for the MPR with t_r =16.4 mm, the percentage increases were approximately 109% and 75%.

The decline in the rate of the increase in differential settlement for the rigid raft can be explained by examining the micropiles loads. The micropiles load (i.e. 0.8 kN) for the micropiled raft with a raft thickness of 8.2 mm subjected to an overall load of 8 kN did not exceed the failure load based on the strain gauges results discussed earlier (i.e. 1.2 kN); therefore, the micropiles did not approach failure and hence resisted the movement at the raft edge. However, for the cases of the 16.4 mm and 12.3 mm thick rafts, the micropiles loads (i.e. 0.8 kN and 0.98 kN, respectively) exceeded the ultimate load based on the strain gauges results discussed above, which means they approached or exceeded their ultimate load and experienced excessive settlement allowing more settlement at the raft edge. Hence, for the stiff rafts the percentage increase in differential settlement decreased as the load increased from 2 kN to 4 kN then to 8 kN.
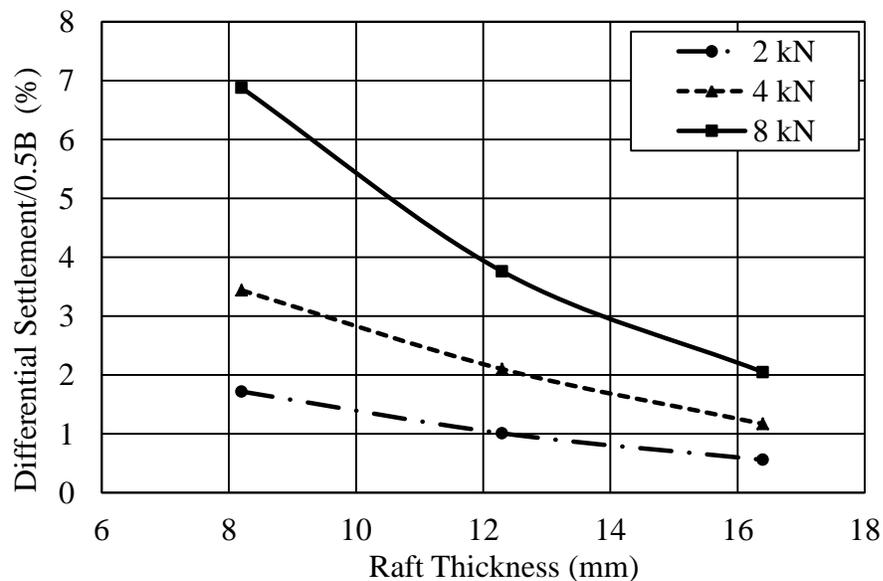
Figure 4.17. Differential settlement normalized by half width of the raft for different raft thickness.

4.3.9. Bending Moments

Evaluating the bending moments at the raft center and edge (both locations are along the centerline of the raft) can shed some light on the overall behaviour of the MPR. It can also aid in providing the necessary information for determining the reinforcement for the raft. Figure 4.18a presents the bending moment at the raft center for different MPR and the individual raft for different raft thicknesses. The bending moment at the raft center increased linearly as the raft thickness increased. Moreover, the bending moment for all cases increased linearly as the load increased. Comparing the bending moment at the raft center for the raft case to that of the raft within the MPR (for the same raft thickness) shows that the micropiles had negligible effect. Figure 4.18b presents the ratio between the bending moments at the center of the raft to the one at the edge of the raft for different cases. The presence of the micropiles in the MPR ($t_r = 16.4$ mm) increased the bending moment at the edge of the raft compared to the case of the raft alone ($t_r = 16.4$ mm). The M_{center}/M_{edge} for the raft alone was about 3.5. On the other hand, the ratio varied between 2.2 to 3 for the MPR. As the load increased, the M_{center}/M_{edge} ratio increased, which indicate that the variation of bending moment was similar to the raft case. As the micropiles reached their full capacity (0.8 kN) in the MPR ($t_r=16.4$ mm), the M_{center} became much higher than the M_{edge}. This was because the micropiles could not resist any additional load and settled as the applied load increased, hence reducing the raft deflection and associated bending stresses.

4.3.10.   Micropiles as a Settlement Reducer

When a raft foundation is subjected to high concentrated loads (i.e. column loads) near the center of the raft, both total and differential settlement will be high. This differential settlement may cause high tensile stress at the raft base, which will require large reinforcement. Also, the settlement underneath the column may lead to damage at the beam-column connections. In order to overcome these adverse effects, the raft thickness may be increased in order to increase its flexural stiffness and hence reduce the settlement. Alternatively, piles can be used as total and differential settlement reducers while keeping the raft thickness unchanged (Burland et al., 1977). This method works by using as low number of piles as possible and allowing the piles to carry loads close to their full capacities to reduce the total settlement of the raft, which will consequently minimize the differential settlements. The piles should be installed right under or close to the concentrated loads.

This study explores using micropiles as settlement reducers. Micropiles can be installed into an existing raft owing to the fact that they can be installed in limited access areas with minimal disturbance. In this section, the results of the centrifuge test for micropiles as a settlement reducer will be presented and discussed. The micropile was fixed at the center of a raft 16.4 mm thick (see Figure 4.1b). Figure 4.19 presents the load-settlement curves for the raft alone and the raft with a micropile at the center. By adding the micropile at the center, the axial stiffness of the MPR system increased by 17.15 MN/m (15% increase) as K_{mpr} for the raft with a single micropile at the center was 131.15 MN/m.

As a result of the increase in the axial stiffness due to the micropile contribution, the differential and total settlements reduced by 31.4% and 33.3%, respectively. At higher load levels, e.g. 8 kN, the effect of the micropile in reducing settlement declined as the load applied to the micropile exceeded its ultimate capacity (0.8 kN) (see Figure 4.20), at which point the micropile carried about 10% of the total applied load. In order to further reduce the total and differential settlement, a larger diameter micropile or group of micropiles should be used.

The presence of the micropile at the raft center reduced the maximum contact pressure by approximately 75% as shown in Table 4.5. This is expected to reduce the bending stresses in the raft tremendously. As the differential settlement reduced, the raft distributed the pressure more uniformly.

Table 4.5. Effect of a micropile as settlement reducer on total and differential settlements and contact pressure at raft center.

Load (kN)	Differential Settlement (mm)			Total Settlement (mm)			$\sigma_{z\ center}$ (kPa)		
	Raft + MP	Only raft	Reduction %	Raft + MP	Only raft	Reduction %	Raft + MP	Only raft	Reduction %
2	0.70	1.02	31.4	0.80	1.20	33.3	108	438	75
4	1.49	2.05	27.3	1.55	2.10	26.2	213	661	68
8	2.71	3.19	15.0	3.07	3.90	21.3	411	1037	60
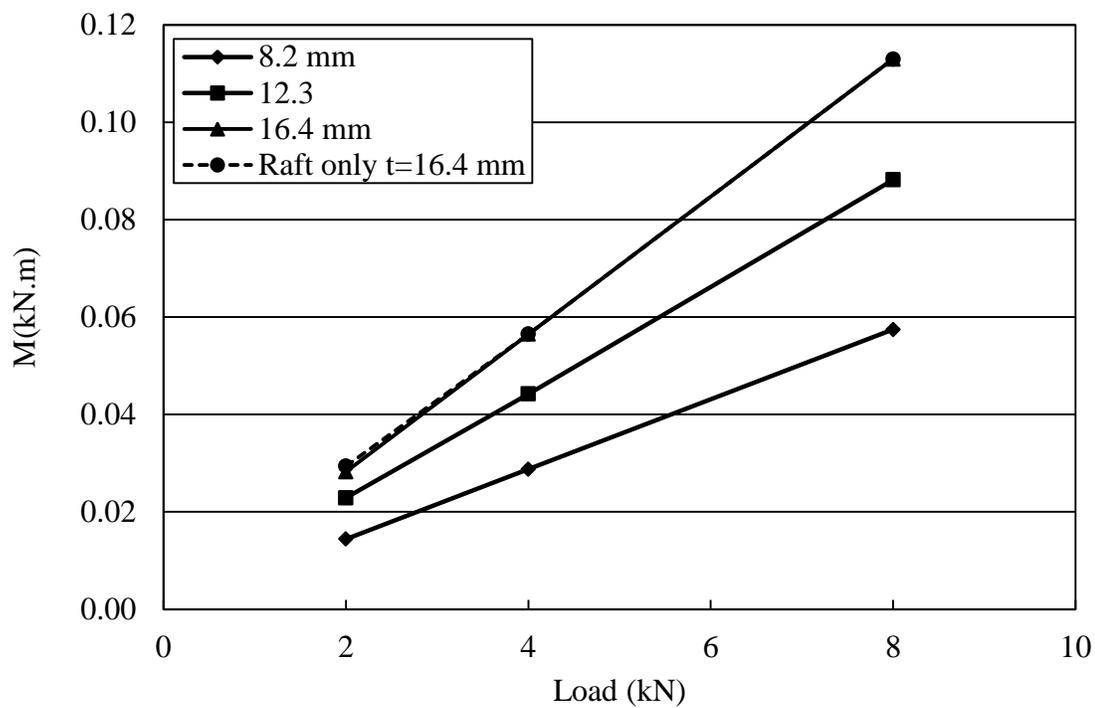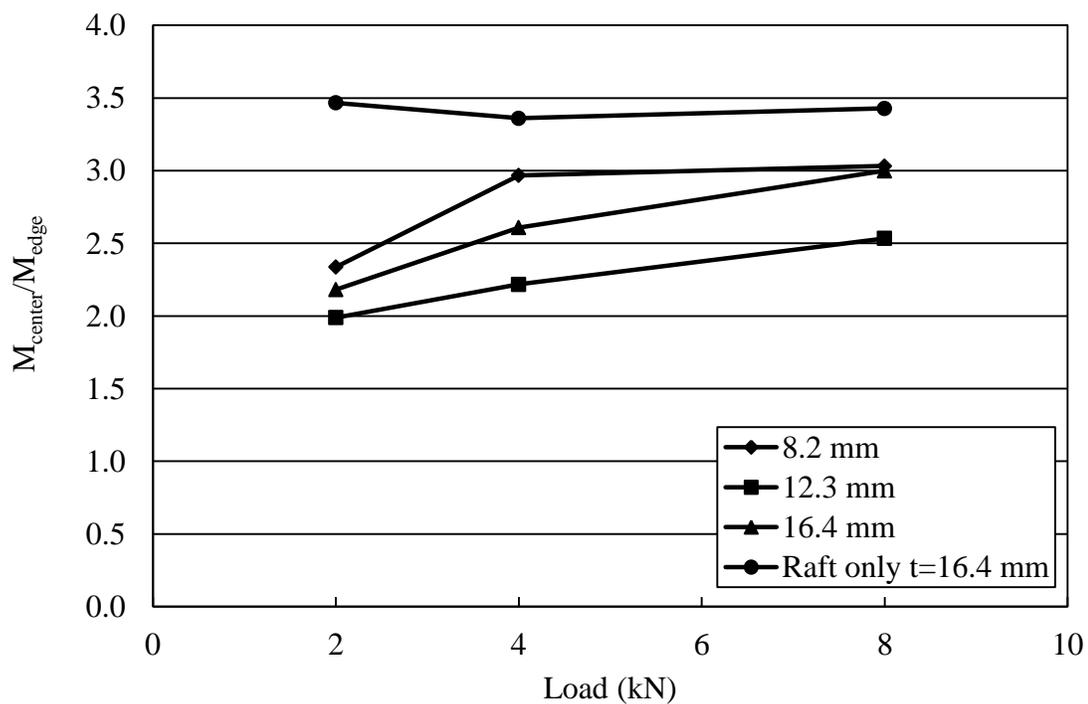
Figure 4.18. (a) Bending moment at raft center at model scale; and (b) ratio between the bending moment at center of the raft to the bending moment at edge of the raft.
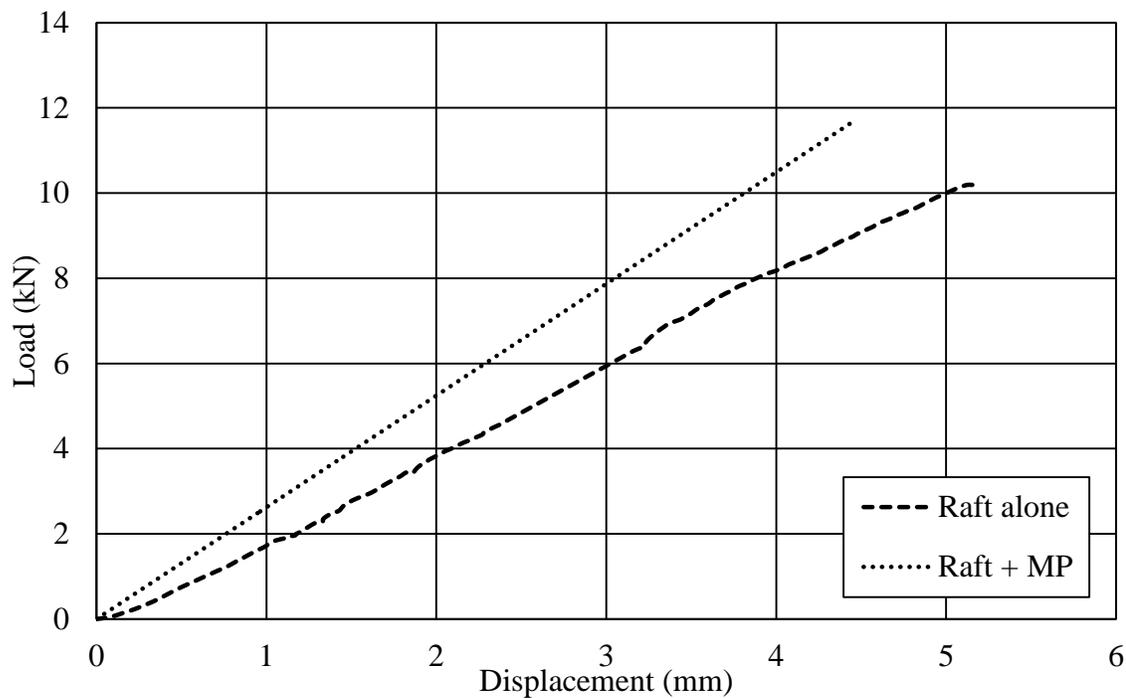
Figure 4.19. Load-displacement curve for: the raft and the raft with a micropile at the center as a settlement reducer.
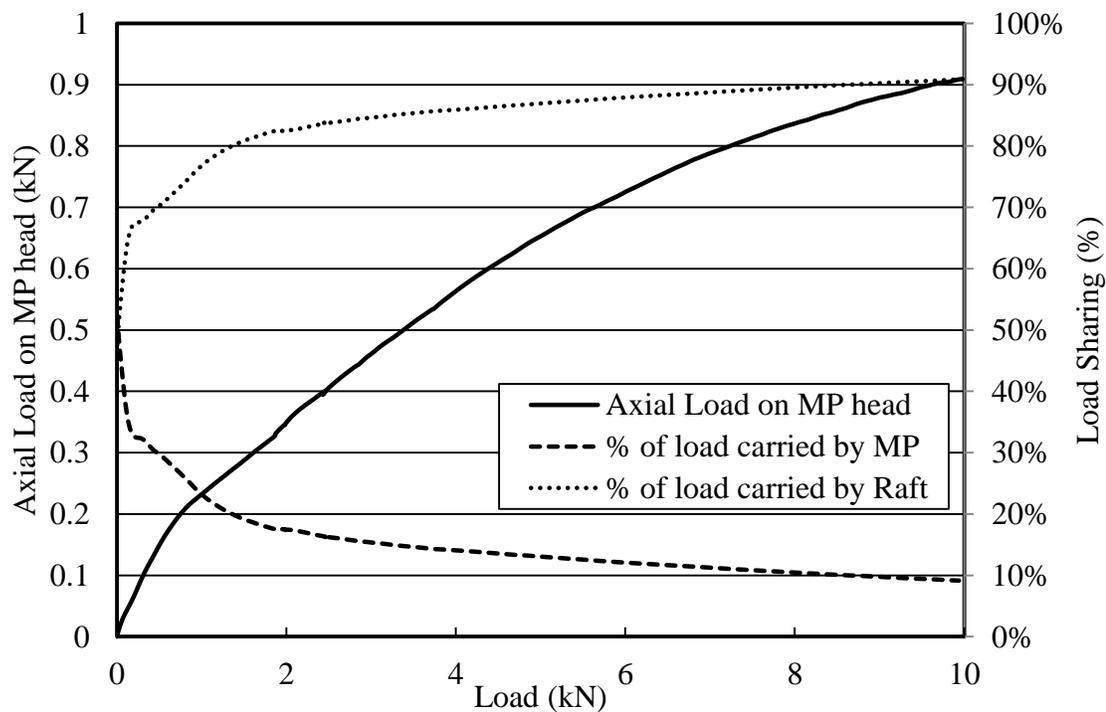
Figure 4.20. Load sharing between micropiles and the raft as well as the axial load applied at the micropile head.

4.4. CONCLUSIONS

Six geotechnical centrifuge tests were conducted at 50g in order to investigate the behaviour of micropiled raft foundations and their components in dry sand and subjected to a concentrated vertical load. The effect of the raft flexibility on the micropiled raft behaviour was studied by varying the raft thickness. In addition, the advantages of using a single micropile as a settlement reducer were examined. The following conclusions may be drawn:

1. The raft thickness has a significant effect on its axial stiffness of the micropiled raft. For example, the MPR axial stiffness increased by 90% and 20% as the raft thickness increased from 0.30 m to 0.45 m then to 0.60 m. This observation is attributed to the uniform distribution of the contact pressure of the rigid raft, which eliminates any stress concentration that could fail the soil as observed in the flexible MPR.

2. The PDR method is suitable for estimating the axial stiffness for the MPR with a relatively stiff raft. However, for flexible micropiled rafts, the PDR method can grossly overestimate the axial stiffness. An adjustment factor (ω_{PR}) was proposed in order to account for the raft flexibility in the PDR method.

3. The contact pressure amounts for the relatively stiff rafts were similar. However, the contact pressure for the flexible raft was almost twice the contact pressure for the stiff rafts due to the high deformation induced by the flexible raft.

4. The raft bending moment ratio, M_{center}/M_{edge}, for the stiff rafts remained constant and approached the ratio of the case of raft only (M_{center}/M_{edge} =3) due to the

yielding of the micropiles as the MPR started to exhibit behaviour like the isolated raft.

5. The skin friction for the MPR was affected by the increase in confining pressure at the upper section of the micropiles due to the high contact pressure of the raft. The skin friction for the MPR with a flexible raft was 2.7 times higher than the MPR with a rigid raft only for the upper section of the micropiles.

6. The reduction in the rate of increase of the differential settlement at higher load levels for the stiff rafts is because the axial force experienced by each micropile approached its ultimate load resulting in larger settlement at the raft edge.

7. The load carried by the raft was 41%, 49% and 58% of the total load applied to the MPR with raft thickness of 8.2 mm, 12.3 mm and 16.4 mm, respectively.

8. Using micropiles as differential and total settlement reducers was proven by a centrifuge test to be a valid option showing reductions of 31.4% and 33.3% reduction in the differential and total settlements, respectively.

Further investigation is necessary, in particular regarding the use of micropiles as total and differential settlements reducer to explore the effects of the diameter, number, length and axial stiffness of micropiles for different relative densities of sands used.

REFERENCES

ASTM Standard D422-63. (2007). Standard Test Method for Particle-Size Analysis of Soils. ASTM International, West Conshohocken, PA.

ASTM Standard D 4253-63. (2007). Standard Test Methods for Maximum Index Density and Unit Weight of Soils Using a Vibratory Table. ASTM International, West Conshohocken, PA.

ASTM Standard D 4253-63. (2006). Standard Test Methods for Minimum Index Density and Unit Weight of Soils and Calculation of Relative Density. ASTM International, West Conshohocken, PA.

ASTM Standard D 3080. (2011). Standard Test Method for Direct Shear Test of Soils under Consolidated Drained Conditions. ASTM International, West Conshohocken, PA.

Alnuaim, A. M., El Naggar, H. and El Naggar, M.H. (2013). Performance of Piled-Raft System under Axial Load. *In* Proceedings of the 18th International Conference on Soil Mechanics and Geotechnical Engineering, Paris, 2-6 September 2013 pp. 2663-2666.

Brown, P.T. (1969). Numerical Analyses of Uniformly Loaded Circular Rafts on Deep Elastic Foundations. Géotechnique, **19**(3):399-404.

Bruce, D.A., DiMillio, A.F. and Juran, I. (1995). Introduction to Micropiles: An International Perspective. Foundation Upgrading and Repair for Infrastructure Improvement, ASCE, Geotechnical Special Publication, **50**:1-26.

Burland, J.B., Broms, B.B. and De Mello, V.B. (1977). Behaviour of Foundations and Structures. *In* Proceedings of the 9th International Conference on Soil Mechanics and Foundation Engineering. Tokyo, Vol. 2, pp. 496-546.

Clancy, P. and Randolph, M. F. (1993). An Approximate Analysis Procedure for Piled Raft foundations. International Journal for Numerical and Analytical Methods in Geomechanics, **17**(12): 849-869.

Clancy, P. and Randolph, M. F. (1996). Simple Design Tools for Piled Raft Foundations. Géotechnique, **46**(2): 313-328.

El Naggar, M.H and Sakr, M. (2000). Evaluation of Axial Performance of Tapered Piles from Centrifuge Tests. Canadian Geotechnical Journal, **37**(6):1295-1308.

Faber, O. (1933). Pressure Distribution under Bases and Stability of Foundations. The Structural Engineer, **11**(3):116-125.

FHWA. (2005). Micropile Design and Construction Guidelines, Implementation Manual. National Highway Institute.

Fleming, K., Weltman, A., Randolph, M. and Elson, K. (2009). Piling Engineering. 3rd ed. Taylor and Francis group, New York.

Horikoshi, K. and Randolph, M. (1997). On The Definition of Raft-Soil Stiffness Ratio for Rectangular Rafts. Géotechnique, **47**(5):1055-1061.

Horikoshi, K. and Randolph, M.F. (1996). Centrifuge Modelling of Piled Raft Foundations on Clay. Géotechnique, **46**(4):741-752.

Horikoshi, K., Matsumoto, T., Hashizume, Y. and Watanabe, T. (2003a). Performance of Piled Raft Foundations Subjected to Dynamic Loading. International Journal of Physical Modelling in Geotechnics, **3**(2):51-62.

Horikoshi, K., Matsumoto, T., Hashizume, Y., Watanabe, T. and Fukuyama, H. (2003b). Performance of Piled Raft Foundations Subjected to Static Horizontal Loads. International Journal of Physical Modelling in Geotechnics, **3**(2):37-50.

Horikoshi, K., Watanabe, T., Fukuyama, H. and Matsumoto, T. (2002). Behaviour of Piled Raft Foundations Subjected to Horizontal Loads. *In* Proceeding of the International conference of Physical Modelling in Geotechnics. St John's, Newfoundland, Canada.

Jeon, S.S. and Kulhawy, F.H. (2001). Evaluation of Axial Compression Behaviour of Micropiles. Proceedings of a specialty conference: Foundations and Ground Improvement, Blacksburg, Virginia. ASCE Geotechnical Special Publication Vol. 113, pp. 460-471.

Juran, I., Benslimane, A. and Hanna, S. (2001). Engineering Analysis of Dynamic Behaviour of Micropile Systems. Transportation Research Record: Journal of the Transportation Research Board, **1772**: 91-106.

Katzenbach, R., Arslan, U., Moorman, C. and Reul, O. (1998). Piled Raft Foundation: Interaction Between Piles and Raft. *In* Proceedings of the International Conference on Soil-Structure Interaction in Urban Civil Engineering, Darmstadt Geotechnics, Vol. .4, pp. 279-296.

Lizzi, F. (1982). The Static Restoration of Monuments: Basic Criteria-Case Histories, Strengthening of Buildings Damaged by Earthquakes. The International Association of Foundation Drilling, Irving, TX and the International Society for Micropiles, Venetia, PA.

Long, J., Maniaci, M., Menezes, G. and Ball, R. (2004). Results of Lateral Load Tests on Micropiles. *In* Proceedings of the GeoSupport Conference: Innovation and Cooperation in the Geo-Industry Orlando, Florida. pp. 122-133.

Mahboubi, A. and Nazari-Mehr, A. (2010). Nonlinear Dynamic Soil-Micropile-Structure Interactions Centrifuge Tests and FEM Analyse. *In* Proceeding of the Deep Foundations and Geotechnical In Situ Testing, GeoShanghai 2010, Shanghai, China. pp. 81-89.

Ovesen, N. K. (1975). Centrifugal Testing Applied to Bearing Capacity Problems of Footing on Sand. Géotechnique, **25**(2): 394-401.

Poulos, H.G. (2001). Piled Raft Foundations: Design and Applications. Géotechnique, **51**(2): 95-113.

Poulos, H.G. and Davis, E.H. (1974). Elastic Solutions for Soil and Rock Mechanics. John Wiley and Sons. Inc. New York.

Randolph, M.F. (1983). Design of Piled Raft Foundations. *In* Proceedings of the International Symposium on Recent Developments in Laboratory and Field Tests and Analysis of Geotechnical Problems, Bangkok, Thailand. pp. 525-537.

Randolph, M.F. (1994). Design Methods for Piled Groups and Piled Rafts. *In* Proceedings of the 13th international conference on soil mechanics and foundation engineering, New Delhi, India. pp. 61-82.

Richards, T.D. and Rothbauer, M.J. (2004). Lateral Loads on Pin Piles (Micropiles). *In* Proceedings of the GeoSupport Conference: Innovation and Cooperation in the Geo-Industry Orlando, Florida. pp. 158-174.

Rose, A.V., Taylor, R.N. and El Naggar, M.H. (2013). Numerical Modelling of Perimeter Pile Groups In Clay. Canadian Geotechnical Journal, **50**(3): 250-258.

Shahrour, I. and Ata, N. (2002). Analysis of the Consolidation of Laterally Loaded Micropiles. Ground Improvement, **6**(1): 39-46.

Shong, I.L. and Chung, F.C. (2003). Design and Construction of Micropiles. Geotechnical Course for Pile Foundation Design and Construction.

Teerawut, J. (2002). Effect of Diameter on the Behaviour of Laterally Loaded Piles in Weakly Cemented Sand. Ph.D. Dissertation, University of California, San Diego, California.

Terzaghi, K. (1942). Discussions on the Progress Report of the Committee on the Bearing Value of Pile Foundations. *In* Proceedings of the American Society of Civil Engineers, **68**(2): 311-323.

Terzaghi, K., Peck, R. and Gholamreza, M. (1996). Soil Mechanics in Engineering Practice. 3rd ed. John Wiley and Sons, New York.

Tomlinson, M.J. (1996). Foundation Design and Construction. Longman Publishing Group, London.

Tsukada, Y., Miura, K., Tsubokawa, Y., Otani, Y. and You, G.L. (2006). Mechanism of Bearing Capacity of Spread Footings Reinforced With Micropiles. Soils and Foundations, **46**(3): 367-376.

Wood, D.M. (2004). Geotechnical Modelling. 1st ed. CRC Press, Boca Raton, FL.

CHAPTER 5: CENTRIFUGE MODELING OF A MICROPILED RAFTS IN CLAY

5.1. INTRODUCTION

Micropiles are small diameter "cast-in-place" piles that are used to repair deficient foundations of existing buildings and to support new construction. For repair of existing foundations, the micropile is installed by drilling through the existing foundation and filling the holes with cement grout and steel bars (Lizzi, 1982). For new construction, the micropiles are constructed first, similar to drilled shafts, then a pile cap is constructed on top of the micropiles to form the foundation system. Different types of micropiles are currently used to provide the load carrying capacity of new foundation systems (FHWA, 2005). In current practices, the diameter of a micropile is typically between 150 mm to 300 mm. The load transmitting mechanism for the micropile is through skin friction to the soil in the bonded zone between the grout and the soil. The skin friction is typically high due to the rough micropile surface and increases in soil strength due to pressurized grout. The advancements in drilling equipment allow drilling through almost any ground condition to install micropiles at any angle with minimum noise, vibration and disturbance. In addition, the relatively small size of the equipment facilitates the underpinning of existing foundations even in restricted access situations (Bruce et al., 1995). Micropiles are nowadays used in a variety of applications, including: (1) serving as the main foundation system for static and dynamic loading; (2) upgrading an existing foundation system; and (3) stabilizing slopes and reinforcing the soil (Bruce et al., 1995).

Several studies have been conducted in order to evaluate the performance of single micropiles and micropile groups under various types of loading. Different testing techniques have been employed such as full-scale micropile load tests, 1g physical modeling, and geotechnical centrifuge modeling. Jeon and Kulhawy (2001) examined the results of 8 full scale tests on micropiles (with high pressure grouting) installed in cohesive soil with diameters of 0.15 and 0.17 m and shaft depths of 9, 12, 13.5 and 19 m. The results indicated that the load-carrying capacity of the micropile is significantly different than the drilled shaft due to how the pressure grouting affects the soil state of stress. Moreover, the micropile load carrying capacity per unit volume can be higher than that of larger diameter drilled shafts.

The use of piles to reduce the total and differential settlements of a raft foundation was investigated in a number of studies; for example, Randolph (1994), Clancy and Randolph (1996), Horikoshi and Randolph (1996 and 1998). On the other hand, the concept of underpinning foundation systems using micropiles as a micropiled raft foundation is relatively new. Han and Ye (2006) performed one micropile load test using a 1.5 m by 1.5 m square raft with four micropiles 150 mm in diameter and spaced at 750 mm. It was found that the load transmitted by the micropiles was about 70% to 86% of the additional load applied to the raft after it was underpinned by the micropiles. However, the effect of raft flexibility on the interaction between the raft and soil, the load sharing between the raft and the micropiles, and the differential settlement of the system has not been thoroughly investigated yet, especially in clayey soil.

The geotechnical centrifuge testing offers an affordable and reasonably accurate option for simulating complicated soil-structure-interaction (SSI) problems. A number of

studies investigated the behaviour of pile groups, piled rafts, and micropile groups. The results of such studies were used to calibrate and verify finite element models (FEM), which were then used for further analysis. Mahboubi and Nazari-Mehr (2010) evaluated the performance of single and micropile groups in sand under dynamic loading employing a FEM that was verified using centrifuge test results. Their results indicated a flexible behaviour of the soil-micropile system, which leads to small stresses introduced to the soil. Juran et al. (2001) performed centrifuge testing on a number of single and group micropile configurations in sand. They evaluated the influence of micropile inclination, spacing-to-diameter ratio and micropile configurations on both the load transfer mechanism and the resisting force of the micropile system. The micropiles were modeled using polystyrene tubes with a roughened surface. The number of micropiles varied between 1 to 18 and the spacing-to-diameter ratio, S/D_{mp}, varied between 3 and 5. The micropile groups were subjected to dynamic excitation with acceleration amplitudes that varied between 0.03 g to 0.5 g. The results indicated a positive group effect was achieved for S/D_{mp}=3 and = 5 compared to a single micropile.

Generally, much fewer centrifuge testing programs were conducted on pile groups and piled rafts in clay. Horikoshi and Randolph (1996) investigated the differential settlement of a piled raft foundation in clay soil with average undrained shear strength of 40 kPa using geotechnical centrifuge testing. Three different arrangements were used: 9, 21 and 69 piles spaced at $S/D_p = 8$ and pile diameter, $D_p = 3.15$ mm (at model scale). A circular raft with a 140 mm diameter was used in this investigation. They concluded that the raft differential settlement can be reduced by 30% by using as few as 9 piles uniformly distributed at the center of the raft. Rose et al. (2013) investigated the

performance of perimeter pile groups in clay using geotechnical configure testing and numerical modeling. They considered different pile group arrangements with pile diameter, $D_p = 300$ mm. It was found that the failure mechanism for the perimeter groups consisting of 14 to 20 piles with 1.75d spacing was block failure with a group efficiency ratio of about 0.9. Several micropile load tests were conducted in order to evaluate their lateral performance, e.g. Richards and Rothbauer (2004), Long et al. (2004), Shahrour and Ata (2002), and Teerawut (2002).

The overall behaviour of micropiles used as retrofitting elements for an existing foundation is similar to a piled raft foundation. In such cases, the load is transmitted by both the foundation and the micropiles. In this study, the behaviour of the micropiled raft foundation will be evaluated. The performances of a single micropile, a single raft and a micropiled raft in clay with average undrained shear strength of about 30 kPa are assessed using geotechnical centrifuge testing. The main objectives of the study are to evaluate the interaction between the different components of a micropiled raft in clay through the interpretation of geotechnical centrifuge testing results. The study also evaluates the micropile-soil-raft interaction effects on the raft differential settlement, contact pressure, the raft bending moment and load sharing between the raft and micropiles.

5.2. Experimental Setup

5.2.1. Centrifuge Facility

The C-Core Centrifuge facility located at Memorial University, St. John's, Newfoundland, was used in the current study. The Acutronic 680-2 geotechnical

centrifuge with a maximum centrifugal rotational speed of up to 189 rpm and a maximum acceleration of 200 g at an effective radius of 5 m was used. A 48 channel data acquisition system was used to collect electrical signals from strain gauges and transducers throughout the tests.

5.2.2. Model Design and Centrifuge Package Setup

The centrifuge testing program consisted of the following tests: (1) one test on micropiled raft (test#7); (2) one test on a single micropile (test#8); and (3) one test on an isolated raft (test#9). The soil bed in all tests was kaolin-silt mixture (K-S), which was consolidated from slurry and had an average undrained shear strength, s_u = 30 kPa. All tests were performed under centrifugal acceleration of 50g. The prototype diameter of the micropile was 150 mm and its length was 10m. In order to work with reasonable size cross-sections, the models of the rafts and micropiles were fabricated using PVC, which has a modulus of elasticity smaller than that of the prototype material (concrete). The geometrical dimensions of the centrifuge models were scaled to simulate the axial rigidity (EA) and flexural rigidity (EI) of the micropile and raft (Wood, 2004) i.e.

$$\frac{E_p A_p}{E_m A_m} = n^2 \tag{5.1}$$

$$\frac{E_p I_p}{E_m I_m} = n^4 \tag{5.2}$$

Where: $E_p A_p$: axial rigidity for the prototype element; $E_m A_m$: axial rigidity for the model element; $E_p I_p$: flexural rigidity for the prototype element; and $E_m I_m$: flexural rigidity for the model element.

The size of the model micropiles facilitated the installation of strain gauges to measure their axial forces, and the size of the model raft relative to the size of the centrifuge box minimized the boundary effects. Table 5.1 summarizes the model dimensions and the scaling factors used in the model design. Figure 5.1 presents the layout for the micropile raft model.
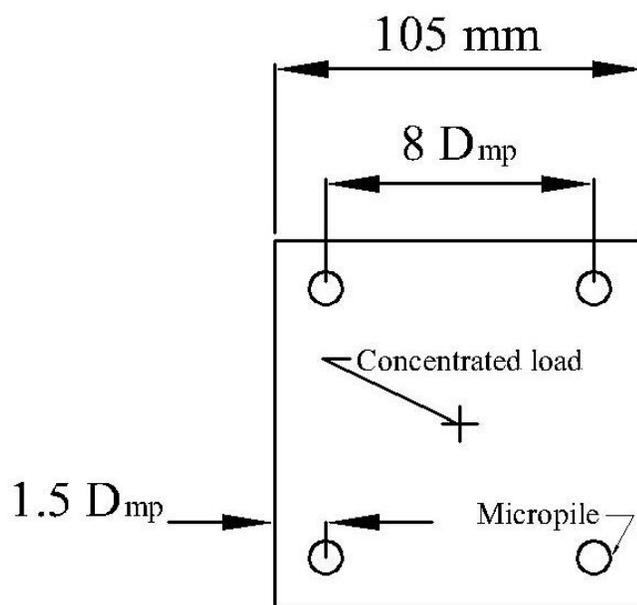
Figure 5.1. Layout for the micropiled raft.

Table 5.1. Scaling laws for centrifuge modeling and models and equivalent prototype dimensions.

Description		Scaling law	Prototype	Model
Micropile Diameter		E_pA_p/n^2	150 mm	9.53 mm
Axial Rigidity (EA)			516737 kN	207 kN
Micropile Length		1/n	10 m	200 mm
Raft Width and Length		1/n	5.25 m	105 mm
t_r=0.6 m	Raft Thickness	E_pI_p/n^4	0.6 m	16.4 mm
	Flexural Rigidity		697950 kN. m^2	0.112 kN. m^2
Force (kN)		-	n^2	1
Stress (kPa)		-	1	1
Stiffness (kN/m)		-	n	1
Moment (kN/m)		-	n^3	1
Displacement (mm)		-	n	1

5.2.3. Soil Material

The Speswhite kaolin clay used in the study as soil bed was manufactured by IMERYS in England. The silt used in the K-S mixture was Sil-Co-Sil 75, which was manufactured by US SILICA. The specific gravity for the kaolin and K-S are 2.63 and 2.62, respectively (Lin, 1995). Several characterization tests were conducted in order to obtain the physical properties of the kaolin and K-S mixture. The hydrometer method was used according to ASTM D422 (ASTM D422-63, 2007) to evaluate the soil particle distribution. The mean grain size, D_{50}, for the kaolin, silt and K-S mixture was found to be approximately 0.00052 mm, 0.017 mm and 0.0025 mm, respectively. These results are consistent with the values reported by Lin (1995) and Paulin (1998). Figure 5.2 presents the particles size distribution for the different materials. The Atterberg limits for the kaolin and K-S mixture were determined according to the ASTM D4318 (ASTM D4318-10, 2010) (see Table 5.2).

Table 5.2. Properties of Kaolin and K-S mixture.

Soil Type	Kaolin	50% kaolin and 50% silt
Liquid Limit, w_L, %	60.6	38
Plastic Limit, w_p, %	34	22.3
Plasticity Index, PI, %	26.6	15.72
Mean Particle size, D+, mm	0.00052	0.0025
Clay Fraction (<2 μm), %	82	50
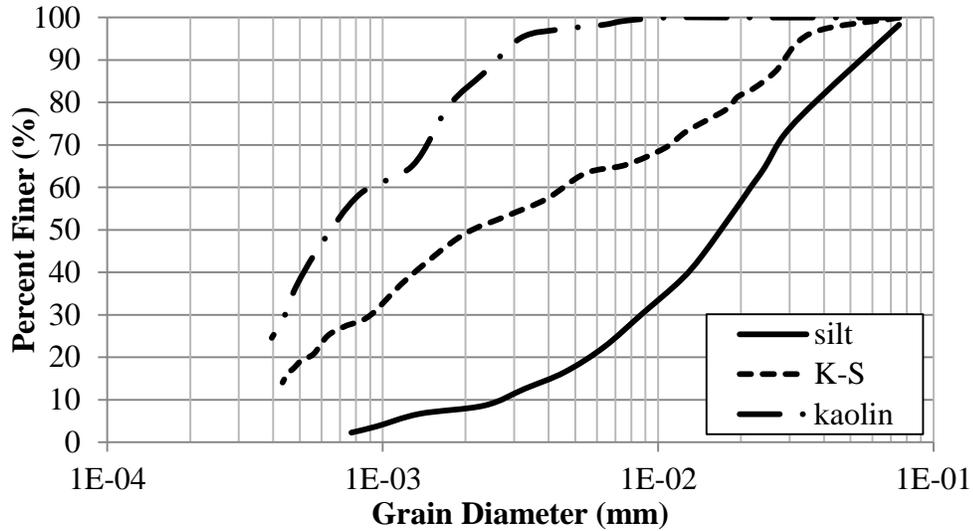
Figure 5.2. Soil particle size distribution for different materials.

5.2.4. Preparing the Clay Testbed

The kaolin clay and silt were mixed using 5HP Bower horizontal paste mixer (180 kg of kaolin clay, 180 kg of silt and 288 kg of water). The material was divided into four batches, each was mixed for about 30 minutes at rotation speed of 14 RPM. The K-S mix was subjected to a vacuum pressure of 65 kPa for a minimum of 3 hours in order to reduce the air trapped in the slurry. The clay slurry was then allowed to consolidate at 1g, under a consolidation pressure estimated considering the required overconsolidation ratio (OCR) in the centrifuge in order to achieve the desired s_u, i.e.

$$s_u = c_1 \sigma'_v OCR^{c_2} \tag{5.3}$$

Where: s_u is undrained shear strength, c_1 and c_2 are coefficients, and σ'_v is the effective vertical stress. Lin (1995) estimated c_1 and c_2 coefficients as 0.253 and 0.657, respectively, based on vane shear test results for the 50% kaolin clay with 50% silt.

A 904 mm diameter and 817 mm extended height container was used to consolidate the slurry. The extended container consisted of a primary tub, 500 mm high and a 317 mm high extension. A steel extrusion plate was placed on the bottom of the tub to facilitate post-test extraction of the clay test bed. A 40 mm saturated sand layer was placed at the bottom of the tub to accelerate the consolidation process. A layer of geotextile and filter paper was placed on top of the sand layer in order to drain the water but retain the clay particles. The container wall was coated using a thin grease layer. The slurry was then poured into the container and another layer of filter paper and geotextile was placed at the top of the mix. The slurry was allowed to consolidate under its self-weight for one day. It was then subjected to a pressure of 3.6 kPa (using a steel plate piston) until 90% consolidation was achieved. The tub was then loaded under the consolidation frame where consolidation pressure was applied in increments such that the applied pressure was doubled after each successive load increment until the maximum consolidation pressure of 300 kPa was achieved. Each load increment was kept until at least 90% consolidation was achieved. The entire process was completed in approximately five weeks, achieving a total consolidation settlement of approximately 200 mm.

5.2.5. Centrifuge Package Setup

The headwork consisted of 2 actuators with 10 kN capacity each (Figure 5.3). Three test models were placed in the clay bed with spacing ensuring a minimum of 200 mm distance (2 times the raft width) between each 2 models and at least 200 mm perpendicular distance between any model and the steel tub wall to minimize the interaction between the models and the boundary effect. Two main cross I-beams were

laid out along the center of the tub and bolted to its rim. A 120 mm distance was maintained between the I-beams in order to allow for actuators movement. The first actuator was used to apply the load to the models. This actuator was located 150 mm away from the center of the tube and the primary load cell was attached to it. The model settlement was measured using both the actuator's movement sensor and a laser sensor mounted on the cross beams. The second actuator was used to perform the T-bar penetration test at the center of the tub. Both actuators were mounted on the cross I-beams as shown in Figure 5.4. Actuator No. 2 for the T-bar was mounted on 2 small I-beams on top of the main I-beams in order to allow for enough room for the T-bar probe. Two LVDTs were mounted on the tub's wall at 0.9 m apart to monitor the in-flight consolidation (see Figure 5.4). An LDT was used to measure the differential settlement of the raft and it was mounted on the inside of the main I-beam. In addition, two pore pressure transducers (PPT) were placed as shown in Figure 5.3 to monitor pore water pressure dissipation during the in-flight consolidation. Table 5.3 provides details of instrumentation used in different tests.

The strain measurements were used to obtain the axial forces in the micropiles and the stress distribution at the raft base resulting from the vertical loading. Each micropile was instrumented with four general purpose strain gauges (CEA-06-125UW-350) evenly distributed along its shaft (at spacing of 67 mm) in order to evaluate the load transfer between the micropiles and the soil. The strain gauges had strain range of $\pm 5\%$. In addition, two extra strain gauges were attached at the top of two micropiles in the micropiled raft to confirm the axial force carried by the micropiles. For the raft, two strain gauges were attached to the raft base along its centerline (at the center and the edge

of the raft) in order to evaluate the bending stresses at the center and at the edge of the raft. Two pressure transducers were utilized to measure the contact pressure between the raft and the soil at the center of the raft and the edge of the raft. Figure 5.5 shows the distribution of the instruments used in micropiles and raft to measure both the strain and the contact pressure.

The micropiles were coated with a layer of sand using epoxy to increase their surface roughness to simulate the actual interface conditions of a prototype micropile, which has a rough surface due to the injection of grout under high pressure. This coating method was used successfully in a number of centrifuge tests such as those conducted by El Naggar and Sakr (2000), Horikoshi et al. (2002) and Horikoshi et al. (2003a, b). Furthermore, one of the factors that contribute to boosting the capacity of a micropile is the increased grout-ground bonding for the soil surrounding the micropile due to the pressurized grout used in its construction. The final diameter of micropiles including the epoxy and sand coating was approximately 12 mm. In order to simulate this increased bonding condition in the centrifuge testing, the micropiles were jacked into a smaller diameter pre-drilled hole (8.7 mm in diameter). The pre-drilling reduced the installation resistance and hence reduced the risk of damaging the model micropile. The complete package for tests 7, 8 and 9 are shown in Figure 5.6.

Table 5.3. Summary of the instrumentation used for each test.

Test	Element	Strain Gauge	LVDTs	Pressure transducer	Laser
Test 7	4 Micropile	4 along the micropile shaft and 2 at top of 2 more micropiles	2 for sand movement/ 1 for differential settlement	2 at raft base	1 for Axial movement
	Raft t_r= 0.6 m	2 at raft base			1 for Axial movement
Tests 8&9	1 Micropile	4 along the micropile shaft	2 for sand movement	-	1 for Axial movement
	Raft t_r= 0.6 m	2 at raft base	2 for sand movement/ 1 for differential settlement	2 at raft base	1 for Axial movement
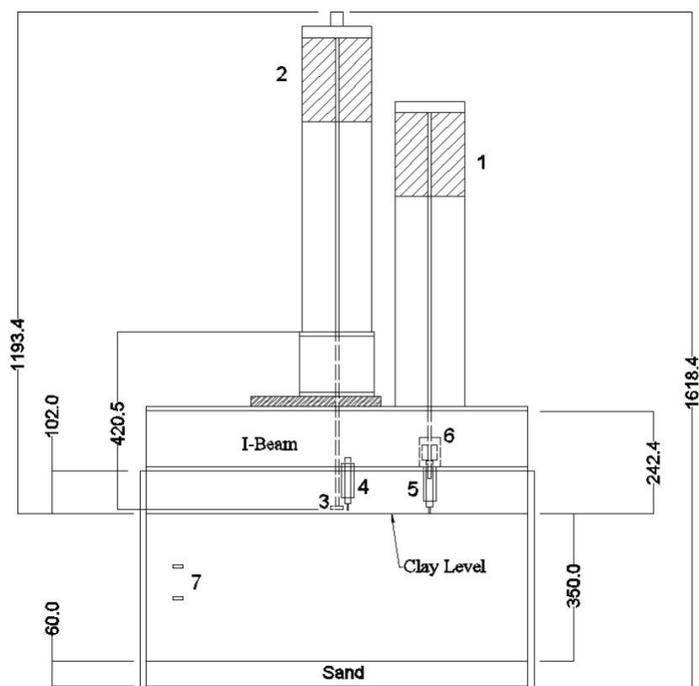
Figure 5.3. Vertical cross-section of centrifuge package including: (1) vertical actuator for applying load; (2) actuator used for T-bar; (3) T-bar; (4) LVDTs to measure clay settlement; (5) load cell; (6) laser; and (7) PPTs (all dimensions in mm).
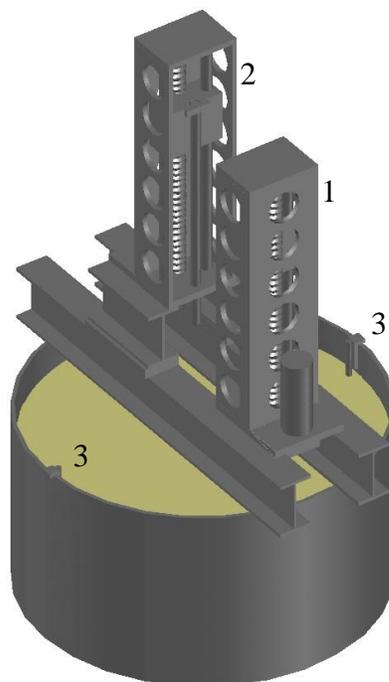
Figure 5.4. 3D model for the clay package consists of: (1) vertical actuator#1; (2) vertical actuator#2; and (3) LVDTs.
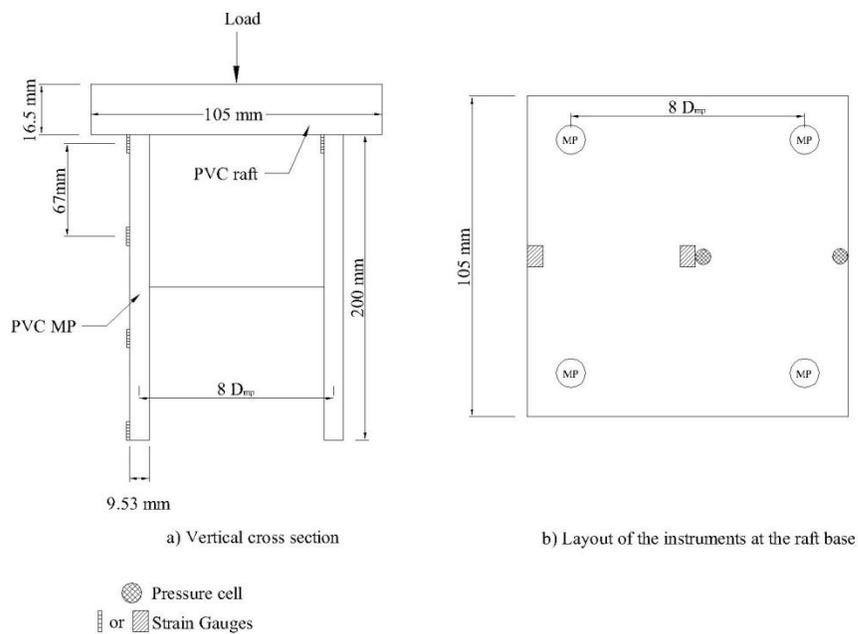
Figure 5.5. Detailed layout of the instruments used to measure the strain and contact pressure (dimensions not to scale).
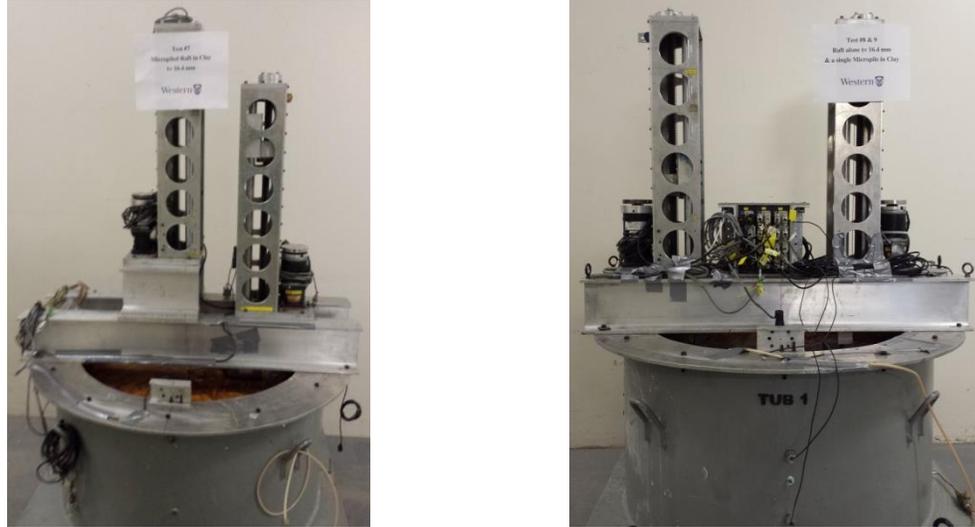
A   B

Figure 5.6. Complete centrifuge package for clay test: (a) for test#7; and (b) for test#8 and 9.

5.2.6. Centrifuge Test Procedure

Once the laboratory 1D consolidation was completed, the tub was removed out of the consolidation frame and the excess water was vacuumed. The loading piston was then removed slowly to minimize any disturbance to the clay due to the suction between the piston and the clay. The tub extension was removed and the surface of the clay was leveled and prepared to install the model. The final height and the weight of the clay were measured in order to calculate the final unit weight, which was found to be 18.4 kN/m^3. The foundation models and PPTs were installed and the clay surface was covered with a thin layer of grease in order to prevent the surface from drying out. Subsequently, the head work was attached and the instrumented package was loaded into the centrifuge and the base valve was opened to allow for the water to drain out of the clay during the in-flight consolidation. The centrifuge was accelerated in 5 steps up to 50g and the reconsolidation step was started. The speed was kept constant for about 5 minutes at each step to check the instruments' readings. At 50g, the clay reached 90% consolidation

under self-weight. The consolidation progress was monitored using 2 LVDTs and 2 PPTs. Figure 5.7 presents the consolidation progress for test 7, in which $t_{90} = 72.25$ minutes. The in-flight consolidation process, and the results, for tests 8 and 9 (same flight) were the same as test 7.
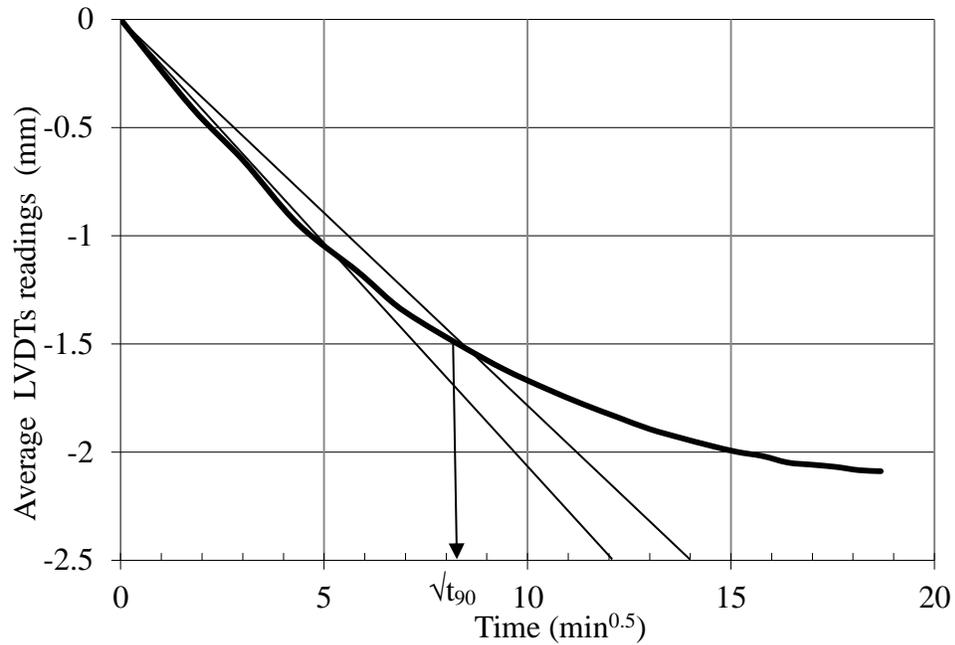
Figure 5.7. Settlement vs. $\sqrt{t}$ for the in-flight consolidation for the clay test bed showing $\sqrt{t_{90}}$.

A T-bar test was performed in-flight at 50 g to evaluate the undrained shear strength for the K-S clay, and its results were interpreted employing Eq. 5.4. The variation of the undrained shear strength with depth is presented in Figure 5.8.

$$s_u = \frac{P_{t-bar}}{N_b\, D_{t-bar}} \tag{5.4}\backslash$$

Where: s_u = undrained shear strength; P_{T-bar} = force per unit length acting on the cylinder; D_{T-bar} = diameter of cylinder; and N_b = bar factor between 9 and 12 with recommended value of 10.5 (Stewart and Randolph,1994).

Figure 5.8 shows the variation of the undrained shear strength with depth. It is noted from Figure 5.8 that the undrained shear strength, s_u, at the top of the soil bed was 25 kPa (due to the high OCR) and increased with depth in a linear fashion at a rate equal to 0.1 kPa/mm (2 kPa/m at prototype scale). In order to establish a correlation between the undrained modulus of elasticity (E_u) for the K-S clay and the undrained shear strength (s_u), four consolidated undrained triaxial tests were performed under consolidation pressures of 40 kPa, 80 kPa, 160 kPa and 320 kPa which corresponded to OCR values of 7.5, 3.8, 1.9 and 1, respectively. As the samples were previously consolidated from the slurry deposition to vertical effective stress of 300 kPa, they were at an overconsolidated state for the confinement pressures of 40 kPa, 80 kPa and 160 kPa. However, for the 320 kPa confinement pressure, the sample was normally consolidated. The CU triaxial tests results demonstrated that c_u = 34 kPa and ϕ_u = 12˚. E_u/s_u varied between 250 and 500 with an average of 375. This value is at the lower bound of the values reported by Jaimolkowski et al. (1979) for clay with a plasticity index (PI) less than 30 and OCR between 4 and 6.

Based on the T-bar results, s_u increased linearly with depth at a rate of 2 kPa/m, which is consistent with the CU triaxial test finding that ϕ_u = 12˚. The variation of undrained elastic modulus with depth, z, can be as approximated by:

$$E_u = 25(250 - 500) + 720z \qquad (5.5)$$
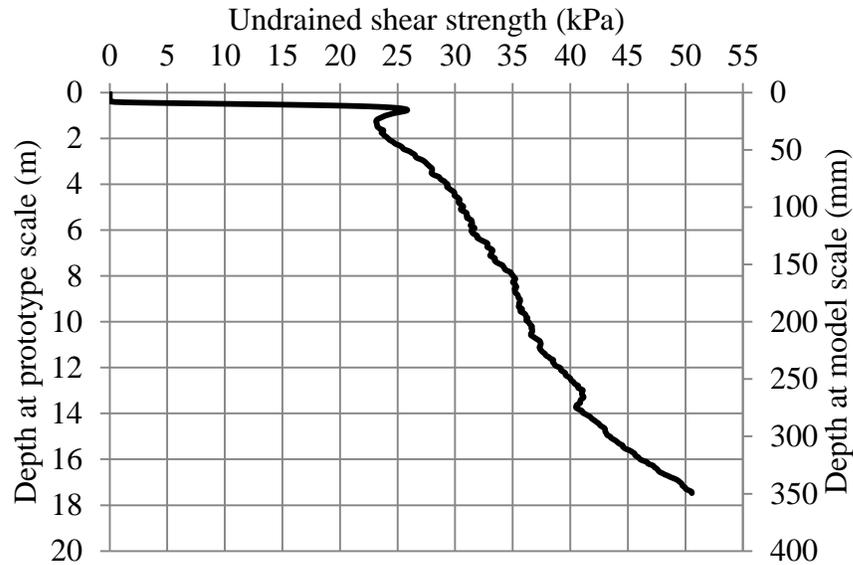
Figure 5.8. Undrained shear strength profile along clay depth using T-bar test results.

The soil shear modulus G_u, was evaluated based on the correlation of the triaxial tests results (i.e. $E_u = 375\ s_u$), and considering the clay undrained Poisson's ratio (0.5), which results in $G_u = 134\ s_u$. Eq. 5.5 can then be rewritten as:

$$G_u = 25(85\sim170) + 235\ z \tag{5.6}$$

The correlation used to estimate the modulus of elasticity and shear modulus (Eqs. 5.5 and 5.6) are considered to be suitable to describe the test clay elastic modulus, and will be used later to calculate the axial stiffness for the micropiles and micropiled raft (MPR) using the Poulos, Davis and Randolph (PDR) method.

Once the in-flight consolidation process was concluded for test 7, actuator No. 1 was moved to apply the load to the foundation at a rate of 6 mm/min. The test was then concluded and the centrifuge was stopped slowly. Once the centrifuge came to a

complete stop, the base valve was closed to prevent the clay from sucking the water from the sand layer. The package was then prepared for the next test.

In the second flight, the test started after the consolidation process was completed by loading the raft only using actuator No. 1 at a rate of 6 mm/min. Subsequently, the loading of the single micropile was performed at the same loading rate.

5.3. RESULTS AND DISCUSSION

5.3.1. Single Micropile Load Test Results

A single micropile was tested to determine its performance characteristics and ultimate capacity without the interaction effects of the raft and other micropiles within the foundation. The results from the single micropile serve as base line for the contribution of the micropiles to the micropiled raft foundation.

Figure 5.9 shows the load-settlement curve for the single micropile under axial compressive loading. The ultimate load was interpreted as the load corresponding to a pile head displacement equal to 10% of the pile diameter (Terzaghi, 1942). The interpreted ultimate load was 0.25 kN at model scale (i.e. 625 kN at prototype scale). This ultimate load was confirmed by using the method proposed by De Beer (Prakash and Sharma, 1990) which yielded an ultimate load equal to 0.25 kN (see Figure 5.10). The axial stiffness of the micropile was evaluated from the initial slope (the linear part) of the load-settlement curve for the single micropile and was found to be 0.52 MN/m at model scale (26 MN/m at prototype scale).
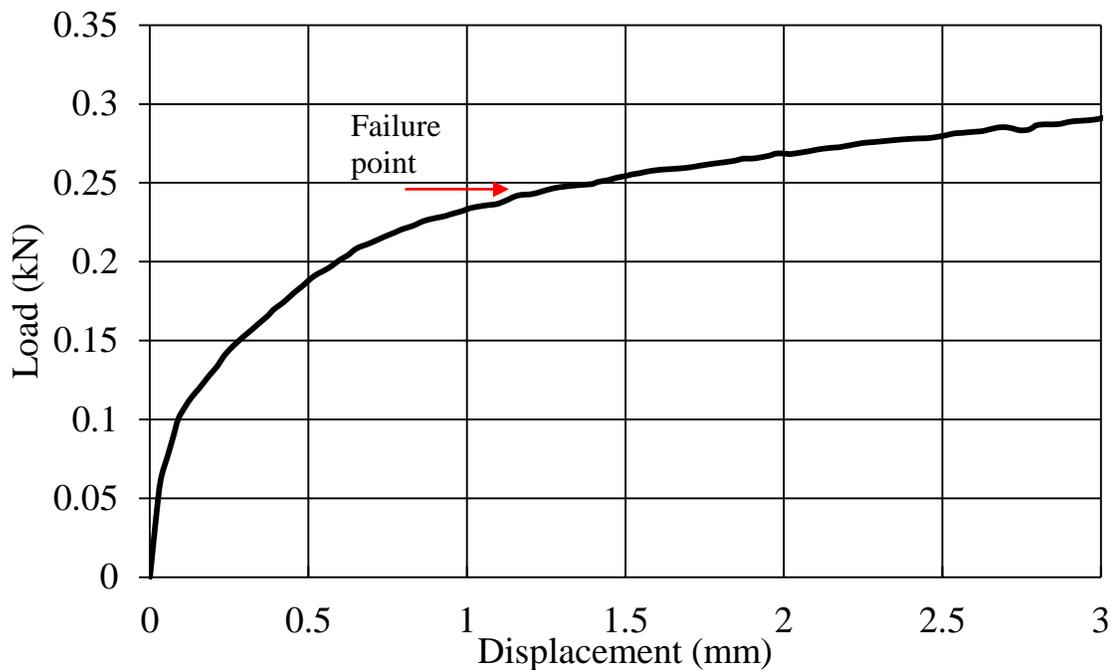
Figure 5.9. Load-settlement curve for a single micropile at model scale (the arrow shows the failure point).
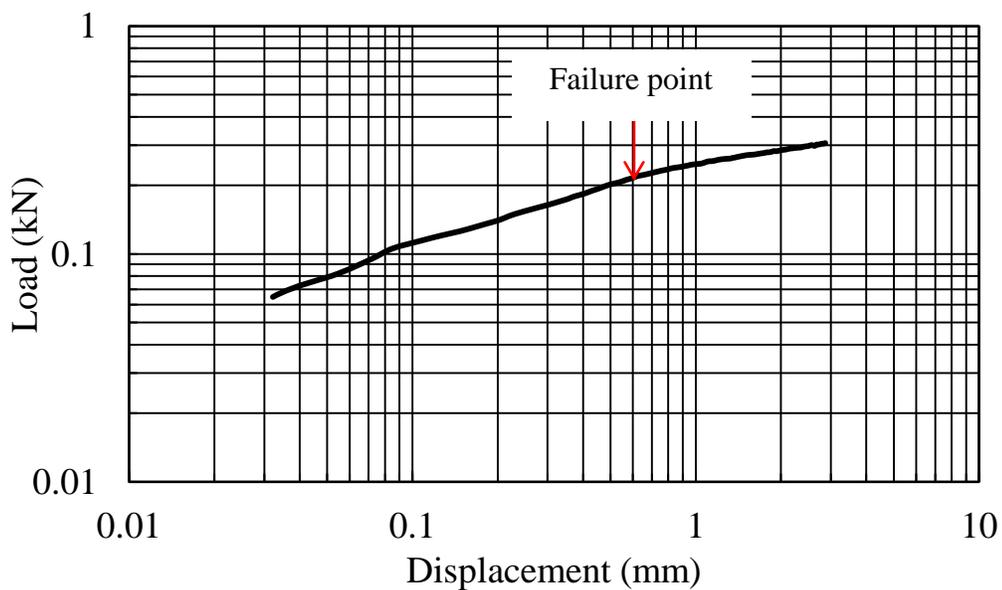
Figure 5.10. Load-settlement curve for a single micropile at model scale using De Beer's method (the arrow shows the failure point).

Wood (2004) proposed to evaluate the initial axial stiffness for micropiles in clay as:

$$K_{mp} = \frac{\pi r_o^2 E_p \eta \, (1 + (\xi \tanh \eta L_{mp})}{(\xi + \tanh \eta L_{mp})} \tag{5.7}$$

Where: $\eta = \frac{1}{r_o} \sqrt{\frac{G_s}{2E_p}}$; r_o are pile length and radius; E_p = Young's modulus; G = average

soil shear modulus; $\xi = \frac{(1-v_b)\pi r_o^2 E_p \eta}{4 r_o G_b}$; G_b and v_s are shear modulus and Poisson's ratio

for soil beneath the pile.

Similarly, Randolph (1994) proposed to evaluate the pile stiffness as (Fleming et al.,

2009):

$$K_p = G_{sl} * D_p * \frac{\frac{2\eta}{(1-v)\xi} + \frac{2\pi\rho}{\zeta} * \frac{\tanh(\mu L)}{\mu L} * \frac{L_p}{D_p}}{1 + \left[\frac{8\eta}{\pi\lambda(1-v_p)\xi} * \frac{\tanh(\mu L_p)}{\mu L_p} * \frac{L_p}{D_p}\right]} \tag{5.8}$$

Where: r_o = pile radius; D_p = pile diameter; $\zeta = \ln(r_m/r_o)$; $r_m = 2.5\rho(1-v)L_p$; $\xi = E_{sl}/E_{sb}$;

$\rho = E_{sav}/E_{sl}$; $\mu L = (2/(\zeta\lambda))^{0.5}*(L/r_o)$; $\lambda = E_p/G_{sl}$; $\eta = r_b/r_o$; L_p = pile length; E_{sl} = soil Young's

modulus at the pile toe level; E_{sb} = soil Young's modulus below pile toe; E_{sav} = average

soil Young's modulus along pile shaft; v = soil Poisson's ratio; G_{sl} = soil shear modulus

at the pile toe level; and E_p = pile material Young's modulus (Fleming et al., 2009).

Based on Eqs. 5.6, 5.7 and 5.8, axial stiffness of the single micropile, k_{mp}, at

prototype scale is 36 MN/m and 33 MN/m. The stiffness evaluated from the centrifuge

results was approximately 26 MN/m, i.e. 27% and 20% lower than the predictions of Eqs.

5.7 and 5.8, respectively.

The skin friction along the micropile shaft was evaluated using four strain gauges as

presented in Figure 5.11. The upper portion of the micropiles yielded higher skin friction,

which indicated full mobilization of shearing resistance along the upper segment of the micropile. The maximum unit skin friction at the ultimate applied load was approximately 34 kPa. This value is almost equal to s_u, which implies the adhesion coefficient was approximately 1.0. Based on the readings of the axial load at the bottom of the micropiles, only about 10% of the total applied load was carried by the toe resistance.
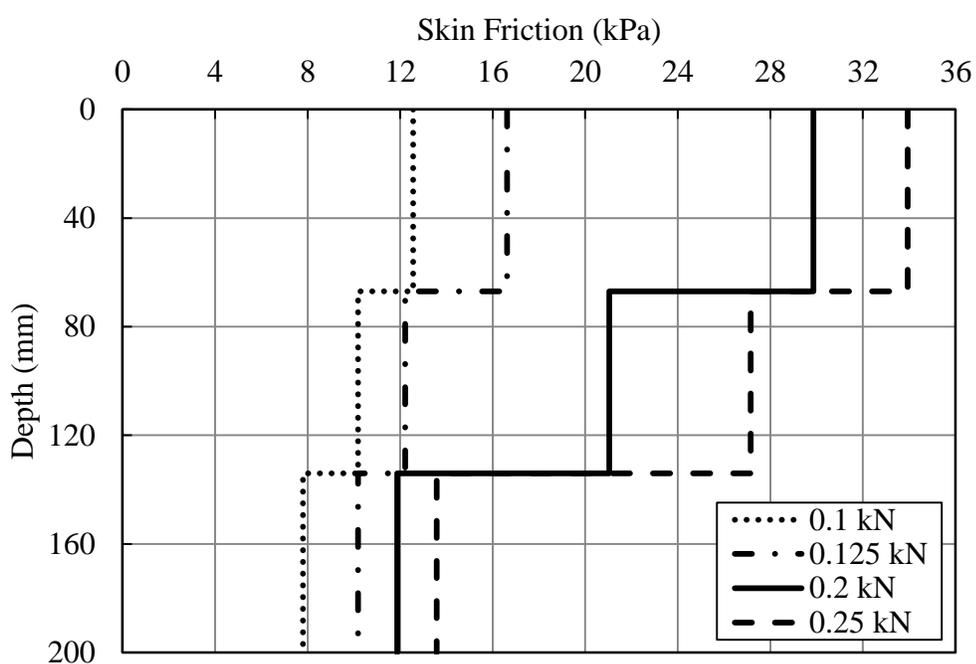
Figure 5.11. Skin friction of single micropile at different applied load levels.

5.3.2. Raft Load Test Results

A load test was conducted on an isolated raft (i.e. no micropiles) in order to establish a reference point for evaluating the behaviours of the MPR. The raft was instrumented with strain gauges to evaluate the bending stresses in the raft, pressure transducers to

evaluate the contact pressure of the raft and LVDTs to evaluate the settlement of the raft edge. The settlement of the raft centre was measured using a precise laser device.

For raft foundations, the bearing capacity is usually evaluated from the vertical load-settlement curve as the load corresponding to a limiting settlement value divided by the raft area. The load-settlement curve is also used to establish the axial stiffness for the raft (K_r). Figure 5.12 presents the load-settlement curve for the raft during the in-flight load test. The load-settlement curve is based on the readings of the settlement under the concentrated load at the raft center. Figure 5.12 shows that the ultimate load of the raft is approximately 1.9 kN at model scale (4800 kN at prototype scale).

The theoretical bearing capacity of a shallow foundation under a vertical centric load based can be evaluated using the Meyerhof's (1963) general bearing capacity equation, i.e.

$$Q_u = s_u N_c F_{cs} BL \tag{5.9}$$

Where: Q_u = ultimate Load; s_u = average undrained shear strength within a depth equal to the raft width; N_c = bearing capacity factor = 5.14 for ϕ =0; F_{cs} = shape factor =1.2 in the case of square footing; and B and L = width and length of the foundation.

Based on the T-bar results (see Figure 5.8), the average s_u within a depth of 5.25 m (the raft width at prototype scale) is approximately 30 kPa. Using Eq. 5.9, the theoretical ultimate load carried by the raft alone was 5100 kN which is only 6% higher than the value obtained from the centrifuge test. The raft axial stiffness, K_r, was evaluated from the initial slope of the curve and was found to be 0.92 MN/m at model scale (46 MN/m at prototype scale).

Horikoshi and Randolph (1997) evaluated the raft-soil stiffness ratio for a rectangular raft from centrifuge studies. They proposed an equation to evaluate the raft flexibility considering an earlier definition of the raft-soil stiffness ratio for a circular raft proposed by Brown (1969), i.e.

$$K_f = 5.57 \, \frac{E_r}{E_s} \frac{(1-v_s^2)}{(1-v_r^2)} \left(\frac{B_r}{L_r}\right)^{\alpha_o} \left(\frac{t_r}{L_r}\right)^3 \tag{5.10}$$

Where: E_r = the raft Young's modulus; v_r = raft Poisson's ratio; t_r = raft thickness; v_s = soil Poisson's ratio; E_s = average soil elastic modulus at depth = $2B_r/3$; and α_o = optimal value = 0.5.

Based on the value of the raft flexibility, K_f, the raft can be characterized according to the following conditions: (i) perfectly rigid if $K_f > 1000$; (ii) perfectly flexible when $K_f < 0.001$; and (iii) intermediately flexible if K_f varies between 0.001 and 1000 (Horikoshi and Randolph, 1997).

Poulos and Davis (1974) proposed evaluating the vertical stiffness of a rectangular raft foundation by:

$$K_r = I\sqrt{B_r L_r} \left(\frac{2G_{sr}}{(1-v_s)}\right) \, (kN/m) \tag{5.11}$$

Where: K_r = axial stiffness for the raft foundation; L_r and B_r are the raft length and width; G_{sr} = shear modulus at depth = $2B/3$; v = soil Poisson's ratio; and I = influence factor which is a function of the raft aspect ratio = 1.03 for a square raft (Wood, 2004).

The raft axial stiffness was calculated using Eq. 5.11 and was found to be 53 MN/m, which is approximately 15% higher than the value evaluated from the centrifuge test.

This difference may be attributed to the relative flexibility of the raft (K_f is equal to 21 based on Eq. 5.10), while Eq. 5.11 is for a rigid foundation. Therefore, an adjustment factor should be used along with Eq. 5.11 to account for the raft flexibility.
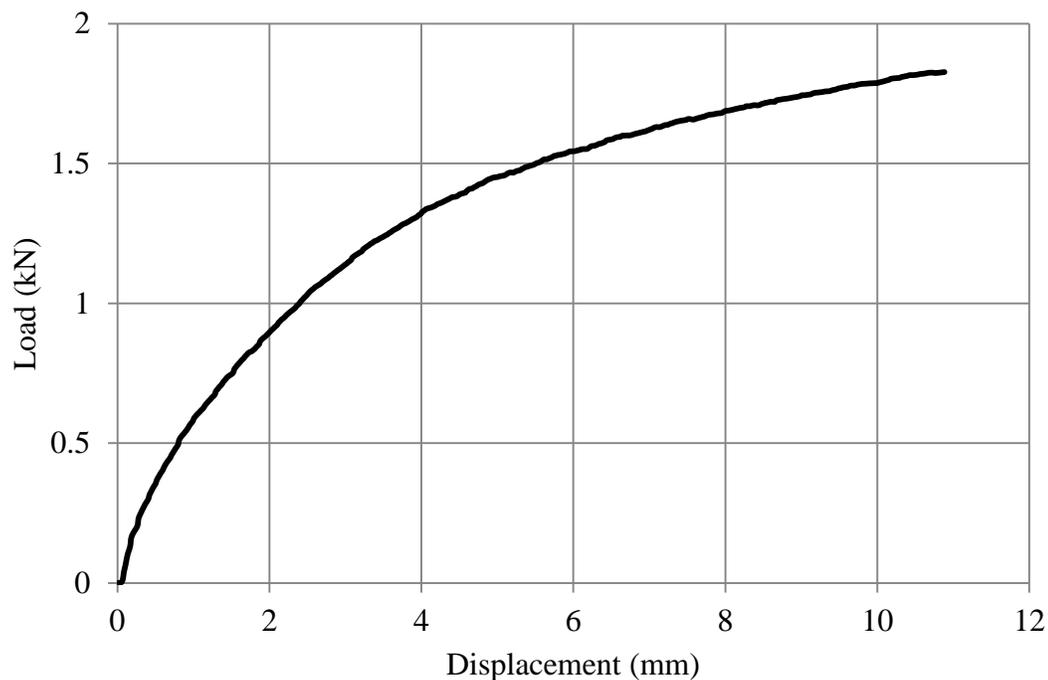
Figure 5.12. Load-displacement curve for the raft center at model scale.

5.3.3. Micropiled Raft Load Test Results

The raft flexibility, influenced primarily by its thickness, has a significant impact on the overall performance of the micropiled raft. It affects the distribution of contact pressure, raft differential settlement and the load sharing between the raft and the micropiles. Although Eq. 5.10 is for a raft foundation, it is used herein to evaluate for the micropiled raft flexibility, but considering B to be the spacing between the micropiles instead of the raft width; i.e.

$$K_f = 5.57 \; \frac{E_r}{E_s} \frac{(1-v_s^2)}{(1-v_r^2)} \left(\frac{S_B}{S_L}\right)^{\alpha_o} \left(\frac{t_r}{S_L}\right)^3 \qquad (5.12)$$

Where S_L and S_B= spacing between micropiles along the length and width of the MPR.

This is justified because the spacing between the micropiles represents the unsupported span of the raft. As the micropile spacing decreases, the deflections at locations between the micropiles and at the raft center will decrease. Thus, it is considered more representative of the micropiled raft width for the purpose of evaluating its flexibility (Alnuaim et al., 2013).

Using Eq. 5.12, K_f = 1750 for t_r = 0.6 m with micropile spacing of 8 D_{mp}, which implies the raft as an element within the MPR could be classified as rigid.

5.3.4. Axial Stiffness of the Micropiled Raft

The results from the centrifuge load test for the MPR are presented in terms of its axial stiffness at different stages. Figure 5.13 presents the load versus displacement for the MPR with a raft thickness of 16.4 mm (0.6 m at prototype scale). As shown in Figure 5.13, the MPR bearing capacity was estimated considering the load at the onset of failure, which was approximately 2.2 kN at model scale. The MPR behaviour displayed in Figure 5.13 is similar the behaviour of a piled raft as described by Poulos (2001) (see Ch.2 section 2.3.2.1). The slope of the first (linear) segment of the curve between points O to A defines the MPR stiffness, which remained constant until the micropile resistance was started to mobilize. The slope of the second segment of the curve (i.e. between points A and B) reflected the stiffness of the raft alone, which remained almost constant until the ultimate bearing capacity of MPR was reached.
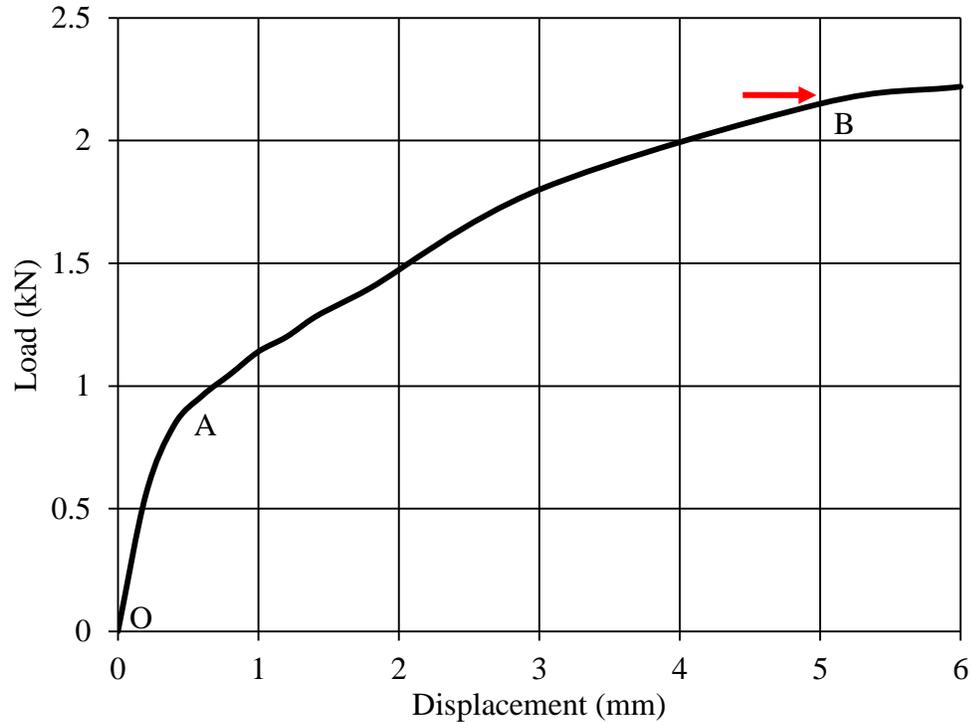
Figure 5.13. Load-Displacement curve of the micropiled raft in K-S clay at model scale the arrow shows the ultimate load carried by MPR (the arrow indicates onset of failure).

Poulos (2001) introduced the simplified Poulos-Davis-Randolph (PDR) method in order to estimate the axial stiffness of a piled raft foundation, which combined the analytical methods proposed by Poulos and Davis (1974) and Randolph (1994). In this method, the axial stiffness of a piled raft is evaluated considering the pile group stiffness and the raft axial stiffness (Randolph, 1994), i.e.

$$K_{pr} = \frac{K_{PG} + (1 - 2a_{rp})K_r}{1 - \left(a_{rp}^2\left(\frac{K_r}{K_{PG}}\right)\right)} \tag{5.13}$$

In Eq. 5.13, K_{PG} is the stiffness of the pile group and is given by (Fleming et al., 2009):

$$K_{PG} = n_p^{1-e_f} K_p \qquad (5.14)$$

Where n_p is the number of piles within the group. The efficiency exponent, e_f, can be estimated based on the design chart developed by Fleming et al. (2009), which account for the piles' spacing, homogeneity of the soil and pile-soil relative stiffness; Poisson's ratio, v_s, of the soil; and K_p is the stiffness of a single pile, which can be calculated from using Eqs. 5.7 and 5.8. The raft stiffness K_r is calculated according to Eq.5.11, while a_{rp} is the raft pile interaction factor, which can be calculated from:

$$a_{rp} = 1 - \{ln(r_c/r_o) / \zeta\} \qquad (5.15)$$

Where: r_c = average radius of pile cap (i.e. equivalent to an area similar to the raft area / number of piles); L_p and r_o are pile length and radius; $\zeta = ln(r_m/r_o)$; $r_m = 2.5\rho(1-v)L_p$; $\xi = E_{sl}/E_{sb}$; $\rho = E_{sav}/E_{sl}$; $\mu L = (2/(\zeta\lambda))^{0.5}*(L/r_o)$; $\lambda = E_p/G_{sl}$; $\eta = r_b/r_o$; E_{sl} = soil Young's modulus at the pile toe level; E_{sb} = soil Young's modulus below pile toe; E_{sav} = average soil Young's modulus along pile shaft; v = soil Poisson's ratio; G_{sl} = soil shear modulus at the pile toe level; and E_p = pile material Young's modulus.

The suitability of the PDR method for the case of a micropiled raft installed in clay needs to be evaluated considering the relatively small axial stiffness of the micropile compared to that of the larger diameter piles. Therefore, the axial stiffness of the micropile raft was evaluated from the centrifuge testing results. The results of the centrifuge load tests that were performed on MPR foundations with an equivalent raft

thickness of 0.6 m is discussed herein and are compared with the predictions of the PDR method.

The initial axial stiffness of the MPR (slope of curve between points O and A in Figure 5.13 for $t_r = 0.6$ m was 140 MN/m, which is 207% higher than the stiffness of the same raft but without micropiles (46 MN/m). This increase in stiffness (94 MN/m) was due to the contribution of the 4 micropiles supporting the raft. Since the load was applied at the raft centre, it is reasonable to assume that each micropile contributed approximately 24 MN/m to the overall stiffness of the micropiled raft. Comparing the axial stiffness of a single micropile (26 MN/m) to that of a micropile within the MPR (24 MN/m), it indicates minimal effect of the micropiles-raft interaction especially at large spacing $(S/D_{mp}= 8)$. However, comparing the axial stiffness of MPR (140 MN/m) to a group of 4 micropiles which has a stiffness of (26x4 =104 MN/m), the MPR system exhibited increased axial stiffens by approximately 35% due to the contribution of the raft. Furthermore, the high soil stresses caused by the raft, overlapped with the stress along the micropile shaft, resulted in an increase in the confining pressure and associated increase in shaft resistance of the upper portion of the micropiles. This interaction needs to be comprehensively investigated.

The slope of the second segment of the load-settlement curve (i.e. between points A and B) represented an axial stiffness of 50 MN/m, which was very close to the axial stiffness of the raft only (46 MN/m). This indicates that the micropiles reached their ultimate capacity as they contributed slightly to the overall stiffness within this range of loading.

The PDR method was used to evaluate the axial stiffness of the MPR based on Eqs. 5.11, to 5.15. In addition, the axial stiffness of the single micropile was evaluated using Eqs. 5.7 and 5.8. The calculated axial stiffness values of the MPR are 132 MN/m and 116 MN/m based on k_{mp} calculated using Eqs. 5.7 and 5.8, respectively, which represented 6% and 17% deviations from the experimentally obtained axial stiffness. This implies the PDR method can provide reasonable estimates of the micropiled raft stiffness. For the current set of soil micropiles parameters, it seems that the method developed by Wood (2004) is more appropriate for evaluating the stiffness of the micropiled raft in clay.

5.3.5. Micropiled Raft Contact Pressures

The soil reaction to the raft deflection (i.e. contact pressure) increased as the raft deflection increased. The magnitude and distribution of the contact pressure depends on a number of parameters such as: type of loading, type of soil, stiffness of soil, spacing of piles and flexibility of the raft. Normally, for a rigid footing resting on clayey soils the maximum contact pressure occurs at the edge and the minimum contact pressure occurs at the center (Terzaghi et al., 1996). On the other hand, Faber (1933) showed experimentally that the contact pressure for a shallow footing resting on cohesive soil increases from a minimum at the center to a maximum at the edge for both flexible and rigid foundations. The micropiled raft is expected to exhibit different pressure distribution due to the presence of the micropiles, especially since it was subjected to a concentrated load.

Figure 5.14 presents the contact pressure distribution for the raft alone subjected to the centric concentrated load. As can be noted from Figure 5.14, the contact pressure at the edge of the raft was slightly higher than that at the center with a maximum difference

of approximately 18% (at the maximum applied load), which represented the behaviour of a rigid foundation resting on clayey soil. The variation of contact pressures at the center and edge of the raft with applied load for the 0.6 m thick MPR is presented in Figure 5.15. Due to the placement of the micropiles at $8D_{mp}$, the raft in the MPR displayed stiffer response compared to the raft only with B = 5.25 m. This observation is clearly demonstrated in Figure 5.16; once the micropiles started to yield at about 0.4 kN applied load on the raft, the contact pressure at the edge of the raft, $\sigma_{z(edge)}$, increased significantly at about 30% compared to the contact pressure at the center of the raft, $\sigma_{z(center)}$. Moreover, as the load progressed and the micropiles reached capacity (at about 1.1 kN), a further increase in $\sigma_{z(edge)}$ to $\sigma_{z(center)}$ (about 40%) occurred as shown in Figure 5.16 and the MPR behaved similar to a rigid raft. At the final stage (between points B and C) when the whole system reached the failure load (about 2 kN), the $\sigma_{z(edge)}$ and $\sigma_{z(center)}$ became constant, which indicated a uniform distribution of the contact pressure. Similar observation was reported by Terzaghi et al., (1996) for a shallow footing resting on clayey soil.
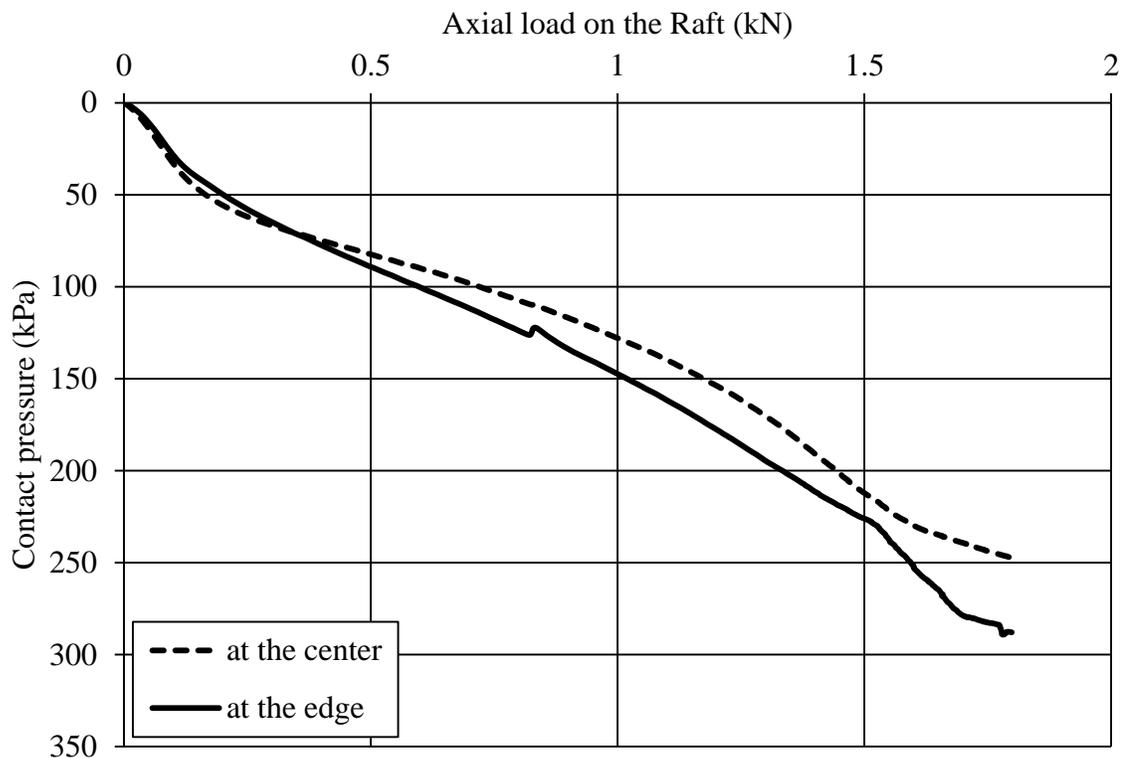
Figure 5.14. Variation of contact pressures with applied load for the case of raft alone.
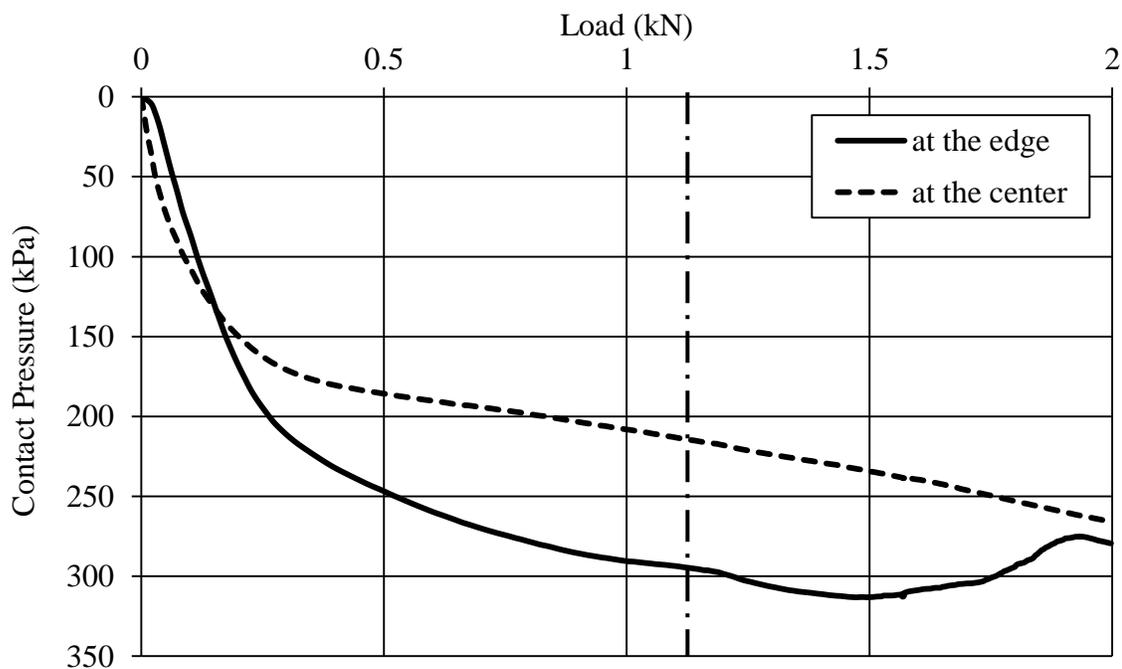
Figure 5.15. Variation of contact pressures with applied load for the MPR (the vertical dashed line indicates the ultimate load of a single micropile).
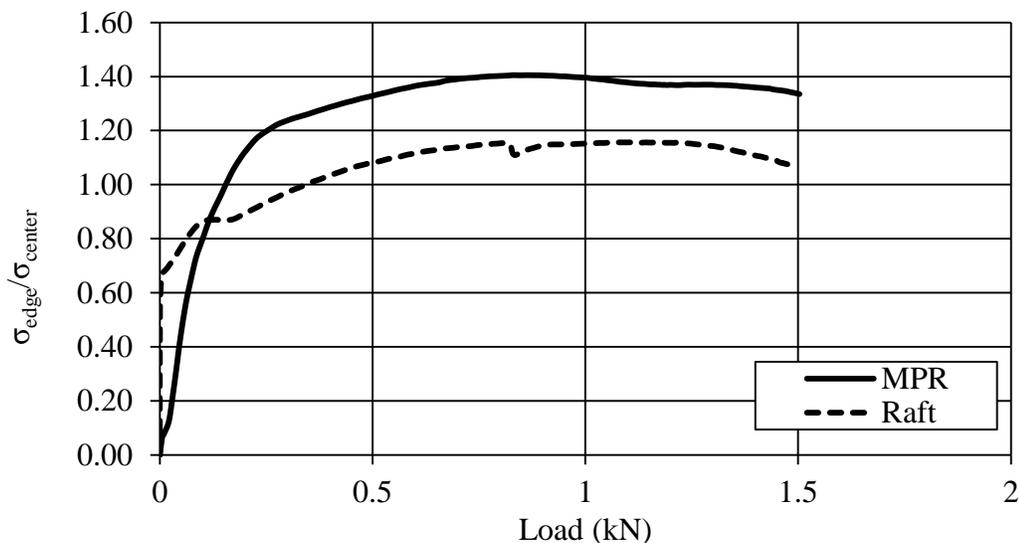
Figure 5.16. Variation of ratio of contact pressure at the center and edge of raft alone and the MPR.

5.3.6. Skin Friction of Micropiles as a MPR Component

Figure 5.17 shows the load-displacement curve for a micropile of the MPR. The curve was based on the readings of the strain gauges at the top of the micropile and the LVDT reading at the edge of the raft. Based on Figure 5.17, the (plunging) failure load for the micropiles was approximately 0.24 kN. Figure 5.18 presents the distribution of skin friction of the micropile at different levels of applied load. The average skin friction at the top segment of the micropile at the failure load was approximately 35 kPa, which is at the lower bound of the range proposed by the FHWA (2005) for a Type B micropile. The results indicate a minimal effect on the skin friction due to the interaction between the micropiles and the raft as the skin friction of the micropile reached the maximum unit shaft friction as it was the case for the single micropile at the ultimate load. However, inspecting the distribution of shaft friction along the micropiles for low applied loads (i.e. 0.1 kN and 0.125 kN), it can be noted that the shaft friction along the top segment of the micropile is higher for the MPR case (Figure 5.18) compared to the single micropile case

(Figure 5.11). This difference may be attributed to the additional confining stress for the case of the MPR, which means that the raft-soil-micropile interaction may result in an increase in the micropile shaft capacity up to the maximum unit friction of the micropile-soil interface condition. In addition, Figure 5.18 shows that the end bearing capacity of the micropile was only about 7% of the total load. Again, these results indicate the effect of the micropile flexibility on reducing the load transmitted to the lower portion of the micropile as the load carried by the micropiles reached its maximum value.
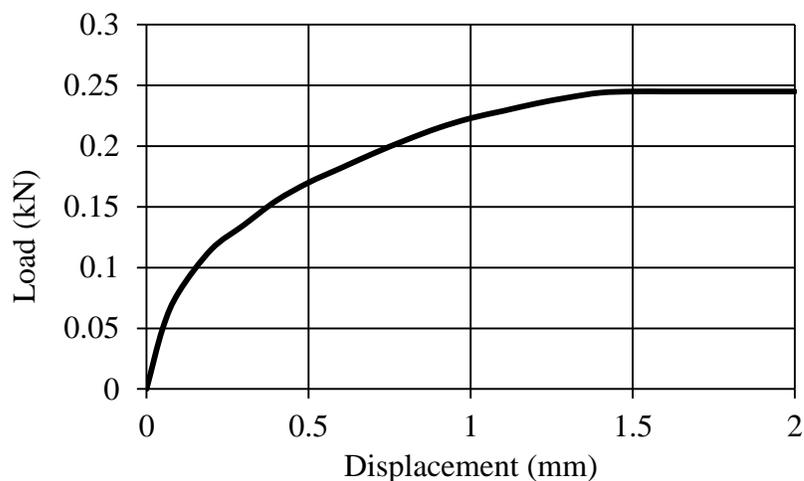
Figure 5.17. Axial load carried by a single micropile as a component of the MPR.
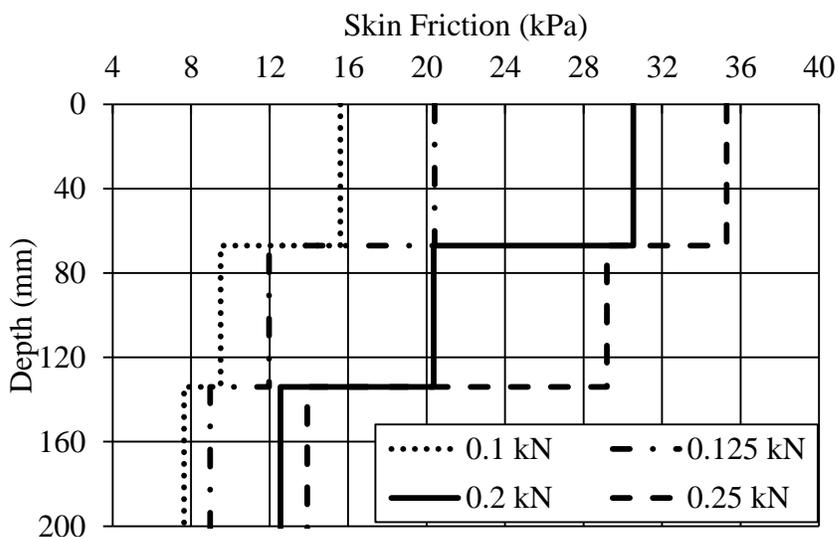
Figure 5.18. Skin friction along the micropile as a component of the MPR.

5.3.7. Load Sharing in a Micropiled Rafts

The axial load carried by the micropiles in a micropiled raft system is affected by the raft flexibility and the direct contact between the raft and subsoil. Figure 5.19 presents the percentage of load carried by the micropiles and the raft at different load levels. At the initial loading stage (less than 0.75 kN), most of the load was carried by the micropiles; this is believed to be due to the lack of intimate contact between the raft and underlying soil, as the clay was consolidated by about 2.25 mm during the in-flight consolidation process (Figure 5.7). Similar behaviour was reported by Horikoshi and Randolph (1996). As the applied load increased, the proportion of the load carried by the micropiles (MPs), decreased at about 0.8 kN and continued to decrease gradually after that. This is because the MPs approached its failure load (0.25 kN) and experienced excessive settlement, which caused the load to be transferred by the raft. At this point, the MPs stiffness decreased significantly. on the other hand, the stiffness of clay beneath the raft was increased because of the consolidation of the clay layer as a result of the raft movement, and hence the raft became much stiffer than the MPs. At an applied load of 2 kN, the load transferred by each component reached a plateau and became almost constant at approximately 52% and 48% for the MPs and the raft, respectively. A similar observation was made by Horikoshi and Randolph (1996) as the piles in the piled raft carried most of the load at the initial stages and decreased with the progression of the loading to reach about 48%.

5.3.8. Raft Differential Settlement

Figure 5.20 presents the differential settlement of the micropiled rafts evaluated as the difference between the laser reading at the center of the raft and the LVDT reading at

the edge of the raft at different load increments for the raft only and MPR cases. For the raft only case, the differential settlement progressed as the load increased, which was expected under centric concentrated load. Once the raft approached its ultimate load (1.9 kN), the differential settlement increased significantly (approximately 30%) because the soil immediately beneath the raft center experienced excessive settlement as it reached its ultimate capacity.
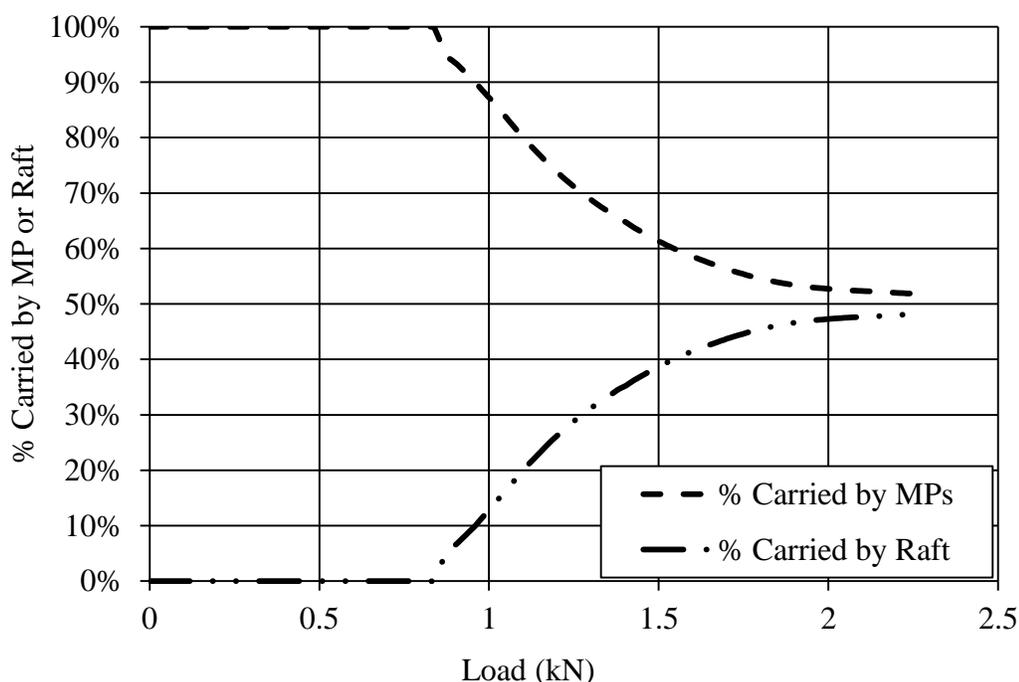
Figure 5.19. Load sharing between the micropiles and the raft varies with the applied load.

At early loading stages, the MPR raft experienced relatively high differential settlement (up to 0.25 mm) because the micropiles supported the raft edge. Since the load was applied to the raft center, combined with the lack of intimate contact between the raft and the clay, the load was transferred by the micropiles and the raft center experienced high settlement. As the load progressed and the micropiles stiffness decreased

significantly, they experienced relatively higher settlement. Due to excessive movement of the micropiles, the edge of the raft experienced similar movement, and as a result, the differential settlement increased slightly. Overall, the MPR differential settlement was only 50% of the differential settlement experienced by the raft only for higher loads.
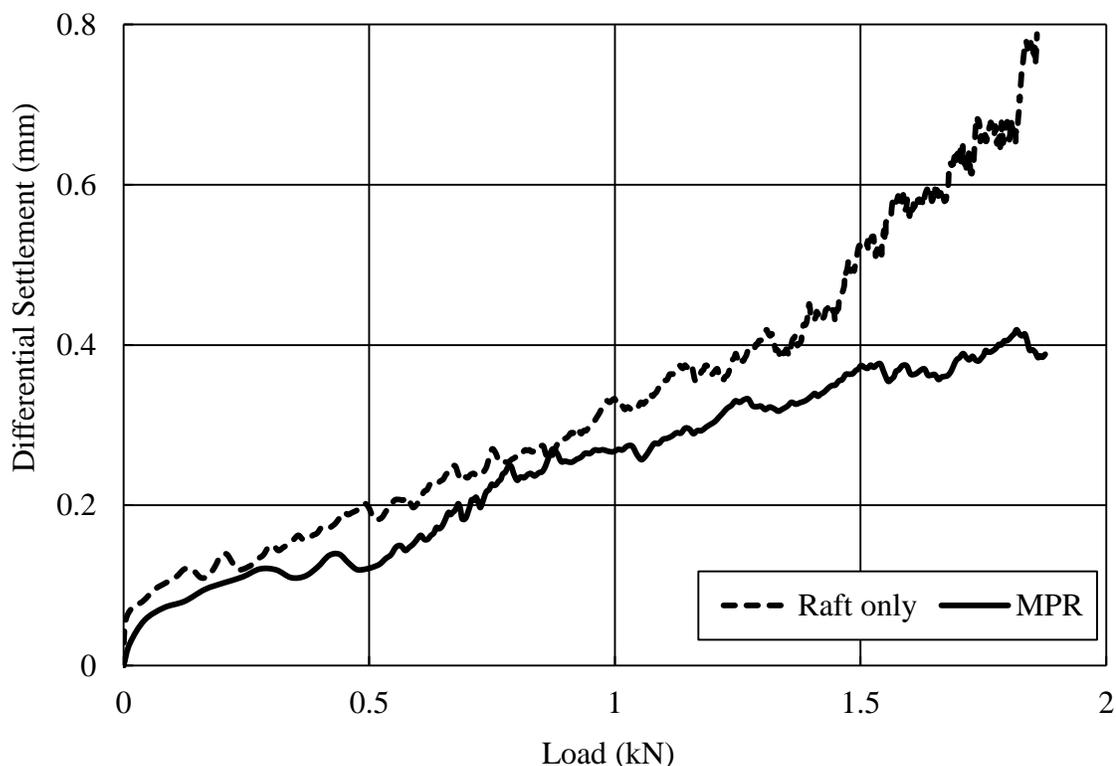
Figure 5.20. Differential settlement of raft only and the MPR cases.

5.3.9. Bending Moments

The bending moments were assessed at the centre, M_{center}, and edge M_{edge}, of the raft (both locations were along the centerline of the raft). Figure 5.21a presents M_{center} for the MPR and the raft only at different loading increments. For both the MPR and raft only cases, M_{center} increased linearly as the load increased. Comparing M_{center} for the raft case

to that of the raft within the MPR shows that the micropiles had a negligible effect on M_{center} and a similar observation was made for the comparable cases on sand soil.

Figure 5.21b presents M_{center}/M_{edge} for both the MPR and raft alone cases. The presence of the micropiles in the MPR (t = 16.4 mm) increased M_{edge} compared to the case of the raft alone. The M_{center}/M_{edge} for the raft alone was approximately 2.65. On the other hand, the ratio varied between 1.8 and 1.9 for the MPR. The M_{center} was much higher than M_{edge} due to applying a concentrated load at the raft center. As the load increased, M_{center}/M_{edge} increased, which indicates that the variation of the bending moment was similar to the raft case. As the micropiles reached their full capacity (0.25 kN each) in the MPR, M_{center} became much higher than M_{edge}. This was because the micropiles could not resist any additional load and settled as the applied load increased, hence reducing the raft deflection and associated bending stresses.
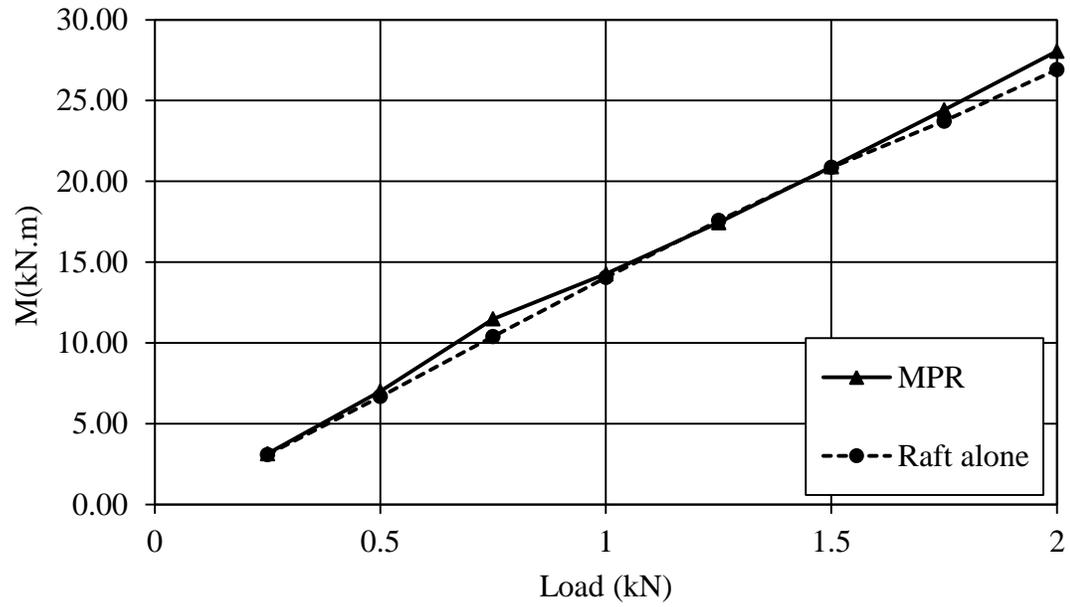
(a)
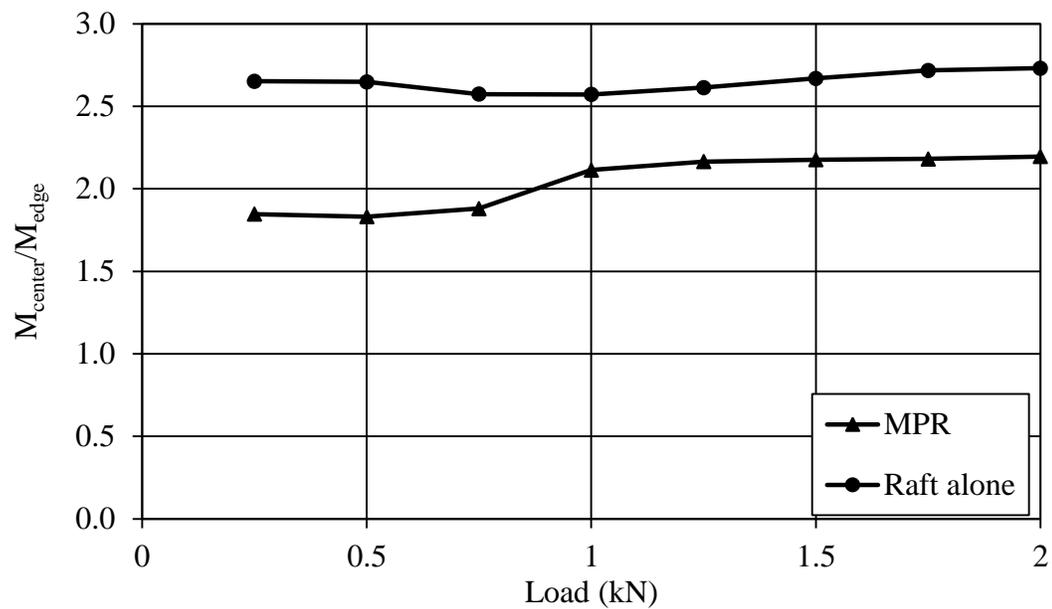
(b)

Figure 5.21. (a) Bending moment at raft center at model scale; and (b) ratio between the bending moment at center of the raft to the bending moment at edge of the raft.

5.4. CONCLUSIONS

Three geotechnical centrifuge tests were conducted at 50g in order to investigate the behaviour of micropiled raft foundations and their components in cohesive soil and subjected to a concentrated vertical load. The responses of the single micropile, the single raft and the micropiled raft to the applied loads were evaluated. Based on the analysis of the test results, the following conclusions may be drawn:

1. The stiffness of the MPR was more than twice the stiffness of the raft alone due to the contribution of a group of 4 micropiles.

2. The PDR method predicted, with reasonable accuracy, the axial stiffness of the MPR of the current study, which was installed in cohesive soil and had a relatively rigid raft. However, the ability of the PDR method to estimate the stiffness of the MPR with flexible raft should be evaluated.

3. As the micropiles reached their ultimate capacity, the contact pressure at the raft edge increased relative to the contact pressure at the raft centre and the MPR behaved similar to the raft alone.

4. At ultimate loading, the skin friction along the top segment of the micropile shaft reached its maximum resistance. The unit shaft friction indicated that the adhesion factor was approximately 1.0. However, the skin friction did not develop fully along the lower segment of the micropile because it did not move downward enough due to the compressibility of the upper segment.

5. The increased confining pressure around the micropile due to the raft load resulted in higher shaft friction along the upper segment of the micropile,

compared to the single micropile case. However, this percentage increase diminishes as the load level increases due to the soil nonlinearity.

6. The contribution of end bearing resistance of the micropiles was only about 7% - 10% of the total applied load.

7. The MPR differential settlement was only 50% of the differential settlement experienced by the raft-only case at higher applied load.

8. The load transferred by the MPR components reached a plateau at approximately 52% and 48% for the MPs and the raft, respectively.

REFERENCES

ASTM Standard D422-63. (2007). Standard Test Method for Particle-Size Analysis of Soils. ASTM International, West Conshohocken, PA.

ASTM Standard D4318-10. (2010). Standard Test Methods for Liquid Limit, Plastic Limit, and Plasticity Index of Soils. ASTM International, West Conshohocken, PA.

Alnuaim, A. M., El Naggar, H. and El Naggar, M. (2013). Performance of Piled-Raft System under Axial Load. Proceedings of the 18th International Conference on Soil Mechanics and Geotechnical Engineering, Paris, pp. 2663-2666.

Brown, P. T. (1969). Numerical Analyses of Uniformly Loaded Circular Rafts on Deep Elastic Foundations. Géotechnique, **19**(3): 399-404.

Bruce, D. A., DiMillio, A. F. and Juran, I. (1995). Introduction to Micropiles: An International Perspective. Foundation Upgrading and Repair for Infrastructure Improvement, ASCE, Geotechnical Special Publication No. 50, pp.1-26.

Clancy, P. and Randolph, M. F. (1996). Simple Design Tools for Piled Raft Foundations. Géotechnique, **46**(2): 313 –328.

El Naggar, M. and Sakr, M. (2000). Evaluation of Axial Performance of Tapered Piles from Centrifuge Tests. Canadian Geotechnical Journal, **37**(6): 1295-1308.

Faber, O. (1933). Pressure Distribution under Bases and Stability of Foundations. The Structural Engineer, **11**(3): 116-125.

FHWA. (2005). Micropile Design and Construction Guidelines, Implementation Manual. National Highway Institute.

Fleming, K., Weltman, A., Randolph, M. and Elson, K. (2009). Piling Engineering. 3rd ed. Taylor and Francis group, New York.

Han, J. and Ye, S. (2006). A Field Study on the Behaviour of a Foundation Underpinned by Micropiles. Canadian Geotechnical Journal, **43**(1): 30-42.

Horikoshi, K. and Randolph, M. (1997). On the Definition of Raft-Soil Stiffness Ratio for Rectangular Rafts. Géotechnique, **47**(5): 1055-1061.

Horikoshi, K. and Randolph, M. F. (1996). Centrifuge Modelling of Piled Raft Foundations on Clay. Géotechnique, **46**(4): 741 –752.

Horikoshi, K. and Randolph, M. F. (1998). A Contribution to Optimum Design of Piled Rafts. Géotechnique, **48**(3): 301-317.

Horikoshi, K., Matsumoto, T., Hashizume, Y., Watanabe, T. and Fukuyama, H. (2003a). Performance of Piled Raft Foundations Subjected to Static Horizontal Loads. International Journal of Physical Modelling in Geotechnics, **3**(2): 37-50.

Horikoshi, K., Matsumoto, T., Hashizume, Y. and Watanabe, T. (2003b). Performance of Piled Raft Foundations Subjected to Dynamic Loading. International Journal of Physical Modelling in Geotechnics, **3**(2): 51-62.

Horikoshi, K., Watanabe, T., Fukuyama, H. and Matsumoto, T. (2002). Behaviour of Piled Raft Foundations Subjected to Horizontal Loads. *In* Proceeding of the International conference on Physical Modelling in Geotechnics. St John's, Newfoundland, Canada, Taylor & Francis.

Jaimolkowski, M., Lancellotta, R., Pasqualini, E., Marchetti, S. and Nova, R. (1979). Design Parameters for Soft Clays. General Report. Proceedings of the 7th European Conference on Soil Mechanics and Foundation Engineering. No. 5, pp. 27–57.

Jeon, S. S. and Kulhawy, F. H. (2001). Evaluation of Axial Compression Behaviour of Micropiles. *In* Proceedings of a specialty conference: Foundations and Ground Improvement (GSP 113), ASCE, Blacksburg, Virginia, pp. 460-471.

Juran, I., Benslimane, A. and Hanna, S. (2001). Engineering Analysis of Dynamic Behaviour of Micropile Systems. Transportation Research Record: Journal of the Transportation Research Board, **1772**(1): 91-106.

Lin, L. (1995). Strength Characteristics of a Modelling Silty Clay. M.Eng. Thesis, Memorial University of Newfoundland. St. John' s, Newfoundland. Canada.

Lizzi, F. (1982). The Static Restoration of Monuments: Basic Criteria-Case Histories, Strengthening of Buildings Damaged by Earthquakes . Genova: Sagep Editrice.

Long, J., Maniaci, M., Menezes, G. and Ball, R. (2004). Results of Lateral Load Tests on Micropiles. *In* Proceedings of sessions of the GeoSupport Conference: Innovation and Cooperation in the Geo-Industry, Orlando, Florida: Geo-Institute of the American Society of Civil Engineers, pp. 122-133.

Mahboubi, A. and Nazari-Mehr, A. (2010). Nonlinear Dynamic Soil-Micropile-Structure Interactions Centrifuge Tests and FEM Analyse. *In* Proceeding of the Deep Foundations and Geotechnical In Situ Testing, GeoShanghai 2010, pp. 81-89.

Meyerhof, G. (1963). Some Recent Research on the Bearing Capacity Of Foundations. Canadian Geotechnical Journal, **1**(1): 16-31.

Poulos, H. G. (2001). Piled Raft Foundations: Design and Applications. Géotechnique, **51**(2): 95-113.

Poulos, H. G. and Davis, E. H. (1974). Elastic Solutions for Soil and Rock Mechanics. New York: John Wiley and Sons. Inc.

Prakash, S. and Sharma, H. (1990). Pile Foundations in Engineering Practice. New York: John Wiley & Sons, Inc.

Randolph, M. F. (1994). Design Methods for Piled Groups and Piled Rafts. *In* Proceeding of the 13th ICSMFE, New Delhi, India, pp. 61-82.

Richards, T. D. and Rothbauer, M. J. (2004). Lateral Loads on Pin Piles (Micropiles). *In* Proceedings of the GeoSupport Conference: Drilled Shafts, Micropiling, Deep Mixing, Remedial Methods, and Specialty Foundation Systems, Orlando Florida, United States: American Society of Civil Engineers, pp. 158-174.

Rose, A. V., Taylor, R. N. and El Naggar, M. (2013). Numerical Modelling of Perimeter Pile Groups in Clay. Canadian Geotechnical Journal, **50**(3): 250-258.

Shahrour, I. and Ata, N. (2002). Analysis of The Consolidation of Laterally Loaded Micropiles. Ground Improvement, **6**(1): 39-46.

Teerawut, J. (2002). Effect of Diameter on The Behaviour of Laterally Loaded Piles in Weakly Cemented Sand. Ph.D. Dissertation, University of California, San Diego.

Terzaghi, K. (1942). Discussions on the Progress Report of the Committee on the Bearing Value of Pile Foundations. Proceedings of the American Society of Civil Engineers, **68**(2): 311-323.

Terzaghi, K., Peck, R. and Gholamreza, M. (1996). Soil Mechanics in Engineering Practice. New York: Wiley-Interscience.

Wood, D. M. (2004). Geotechnical Modelling (Applied Geotechnics). 1 ed. London and New York: Spon Press.

CHAPTER 6: MICROPILED RAFTS IN SAND: A FINITE ELEMENT PARAMETRIC STUDY

6.1. INTRODUCTION

6.1.1. Background

A Micropile is a small diameter "cast-in-place" pile, which is constructed by drilling a hole in the ground and filling it with cement grout and a steel bar. In current practice, the diameter of a micropile is typically less than 300 mm. A micropile transfers its load primarily through skin friction to the soil in the bonded area between the grout and the soil. The micropile construction methods have improved considerably and new construction techniques have been developed. The advancements in drilling equipment have resulted in the ability to drill through almost any ground condition to install micropiles at any angle with minimum noise, vibration and disturbance. In addition, the relatively small size of the equipment has allowed the underpinning of existing foundations even in restricted access situations (Bruce et al., 1995).

Different types of micropiles are used to provide the load carrying capacity for new or existing foundation systems. The Federal Highway Administration (FHWA, 2005) classifies the micropiles as follows. Type A: is constructed by placing the grout solely by gravity action. Type B: neat cement grout is placed into the micropile shaft by applying injection pressure, normally at about 0.5 to 1 MPa. Type C: is constructed in two steps: (1) grout is placed under gravity head, and (2) before the cement grout is hardened (about 15 to 25 minutes), a sleeved grout pipe is used to inject similar grout at a pressure of a minimum 1 MPa without using packers at the bond zone. Type D: is similar to type C,

but may use a packer at desirable locations inside the sleeved pipe in order to increase the friction capacity of the bond.

The basic concept of micropiled raft (MPR) is similar to the concept of piled raft, which is a composite structure with three components: subsoil, raft and piles. These components interact through a complex soil-structure interaction scheme, including pile-soil interaction, pile-soil-pile interaction, raft-soil interaction, and piles-raft interaction. The piled raft foundation system offers some advantages over the pile group design in terms of serviceability and efficient utilization of materials. For a piled raft, the piles will provide sufficient stiffness to control the total and differential settlements at the serviceability load while the raft will provide additional capacity at the ultimate load. Knowledge and experienced gained from investigating piled rafts may be helpful when considering micropiled rafts, therefore, some of studies are reported herein.

6.1.2. Literature Review

6.1.2.1. Micropile studies

Numerous studies have been conducted to evaluate the performance of single micropiles and micropile groups in sand under various types of loading. Different testing techniques have been employed such as full-scale load tests, 1g physical modeling, and geotechnical centrifuge modeling. Jeon and Kulhawy (2001) examined the results of 21 full-scale field tests on different types of micropiles (Type B and Type C or D) with diameters that varied between 0.15 m and 0.19 m and shaft depths that varied between 9 m and 30 m. Eight micropiles were installed in cohesive soils and 13 micropiles were installed in cohesionless soils with a wide range of soil parameters. The analysis of the test results indicated that the load-carrying capacity of the micropile is significantly

different than the drilled shaft due to how the pressure grouting affects the state of stress in the soil. Moreover, the micropile capacity can be higher than larger diameter drilled shafts for shaft depth-to-diameter ratios that are less than 100. This increase is in the order of 1.5 to 2.5 for micropiles installed in sand. Meanwhile, Tsukada et al. (2006) evaluated the improvement in the bearing capacity of spread footings reinforced with micropiles through load testing small models that represented the footing and the micropiles in sand with different densities. They reported that the load capacity of the spread footing reinforced with micropiles was double the summation of the individual load capacity of the surface footing and the capacity of the micropiles. They attributed the significant increase in bearing capacity to the dilation effect and

It may be difficult to load test a full-scale micropile group, especially with a large number of micropiles due to the limitation in equipment that can apply the load to reach the group capacity and the associated high cost. Alternatively, geotechnical centrifuge testing may be used for that purpose. Juran et al. (2001) performed different load tests on a number of single and micropile group configurations installed in sand in a centrifuge study. They evaluated the influence of micropile inclination, spacing-to-diameter ratio and group configuration on both the load transfer mechanism and the load carrying capacity of the micropile foundation systems. The number of micropiles varied between 1 and 18 with spacing-to-diameter ratio varying between 3 and 5. The micropile groups were subjected to dynamic excitation with acceleration amplitudes that varied between 0.03 g and 0.5 g. The results indicated a positive group effect was achieved for spacing-to-pile diameter ratios (S/D_{mp}) 3 and 5 compared to a single pile. For the inclined micropile group, the bending moment was reduced and the axial stress increased

compared to vertical groups, indicating improved seismic resistance for the network configuration. In addition, several micropile load tests were conducted in order to evaluate the lateral performance of micropiles (e.g. Richards and Rothbauer (2004), Long et al. (2004), Shahrour and Ata (2002), Teerawut (2002), and Rose et al. (2013)).

The finite element analysis (FEA) is a powerful tool to conduct comprehensive parametric studies of piled and micropiled rafts. Employing 2-D FEA, Babu et al. (2004) investigated enhancing the bearing capacity of an existing rectangular shallow foundation on sand using micropiles. The soil was modeled using linear elastic-perfectly plastic constitutive model and the micropile with Mohr-Coulomb failure criterion. The base boundary of the model was set at distance equal to 3.5 times the micropile length from the top of the model and the side boundaries were placed at 140 times the micropile diameter. They found that using micropiles at spaced 2 times its diameter along the outer perimeter of an existing foundation increased its bearing capacity by about 145%. Shahrour et al. (2001) conducted a 3D finite element analysis on a single micropile and micropile groups in order to evaluate their seismic performance considering the number of micropiles and their spacing. They used 20-node solid elements, and placed the base of the model at depth equal to 1.5 times the micropiles length and the lateral boundaries at 6 times the micropile length from the group center. They observed a positive group effect, especially at small spacing $S/D_{mp} = 3$ compared to $S/D_{mp} = 7$. Sadek and Shahrour (2004) investigated the behaviour of inclined micropiles subjected to dynamic loading using 3D FEA. The soil was modeled as linear elastic material employing 8-node elements. The micropiles were modeled using 3D-beam elements. The lateral boundaries

were placed at distance of 240 micropile diameter (D_{mp} = 0.25 m) from the central axis of micropile group. The spacing-to-diameter ratio (S/D_{mp}) for the micropile group was 5.

6.1.2.2. Piled raft studies

The raft in a piled raft foundation transmits approximately 30% to 50% of the applied load to the soil depending on the spacing between the piles (Clancy and Randolph, 1993). Numerous studies have been conducted in order to evaluate the piled raft performance such as Poulos and Davis (1974); Clancy and Randolph (1993 and 1996); Randolph (1994); and Poulos (2001). As a result of these studies, an analytical approach widely known as Poulos-Davis-Randolph (PDR) was developed in order to evaluate the axial stiffness of a piled raft for preliminary design purposes.

Reviewing the behaviour of existing full scale piled raft foundations under the complex conditions of subsoil and soil-structure interaction, through well documented case histories, provides a deeper understanding of the performance of the piled raft foundation. Mandolini et al. (2005) reviewed 22 well documented case histories of full scale piled raft foundation supporting different types of structures. The foundations were instrumented to measure the average settlement, differential settlement, contact pressure and load sharing. The review highlighted the influence of different factors on the overall performance of piled rafts, i.e.: (i) as the number of piles increases, it has a positive impact on the piled raft to a certain extent, beyond which no further improvement in performance can be gained; (ii) for small and medium size rafts, the piles length should be equal to the raft width to control the average settlement; (iii) placing long piles at suitable locations is the optimum method to control the differential settlement; and (iv)

the thickness of the raft plays a significant role in distributing bending moment and controlling differential settlement.

Yamashita et al. (2011) reviewed five recent case histories of piled raft foundation constructed in Japan between 2005 and 2009 for buildings with heights varying from 19 to 162 m. Four cases involved piled rafts constructed in sand soil and one case for piled raft constructed in clay soil. The piled rafts were instrumented to measure the raft settlement and contact pressure, the pore water pressure and the axial loads of the piles. They compared the observed response with the numerical predictions and concluded that using numerical analysis for designing the piled rafts can yield good predictions of the maximum settlement and load sharing between piles and raft. They also observed that the percentage of load carried by the piles, α'_p, was affected by the piles spacing ratio (S/D_p); as S/D_p increased from 4 to 6, the load carried by the piles decreased significantly. However, α'_p decreased gradually for $S/D_p > 6$.

Several studies have been conducted to examine the effects of a number of design aspects on the overall performance of piled raft utilizing geotechnical centrifuge and 1g physical modeling. Fioravante and Giretti (2010) and Fioravante (2011) investigated the effect of the direct contact between the piles and the raft in the piled raft foundation compared to non-contact piled raft foundation by placing an interposed granular layer between the raft and the piles. They performed 21 centrifuge tests of piled rafts installed in sand soil with final relative density of 70% (under centrifugal acceleration of 65g). They reported that the stress induced by the raft enhanced the shaft capacity of the piles and the piles reduced the settlement in connected raft compared to the non-contact piled raft. For the non-contact piled raft, they reported that piles were not fully utilized and the

load was transmitted mainly by the raft; however, the piles increased the stiffness of the soil. Fioravante et al. (2008) performed geotechnical centrifuge tests on rigid circular raft foundation constructed in loose sand to investigate the effect of the number and location of the piles on settlement reduction. Two types pile installation techniques were used: (i) quasi displacement (QD) similar to driven pile; and (ii) quasi non-displacement (QND) similar to bored pile. The tests results revealed that the effectiveness of the piles to reduce the raft settlement. They reported that the axial stiffness of QD piled raft was higher than the axial stiffness of QND piled raft and fewer QD piles were required to achieve the same performance compared to QND piles at the same load applied on the raft.

Matsumoto et al. (2010) carried out a series of laboratory scaled model tests of piled raft pile group and isolated raft in dray dense sand with relative density of 80%. They investigated the effect of pile head connectivity on the performance of the foundation subjected to both vertical and horizontal static loading. Four different connections were used: rigid, semi-rigid, semi-hinged and hinged. The results demonstrated that the piled raft had larger vertical and horizontal stiffness compared to that of the pile group. The pile head connection had minimal effect on the performance of piled raft and pile group under vertical loading; however, it had an important effect on the rotation of the raft in the case of piled raft, i.e., the rotation increased and the horizontal stiffness reduced as the stiffness of the connection decreased.

The FEA was also used to conduct comprehensive parametric studies of piled rafts foundations in sand. Oh et al. (2008) investigated the effect of raft thickness and piles spacing ratio, S/D_p, on the performance of piled raft resting on sand and subjected to static vertical loading using 2-D FEM. The raft was 8 m x 8m and different thickness

values (0.25 m to 3 m) were considered. 16 piles were used with length, L_p = 16 m. The soil was modeled using linear elastic-perfectly plastic constitutive model and the micropile with Mohr-Coulomb failure criterion. The piles were modeled using beam elements. The bottom boundary of the model was set at distance equal to 2.2 L_p from the top of the model and the lateral boundaries were placed at a distance equal to 2 times the raft width from the edge of the raft. They concluded that the raft thickness has a significant influence on the raft bending moment and differential settlement; however, it has a miner effect on the maximum settlement. Baziar et al. (2009) performed a 1g small model and a 3-D finite difference method (FDM) on piled raft installed in medium dense sand (D_r =45%). The soil was modeled using linear elastic-perfectly plastic constitutive model with Mohr-Coulomb failure criterion. The side boundary was at about 2 B_r away from the edge of the raft and the bottom boundary was placed at 1.5 B_r from the top of the model. It was found that the Mohr-Coulomb failure criteria yielded an excellent agreement between the 1g model results and numerical simulation. In addition, the axial stiffen of piled raft using PDR method was with agreement with the results of the 1g model.

Katzenbach et al. (2005) performed 3D FEA analyses to assess the settlement of high-rise buildings. The piles and raft materials were modeled using the linear elastic model and the soil was modeled using elasto-plastic cap model. The vertical boundaries of the model were placed at distance = 2.2~2.7 B_r from the center of the raft. The horizontal boundary at the bottom of the model was located at depth equal to 2.75 L_p. They confirmed the effectiveness of numerical modeling in design process, especially for assessing the settlement of high-rise buildings.

6.1.3. Objectives and Scope of Work

A micropiled raft offers an efficient foundation system that combines the advantages of micropiles and piled rafts. However, to the knowledge of the author, there have been no studies considering the performance of micropiled rafts or any guidelines for their design. There is a need to thoroughly assess the behaviour of micropiled rafts. Therefore, this study attempts to evaluate the effect of different factors on the MPR axial stiffness, including; differential settlement; load sharing between the MPs and the raft; and the raft bending moment. The factors investigated include: the number of micropiles (MPs), the spacing to micropile diameter (S/D_{mp}), the raft thickness and soil density. This investigation is conducted using a three dimensional finite element model (FEM) calibrated using the experimental results obtained from the geotechnical centrifuge tests of MPRs installed in sand reported in Chapter 4. In addition, the ability of the PDR method to evaluate the axial stiffness of a MPR for the preliminary design stage is examined.

6.1.4. Centrifuge Testing

A brief summary of the centrifuge tests conducted is provided herein. The centrifuge testing program consisted of the following tests: (1) one test on a single micropile; (2) one test on a raft with a thickness equivalent to 0.6 m at prototype scale; and (3) three tests on micropiled rafts with different raft thicknesses (i.e., 0.3 m, 0.45 m and 0.6 m at prototype scale). All tests were performed on dry silica sand soil with a relative density (D_r) of 70% and under a centrifugal acceleration of 50g. The soil model in the strong box was 350 mm thick (i.e., 17.5 m at prototype scale). The prototype diameter of the micropile was 150 mm and its length was 10 m. The models of the rafts and micropiles

were fabricated using PVC. Eqs 6.1 and 6.2 were used for evaluating the geometrical dimensions of the models, i.e.,

$$\frac{E_p A_p}{E_m A_m} = n^2 \tag{6.1}$$

$$\frac{E_p I_p}{E_m I_m} = n^4 \tag{6.2}$$

Where: $E_p A_p$: axial rigidity for the prototype element; $E_m A_m$: axial rigidity for the model element; $E_p I_p$: flexural rigidity for the prototype element; and $E_m I_m$: flexural rigidity for the model element.

Table 6.1 provides details about the dimensions of the model and prototype along with the appropriate scaling laws. In order to model the rough surface of Type B micropiles, which is constructed by injecting the grout under pressure, the surface of the model micropiles was roughened by gluing sand particles to it. This method was used successfully by El Naggar and Sakr (2000), Horikoshi et al. (2002) and Horikoshi et al. (2003a, b). Moreover, to simulate the increase in confinement around the micropiles due to the pressurized grout used in type B micropile construction in the centrifuge testing, the micropile was jacked into the soil after coating the micropile surface with sand, hence increasing the confining pressure of the soil on the pile leading to increased micropile-soil frictional resistance.

Figure 6.1 presents the layout plans for the micropiled raft model and Figure 6.2 shows a schematic for the setup used during the testing program. The load was applied vertically to the raft center using an electrical actuator at a constant displacement rate of 0.1 mm/sec (model scale).
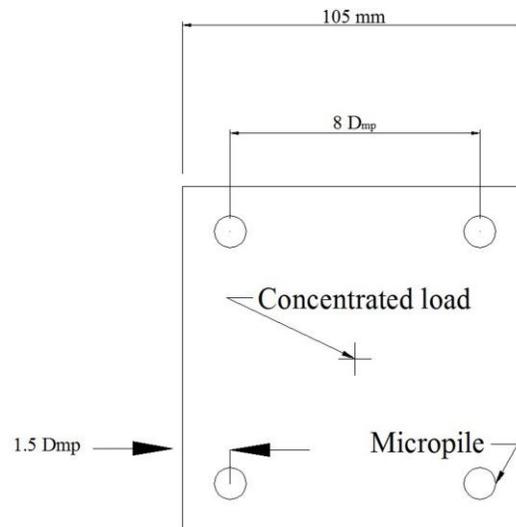
Figure 6.1. Layout for the micropiled raft.

A miniature cone penetrometer was advanced in the soil bed in-flight at 50 g to evaluate the soil strength and stiffness profiles. The results of the cone penetration test (CPT) performed at 50g are presented in Figure 6.3. As can be noted from Figure 6.3, the cone tip resistance, q_c, increased almost linearly with depth. The in-flight CPT results varied by about 25% which is reasonable due to a number of factors such as over- or under-compacting some of the layers, the change of the sand density during loading the test package into the centrifuge, and the error produced by CPT's load cell; a similar variation was reported by Horikoshi et al. (2003a). The CPT measurements could be correlated to the soil modulus of elasticity, e.g. (Tomlinson, 1996):

$$E_s = 2 \sim 4 \, q_c \qquad (6.3)$$

Thus, the CPT measurements demonstrate that the stiffness of the soil increased almost linearly with depth.
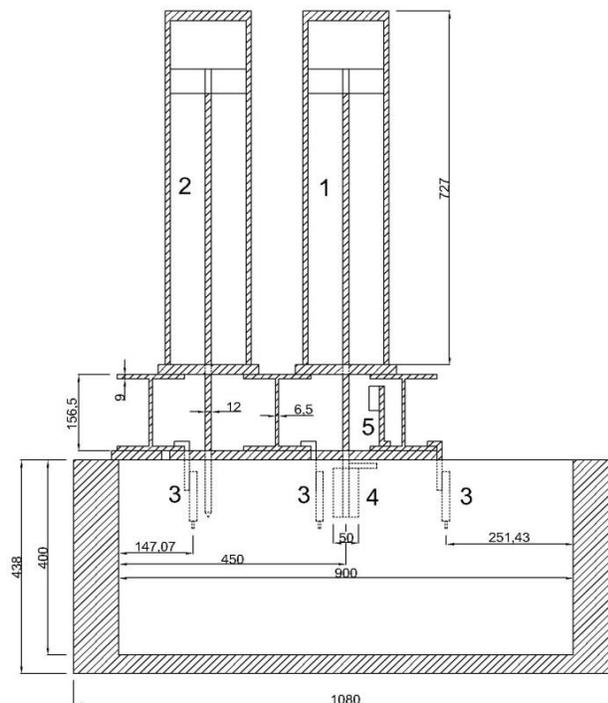
Figure 6.2. Vertical cross-section of centrifuge package including: (1) vertical actuator for applying load; (2) sand cone for CPT; (3) LVDTs; (4) load cell; and (5) laser (all dimensions in mm).

Table 6.1. Scaling laws for centrifuge modeling and models and equivalent prototype dimensions.

Description	Scaling law	Prototype	Model
Micropile Diameter	E_pA_p/n^2	150 mm	9.53 mm
Axial Rigidity (EA)		516737 kN	207 kN
Micropile Length	$1/n$	10 m	200 mm
Raft Width and Length	$1/n$	5.25 m	105 mm
Raft Thickness	E_pI_p/n^4	0.6 m	16.4 mm
Flexural Rigidity		697950 kN. m^2	0.112 kN. m^2
Force (kN)	-	n^2	1
Stress (kPa)	-	1	1
Stiffness (kN/m)	-	n	1
Moment (kN.m)	-	n^3	1
Unit weight (kN/m3)	-	1	1
Displacement (mm)	-	n	1
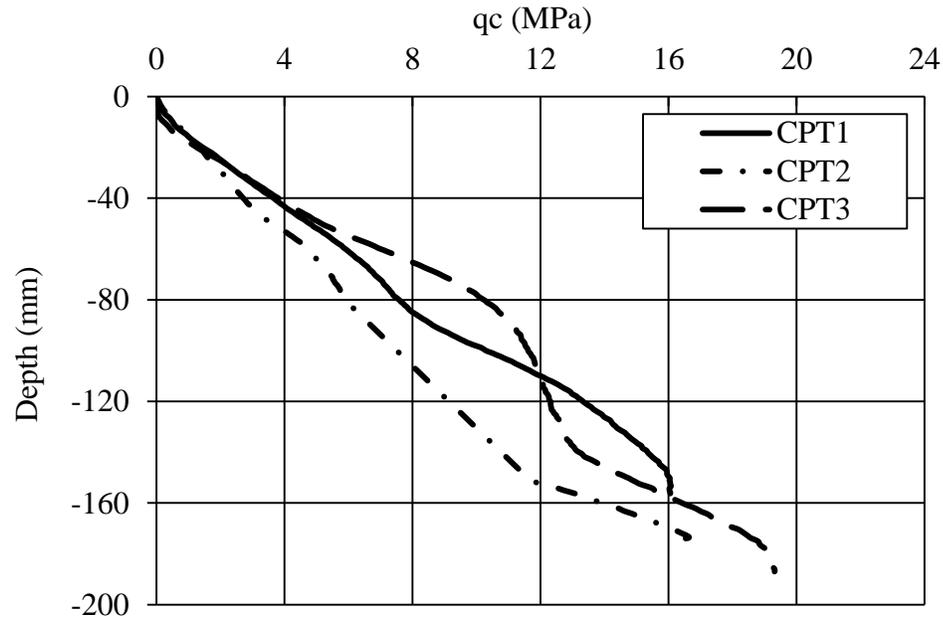
Figure 6.3. In-flight CPT results at model scale.

6.2. FINITE ELEMENT MODELLING (FEM)

This section presents the development and calibration of the FEM that was used to carry out the numerical parametric study for a micropiled raft (MPR) installed in sand. The 3D FEM was established using the computer program PLAXIS 3D (PLAXIS BV, 2013) considering an appropriate size mesh and a number of elements following a sensitivity study. The results of the centrifuge study of the MPR were then used to calibrate the FEM considering the prototype dimensions of the MPR tested in the centrifuge. The calibrated FEM was then employed to perform the parametric study to evaluate the effect of different factors on the performance of the MPR system.

6.2.1. Description of the FEM

A quarter of the MPR foundation system was modeled taking advantage of the symmetry across the x- and y-axes to reduce the computation effort and time. The side boundaries of the model were set at a distance equal to $2.5B_r$ (where B_r is raft width) measured from the edge of the raft, and the depth of the model was approximately two times the micropile length (L_{mp}) as shown in Figure 6.4. The soil and micropiles were modeled using 3D 10-node tetrahedral elements, while the raft was modeled using 6-node triangular plate elements. The total number of elements of the model was 250,000 with an average element size of 110 mm. The large number of small size elements assured high accuracy of the results at locations where non-linear behaviour was anticipated (e.g. raft base, micropile base and micropile circumference). The load was applied as a concentrated load (i.e. a quarter of the full load applied to the full MPR) at the center of the raft.

6.2.2. Model Parameters

The behaviour of the raft and micropiles was simulated considering a linear elastic model considering the mechanical properties of concrete (elastic modulus, E_c, and Poisson's ratio, v_c). The behaviour of the silica sand was simulated using a linear elastic-perfectly plastic constitutive model and the Mohr-Coulomb failure criterion. The constitutive model requires conventional soil parameters including: unit weight (γ), cohesion (c), friction angle (ϕ), dilation angle (ψ) and Poisson's ratio (v). The peak friction angle (ϕ) for silica sand was evaluated as 40° from direct shear tests conducted with different vertical stress values. Table 6.2 summarizes the sand properties. The modulus of elasticity was correlated to the cone tip resistance, q_c, using the relationship

proposed by Tomlinson (1996) (i.e. Eq. 6.3). In order to properly simulate the true behaviour of the sand soil in which the stiffness of the sand depends on the confining stress, PLAXIS 3D offers an advanced function which allows the increases in the modulus of elasticity (E_s) with depth (see Eq. 6.4), i.e.

$$E(z) = E_o + (z_{ref} - z)E_{inc} \quad \text{for } z < z_{ref} \tag{6.4}$$

Where: $E(z)$= modulus of elasticity (kPa); E_o = initial modulus of elasticity (kPa); Z_{ref} = the reference depth (m); z = depth of interest (m); and E_{inc} = the rate of the increase in modulus of elasticity (kPa/m).

Table 6.2. Properties of sand used in the centrifuge tests.

Test	Standard	Result
Maximum unit weight, γ_{max}	ASTM D 4253	16.39 kN/m^3
Minimum unit weight, γ_{min}	ASTM D 4254	12.44 kN/m^3
Angle of internal friction, ϕ	ASTM D 3080	40°
Mean grain size, D_{50}		0.21 mm
Effective grain size, D_{10}	ASTM D 422	0.13 mm
Uniformity coefficient, C_u		1.7

Figure 6.4. 3D FEM used in the calibration and verification of centrifuge tests.

6.2.3. Soil-Structure Interaction (SSI)

In finite element analysis, the interaction between the micropile or the raft and the adjacent soil is simulated using interface elements. In the current analysis, 12-noded (i.e., 6 pairs of nodes) interface elements are used to simulate the interaction between the micropile or the raft and adjacent soil. For each interface element, 6 nodes are connected

to the 6-noded triangular side of a soil element and the other 6 nodes are connected to a plate element simulating the raft or an element representing the micropile. This interface element allows the relative movement between the micropiles (or raft) and the soil (slippage). The interface elements use the Mohr-Coulomb failure criterion; as the shear stress reaches the yield shear strength of the soil, slippage occurs at the interface. The interface element in PlAXIS 3D is modeled by using an interface reduction factor, R_{int}, which represents the strength of the interface element as a percentage of the shear strength of adjacent soil. The value of R_{int} depends on the state of the soil at the soil-structure interface. For example, if the soil is highly disturbed during the construction (bored pile), R_{int} is expected to be small. In the current study, R_{int} was expected to be high since the micropiles in the experimental program were jacked into the sand which caused the soil surrounding the micropiles to densify.

The construction technique of micropiles can affect the lateral earth pressure coefficient (K_s). For Type B micropiles, the pressurized grout induces a high confining pressure to the soil along the micropile shaft, which would densify the surrounding soil and increase the K_s value. The lateral earth pressure coefficient was estimated using an advanced function in PLAXIS 3D, which allows the solid element to expand and as a result the horizontal effective stress, σ'_h increase. Thus, K_s was evaluated as σ'_h / σ'_v ($\sigma'_v=$ geostatic pressure ($\gamma_s h$ Where h is depth from ground surface). As the MPR was installed at 1g, the densification that occurred in the surrounding soil was equal to the diameter of the model micropile ($D_{mp} \approx 10$ mm). Therefore, in the FEM, the micropile was expanded by 10 mm. Similar approach was used by Khan et al. (2008) to evaluate change in K_s due to ground expansion associated with loading tapered piles. It was found that the average

K_s was approximately 1.5 and the influence of the increases of the micropile volume was extended to a distance of up to 5 D_{mp}.

6.2.4. Calibration and Verification of FEM

The results of the MPR centrifuge test with raft thickness = 0.6 m (at prototype scale) were used to calibrate the FEM and the results of the remaining tests were used to verify the FEM. The process of calibration was performed by refining the soil and interface properties in the FEM. This was done by adjusting the values of the interface reduction factor at the micropile-soil interface, and the estimated initial modulus of elasticity and incremental increase of modulus of elasticity with depth (i.e., within the range stipulated in Eq. 6.3). The calibration process demonstrated that using a coefficient of 4 in Eq. 6.3 to determine the initial E_o and a coefficient of 3 to determine the incremental modulus of elasticity yielded good results. The interface reduction factor, R_{int} was found to be 0.95. With these values, a reasonable match with the centrifuge test results was achieved as demonstrated in Figure 6.5a.

The model was verified using the centrifuge results for the MPR with raft thickness of 0.45 m and 0.3 m, the raft alone with a raft thickness of 0.6 m, and a single micropile (MP) (see Figure 6.5b to e). The reduction factor at the micropile-soil interface reflected the high friction of the micropiles' surface and the effect of the installation technique of the micropiles (jacking) in centrifuge testing. All input parameters used in the FEM for both sand and concrete elements are listed in Table 6.3.

Table 6.3. Input parameters used in the FEM

Parameter	Soil	Micropiled-raft
Constitutive Modeling	Mohr-Coulomb	Linear Elastic
Unit Weight (kN/m^3), γ_d	15	24
Angle of internal friction, ϕ	40°	-
Dilation angle, ψ	10°	-
Average Modulus of Elasticity of raft	-	24 GN/m^2
Average Modulus of Elasticity of MP	-	30 GN/m^2
Thickness of the raft	-	0.6 m
Initial Modulus of Elasticity, E_o	8000 kN/m^2	-
Stiffness increases with depth	Yes	No
Incremental Modulus of Elasticity (kN/m^2/m), E_{inc}	6000	-
Poisson's ratio, ν	0.3	0.17
Interface reduction factor, R_{intr}	0.95	-

6.3. PARAMETRIC STUDY

6.3.1. Introduction

The main objective of the parametric study is to evaluate the effect of important MPR parameters on the tolerable bearing pressure and axial stiffness of MPR; maximum settlement; differential settlement; and bending moment of the raft. The parameters considered in the analysis are the number of micropiles, spacing of micropiles, raft thickness and sand density. The study was carried out using the calibrated/verified FEM as described earlier with some modification to allow for the much wider raft. In order to produce results that can be helpful to practicing engineers, two types of loadings were considered. First, a uniform distributed load which is similar to the load of a silo, an oil tank, a large storage area or a commercial one or two storey building. Second, the loads of a multi-storey building with total of 16 columns were calculated and the column loads were applied to the raft.
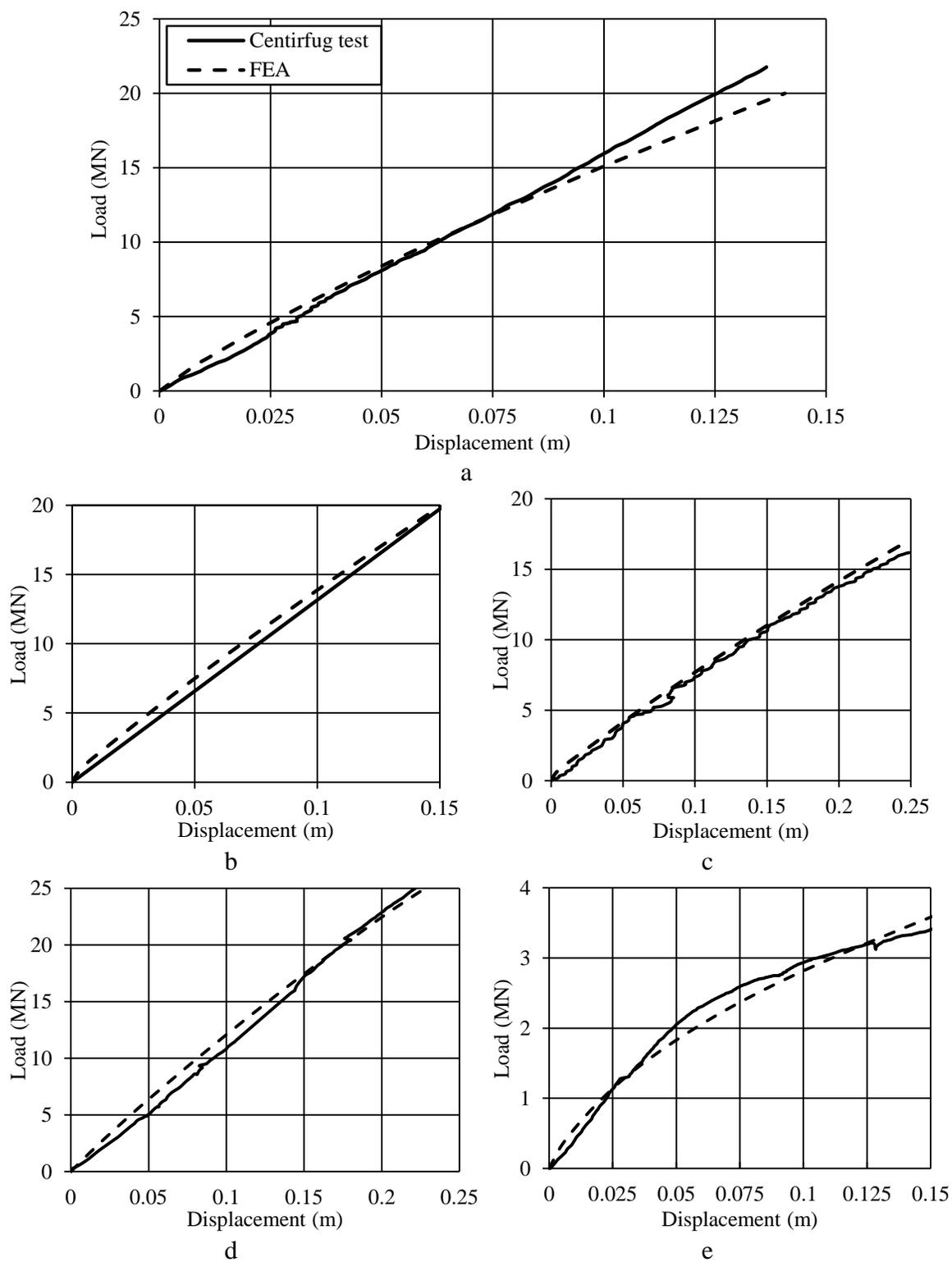
Figure 6.5. 3D FEA calibration and verification results: (a) MPR with 0.6 m raft; (b) MPR with 0.45 m raft; (c) MPR with 0.3 m raft; (d) 0.6 m raft only; and (e) single MP.

The micropiles used throughout this parametric study were 250 mm in diameter and 10 m in length. The raft size was 21 m by 21 m. A total of 78 different cases were considered in the analysis for the two types of loading. Five different micropile spacings, $S = 5 D_{mp}$, $8 D_{mp}$, $10 D_{mp}$, $16 D_{mp}$ and $20 D_{mp}$, with three different values of raft thickness, $t_r = 1.2$ m, 0.6 m and 0.3 m, were investigated. Furthermore, to evaluate the efficiency of micropiles to enhance the tolerable bearing pressure capacity of the single raft, rafts with $t_r = 0.3$ m, 0.6 m and 1.2 m were modeled. These cases were repeated for three different values of sand relative density: dense sand ($D_r = 70\%$), medium dense sand ($D_r = 50\%$) and loose sand ($D_r = 25\%$). However, not all parameters were considered in the case of the concentrated loads.

6.3.1.1. Soil parameters

Three different values of sand relative density were considered in the analysis. The first case was dense sand, $D_r = 70\%$ (i.e., similar to D_r used in the centrifuge tests), and hence sand properties were the same as those evaluated from the centrifuge study. For the other two cases (medium dense sand, $D_r = 50\%$ and loose sand, $D_r = 25\%$), the relationship between sand relative density and cone penetration resistance proposed by Meigh (1987) was used to evaluate the cone penetration resistance with depth, i.e.,

$$D_r = -98 + 66 \log_{10} \frac{q_c}{(\sigma_v')^{0.5}}$$

(6.5)

Where: q_c = cone resistance (ton/m^3); and σ_v' = overburden pressure (ton/m^3)

Eq. 6.5 demonstrated a good agreement with the CPT results obtained from the centrifuge tests. The average variation of cone resistance with depth (q_c/z) was

approximately 2 and from the in-flight CPT, for Dr=70%, Eq. 6.5 predicted $q_c/z =$, i.e., a margin of error = 10%. Applying Eq. 6.5 q_c/z was found to be 0.88, and 0.35, for $D_r =$ 50% and 25%, respectively. Subsequently, Eq. 6.3 was used to assess the variation of elastic modulus of sand, E_s, with depth (using a coefficient of 4 for evaluating E_o and a coefficient of 3 for evaluating the incremental modulus of elasticity as established from the calibration process).

In the parametric study, the raft width, $B_r = 21$ m; therefore, the depth of the FEM was set to be 50 m (see section 6.3.1.3). The in-flight centrifuge CPT results were for 20 m at prototype scale, which is the governing depth for the performance of the MPR with a raft width of 21 m. For the bottom 30 m of the FEM, the sand elastic modulus was evaluated using the equation proposed by Janbu (1963), i.e.,

$$E_s = KP_a \left(\frac{\sigma_3}{P_a}\right)^n \tag{6.6}$$

Where: E_s = soil modulus of elasticity (kPa); K= modulus number; P_a =atmospheric pressure (kPa); n_e= exponent varies between 0.45 and 0.6 for sand (Kulhawy et al., 1962); σ_3 = confining pressure.

Equation 6.6 was verified with the CPT results as shown in Figure 6.6 and was used to evaluate the average modulus of elasticity at a depth of 27 m and 42 m. The increase in E_s follows a power function in which the rate of increase in E_s at a small confining pressure (σ_3) is high and decreases as σ_3 increases. The value of K in Eq. 6.6 depends on D_r and varies between 200 and 1200 (Kulhawy et al., 1962). Table 6.4 summarizes all input parameters used in the FEM for different sand densities. The lateral earth pressure coefficient (K_s) values for the sand with a relative density of 50% and 25% were obtained in a similar fashion as described in section 6.2.3.

Table 6.4. Input parameters used in the FEM for different sand densities.

	Layer	Depth	D_r	γ	E_o	E_{inc}	ϕ	ψ	K_o
		m	%	kN/m³	kPa	kPa/m	o	o	-
Dense Sand	Sand at MP	0-10	70	15	8000	6000	40	10	1.5
	Top Sand	0-20							
	Middle Sand	20-35			132E3	-			0.344
	Lower Sand	35-50			157E3	-			
Medium Dense Sand	Sand at MP	0-10	50	14.14	3520	2660	35	5	1
	Top Sand	0-20							
	Middle Sand	20-35			60E3	-			0.426
	Lower Sand	35-50			72E3	-			
Loose Sand	Sand at MP	0-10	25	13.24	1377.3	1039.4	30	0	0.8
	Top Sand	0-20							
	Middle Sand	20-35			25E3	-			0.5
	Lower Sand	35-50			30E3	-			
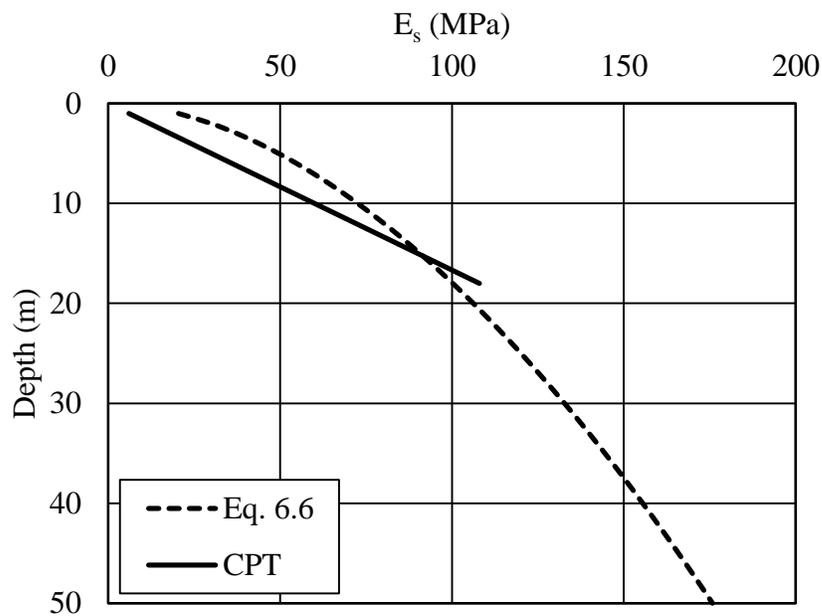
Figure 6.6. Comparison of CPT results and Eq. 6.6.

6.3.1.2. Applied loads

The uniformly distributed load was applied as pressure to the raft surface. The performance-based design method was adopted in this study, in which the performance was evaluated at certain displacement levels of the MPR. Therefore, for each FEA case, the applied pressure was increased until the specified displacement was attained. Details regarding the performance-based design method are provided in section 6.3.2.

For the case of concentrated loads, an 18.6 m by 18.6 m building was considered with spacing between the columns of 6 m. A total of 16 columns were considered to carry the load acting on the 21.0 m by 21.0 m concrete raft foundation. Figure 6.7 shows the layout of the raft and columns. Only one quarter of the raft was modeled in the FEM, which contained a single core column, two edge columns and a single corner column. The columns' loads were estimated according to the tributary area of each column. The load applied to each floor included dead load, live load and superimposed dead load. Load factors of 1.25 and 1.5 were applied to dead and live loads according to the National Building Code of Canada (2010). Similar to the uniformly distributed case, the concentrated load was increased (i.e., increasing number of floors floors) until the specified displacement was reached.
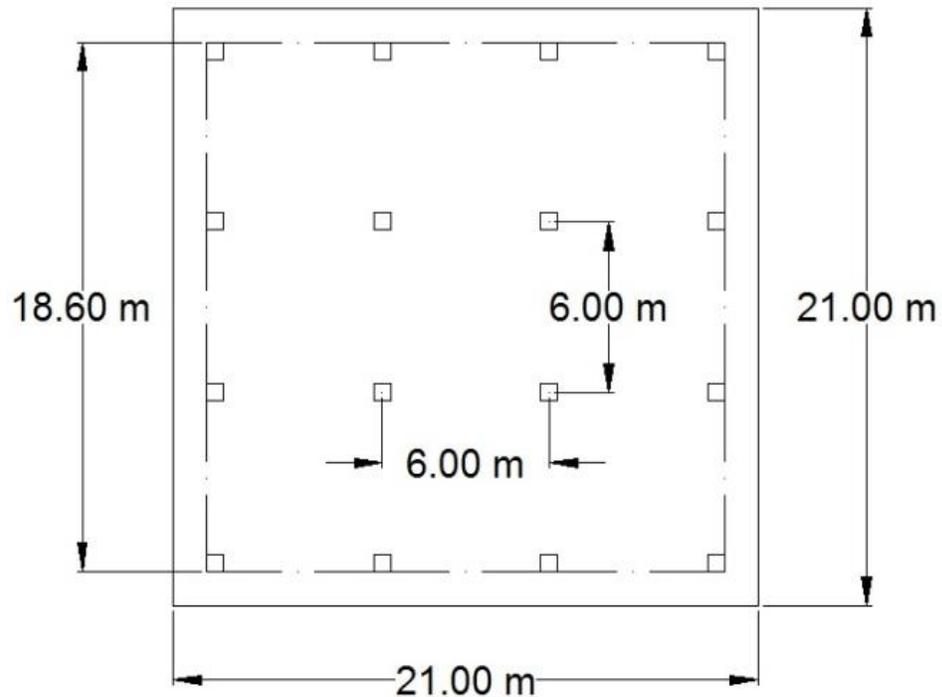
Figure 6.7. Layout of columns on top of the raft.

6.3.1.3. FEM sensitivity analysis

The purpose of this analysis is to attain the optimum size of the FEM as well as the number of elements. The size of the model and the location of the boundaries of the model were assessed by performing a number of analyses considering different depths (20 m, 30 m, 40 m, and 50 m) and different widths (25 m, 35 m, 40 m, and 50 m). In addition, a number of analyses were performed using three different total number of elements (170326, 318224, and 623045). Figure 6.8 shows the results for the different parameters considered in respect to the percentage change in maximum settlement (δ), differential settlement (δ_d) and the raft's maximum bending moment (M_{max}). It was found that the optimum model width, model depth and number of elements were 35 m, 50 m and 318224 elements, respectively.

6.3.2. Tolerable Bearing Pressure of MPRs

The performance-based design method is adopted for the design of many high-rise buildings. In this method, a tolerable movement that will cause a minor functionality or maintenance issue for the building under working loads is identified (service limit). By knowing the tolerable settlement, the foundation system should be designed to sustain the working loads within the tolerable movement (Roberts, 2011). Since the ultimate capacity of a foundation system is normally reached at a high level of movement, adopting the design criteria will ensure the functionality of the building within the tolerable settlement along with satisfying the differential settlement criteria (see section 6.3.5). The advantage of this method over the strength limit state is eliminating the need to identify the ultimate capacity of the foundation. For example, there is a possible range of ultimate capacities for a pile foundation which depends on the failure criteria adopted (piled load test) or the design equations.

By reviewing a number of case histories published in the literature for piled raft foundations, the maximum overall settlement of buildings was found to be between 60 mm and 100 mm with the maximum settlement reported as 150 mm (Katzenbach et al., 2000). Therefore, the 75 and 150 mm tolerable settlement criteria were adopted to determine the corresponding load for each MPR with a different number of micropiles evenly distributed across the raft. Table 6.5 summarizes the tolerable bearing pressure, q, values for different MPR systems and different sand densities as well as the average percentage increase in tolerable bearing pressure (PIBP) of the MPR with different micropile spacings compared to that of the raft without micropiles.
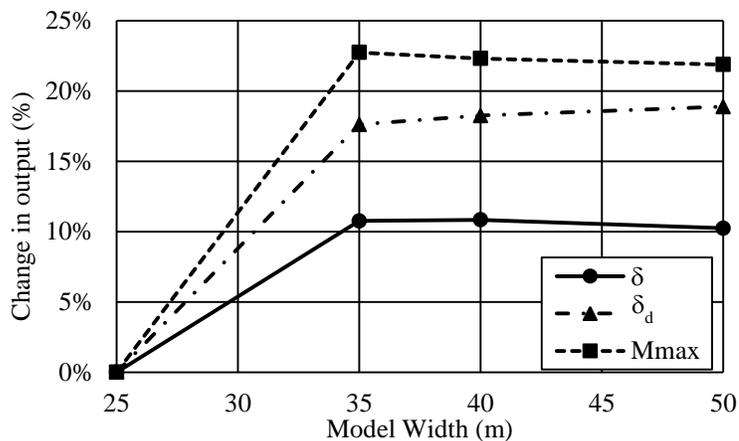
(a)
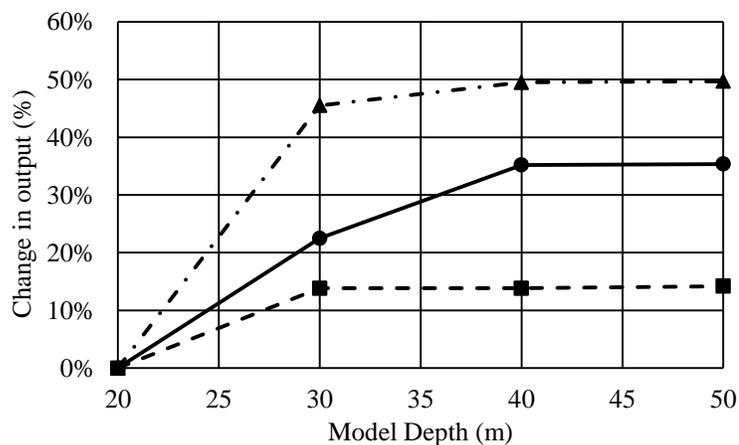
(b)
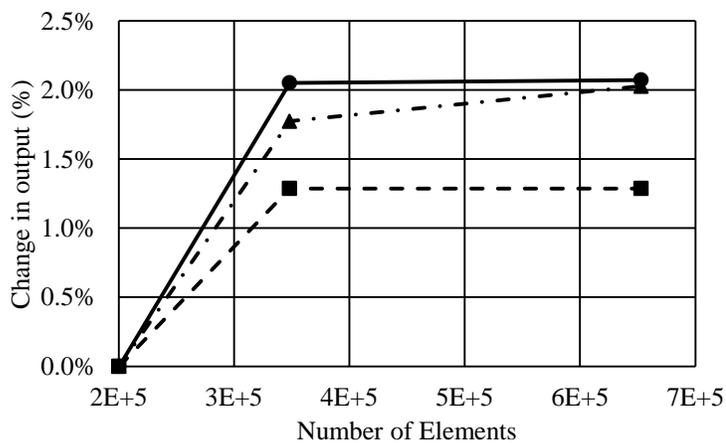
(c)

Figure 6.8. Percentage change in FEA output due to the change in: (a) model width; (b) model depth; and (c) the number of elements (δ= maximum settlement; δ_d= Differential settlement; and M_{max} =maximum bending moment in the raft).

Table 6.5. Tolerable bearing pressure for different MPR systems and different sand densities

S/D$_{mp}$	0.075 m						0.15 m						Avg. PIBP(%) For 0.075m and 0.15 m
	Raft Thickness						Raft Thickness						
	0.3 m		0.6 m		1.2 m		0.3 m		0.6 m		1.2 m		
	q (KPa)	PIBP	q (KPa)	PIBP	q (KPa)	PIBP	q (KPa)	PIBP	q (KPa)	PIBP	q (KPa)	PIBP	
Raft	196	0%	202	0%	214	0%	393	0%	415	0%	431	0%	0%
5	536	174%	542	168%	568	166%	995	153%	1028	148%	1068	148%	159%
8	450	129%	452	123%	484	126%	810	106%	825	99%	882	105%	115%
10	361	84%	370	83%	394	84%	662	69%	682	64%	731	70%	76%
16	265	35%	270	34%	288	35%	511	30%	524	26%	566	31%	32%
20	237	21%	238	18%	253	18%	456	16%	468	13%	500	16%	17%

S/D$_{mp}$	0.075 m						0.15 m						Avg. PIBP(%) For 0.075m and 0.15 m
	Raft Thickness						Raft Thickness						
	0.3 m		0.6 m		1.2 m		0.3 m		0.6 m		1.2 m		
	q (KPa)	PIBP	q (KPa)	PIBP	q (KPa)	PIBP	q (KPa)	PIBP	q (KPa)	PIBP	q (KPa)	PIBP	
Raft	85	0%	92	0%	100	0%	178	0%	185	0%	193	0%	0%
5	256	199%	263	186%	287	188%	474	167%	495	167%	525	172%	180%
8	214	151%	216	135%	234	134%	380	114%	393	112%	438	127%	129%
10	163	91%	171	86%	189	89%	297	68%	322	74%	342	77%	81%
16	119	40%	128	39%	134	34%	230	30%	241	30%	322	67%	40%
20	104	22%	106	15%	112	12%	195	10%	206	11%	223	15%	14%

S/D$_{mp}$	0.075 m						0.15 m						Avg. PIBP(%) For 0.075m and 0.15 m
	Raft Thickness						Raft Thickness						
	0.3 m		0.6 m		1.2 m		0.3 m		0.6 m		1.2 m		
	q (KPa)	PIBP	q (KPa)	PIBP	q (KPa)	PIBP	q (KPa)	PIBP	q (KPa)	PIBP	q (KPa)	PIBP	
Raft	15.25	0%	16.21	0%	19.50	0%	31.00	0%	33.40	0%	36.00	0%	0%
5	45.50	198%	46.77	189%	57.03	192%	89.85	190%	96.19	188%	103.42	187%	191%
8	40.13	163%	42.30	161%	48.99	151%	74.10	139%	78.22	134%	85.72	138%	148%
10	32.16	111%	34.45	113%	36.81	89%	56.13	81%	59.45	78%	63.66	77%	91%
16	22.32	46%	23.44	45%	25.61	31%	43.15	39%	46.41	39%	47.57	32%	39%
20	17.70	16%	18.83	16%	21.38	10%	34.94	13%	36.41	9%	38.86	8%	12%

Figure 6.9 shows the average percentage increases in tolerable bearing pressure (PIBP) of the MPR with different micropile spacings compared to the raft without micropiles. The results in Figure 6.9 and Table 6.5 clearly demonstrate that the MPR concept resulted in a significant increase in capacity compared to the raft case, especially for S/D_{mp} = 5 to 10. As S/D_{mp} decreased, i.e., the number of micropiles increased, the average PIBP increased up to 191% for micropiles distributed at S/D_{mp} = 5. This increase in capacity is attributed to the load transmitted to deeper soil by the micropiles and decreased stress concentration under the raft, which allowed the MPR to sustain a higher load before reaching the tolerable settlement. From Table 6.5, it is noted that the PIBP for soil in a looser condition is higher. This is because the tolerable bearing pressure (BP) for the isolated raft supported on loose sand is relatively small. By introducing the micropiles in the MPR, a portion of the load is transmitted to deeper soil with higher confining pressure and resistance. For the dense sand, the BP of isolated raft is relatively high and introducing the micropiles will increase the BP, but the percentage increase would be lower than the case for loose sand. Equation 6.7 is obtained by curve fitting the results and can be used to assess the PIBP for different D_r.

$$PIBC\ (\%) = -1.33 \ln\left(\frac{S}{D_{mp}}\right) + 4.1 \qquad For\ D_r = 25\%$$

$$PIBC\ (\%) = -1.2 \ln\left(\frac{S}{D_{mp}}\right) + 3.75 \qquad For\ D_r = 50\% \qquad (6.7)$$

$$PIBC\ (\%) = -1.06 \ln\left(\frac{S}{D_{mp}}\right) + 3.29 \qquad For\ D_r = 70\%$$

It is also important to note that by increasing the raft thickness from 0.3 m to 1.2 m, the average increase in tolerable bearing pressure for the same micropile spacing was

only 15%, which is not as significant as increasing the number of micropiles. However, the raft thickness has a major impact in controlling the differential settlement, which will be discussed later.
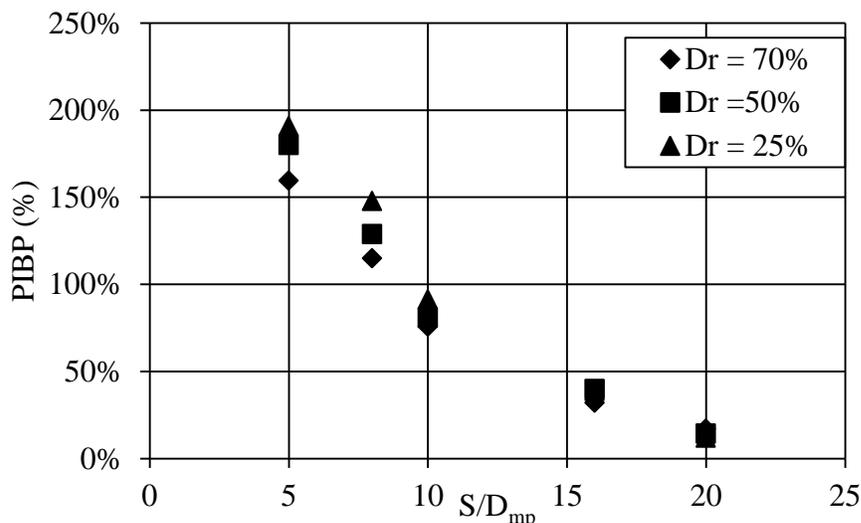
Figure 6.9. PIBP of MPR at different S/D_{mp} and D_r.

6.3.3. Axial Stiffness of the MPRs

This section examines the effect of the number of micropiles, the raft thickness and sand relative density on the axial stiffness of the MPR (k_{mpr}). The value of k_{mpr} is evaluated from the load displacement curve for each case. Figure 6.10 presents k_{mpr} values for the different cases, which shows that an increase in the raft thickness has a minimal effect on the k_{mpr}, especially for the relatively flexible rafts ($t_r = 0.3$ m and 0.6 m) as k_{mpr} increases by only 6% as t_r increased from 0. 3 to 0.6 m. However, as t_r increased to 1.2 m, k_{mpr} increased by approximately 15%. This is because a rigid raft ($t_r = 1.2$ m) tends to transfer the pressure to the soil more evenly compared to the flexible raft ($t_r = 0.3$ m and 0.6 m), which reduces stress concentration in the soil, and consequently increased k_{mpr}.
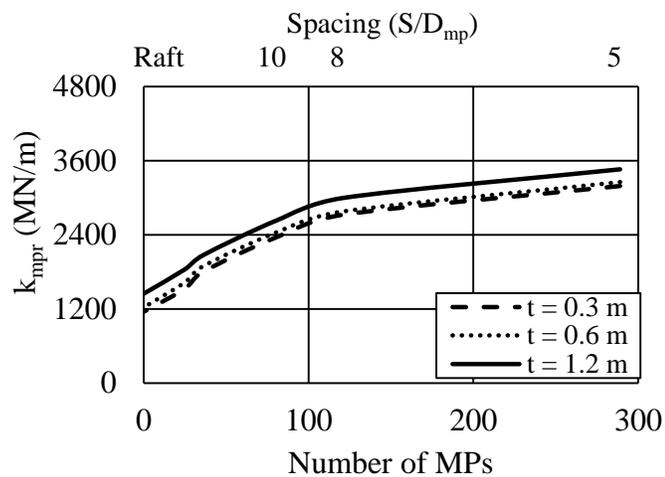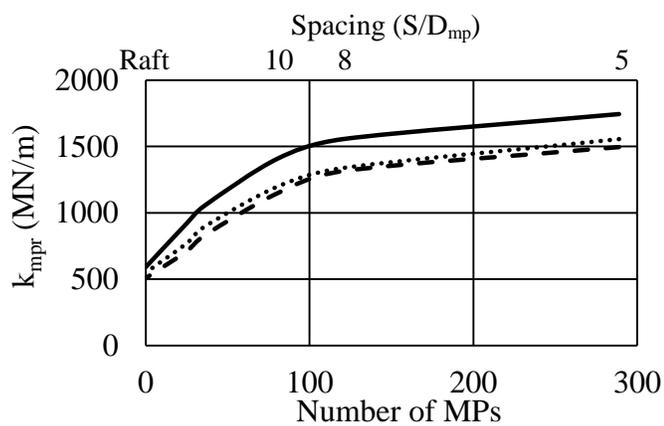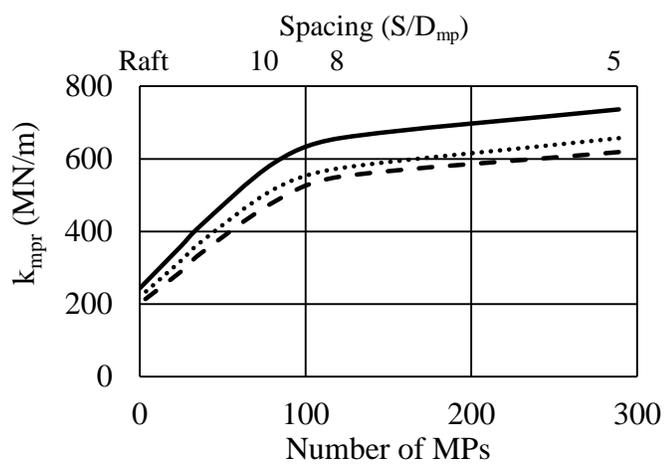
Figure 6.10. k_{mpr} for different numbers of micropiles and raft thickness: (a) D_r= 70%; (b) D_r= 50%; and (c) D_r= 25%.

To examine the effect of the number of micropiles on the MPR axial stiffness, MPR were considered with 25, 36, 81, 121 and 289 uniformly distributed micropiles, which corresponded to $S/D_{mp} = 20, 16, 10, 8$ and 5, respectively. As expected, an increase in the number of micropiles resulted in a higher k_{mpr} value for all cases. This is attributed to the stiffening action of the micropiles and their transfer of some load to deeper soil with higher shear strength; consequently, the displacement decreased and k_{mpr} increased. Interestingly, the rate of increase of k_{mpr} was not constant with decrease in S/D_{mp}. For up to $S/D_{mp} \approx 9$, the average rate of increase between two successive spacing was approximately 30%; however, beyond $S/D_{mp} \approx 9$, the rate of increase was only 14% (see Figure 6.10). This is because reducing the micropile spacing results in overlapping in shear stress within the adjacent soil. Therefore, the number of micropiles should be optimized to achieve most efficient design.

Comparing Figures 6.10 a, b and c, it is noted that as expected, k_{mpr} increases as the relative density of the sand increases, due to the increase in its shear strength As D_r increased from 25% to 50% to 70%, k_{mpr} increased by approximately 142% and 111%, respectively.

6.3.4. Estimating Axial Stiffness of the MPR using the PDR Method

Poulos (2001) introduced the simplified Poulos-Davis-Randolph (PDR) method in order to estimate the axial stiffness of a piled raft foundation. This method combines the analytical methods proposed by Poulos and Davis (1974) and Randolph (1994), which were developed for the analysis of piled rafts. In this method, the axial stiffness of a piled raft is evaluated considering the pile group stiffness and the raft axial stiffness (Randolph, 1994), i.e.,

$$K_{pr} = \frac{K_{PG} + (1 - 2a_{rp})K_r}{1 - \left(a_{rp}^2 \left(\frac{K_r}{K_{PG}}\right)\right)} \qquad (6.8)$$

In Eq. 6.8, K_{PG} is the stiffness of the pile group and is calculated using the following equation:

$$K_{PG} = n_p^{1-e_f} K_p \qquad (6.9)$$

Where n_p is the number of piles within the group, e_f is an exponent and K_p is the stiffness of a single pile. The e_f value varies between 0.3 and 0.5 for frictional piles and up to 0.6 for end-bearing piles (Fleming et al., 2009). This exponent is primarily affected by the pile slenderness ratio (L_p/D_p) and spacing between the piles. The e values used in this study are 0.45, 0.4, 0.38, 0.37 and 0.37 for S/D_{mp} equal to 5, 8, 10, 16 and 20, respectively. The vertical stiffness for a rectangular raft foundation (K_r) is calculated according to Poulos and Davis (1974) i.e.,

$$K_r = I\sqrt{B_r L_r}\left(\frac{2G_{sr}}{(1-\nu_s)}\right) \text{ (kN/m)} \qquad (6.10)$$

Where: K_r = axial stiffness for the raft foundation; L_r and B_r = length and width of the raft foundation; G_{sr} = shear modulus at depth = 2B/3; ν_s = soil Poisson's ratio =0.3; and β_z = influence factor which is a function of the raft aspect ratio = 1.03 for square raft. The stiffness of a single pile, K_p can be calculated from:

$$K_p = G_{sl} * D_p * \frac{\frac{2\eta}{(1-\nu)\xi} + \frac{2\pi\rho}{\zeta} * \frac{\tanh(\mu L)}{\mu L} * \frac{L_p}{D_p}}{1 + \left[\frac{8\eta}{\pi\lambda(1-\nu_p)\xi} * \frac{\tanh(\mu L_p)}{\mu L_p} * \frac{L_p}{D_p}\right]} \qquad (6.11)$$

Where: r_c = average radius of pile cap (i.e., equivalent to an area similar to the raft area / number of piles); r_o = pile radius; D_p = pile diameter; $\zeta = \ln(r_m/r_o)$; $r_m = 2.5\rho(1-v)L_p$; $\xi = E_{sl}/E_{sb}$; $\rho = E_{sav}/E_{sl}$; $\mu L = (2/(\zeta\lambda))^{0.5}*(L/r_o)$; $\lambda = E_p/G_{sl}$; $\eta = r_b/r_o$; L= pile length; E_{sl} = soil Young's modulus at the pile toe level; E_{sb} = soil Young's modulus below pile tip; E_{sav} = average soil Young's modulus along pile shaft; v = soil Poisson's ratio; G_{sl} = soil shear modulus at the pile toe level; and E_p = pile material Young's modulus.

Finally, a_{rp} is the raft pile interaction factor, which can be calculated from:

$$a_{rp} = 1 - \{\ln(r_c/r_o) /\zeta\} \quad\quad\quad (6.12)$$

The suitability of these analyses for the case of a micropiled raft needs to be evaluated considering the relatively small axial stiffness of the micropile compared to that of the larger diameter piles. The PDR method was employed to estimate k_{mpr} for all MPR cases with different S/D_{mp} and D_r values. The results are presented in Table 6.6 demonstrate that the PDR method has the ability to estimate k_{mpr} for a MPR with a rigid raft within 3% error of the calibrated FEA results. However, as the raft thickness decreased the error in estimating k_{mpr} using the PDR method increased to 11% and 15% for raft thicknesses of 0.6 m and 0.3 m, respectively. This is because Eqs. 6.8 and 6.10 do not account for the effect of the raft flexibility, influenced primarily by its thickness, which has a major impact on the overall performance of the micropiled raft. Therefore, an adjustment factor (ω_{PR}) should be applied to the axial stiffness of the MPR in order to accounting for the raft flexibility in the PDR method. Using the adjustment factor (ω_{PR}), Eq. 6.8 can be rewritten to account for the raft flexibility, i.e.,

$$k_{mpr} = \omega_{PR} \frac{K_{PG} + (1 - 2a_{rp})K_r}{1 - \left(a_{rp}^2\left(\frac{K_r}{K_{PG}}\right)\right)} \tag{6.13}$$

The adjustment factor (ω_{PR}) was evaluated by comparing the axial stiffness obtained from the results of the calibrated FEM for the different MPR configurations.

Table 6.6. k_{mpr} (MN/m) obtained from both PDR method and FEA for different cases.

		$D_r = 70\%$				
		Raft Thickness (m)				
		1.2		0.6		0.3	
S/D_{mp}	k_{mpr} (PDR)	k_{mpr} (FEA)	Error	k_{mpr} (FEA)	Error	k_{mpr} (FEA)	Error
5	3298	3459	5%	3253	1%	3189	3%
8	2947	2996	2%	2777	6%	2724	8%
10	2567	2635	3%	2444	5%	2365	8%
16	2022	2068	2%	1889	7%	1799	11%
20	1881	1840	2%	1629	13%	1525	19%
		Avg.	3%	Avg.	6%	Avg.	10%
		$D_r = 50\%$				
		Raft Thickness (m)				
		1.2		0.6		0.3	
S/D_{mp}	k_{mpr} (PDR)	k_{mpr} (FEA)	Error	k_{mpr} (FEA)	Error	k_{mpr} (FEA)	Error
5	1700	1744	3%	1555	9%	1495	12%
8	1493	1556	4%	1339	10%	1315	12%
10	1369	1411	3%	1200	12%	1151	16%
16	1024	1054	3%	896	12%	830	19%
20	870	813	7%	770	11%	710	18%
		Avg.	4%	Avg.	11%	Avg.	15%
		$D_r = 25\%$				
		Raft Thickness (m)				
		1.2		0.6		0.3	
S/D_{mp}	k_{mpr} (PDR)	k_{mpr} (FEA)	Error	k_{mpr} (FEA)	Error	k_{mpr} (FEA)	Error
5	750	736	2%	657	12%	619	18%
8	669	657	2%	575	14%	551	18%
10	578	589	2%	517	11%	481	17%
16	433	413	4%	368	15%	337	22%
20	367	360	2%	320	13%	290	21%
		Avg.	3%	Avg.	14%	Avg.	20%

In order to more appropriately evaluate ω_{PR} considering the effect of raft flexibility, it is correlated with the raft relative flexibility coefficient (K_f) proposed by Horikoshi and

Randolph (1997). They proposed an equation to evaluate the raft flexibility considering an earlier definition of the raft-soil stiffness ratio for a circular raft proposed by Brown (1969). Thus, the flexibility of a rectangular raft is given by (Horikoshi and Randolph, 1997):

$$K_f = 5.57 \, \frac{E_r}{E_s} \frac{(1-v_s^2)}{(1-v_r^2)} \left(\frac{B_r}{L_r}\right)^{\alpha_o} \left(\frac{t_r}{L_r}\right)^3 \tag{6.14}$$

Where: E_r = the raft Young's modulus; v_r = raft Poisson's ratio = 0.2; t_r = raft thickness; and v_s = soil Poisson's ratio =0.3; E_s = average soil elastic modulus at depth = $2B_r/3$; and α = optimal value = 0.5.

Although Eq. 6.14 is for a raft foundation, it is used for the micropiled raft in this study but the micropile spacing is used instead of the raft width, B_r, and length, L_r, i.e.,

$$K_f = 5.57 \, \frac{E_r}{E_s} \frac{(1-v_s^2)}{(1-v_r^2)} \left(\frac{S_B}{S_L}\right)^{\alpha_o} \left(\frac{t_r}{S_L}\right)^3 \tag{6.15}$$

Where S_L and S_B= spacing between micropiles along the length and width of the MPR.

This is justified because the micropile spacing represents the unsupported span of the raft. As the pile spacing decreases, the deflections at locations between the micropiles and at the center of the raft decreases. Thus, it is considered more representative of the micropiled raft width for the purpose of evaluating its flexibility (Alnuaim et al., 2013).

By curve fitting the relationship between ω_{PR} and K_f, the following equation is obtained for different sand relative densities:

$$\omega_{PR} = \kappa \, \ln(K_f) + \mu \tag{6.16}$$

Where κ and μ are functions of sand relative density and can be estimated using the following equations:

$$\kappa = 0.01 \, \ln(D_r) + 0.04$$
$$\mu = -0.14 \, \ln(D_r) + 0.66$$

Table 6.7 summarizes the k_{mpr} (MN/m) obtained from both the revised PDR method and the FEA results for different S/D_{mp} and relative densities. As can be noted from Table 6.7, the errors in evaluating the MPR axial stiffness using Eq. 6.13 and Eq. 6.16 vary between 0% and 9% with an average of 5%.

Table 6.7. k_{mpr} (MN/m) obtained from both the revised PDR method and FEA.

		$D_r = 70\%$								
		Raft Thickness (m)								
		1.2			0.6			0.3		
S/D_{mp}	k_{mpr} (PDR)	k_{mpr} (FEA)	k_{mpr} (Eq. 6.13)	Error	k_{mpr} (FEA)	k_{mpr} (Eq. 6.13)	Error	k_{mpr} (FEA)	k_{mpr} (Eq. 6.13)	Error
5	3298	3459	3443	0%	3253	3271	1%	3189	3100	3%
8	2947	2996	2972	1%	2777	2819	2%	2724	2666	2%
10	2567	2635	2546	3%	2444	2413	1%	2365	2279	4%
16	2022	2068	1934	6%	1889	1829	3%	1799	1724	4%
20	1881	1840	1767	4%	1629	1670	2%	1525	1572	3%
		Average		3%	Average		2%	Average		3%
		$D_r = 50\%$								
		Raft Thickness (m)								
		1.2			0.6			0.3		
S/D_{mp}	k_{mpr} (PDR)	k_{mpr} (FEA)	k_{mpr} (Eq. 6.13)	Error	k_{mpr} (FEA)	k_{mpr} (Eq. 6.13)	Error	k_{mpr} (FEA)	k_{mpr} (Eq. 6.13)	Error
5	1700	1744	1795	3%	1555	1671	7%	1495	1548	3%
8	1493	1556	1503	3%	1339	1394	4%	1315	1286	2%
10	1369	1411	1346	5%	1200	1247	4%	1151	1147	0%
16	1024	1054	971	8%	896	882	2%	830	807	3%
20	870	813	792	3%	770	729	5%	710	665	6%
		Average		4%	Average		4%	Average		3%
		$D_r = 25\%$								
		Raft Thickness (m)								
		1.2			0.6			0.3		
S/D_{mp}	k_{mpr} (PDR)	k_{mpr} (FEA)	k_{mpr} (Eq. 6.13)	Error	k_{mpr} (FEA)	k_{mpr} (Eq. 6.13)	Error	k_{mpr} (FEA)	k_{mpr} (Eq. 7.13)	Error
5	750	736	764	4%	657	709	8%	619	655	6%
8	669	657	671	2%	575	618	8%	551	565	3%
10	578	589	565	4%	517	519	0%	481	473	2%
16	433	413	399	3%	368	365	1%	337	331	2%
20	367	360	329	9%	320	300	6%	290	271	6%
		Average		4%	Average		5%	Average		4%

6.3.5. Differential Settlement

It is important to satisfy the tolerable settlement criteria under the building working load to ensure ideal performance of a MPR to support a building. Also, it is equally important to control the differential settlement in a MPR foundation as an excessive differential settlement can cause serious damage to the superstructure in terms of serviceability and safety. A widely adopted criterion for limiting the differential settlement is angular distortion (θ), which is defined as the difference in the settlement of two points or adjacent columns divided by the distance between the points or columns. The value of θ typically ranges between 1/300 and 1/500 to ensure safe design (Tan and Chow, 2004). This section examines the effect of the micropile spacing, the raft thickness and soil density on the maximum angular distortion of the MPR under uniform loading and concentrated loading conditions. Two methods were adopted to perform this analysis. First, the differential settlement of the MPR with different S/D_{mp} was compared to the differential settlement of an isolated raft (with same raft thickness) at loads corresponding to isolated raft maximum settlements of 75 mm and 150 mm. Second, angular distortion for all cases at $\delta = 75$ mm and 150 mm.

Table 6.8 and Table 6.9 present the angular distortion for different MPR cases normalized by angular distortion for the raft alone case (θ/θ_r) under similar uniform or concentrated loading for each case. As the differential settlement depended on different factors such as the soil stiffness and the location of the loads, there was not an obvious trend; however, for a MPR with spacing less than 10 D_{mp} and subjected to concentrated loads, there was approximately 20% to 40% reduction in differential settlement for different soil density (see Table 6.8). For $S/D_{mp} > 10$, a negative effect of micropiles on

differential settlement was observed only for dense sand (Dr = 70%) as θ increased by about 17%. This is because the micropiles close to the edge column reduced the settlement more than the micropiles at the center column, which carries higher loads. A similar observation was made by Poulos (2001). This is a disadvantage of distributing the micropiles uniformly. The optimum way is to distribute the micropiles uniformly to achieve the desired tolerable bearing pressure and strategically locate a number of micropiles with small spacing where high loads are located; for example, in the case presented in this chapter, more micropiles should have been located at the center columns to reduce the differential settlement the center and edge columns.

Table 6.8. θ/θ_r for different MPR cases under concentrated loading.

D_r=70%								
t_r (m)	1.2				0.6			
q (kPa)	222		414		175		375	
S/D_{mp}	θ	θ/θ_r	θ	θ/θ_r	θ	θ/θ_r	θ	θ/θ_r
Raft	0.00112	1	0.00188	1	0.00216	1	0.00422	1
5	0.00088	0.79	0.00161	0.86	0.00081	0.37	0.00171	0.40
10	0.0011	0.98	0.00197	1.05	0.00124	0.57	0.00303	0.72
16	0.00139	1.24	0.00251	1.34	0.00237	1.10	0.00482	1.14
D_r=50%								
t_r (m)	1.2				0.6			
q (kPa)	111		206		84		175	
S/D_{mp}	θ	θ/θ_r	θ	θ/θ_r	θ	θ/θ_r	θ	θ/θ_r
Raft	0.00132	1	0.00232	1	0.00377	1	0.00781	1
5	0.00076	0.58	0.00133	0.57	0.00083	0.22	0.00174	0.22
10	0.00079	0.60	0.00131	0.56	0.00118	0.31	0.00298	0.38
16	0.00091	0.69	0.00151	0.65	0.0023	0.61	0.00455	0.58
D_r=25%								
t_r (m)	1.2				0.6			
q (kPa)	50		86		41		70	
S/D_{mp}	θ	θ/θ_r	θ	θ/θ_r	θ	θ/θ_r	θ	θ/θ_r
Raft	0.00059	1	0.00098	1	0.0029	1	0.00491	1
5	0.00053	0.91	0.00082	0.84	0.00091	0.31	0.00158	0.32
10	0.00046	0.78	0.00066	0.67	0.00122	0.42	0.00215	0.44
16	0.0004	0.68	0.00065	0.67	0.00218	0.75	0.00345	0.70

For the uniformly distributed loading cases, the angular distortion for dense sand was generally reduced by approximately 5%, 30% and 40% for MPR with spacing less than 10 D_{mp} and t_r = 1.2 m, 0.6 m and 0.3 m, respectively. As D_r reduced, the differential settlement reduced; this is because of the reduction in the stiffness of soil which results in additional settlement at the edges of the raft and decreases the difference in settlement between the edge and the center of the raft. Increasing the raft thickness to 1.2 m for the MPR has a significant impact in terms of differential settlement as θ are 1/800, 1/1600, and 1/3700 for sand with relative densities of 70%, 50% and 25%, respectively, which are significantly less than 1/300. By comparing the θ for the MPR with a raft thickness of 1.2 m and 0.6 m, there is an approximate 50% reduction in angular distortion.

Table 6.9. θ/θ_r for different MPR cases under uniform loading.

D_r=70%												
t_r (m)	1.20				0.60				0.30			
q(kPa)	215		431		202		415		195		392	
S/D_{mp}	θ	θ/θ_r	θ	θ/θ_r	θ	θ/θ_r	θ	θ/θ_r	θ	θ/θ_r	θ	θ/θ_r
Raft	0.0008	1.00	0.0013	1.00	0.0019	1.00	0.0033	1.00	0.0024	1.00	0.0042	1.00
5	0.0007	0.90	0.0012	0.94	0.0009	0.47	0.0019	0.57	0.0009	0.39	0.0019	0.44
8	0.0008	1.00	0.0013	1.00	0.0011	0.60	0.0023	0.69	0.0012	0.50	0.0025	0.58
10	0.0009	1.11	0.0016	1.24	0.0014	0.74	0.0030	0.91	0.0016	0.65	0.0035	0.84
16	0.0012	1.48	0.0021	1.60	0.0023	1.20	0.0044	1.34	0.0026	1.08	0.0054	1.29
20	0.0012	1.51	0.0021	1.65	0.0026	1.38	0.0049	1.46	0.0032	1.30	0.0059	1.40
D_r=50%												
t_r (m)	1.20				0.60				0.30			
q(kPa)	100		193		91		184		84		177	
S/D_{mp}	θ	θ/θ_r	θ	θ/θ_r	θ	θ/θ_r	θ	θ/θ_r	θ	θ/θ_r	θ	θ/θ_r
Raft	0.0004	1.00	0.0005	1.00	0.0014	1.00	0.0022	1.00	0.0021	1.00	0.0037	1.00
5	0.0005	1.32	0.0010	2.02	0.0008	0.57	0.0016	0.74	0.0008	0.39	0.0017	0.48
8	0.0005	1.36	0.0009	1.67	0.0010	0.74	0.0020	0.88	0.0010	0.47	0.0022	0.61
10	0.0005	1.44	0.0009	1.75	0.0012	0.90	0.0026	1.17	0.0014	0.66	0.0034	0.93
16	0.0006	1.63	0.0011	2.10	0.0020	1.46	0.0036	1.63	0.0024	1.13	0.0052	1.42
20	0.0006	1.57	0.0010	2.06	0.0023	1.64	0.0039	1.77	0.0031	1.44	0.0060	1.64
D_r=25%												
t_r (m)	1.20				0.60				0.30			
q(kPa)	39		79		36		75		32		70	
S/D_{mp}	θ	θ/θ_r	θ	θ/θ_r	θ	θ/θ_r	θ	θ/θ_r	θ	θ/θ_r	θ	θ/θ_r
Raft	0.0001	1.00	0.0002	1.00	0.0008	1.00	0.0012	1.00	0.0017	1.00	0.0031	1.00
5	0.0003	2.58	0.0005	3.80	0.0006	0.81	0.0014	1.22	0.0007	0.42	0.0017	0.53
8	0.0003	2.50	0.0005	3.54	0.0007	0.92	0.0016	1.38	0.0009	0.50	0.0020	0.63
10	0.0003	2.39	0.0004	2.56	0.0008	1.07	0.0020	1.73	0.0010	0.61	0.0030	0.95
16	0.0003	2.39	0.0004	2.82	0.0015	1.91	0.0027	2.26	0.0020	1.16	0.0048	1.54
20	0.0003	2.51	0.0004	2.73	0.0016	2.04	0.0027	2.26	0.0031	1.80	0.0059	1.89

Figure 6.11 illustrates the angular distortion (θ) values for all cases under a total settlement, δ = 75 mm and 150 mm. For different MPR with t_r = 1.2 m, θ was significantly lower than the limit of 1/300. This indicates the important role of raft thickness in controlling the differential settlement. The MPR with t_r = 0.6 m performed quite well under moderate loading (corresponding to 75 mm maximum settlement). Furthermore, θ for the MPR with t_r = 0.3 and $S/D_{mp} \leq 10$ was within the limit under moderate loading (corresponding to δ = 75 mm). As δ increased (at higher pressure), θ increased for all cases because the soil at the interface between the micropiles and the soil reached the plastic condition which caused excessive settlement at the center of the raft.

6.3.6. Load Sharing

The percentage of the load transmitted by raft and the micropiles is affected by the raft flexibility, which is influenced primarily by the micropile spacing and the raft thickness as demonstrated by Eq. 6.15. Figure 6.12 presents the percentage of load carried by the raft with different values of micropile spacing, raft thickness and sand density. The effect of S/D_{mp} is prominent because as the spacing increased, the MPR became more flexible and as a result the load carried by the raft increased by up to 90% for micropile spacing of $20D_{mp}$. Reducing the raft thickness had a minor effect on the load carried by the raft. As t_r decreases from 1.2 m to 0.3 m, the load carried by the raft increased by only 4%.
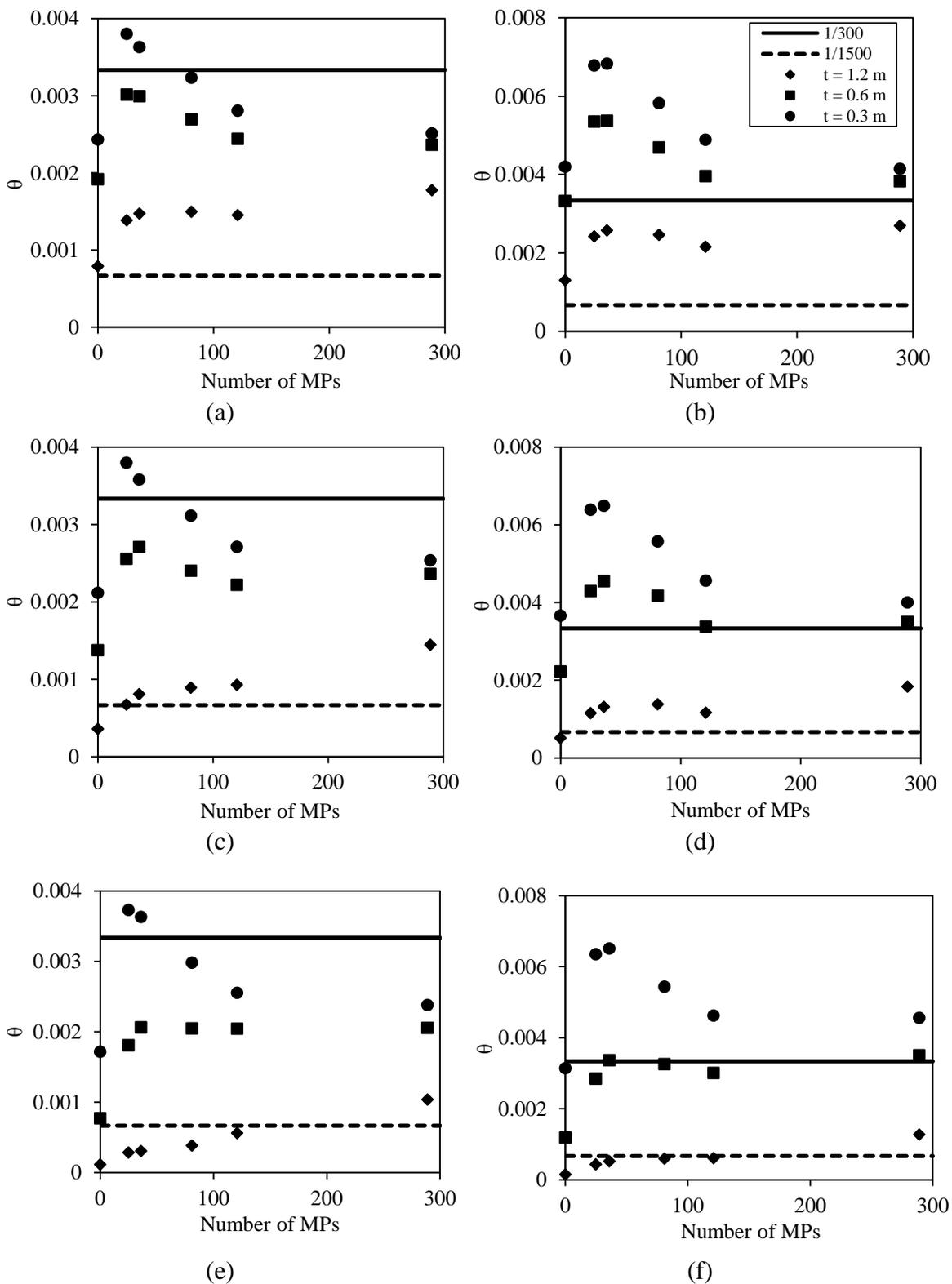
Figure 6.11 θ for: (a) D_r=70% and δ=75 mm; (b) D_r=70% and δ=150 mm; (c) D_r=50% and S=75 mm; (d) D_r=50% and δ=150 mm; (e) D_r=25% and δ=75 mm; and (f) D_r=25% and δ=150 mm.
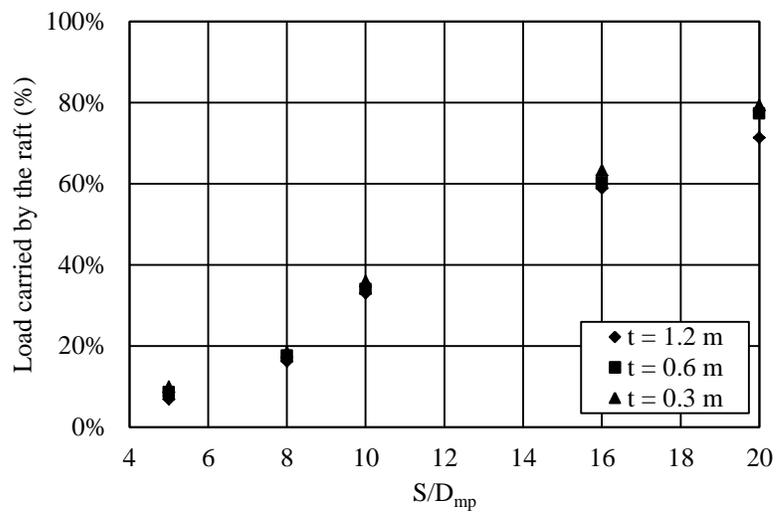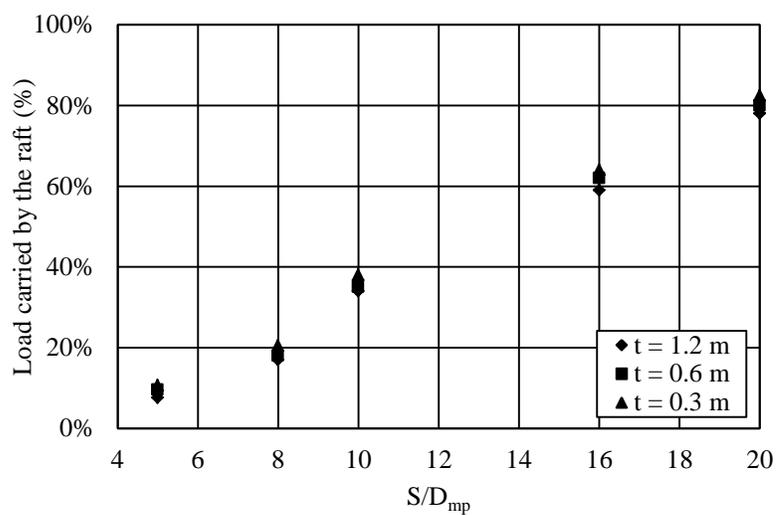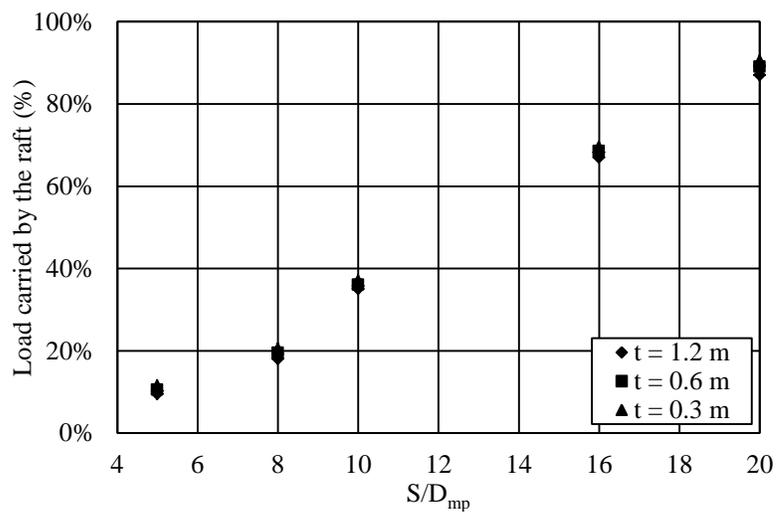
Figure 6.12. Load carried by the raft for: (a) $D_r = 70\%$; (b) $D_r = 50$; and (c) $D_r = 25\%$.

The sand relative density had some moderate impact on the load carried by the raft, especially for high S/D_{mp} (16 and 20). As D_r decreased from 70% to 50% and then to 25%, the load carried by the raft increased by 5% and 13%, respectively. This load increase is attributed to yielding of the lower strength and stiffness of the loose soil at the micropile interface, which resulted in more load transmitted through the raft.

6.3.7. Bending Moment

Evaluating the bending moment for the raft component of the MPR system is essential for the design of raft reinforcement. Therefore, the bending moment for different MPR configurations is evaluated for both uniform and concentrated column loads. It was found that, in general, the maximum bending moment occurred at the central area of the raft for the uniform loading case, while for the concentrated loading case, it occurred beneath the core columns.

Table 6.10 presents the bending moment (M_u) that was calculated for applied uniform pressure, q, that resulted in maximum settlement, $\delta = 0.075$ m and 0.15 m. The normalized moments (M_u/Q) and (M_{cl}/Q), where Q is the total applied load, are also presented in Table 6.10 and Table 6.11. For the case of uniform loading, $Q = qB_rL_r$. The normalized moment is deemed to be more representative of the MPR performance as the loads required to achieve specified settlement varied between different MPR configurations.

Table 6.10 demonstrates that as the rigidity of the MPR system increased (i.e., smaller S/D_{mp}), the bending moment under uniform loading (M_u) increased; however, M_u/Q decreased indicating better performance. This finding implies that the flexible MPR

would experience higher bending moment if it is subjected to the same load level. For example, at $Q = 220$ MN for an MPR with $t_r = 1.2$ m and $D_r = 70\%$, $M_u = 1.36$ MN.m/m and 1.87 MN.m/m for $S/D_{mp} = 5$ and 20, respectively. For MPR with $t_r = 1.2$ m and 0.6 m, M_u/Q increased by approximately 60% and 200% as D_r decreased from 70% to 25%.

Table 6.10. Bending moment (M_u) for different MPR cases under uniform loading (moment unit is MN.m/m).

	$D_r = 70\%$											
t_r (m)	1.2				0.6				0.3			
δ (m)	0.075		0.15		0.075		0.15		0.075		0.15	
S/D_{mp}	M_u	M_u/Q	M_u	M_u/Q	M_u	M_u/Q	M_u	M_u/Q	M_u	M_u/Q	M_u	M_u/Q
5	1.48	0.006	2.22	0.005	0.3	0.001	0.51	0.001	0.3	0.001	0.52	0.001
8	1.26	0.006	1.85	0.005	0.3	0.002	0.50	0.001	0.3	0.001	0.51	0.001
10	1.37	0.008	2.19	0.007	0.29	0.002	0.49	0.002	0.27	0.002	0.48	0.002
16	1.22	0.01	2.00	0.008	0.28	0.002	0.45	0.002	0.25	0.002	0.41	0.002
20	1.16	0.01	1.87	0.009	0.25	0.003	0.43	0.002	0.22	0.002	0.35	0.002
Raft	0.66	0.007	1.04	0.006	0.17	0.002	0.28	0.002	0.05	0.001	0.07	0.001
	$D_r = 50\%$											
t_r (m)	1.2				0.6				0.3			
δ (m)	0.075		0.15		0.075		0.15		0.075		0.15	
S/D_{mp}	M_u	M_u/Q	M_u	M_u/Q	M_u	M_u/Q	M_u	M_u/Q	M_u	M_u/Q	M_u	M_u/Q
5	1.35	0.01	1.66	0.007	0.29	0.002	0.43	0.002	0.11	0.001	0.2	0.001
8	0.95	0.01	1.21	0.006	0.29	0.003	0.42	0.003	0.1	0.001	0.19	0.001
10	0.96	0.01	1.39	0.009	0.28	0.004	0.41	0.003	0.1	0.001	0.17	0.001
16	0.78	0.01	1.15	0.01	0.26	0.005	0.41	0.004	0.1	0.002	0.16	0.002
20	0.70	0.01	1.03	0.01	0.25	0.006	0.4	0.005	0.1	0.002	0.16	0.002
Raft	0.38	0.001	0.50	0.006	0.14	0.004	0.22	0.003	0.03	0.001	0.04	0.001
	$D_r = 25\%$											
t_r (m)	1.2				0.6				0.3			
δ (m)	0.075		0.15		0.075		0.15		0.075		0.15	
S/D_{mp}	M_u	M_u/Q	M_u	M_u/Q	M_u	M_u/Q	M_u	M_u/Q	M_u	M_u/Q	M_u	M_u/Q
5	1.14	0.02	1.35	0.01	0.25	0.01	0.4	0.004	0.1	0.001	0.15	0.002
8	0.75	0.015	0.82	0.01	0.24	0.01	0.39	0.005	0.08	0.002	0.15	0.002
10	0.61	0.017	0.82	0.01	0.24	0.01	0.39	0.007	0.09	0.003	0.14	0.003
16	0.47	0.02	0.63	0.01	0.24	0.01	0.36	0.008	0.09	0.005	0.14	0.003
20	0.43	0.02	0.54	0.01	0.22	0.01	0.31	0.009	0.09	0.006	0.13	0.004
Raft	0.20	0.01	0.23	0.01	0.11	0.01	0.15	0.005	0.02	0.002	0.04	0.001

Table 6.11 presents the maximum bending moment beneath the core columns (M_{cl}) for different MPR cases. As expected, due to the concentrated loads, the moment was significantly higher than the moment obtained from the uniform loading case. The ratio between the moments under concentrated loads and uniform loads (M_{cl}/M_u) is 3.4 and 7.5

for MPR with t_r = 1.2 m and 0.6 m, respectively. The flexible raft (t_r = 0.6 m) experienced higher bending moment compared to the case of uniformly distributed load. The area of maximum bending moment affected the tributary area around the core column with dimensions approximately 6 times the column dimensions. For the rest of raft area, the bending moment was similar to the uniform loading case. These findings should be used for the reinforcement design.

Table 6.11. Bending moment (M_{cl}) for different MPR cases under concentrated loading (moment unit is MN.m/m).

$D_r = 70\%$							
t_r (m)	1.2				0.6		
δ (m)	0.075		0.15		0.075		0.15	
S/D_{mp}	M_{cl}	M_{cl}/Q	M_{cl}	M_{cl}/Q	M_{cl}	M_{cl}/Q	M_{cl}	M_{cl}/Q
5	5.74	0.024	10.33	0.019	4.20	0.019	7.95	0.019
10	4.66	0.026	7.95	0.025	3.11	0.020	5.85	0.020
16	3.70	0.029	6.61	0.028	2.34	0.021	4.32	0.021
0	2.66	0.027	4.75	0.026	1.64	0.021	3.46	0.021
$D_r = 50\%$							
t_r (m)	1.2				0.6		
δ (m)	0.075		0.15		0.075		0.15	
S/D_{mp}	M_{cl}	M_{cl}/Q	M_{cl}	M_{cl}/Q	M_{cl}	M_{cl}/Q	M_{cl}	M_{cl}/Q
5	3.46	0.029	5.57	0.026	2.19	0.020	4.02	0.020
10	2.57	0.030	4.44	0.028	1.62	0.022	2.98	0.021
16	1.94	0.033	3.34	0.030	1.18	0.024	2.21	0.024
0	1.76	0.036	3.10	0.034	0.95	0.026	1.98	0.026
$D_r = 25\%$							
t_r (m)	1.2				0.6		
δ (m)	0.075		0.15		0.075		0.15	
S/D_{mp}	M_{cl}	M_{cl}/Q	M_{cl}	M_{cl}/Q	M_{cl}	M_{cl}/Q	M_{cl}	M_{cl}/Q
5	1.99	0.037	3.03	0.031	1.07	0.023	2.04	0.023
10	1.32	0.034	2.16	0.032	0.85	0.025	1.57	0.025
16	0.94	0.039	1.47	0.034	0.65	0.030	1.11	0.027
0	0.83	0.039	1.35	0.036	0.58	0.032	0.96	0.031

6.3.8. Micropile Skin Friction

This section examines the effect of soil density and micropile spacing on the skin friction along the micropiles. The skin friction is evaluated from the interface elements along the micropile shaft. Table 6.12 presents the average skin friction along the micropiles for different cases. All results are based on δ = 0.075 m and 0.15 m. At δ = 0.075 m, the micropile shaft capacity was not mobilized fully except for cases with S/D_{mp} = 16 and 20 for D_r = 70% because the axial load was high. However, at δ = 0.15 m, the micropiles ultimate capacity was fully mobilized and the micropile-soil interface reached the plastic condition.

Table 6.12 shows that the average skin friction was 133 kPa, 70 kPa and 42 kPa for sand with D_r = 70%, 50%, and 25%, respectively. The average skin friction for dense and medium sand (D_r =70% and 50%) was near the lower end of the range reported by the Federal Highway Administration (FHWA) (2005) for Type B micropiles. According to FHWA (2005), the ultimate bond strengths for dense sand and medium dense sand is 70-190 kPa and 120-390 kPa, respectively. This is expected as for the actual construction of Type B micropiles, the pressurized grout penetrates through the sand, which improves the grout-ground strength and hence increases the shaft friction. This additional increase in strength was not simulated in the current study. For the very loose sand (D_r =25%), it was not specified in the FHWA (2005); however, the skin friction for the loose sand condition was within the theoretical values (39 kPa) given by (Meyerhof, 1976):

$$f_s = \beta \sigma_z'$$

(6.17)

Where: β = Coefficient is a function of coefficient of lateral earth pressure and the sand angle of internal friction (β = 0.44, 0.75 and 1.2 for ϕ' = 28°, 35° and 37°), and σ'_v = the vertical effective stress at 2/3 of the pile length.

For S/D_{mp} = 5, the skin friction was not fully mobilized because the applied axial load was less than the capacity of the micropiles within the MPR. As the number of micropiles in the MPR decreased (S/D_{mp} > 5), the share of each micropile increased. In addition, as the load increased and the skin friction was fully mobilized, the percentage of the axial load carried by the micropile toe increased, especially for the dense sand case. The total axial load on the pile top (P_{tmp}) was calculated using Eq. 6.18, i.e.

$$P_{tmp} = \sigma_{zt}A_{mp} \qquad (6.18)$$

Where: σ_{zt} = axial stress at top of micropile; and A_{mp} = cross-sectional area of micropile.

The axial force carried by shaft of micropiles was estimated using the skin friction obtained from interface elements along micropile at different segments, i.e.,

$$P_s = \sum_{i=1}^{n} f_{si}C_{mp}h_{si} \qquad (6.19)$$

Where: i = segment number; n_s = total number of segments which is 20; f_{si} = skin friction corresponding for each segment; C_{mp} = circumference of a micropile; and h_{si} = the height of each segment (which was 0.5 m).

Table 6.12. Micropile skin friction for different cases.

δ (m)		0.075			0.15		
D_r =70%							
n	S/D_{mp}	F_s(kPa)	P_s/P_t	P_t (MN)	F_s(kPa)	P_s/P_t	P_t (MN)
289	5	74.71	70%	0.83	112.42	55%	1.58
121	8	104.86	54%	1.54	146.14	48%	2.44
81	10	99.75	51%	1.56	141.53	44%	2.54
36	16	95.10	47%	1.64	128.63	36%	2.62
25	20	92.81	46%	1.73	127.25	36%	2.75
D_r =50%							
289	5	36.74	59%	0.48	50.64	48%	0.84
121	8	58.26	55%	0.83	75.96	47%	1.28
81	10	56.41	53%	0.86	75.14	47%	1.28
36	16	55.45	51%	0.91	76.20	46%	1.31
25	20	55.60	51%	0.92	71.59	44%	1.33
D_r =25%							
289	5	21.34	64%	0.27	29.66	57%	0.41
121	8	33.03	59%	0.45	45.46	57%	0.63
81	10	34.77	56%	0.48	42.61	54%	0.66
36	16	36.43	56%	0.50	44.84	53%	0.67
25	20	36.04	52%	0.52	40.48	46%	0.70

[*] F_s =skin Friction; P_s = axial force carried by shaft of micropile; and
P_t = total applied axial load at the top of micropile.

6.4. CONCLUSIONS

Seventy eight finite element analyses were carried out to investigate the performance of the micropiled rafts installed in sand using a 3D finite element model that was calibrated and verified using centrifuge testing results. The effect of different factors on the MPR's tolerable bearing pressure, axial stiffness, differential settlement, load sharing, bending moment and micropile skin friction were examined. The factors that were considered in the analysis are micropile spacing, raft thickness, sand density and load type. A number of conclusions can be drawn from the numerical program:

1. The tolerable bearing pressure and axial stiffness of MPR increased significantly compared to an isolated raft as the micropile spacing decreased; however, the rate of increase declined for $S/D_{mp} > 9$. For MPR with $S/D_{mp} = 5$, the percentage increase in

tolerable bearing pressure compared to an isolated raft foundation was 160%, 180% and 190% for sand with D_r = 70%, 50% and 25%, respectively.

2. The PDR method has the ability to estimate k_{mpr} for MPR with rigid raft within 3% error of the calibrated FEA results.

3. To use the PDR method for the MPR with flexible raft, an adjustment factor (ω_{PR}) should be used to evaluate the axial stiffness in order to account for raft flexibility. A method is proposed to calculate the adjustment factor.

4. A reduction of 20% to 40% in differential settlement occurs for MPR with spacing less than 10 D_{mp} and subjected to concentrated loads. However, for S/D_{mp} > 10, a negative effect of micropiles on differential settlement was observed for dense sand only (Dr = 70%) as θ increased by about 17%. This was because the micropiles close to the edge column reduce the settlement more than micropiles at the center column.

5. For the uniformly distributed load cases, the effect of micropiles is more prominent for MPR with flexible raft (t_r =0.3 m). The angular distortion decreased by 40% for MPR with spacing less than 10 D_{mp} and t_r = 0.3 m and D_r = 70% compared to a reduction in the differential settlement of 5% and 30% for MPR with t_r = 1.2 m and 0.6 m, respectively.

6. The effect of S/D_{mp} is prominent as the MPR becomes more flexible as spacing increases and as a result the load carried by the raft increases. For example, the raft load increased to 90% for MPR with S/D_{mp} = 20.

7. The raft bending moment under column loads is 3.4 to 7.5 times higher than the raft bending moment under uniform loading for MPR with t_r = 1.2 m and 0.6 m, respectively. The maximum bending moment for the case of concentrated loads

occurs over a tributary area around the core column with dimensions 6 times the column dimensions.

REFERENCES

ASTM Standard D422-63. (2007). Standard Test Method for Particle-Size Analysis of Soils. ASTM International, West Conshohocken, PA.

ASTM Standard D 4253-63. (2007). Standard Test Methods for Maximum Index Density and Unit Weight of Soils Using a Vibratory Table. ASTM International, West Conshohocken, PA.

ASTM Standard D 4253-63. (2006). Standard Test Methods for Minimum Index Density and Unit Weight of Soils and Calculation of Relative Density. ASTM International, West Conshohocken, PA.

ASTM Standard D 3080. (2011). Standard Test Method for Direct Shear Test of Soils Under Consolidated Drained Conditions. ASTM International, West Conshohocken, PA.

Alnuaim, A. M., El Naggar, H. and El Naggar, M. (2013). Performance of Piled-Raft System under Axial Load. *In* Proceedings of the 18th International Conference on Soil Mechanics and Geotechnical Engineering (ICSMGE), Paris, pp. 2663-2666.

Babu, S. G. L., Murthy, S. B. R., Murthy, D. S. and Nataraj, M. S. (2004). Bearing Capacity Improvement Using Micropiles a Case Study. *In* Proceedings of the GeoSupport Conference: Drilled Shafts, Micropiling, Deep Mixing, Remedial Methods, and Specialty Foundation Systems, Orlando Florida, United States: American Society of Civil Engineers, pp. 692-699.

Baziar, M. H., Ghorbani, A. and Katzenbach, R. (2009). Small-Scale Model Test and Three-Dimensional Analysis of Pile-Raft Foundation on Medium-Dense Sand. International Journal of Civil Engineering, **7**(3): 170-175.

Brown, P. T. (1969). Numerical Analyses of Uniformly Loaded Circular Rafts on Deep Elastic Foundations. Géotechnique, **19**(3): 399-404.

Bruce, D. A., DiMillio, A. F. and Juran, I. (1995). Introduction to Micropiles: An International Perspective. Foundation Upgrading and Repair for Infrastructure Improvement, ASCE, Geotechnical Special Publication No. 50, pp.1-26.

Clancy, P. and Randolph, M. F. (1993). An Approximate Analysis Procedure for Piled Raft foundations. International Journal for Numerical and Analytical Methods in Geomechanics, **17**(12):849-869.

Clancy, P. and Randolph, M. F. (1996). Simple Design Tools for Piled Raft Foundations. Géotechnique, **46**(2): 313-328.

El Naggar, M. and Sakr, M. (2000). Evaluation of Axial Performance of Tapered Piles From Centrifuge Tests. Canadian Geotechnical Journal, **37**(6): 1295-1308.

FHWA. (2005). Micropile Design and Construction Guidelines, Implementation Manual. National Highway Institute.

Fioravante, V. and Giretti, D. (2010). Contact Versus Noncontact Piled Raft Foundations. Canadian Geotechnical Journal, **47**(11): 1271-1287.

Fioravante, V. (2011). Load Transfer From a Raft to a Pile with an Interposed Layer. Géotechnique, **61**(2): 121-132.

Fioravante, V., Giretti, D. and Jamiolkowski, M. (2008). Physical Modeling of Raft on Settlement Reducing Piles. *In* Proceedings of From Research to Practice in Geotechnical Engineering, ASCE, pp. 206-229.

Fleming, K., Weltman, A., Randolph, M. and Elson, K. (2009). Piling Engineering (3rd ed.). New York,: Taylor and Francis group .

Han, J. and Ye, S. (2006). A Field Study on the Behaviour of A Foundation Underpinned By Micropiles. Canadian Geotechnical Journal, **43**(1): 30-42.

Horikoshi, K., and Randolph, M. (1997). On The Definition of Raft-Soil Stiffness Ratio for Rectangular Rafts. Géotechnique, **47**(5): 1055-1061.

Horikoshi, K., Matsumoto, T., Hashizume, Y., Watanabe, T. and Fukuyama, H. (2003a). Performance of Piled Raft Foundations Subjected to Static Horizontal Loads. International Journal of Physical Modelling in Geotechnics, **3**(2): 37-50.

Horikoshi, K., Matsumoto, T., Hashizume, Y. and Watanabe, T. (2003b). Performance of Piled Raft Foundations Subjected to Dynamic Loading. International Journal of Physical Modelling in Géotechnique, **3**(2): 51-62.

Horikoshi, K., Watanabe, T., Fukuyama, H. and Matsumoto, T. (2002). Behaviour of Piled Raft Foundations Subjected to Horizontal Loads. *In* Proceeding of the International Conference on Physical Modelling in Geotechnics. St John's, Newfoundland, Canada: Taylor & Francis.

Jaimolkowski, M., Lancellotta, R., Pasqualini, E., Marchetti, S. and Nova, R. (1979). Design Parameters for Soft Clays. General Report. *In* Proceedings of the 7th European Conference on Soil Mechanics and Foundation Engineering. n. 5, pp. 27–57.

Janbu, N. (1963). Soil Compressibility as Determined by Oedometer and Triaxial Tests. *In* Proceedings of 3rd European Conference on Soil Mechanics and Foundation Engineering, Wiesbaden, Vol. 1, pp. 19-25.

Jeon, S. S. and Kulhawy, F. H. (2001). Evaluation of Axial Compression Behaviour of Micropiles. *In* Proceedings of a specialty conference: Foundations and Ground Improvement (GSP 113), Blacksburg, Virginia: ASCE pp. 460-471.

Juran, I., Benslimane, A. and Hanna, S. (2001). Engineering Analysis of Dynamic Behaviour of Micropile Systems. Transportation Research Record: Journal of the Transportation Research Board, **1772**(1): 91-106.

Katzenbach, R., Arslan, U. and Moormann, C. (2000). Piled Raft Foundation Projects in Germany. In J. A. Hemsley (Ed.), Design Applications of Raft Foundation. London: Thomas Telford.

Katzenbach, R., Schmitt, A. and Turek, J. (2005). Assessing Settlement of High-Rise Structures by 3D Simulations. Computer-Aided Civil and Infrastructure Engineering, **20**(3): 221-229.

Khan, M.K., El Naggar, M.H. and Elkasabgy, M. (2008). Compression Testing of Drilled Concrete Tapered Piles in Cohesive-Frictional Soil. Canadian Geotechnical Journal, **45**(3): 377-392.

Kulhawy, F. H., Duncan, J. M. and Seed, H. B. (1962). Finite Element Analysis of Stresses and Movement in Embankments during Construction. University of California, Berkeley, College of Engineering. Under contract with US Army Engineers Waterways Experiment Station, Vicksburg, MI.

Lizzi, F. (1982). The Static Restoration Of Monuments: Basic Criteria-Case Histories, Strengthening of Buildings Damaged by Earthquakes . Genova: Sagep Editrice.

Long, J., Maniaci, M., Menezes, G. and Ball, R. (2004). Results of Lateral Load Tests on Micropiles. *In* Proceedings of sessions of the GeoSupport Conference: Innovation and Cooperation in the Geo-Industry, Orlando, Florida: Geo-Institute of the American Society of Civil Engineers, pp. 122-133.

Mandolini, A., Russo, G. and Viggiani, C. (2005). Pile Foundations: Experimental Investigations, Analysis and Design. *In* Proceedings of the 16th International Conference on Soil Mechanics and Geotechnical Engineering (ICSMGE), Osaka, Japan, Vol. 16, pp. 177-213.

Matsumoto, T., Nemoto, H., Mikami, H., Yaegahi, K., Arai, T. and Kitiyodom, P. (2010). Load Tests of Piled Raft Models with Different Pile Head Connection Conditions and Their Analyses. Soils and Foundations, **50**(1): 63-81.

Meigh, A. C. (1987). Cone Penetration Testing: Methods and Interpretation. Butterworth-Heinemann.

Meyerhof, G. G. (1976). Bearing Capacity and Settlement of Pile Foundations. Journal of the Geotechnical Engineering Division, ACSE, **102**(3): 195-228.

National Building Code of Canada (NBC). (2010). Ottawa: National Research Council Canada (NRC).

Oh, E. Y., Huang, M., Surarak, C., Adamec, R. and Balasurbamaniam, A. S. (2008). Finite Element Modelling for Piled Raft Foundation in Sand. *In* Proceedings of the Eleventh East Asia-Pacific Conference on Structural Engineering and Construction (EASEC-11) "Building a Sustainable Environment", Taipei, Taiwan, Vol. 8.

PLAXIS BV. (2013). PLAXIS 3D 2013 Reference Manual. Delft: PLAXIS BV.

Poulos, H. G. (2001). Piled Raft Foundations: Design and Applications. Géotechnique, **51**(2): 95-113.

Poulos, H. G. and Davis, E. H. (1974). Elastic Solutions for Soil and Rock Mechanics. New York: John Wiley and Sons. Inc.

Randolph, M. F. (1994). Design Methods for Piled Groups and Piled Rafts. Proc. 13th ICSMFE, New Delhi, India, pp. 61-82.

Richards, T. D. and Rothbauer, M. J. (2004). Lateral Loads on Pin Piles (Micropiles). *In* Proceedings of sessions of the GeoSupport Conference: Innovation and Cooperation in the Geo-Industry. Orlando, Florida: Geo-Institute of the American Society of Civil Engineers.

Roberts, L., Fick, D. and Misra, A. (2011). Performance-Based Design of Drilled Shaft Bridge Foundations. Journal of Bridge Engineering, **16**:(Special issue): 749-758.

Rose, A. V., Taylor, R. N. and El Naggar, M. (2013). Numerical Modelling of Perimeter Pile Groups In Clay. Canadian Geotechnical Journal, **50**(3): 250-258.

Sadek, M. and Shahrour, I. (2004). Three-Dimensional Finite Element Analysis of The Seismic Behaviour of Inclined Micropiles. Soil Dynamics and Earthquake Engineering, **24**(6): 473-485.

Shahrour, I. and Ata, N. (2002). Analysis of The Consolidation of Laterally Loaded Micropiles. Ground Improvement, **6**(1): 39-46.

Shahrour, I., Sadek, M. and Ousta, R. (2001). Seismic Behaviour of Micropiles: Used as Foundation Support Elements: Three-Dimensional Finite Element Analysis. Transportation Research Record: Journal of the Transportation Research Board, **1772**(1): 84-90.

Stewart, D. and Randolph, M. (1994). T-Bar Penetration Testing in Soft Clay. ASCE Journal of Geotechnical Engineering, **120**(12): 2230-2235.

Tan, Y. C. and Chow, C. M. (2004). Design of Piled Raft Foundation on Soft Ground. *In* GSM-IEM Forum: The roles of engineering geology and geotechnical engineering in construction works.

Teerawut, J. (2002). Effect of Diameter on the Behaviour of Laterally Loaded Piles in Weakly Cemented Sand. Ph.D. Dissertation, University of California, San Diego.

Tomlinson, M. J. (1996). Foundation Design and Construction. London: Longman Publishing Group.

Tsukada, Y., Miura, K., Tsubokawa, Y., Otani, Y. and You, G.-L. (2006). Mechanism of Bearing Capacity of Spread Footings Reinforced With Micropiles. Soils and Foundations, **46**(3): 367-376.

Wood, D. M. (2004). Geotechnical Modelling (Applied Geotechnics). 1st edition. London and New York: Spon Press.

Yamashita, K. Yamada, T. and Hamada, J. (2011). Investigation of Settlement and Load Sharing on Piled Rafts by Monitoring Full-Scale Structures. Soils and Foundations, **51**(3): 513-532.

CHAPTER 7: MICROPILED RAFTS IN CLAY: FINITE ELEMENT PARAMETRIC STUDY

7.1. INTRODUCTION

7.1.1. Background

Similar to cast-in-place piles, micropiles are constructed by drilling a hole into the ground and filling the hole with cement grout and a reinforcing element. In current practice, micropiles of diameter up to 300 mm are used to provide the load-carrying capacity of new or existing foundation systems (FHWA, 2005). They can be constructed by placing the grout solely under gravity action or by applying injection pressure, which is normally about 0.5 to 1 MPa. A micropile transfers its load through skin friction to the soil in the bonded area between the grout and the soil.

Recent developments in drilling equipment have resulted in the ability to drill through almost any ground condition to install micropiles at any angle with minimum noise, vibration and disturbance. In addition, the relatively small size of the equipment has allowed the underpinning of existing foundations, even in restricted access situations (Bruce et al., 1995). The range of micropiles capacity has increased considerably, and consequently, micropiles are becoming a preferred foundation option in many applications including high rise buildings.

The basic concept of micropiled raft (MPR) is similar to the concept of piled raft, which is a composite structure with three components: subsoil, raft and piles. These components interact through a complex soil-structure interaction scheme, including pile-soil interaction, pile-soil-pile interaction, raft-soil interaction, and piles-raft interaction.

The piled raft foundation system offers some advantages over the pile group design in terms of serviceability and efficient utilization of materials. For a piled raft, the piles will provide sufficient stiffness to control the total and differential settlements at the serviceability load while the raft will provide additional capacity at the ultimate load. Micropiled rafts combine the advantages of micropiles and piled rafts, but there are no guidelines on their performance or design.

7.1.2. Literature Review

7.1.2.1. Micropiles studies

Abd Elaziz and El Naggar (2014a) conducted field load testing to investigate the performance of hollow bar micropiles in cohesive soil. Three axial compression tests and two axial tension tests were performed on single micropiles. It was concluded that the axial capacity of hollow bar micropiles are higher than the values suggested by FHWA Type B micropile. Drbe and El Naggar (2014) evaluated the suitability of FHWA (2005) to design hollow bar micropile in cohesive soil as well as to evaluate the performance of hollow bar micropile with different drilling bit to hollow bar diameter ratios. Eight micropiles were installed using 76 mm hollow bars with total depth of 5.75 m. Six micropiles were constructed using 228 mm drill bit and two were constructed using 178 mm. the micropile were tested in the filed under both axial monotonic and cyclic axial loading. They found that the grout/ground bond strength value suggested by FHWA (2005) for Type B micropiles underestimates the actual bond strength for hollow bar micropiles. They also found that the micropile diameter increased by 10% to 20% over the size of the drill bit.

Han and Ye (2006) performed load testing on a square raft (1.5 m x 1.5 m) supported by four micropiles with diameter, D_{mp} = 150 mm and spaced at 750 mm (i.e. $5D_{mp}$). The results showed that the micropiles carried about 70% to 86% of the additional load that was applied to the raft after it was underpinned by the micropiles. Abd Elaziz and El Naggar (2014 b) conducted full scale load tests on two hollow bar micropiles groups installed in clayey soil. The results suggested that the group capacity can be calculated using group efficiency factor of one. However, these studies did not evaluate the effects of raft flexibility on the interaction between the raft and soil, the load sharing between the raft and the micropiles, and the differential settlement of the system.

It is difficult to carry out full scale testing on a micropile group (MPG) or micropiled aft (MPR), especially with a large number of micropiles due to the limitation in equipment, as well as the high cost of such test. Alternatively, the geotechnical centrifuge is employed to in order to study the behaviour of micropiles and MPGs subjected to different loading conditions. Rose et al. (2013) investigated the performance of different configurations of groups of small diameter piles (300 mm) installed in clay using geotechnical centrifuge testing and numerical modeling. It was found that the failure mechanism for the perimeter groups consisting of 14 to 20 piles with $1.75D_p$ spacing was a block failure with a group efficiency ratio of about 0.9. Several micropile load tests were conducted in order to evaluate the lateral performance of micropiles. For example, Richards and Rothbauer (2004), Long et al. (2004), Shahrour and Ata (2002), and Teerawut (2002).

Many researchers used the finite element method (FEM) to perform comprehensive parametric studies of MPG and MPR. Shahrour et al. (2001) conducted a 3D finite

element analysis on a single micropile and a MPG in order to evaluate their performance under seismic loading. They found that the micropiles behaviour was affected by the number and spacing of micropiles and the location of the micropile within the group were investigated in this study. They used 20-node solid elements to represent the soil. To eliminate the boundary effect, the base of the model was placed at a depth equal to 1.5 times the micropile length and the lateral boundaries were placed at 6 L_{mp} from the micropile axis. Sadek and Shahrour (2004) investigated the behaviour of inclined micropiles subjected to dynamic loading using 3D FEA. They compared the behaviour of a vertical MPG with a group of inclined micropiles ($\alpha_i = 7°$, 13° and 20°) with spacing-to-diameter ratio, $S/D_{mp} = 5$. The soil was considered to be homogeneous and was modeled as linear elastic material. The 10 m micropiles were modeled using 3D-beam elements. The lateral boundaries were placed at distance of 240 micropile diameter ($D_{mp} = 0.25$ m) from the central axis of the MPG. They demonstrated that the numerical model has successfully modeled the behaviour of the micropiles.

Abd Elaziz and El Naggar (2014a) investigated the behaviour of hollow bar micropiles installed in clay using 2D axisymmetric finite element model, which was calibrated using field test results. The calibrated model was then used to study the effect of installation methodology, geometry of hollow bar micropile and shear strength of surrounding soils on the overall capacity of micropile. The hollow bar was modeled as a linear elastic material and the grout was simulated using a nonlinear elastic-plastic model. The soil was simulated as elastic-plastic material with Mohr-Coulomb failure criterion. The horizontal boundary at the base of the model was placed at 1.75 L_{mp} from the top of the model and the side boundary was located at 25 D_{mp} from the micropile center.

Abd Elaziz and El Naggar (2014b) extended this study to evaluate the performance of the hollow bar micropile groups in cohesive soil. The vertical boundaries were located at 3.5 times the width of the pile cap and the base boundary was at depth equal to 1.75 L_{mp} from the ground surface. Their study showed that the group efficiency factor was approximately 1. In addition, they produced interaction factors diagrams that can be used to calculate the group settlement using the interaction factors method.

7.1.2.2. Piled raft studies

Numerous studies have been conducted in order to evaluate the piled raft performance and the use of piles as total and differential settlements reducer for raft foundation. Of particular note, the studies by Poulos and Davis (1974); Clancy and Randolph (1993 and 1996); Randolph (1994); and Poulos (2001) resulted in an analytical method widely known as Poulos-Davis-Randolph (PDR) method, which can be employed to evaluate the axial stiffness of piled raft for preliminary design purposes. Katzenbach et al. (2000) reported 10 case histories of piled raft foundations constructed in Frankfort clay between 1983 and 2001. These foundations support high-rise buildings with height ranging from 52 m to 257 m. The piled raft foundation reduced the total and differential settlements compared to shallow foundations and conventional rafts. In addition, the internal forces and bending moment of the raft were reduced due to the use of piles. It was found that the load carried by the raft ranged between 20% and 70% of the total load. They concluded that the piled raft design concept can lead to reducing the number of piles by up to 60% compared to conventional pile foundation.

Centrifuge testing was used as an effective technique to investigate the behaviour of piles, pile groups and piled rafts in clay. For example, Horikoshi and Randolph (1996)

investigated the differential settlement of a piled raft foundation in clay soil with average undrained shear strength of 40 kPa. They considered three different configurations as follows: 9, 21 and 69 piles placed at spacing to diameter ratio, $S/D_p = 8$ and pile. The piles were 3.15 mm in diameter and the circular raft was 140 mm in diameter (model scale). They concluded that the raft differential settlement could be reduced by 30% by using 9 piles uniformly distributed at the raft center.

FEA was also used to conduct comprehensive parametric studies of piled rafts foundations in clay. Maharaj and Gandhi (2004) performed 3D analysis of piled raft foundation installed in clay soil. They investigated the effects of soil elastic modulus and raft thickness on the load-displacement curve for both a raft and a piled raft. The side boundaries were placed at a distance equal to the raft width, B_r, from the raft center and the bottom boundary was a distance B_r from the bottom of the piles. Reul and Randolph (2003) demonstrated the ability of FEA to predict the overall settlement, differential settlement and the load carried by the piles for various piled raft foundations supporting existing high-rise buildings resting on overconsolidated clay. The finite element model was 4.8 B_r wide and 2.2 B_r deep. The results from the finite element analyses were in good agreement with the measured values. Katzenbach et al. (2005) performed 3D finite element analyses to assess the settlement of piled rafts supporting high-rise buildings founded on cohesive soil. The piles and raft were modeled as linear elastic material and the soil was modeled using elasto-plastic cap model. The vertical boundaries of the model were placed at distance = 2.2~2.7 B_r from the center of the raft. The model depth was equal to 2.75 L_p. They confirmed the effectiveness of numerical modeling in the design process, especially for assessing the settlement of high-rise buildings.

Lee et al. (2010) investigated the behaviour of piled raft installed in soft clay using 3D finite element analysis. The soil materials were modeled using elastic-perfectly plastic material with Mohr-Coulomb failure criterion and the piles were modeled as isotropic elastic material. The raft width, B_r = 10 m and the pile length was varied from 8 m to 20 m. The model was about 4 B_r wide and 2.4 B_r deep. It was found that the load carried by the raft was increased as the pile spacing increased. They demonstrated that using a limited number of strategically located piles has increased the raft bearing capacity and reduced its settlement. Cho et al. (2012) utilized 3D FEM to study the settlement behaviour of pile raft foundation in clay soils. The soil was modeled using elastic-perfectly plastic material with Mohr-Coulomb failure criterion and the piles were modeled as linear elastic material. The vertical boundaries of the model were placed at distance = 1.55 B_r from the center of the raft and the bottom boundary was located at depth equal to 1.6 L_p. The results indicated that the average settlement of the pile raft can be effectively reduced by widely spaced piles, while the differential settlement was reduced by placing the piles within the central area of the raft.

7.1.3. Objectives and Scope of Work

A MPR offers an effective foundation system that combines the benefits of micropiles and piled rafts. However, to the knowledge of the author, there have been no studies considering the performance of MPR or any guidelines for their design. Therefore, there is a need to thoroughly assess the performance of MPR installed in clay and develop some guidelines for their design. In this study, the effects of number of micropiles, spacing-to-micropile diameter ratio, S/D_{mp}, and raft thickness on different MPR performance are evaluated using 3D finite element analysis. The performance of the

MPR is evaluated in terms of: axial stiffness; differential settlement; load sharing between the micropiles and the raft; and the raft bending moment. The numerical model used in the current study was calibrated using results obtained from geotechnical centrifuge tests of MPR in clay. In addition, the FEA examined the ability of PDR method to evaluate the axial stiffness of MPR for preliminary design stage.

7.1.4. Centrifuge Testing Program

The centrifuge tests were conducted at C-Core Centrifuge facility located at Memorial University, St. John's, Newfoundland. The centrifuge testing program consisted of the following tests: (1) a micropiled raft with an equivalent raft thickness of 0.6m at prototype scale (test#7); (2) a raft with a thickness equivalent to 0.6 m at prototype scale (test#9); and (3) a single micropile (test#8). The soil bed in these tests was Kaolin-Silt mixture (K-S), which was consolidated from slurry and had an average undrained shear strength, s_u = 30 kPa. All tests were performed under a centrifugal acceleration of 50g. The prototype diameter of the micropile was 150mm and its length was 10m. The raft and micropiles models were fabricated using PVC and were sized to represent prototype axial and flexural stiffness values of concrete raft and piles as shown in Table 7.1.

Figure 7.1 presents the layout for the MPR model while Figure 7.2 shows a schematic for the setup used during the testing program. The soil model in the strong box was 350 mm thick (i.e., 17.5 m at prototype scale). A vertical load was applied to the raft center using an electrical actuator at a constant displacement rate of 5 mm/sec (prototype scale). In order to model the rough surface of Type B micropiles, the surface of the model micropiles was roughened by gluing sand particles to it. This method was used

successfully by El Naggar and Sakr (2000), Horikoshi et al. (2002) and Horikoshi et al. (2003a, b). Moreover, the micropile models were installed into the clay bed in such a way to simulate the increase in confinement around the micropiles due to the pressurized grout used in Type B micropile construction. A hole with a diameter 0.9 D_{mp} was drilled vertically. The micropile was then jacked into the pre-drilled hole expanding it to the full size of the micropile diameter. The pre-drilling reduced the installation resistance and hence reduced the risk of damaging the model micropile.

Table 7.1. Scaling laws for centrifuge modeling and model and equivalent prototype dimensions.

Description		Scaling law	Prototype	Model
Micropile Diameter		E_pA_p/n^2	150 mm	9.53 mm
Axial Rigidity (EA)			516737 kN	207 kN
Micropile Length, L_{mp}		1/n	10 m	200 mm
Raft Width, B_r, and Length, L_r		1/n	5.25 m	105 mm
t=0.6 m	Raft Thickness	E_pI_p/n^4	0.6 m	16.4 mm
	Flexural Rigidity		697950 kN. m^2	0.112 kN. m^2
Force (kN)		-	n^2	1
Stress (kPa)		-	1	1
Stiffness (kN/m)		-	N	1
Moment (kN/m)		-	n^3	1
Displacement (mm)		-	N	1

Figure 7.1 Layout for the MPR.
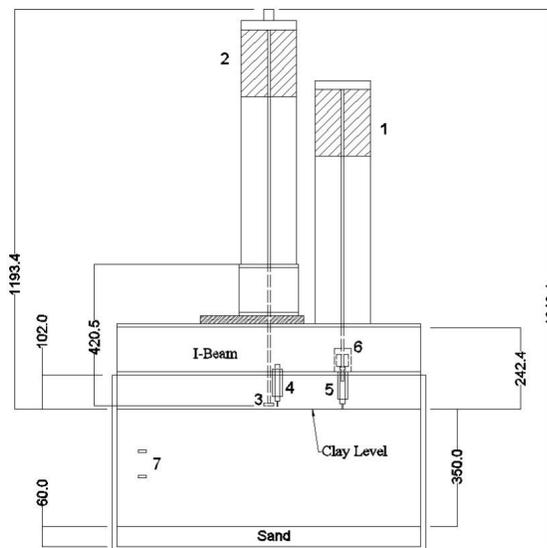
Figure 7.2 Vertical cross-section of centrifuge package consists of: (1) vertical actuator for applying load; (2) actuator used for T-bar; (3) T-bar; (4) LVDTs to measure clay settlement; (5) load cell; (6) laser; and (7) PPTs (all dimensions in mm).

7.1.5. Clay Test bed

The kaolin clay-silt bed was prepared by mixing clay and silt at a ratio of 1:1 as slurry, and was allowed to consolidate at 1g under a consolidation pressure of 300 kPa to achieve overconsolidation ratio (OCR) of 6 and the desired undrained shear strength, s_u of 30 kPa in the centrifuge at the half depth of the micropile, as per the guidance provided by Lin (1995). The clay bed was then subjected to further consolidation in the centrifuge at the beginning of the test flight until a 90% degree on the consolidation was achieved. A T-bar test was performed in-flight at 50g to evaluate the clay undrained shear strength. The results of the T-bar test were used to estimate the shear strength profile of the soil bed, i.e.

$$s_u = \frac{P}{N_b\, d} \tag{7.1}$$

Where: s_u = undrained shear strength; P = force per unit length acting on the cylinder; $D_{T\text{-bar}}$ = diameter of cylinder; and N_b = bar factor between 9 and 12 with a recommended value of 10.5 (Stewart and Randolph, 1994).

The undrained shear strength profile of the soil bed is presented in Figure 7.3. As can be noted from Figure 7.3., the average s_u value within the top 10 mm was about 17 kPa and increased linearly with depth at a rate equal to 2 kPa/m (prototype scale). In addition, four consolidated, undrained triaxial tests were performed under effective consolidation pressures of 40 kPa, 80 kPa, 160 kPa and 320 kPa, which corresponded to OCR values of 7.5, 3.8, 1.9 and 1, respectively. As the samples were previously consolidated from the slurry deposition to vertical effective stress of 300 kPa, they were at an overconsolidated state for the confinement pressures of 40 kPa, 80 kPa and 160 kPa; however, for the 320 kPa confinement pressure, the sample was normally consolidated. The soil undrained shear strength and elastic modulus (E_u) values determined from the triaxial tests results were used to establish the ratio E_u/s_u for the K-S clay and was found to vary between 250 and 500 with an average of 375. This value is at the lower bound of the values reported by Jaimolkowski et al. (1979) for clay with a plasticity index (PI) less than 30 and OCR between 4 and 6.

Based on the T-bar results, the s_u at the first 1 m was approximately 25 kPa and it increased linearly with depth at a rate of 2 kPa/m. Moreover, by extending the linear portion of the undrained shear strength line to the clay surface level, the undefined shear strength is approximately 17~19 kPa (see Figure 7.3). Therefore, the variation of undrained elastic modulus with depth (z) can be expressed as:

$$E_u = (250 - 500)s_{u\,o} + 750z \qquad\qquad (7.2)$$
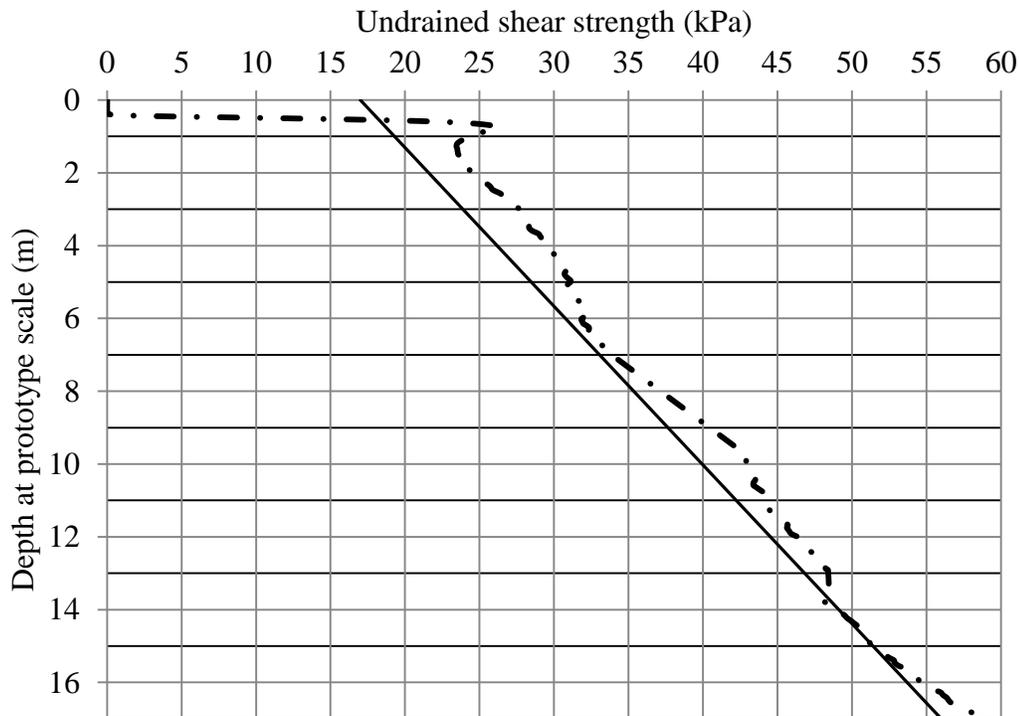
Figure. 7.3 Undrained shear strength profile along the clay depth using the T-bar test results.

7.2. FINITE ELEMENT MODEL (FEM)

This section presents the development and calibration of the finite element model used in the analysis. The 3D model was established using the computer program PLAXIS 3D (PLAXIS BV, 2013) considering an appropriate size mesh and a number of elements following a sensitivity study. The results of the centrifuge study of the MPR were then used to calibrate the model considering the prototype dimensions of the MPR tested in the centrifuge. The calibrated model was then employed to perform the parametric study to evaluate the effect of different factors on the performance of the MPR system.

7.2.1. Description of the FEM

The model simulated only quarter of the MPR foundation system by taking advantage of symmetry across the x- and y-axes to reduce the computational effort and time. The boundaries of the model were set at a distance equal to $2.5B_r$ measured from the edge of the raft, and the depth of the model was approximately two times the micropile length (L_{mp}) or $4B_r$ as shown in Figure 7.4. The soil and micropiles were modeled using 3D 10-node tetrahedral elements and the raft was modeled using 6-node triangular plate elements. The model comprised 250,000 elements with an average element size of 110 mm. The large number of small-size elements assured high accuracy, especially at locations where nonlinear behaviour was anticipated (e.g. raft base, micropile base and micropile circumference). The load was applied as a concentrated load of 800 kN (i.e. a quarter of the full load applied to the full MPR) at the raft center.

7.2.2. Model Parameters

The behaviour of the K-S clay was simulated using a bi-linear, elastic-perfectly plastic constitutive model and the Mohr-Coulomb failure criterion under undrained condition. The constitutive model requires conventional soil parameters including: unit weight (γ), undrained shear strength (s_u), undrained modulus of elasticity (E_u) and undrained Poisson's ratio (ν_u). Table 7.2 summarizes the K-S properties. The undrained modulus of elasticity was estimated based the T-bar test and CIU triaxial tests (i.e., Eq. 7.2). In order to properly simulate the true behaviour of the K-S clay in which the undrained shear strength increases with depth and thus the undrained shear modulus increases with depth, PLAXIS 3D offers an advanced function which allows the increases in both s_u and E_u with depth, i.e.

$$s_u(z) = s_{u\,o} + (z_{ref} - z)s_{u\,inc} \quad \text{for } z < z_{ref} \tag{7.3}$$

$$E_u(z) = E_{u\,o} + (z_{ref} - z)E_{u\,inc} \quad \text{for } z < z_{ref} \tag{7.4}$$

Where: $s_u(z)$= undrained shear strength (kPa); $s_{u\,o}$ = initial undrained shear strength (kPa); $E_u(z)$= undrained modulus of elasticity (kPa); E_{uo} = initial undrained modulus of elasticity (kPa); $E_{u\,inc}$ = the rate of the increase in undrained modulus of elasticity (kPa/m); and Z_{ref} = the reference depth (m); z = depth of interest (m)

The behaviour of the raft and micropiles was simulated considering a linear elastic model for the mechanic properties of concrete (elastic modulus, E_c, and Poisson's ratio, v_c).
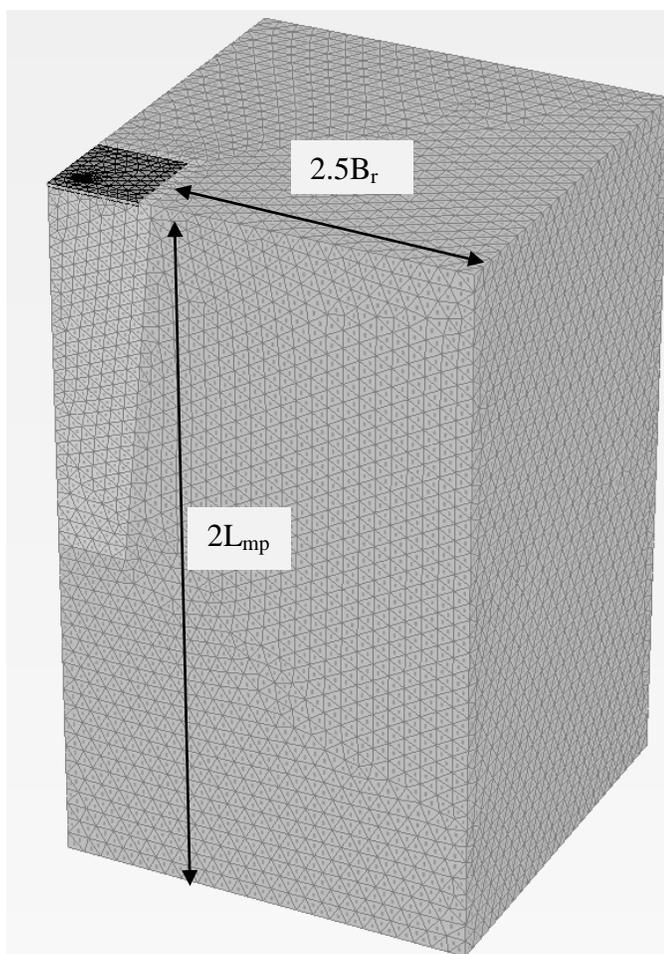
Figure 7.4 Mesh used in the calibration and verification of centrifuge tests.

7.2.3. Soil-Structure Interaction (SSI)

In the finite element analysis, the interaction between the micropile or the raft and the adjacent soil is simulated using interface elements. In the current analysis, 12-noded (i.e. 6 pairs of nodes) interface elements are used to simulate the interaction between the micropile or the raft and adjacent soil. For each interface element, 6 nodes are connected to the 6-noded triangular side of a soil element, and the other 6 nodes are connected to a plate element simulating the raft or an element representing the micropile. This interface element allows the relative movement between the micropiles (or raft) and the soil (slippage). The interface elements use the Mohr-Coulomb failure criterion; as the shear stress reaches the yield shear strength of the soil, slippage occurs at the interface. The interface element in PLAXIS 3D is modeled by using an interface reduction factor, R_{int}, which represents the strength of the interface element as a percentage of the shear strength of the adjacent soil. The value of R_{int} depends on the state of the soil at the soil-structure interface. For example, if the soil is highly disturbed during the construction (bored pile), the R_{int} is expected to be small. In the current study, R_{int} was expected to be high since the micropiles in the experimental program were jacked into the clay that caused the soil surrounding the micropiles to densify.

The lateral earth pressure coefficient (K_s) for the overconsolidated K-S clay was calculated as a function of the effective angle of internal friction (ϕ') and overconsolidation ratio (OCR) as suggested by Mayne and Kulhawy (1982), i.e.:

$$K_s = (1 - \sin\phi')(\text{OCR})^{\sin\phi'} \tag{7.5}$$

Based on laboratory testing of clay specimens (as discussed in Chapter 3), the effective angle of internal friction (ϕ') was found to be 25° and OCR varied between 7.5 and 2, hence K_s was found to be approximately 1.0. The construction technique of micropiles Type B can also affect K_s as a result of the pressurized grout which could induce high confining pressure to the soil along the micropile shaft, thus increasing the value of K_s. The effect of increased confining pressure on the lateral earth pressure coefficient was estimated using an advanced function in PLAXIS 3D, which allows the expansion of the elements representing the micropile, and as a result the horizontal effective stress, σ'_h increases. Thus, K_s was evaluated as σ'_h / σ'_v (σ'_v= geostatic pressure ($\gamma_s h$ Where h is depth from the ground surface). As the MPR was installed at 1g, the densification that occurred in the surrounding soil was equal to the diameter of the model micropile ($D_{mp} \approx 10$ mm). Therefore, in the FEM, the micropile diameter was expanded by 10 mm. A similar approach was used by Khan et al. (2008) to evaluate the change in K_s due to ground expansion associated with loading tapered piles. It was found that the average K_s was approximately 1.2 and that the influence of the increase of the micropile volume affected the soil up to a distance equal to 5 D_{mp}.

7.2.4. Calibration and Verification of Numerical Model

The results of the centrifuge test for MPR with raft thickness = 0.6 m were used to calibrate the numerical model and the results of the remaining tests were used to verify it. The process of calibration was performed by refining the soil and interface properties in the model. This was done by adjusting the values of the interface reduction factor at the micropile-soil interface, as well as the estimated initial undrained shear strength and incremental increase of undrained shear strength with depth based on the in-flight T-bar

test. The undrained modulus of elasticity was calibrated according to the range proposed in Eq. 7.2. The calibration process demonstrated that using a E_u/s_u of within the range proposed in Eq. 7.2 for the E_{uo} and the incremental undrained modulus of elasticity yielded good results. The interface reduction factor, R_{int} was found to be 0.95. With these values, a reasonable match with the centrifuge test results was achieved as demonstrated in Figure 7.5a. The model was verified using the centrifuge results for the raft alone with a raft thickness of 0.6m, and a single micropile (see Figure 7.5b and c). The reduction factor at the micropile-soil interface reflected the high friction of the micropiles' surface and the effect of the installation technique of the micropiles (jacking) in centrifuge testing. All input parameters used in the numerical model are listed in   Table 7.2.

Table 7.2. Input parameters used in the FEM

Parameter	Soil	Micropiled-raft
Constitutive Modeling	Elastic-plastic	Linear Elastic
Total Unit Weight (kN/m^3), γ	18.4	24
Average Modulus of Elasticity raft	-	24 GN/m^2
Average Modulus of Elasticity MP	-	30 GN/m^2
Thickness of the raft	-	0.6 m
Initial undrained shear strength at the surface of clay, $s_{u\,o}$, (kPa)	17	-
Incremental shear strength (kPa/m), $s_{u\,inc}$	2	-
Initial undrained Modulus of Elasticity, $E_{u\,o}$, (kPa)	6800	-
Incremental undrained Modulus of Elasticity, $E_{u\,inc}$ (kPa/m),	750	-
Stiffness and strength increases with depth	Yes	No
Poisson's ratio, ν	0.49	0.19
Interface reduction factor, R_{intr}	0.95	-

7.3. PARAMETRIC STUDY

7.3.1. Introduction

The main goal of the parametric study is to evaluate the effect of different factors on performance of MPR installed in clay, including: tolerable bearing pressure; axial stiffness; maximum and differential settlements; and bending moment of the raft. The factors considered are: the number of micropiles; spacing of micropiles and raft thickness. The study was carried out using the calibrated/verified numerical model as described above with some modification to allow for the much wider raft. In order to produce results that can be helpful to practicing engineers, two types of loadings were considered. First, a uniform distributed load which is similar to the load of a silo, an oil tank, a large storage area, a commercial one or two-storey building. Second, the loads of a multi-storey building with a total of 16 columns were calculated and the column loads were applied to the raft.

The micropiles used throughout this parametric study were 250 mm in diameter and 10 m long. The square raft was 21 m x 21 m. A total of 26 different cases were considered in the analysis for the two types of loading. Five different micropile spacings, $S = 5\ D_{mp}$, $8D_{mp}$, $10\ D_{mp}$, $16\ D_{mp}$ and $20\ D_{mp}$, with three different values of raft thickness, $t_r = 1.2$ m, 0.6 m and 0.3 m, were investigated. Furthermore, three cases for a raft ($t_r = 0.3$ m, 0.6 m and 1.2 m) without micropiles were analyzed. These cases were performed for clay soil with an average undrained shear strength of 30 kPa. However, not all parameters were considered in the case of the concentrated loads.
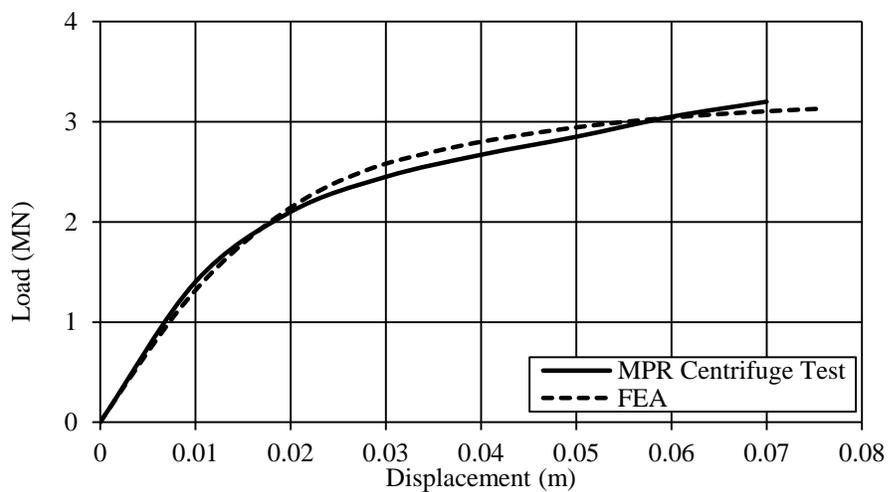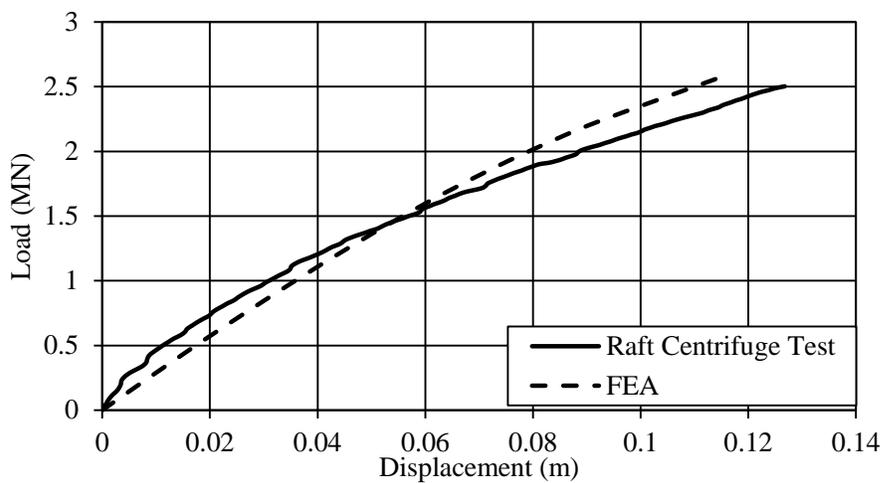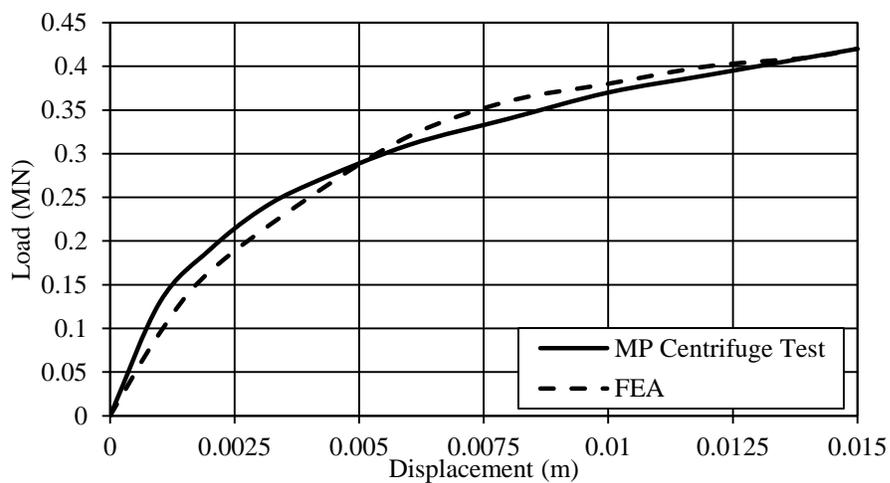
Figure 7.5. Calibration and verification results: (a) MPR with 0.6 m raft; (b) 0.6 m raft only; and (c) single micropile.

7.3.1.1. Soil Parameters

In the parametric study, the raft width $B_r = 21$ m and the depth of the mesh was 50 m. The in-flight centrifuge T-bar test results were for 20 m of soil (prototype scale). For the bottom 30 m of the soil considered in the numerical model, the undrained shear strength was calculated based on the results and employing the following equation, which was obtained by curve fitting the results of a series of CIU triaxial tests:

$$s_u = 0.31 \, \sigma'_m \, (OCR)^{0.51} \tag{7.6}$$

Equation 7.6 was verified with the in-flight T-bar results as shown in Figure 7.6, and was used to evaluate the average modulus of elasticity at a depth of 27 m and 42 m. The increase in E_u is a function of undrained shear strength, which was evaluated using Eq. 7.2. Table 7.3 summarizes all input parameters used in the FEM for different clay layers.
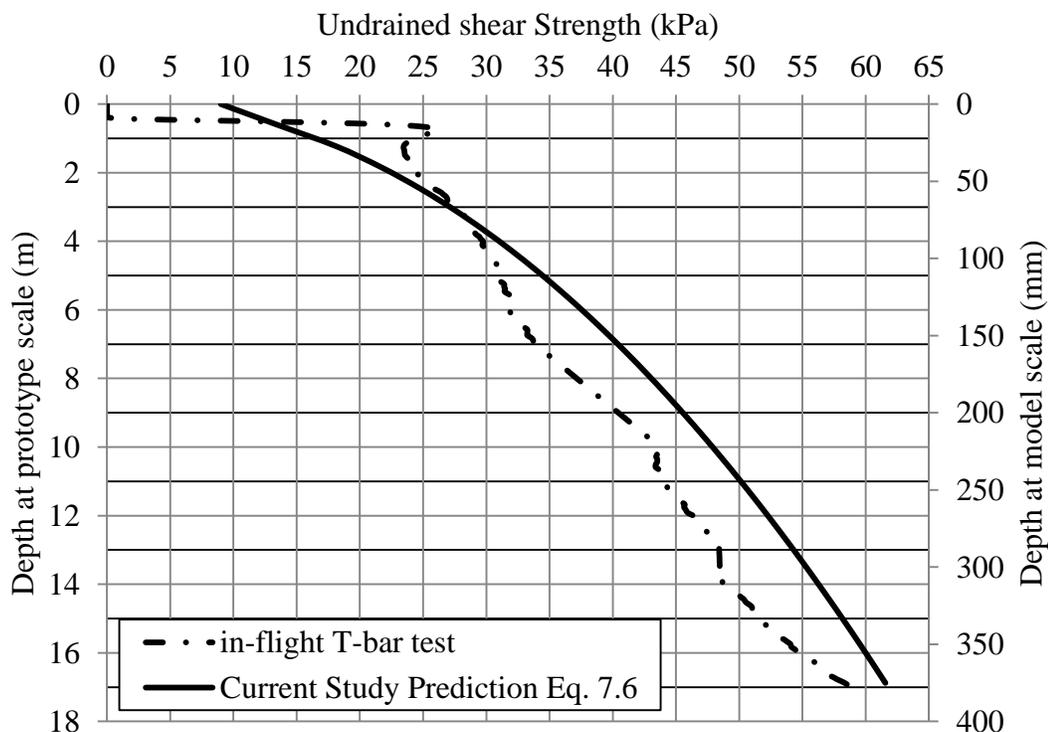
Figure 7.6. Comparison between estimated s_u and the in-flight T-bar test.

Table 7.3. Input parameters used in the FEM for clay.

Layer	Depth	γ	E_o	E_{inc}	s_{uo}	$s_{u\,inc}$	K_o
	m	kN/m^3	kPa	kPa/m	kPa	kPa/m	-
Top clay	0-20		6800	750			
Middle clay	20-35	18.4	35E3	-	17	2	1.2
Lower clay	35-50		48E3	-			

7.3.1.2. Applied Loads

The uniformly distributed load was applied as pressure to the raft surface. The MPR performance was evaluated at certain displacement levels (consistent with the performance-based design approach). Therefore, for each analysis case, the applied pressure was increased until the specified displacement was attained.

For the case of concentrated loads, a square raft 21.0 m x 21.0 m supporting a building with 16 columns spaced at 6.0 m center to center was considered in the analysis. Figure 7.7 shows the layout of the raft and columns. Only one quarter of the raft was modeled, which contained a single core column, two edge columns and a single corner column. The columns' loads were estimated according to the tributary area of each column. The load applied to each floor included dead load (5.76 kPa/m^2), live load (2 kPa/m^2) and superimposed dead load (1.2 kPa/m^2). Load factors of 1.25 and 1.5 were applied to dead and live loads according to the National Building Code of Canada (2010). The concentrated load was increased (i.e. increasing number of floors) until the specified displacement was reached.

7.3.1.3. Numerical Model Boundaries and Mesh

The size of the model and the location of its boundaries were selected according to a sensitivity analysis. It was found that the optimum mesh width and depth were 35 m (1.7

B$_r$ from centerline of the raft) and 50 m (2.4 B$_r$ from the top of the model), respectively. The total number of elements used in the mesh was about 318224. At locations where high stress concentration was anticipated (e.g., at micropile interface, at micropile base and at the interface between soil and raft), denser mesh was used.
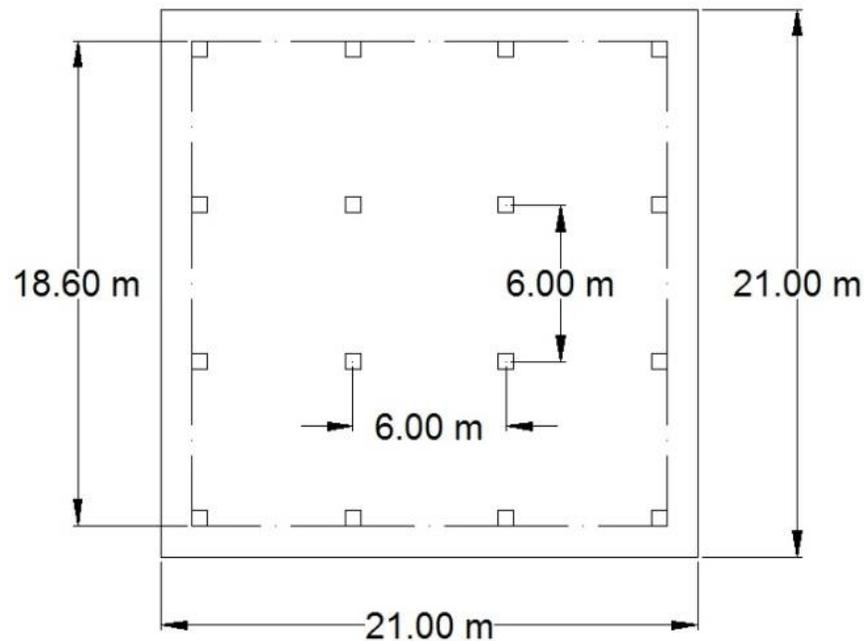
Figure 7.7. Layout of the columns on top of the raft.

7.3.2. Tolerable Bearing Pressure of MPRs

The performance-based design method is adopted for the design of many high-rise buildings. In this method, a tolerable movement that will cause a minor functionality or maintenance issue for the building under working loads is identified (service limit). By knowing the tolerable settlement, the foundation system should be designed to sustain the working loads within the tolerable movement (Roberts, 2011). Since the ultimate capacity of a foundation system is normally reached at a high level of movement, adopting the design criteria will ensure the functionality of the building within the tolerable settlement,

along with satisfying the differential settlement criterion. The advantage of this method over the limit states approach is eliminating the need to identify the ultimate capacity of the foundation. For example, there is a possible range of ultimate capacities for a pile foundation which depends on the failure criteria adopted (piled load test) or the design equations.

By reviewing a number of case histories published in the literature for piled raft foundations, the maximum overall settlement of buildings was found to be between 60 mm and 100 mm with the maximum settlement reported as 150 mm (Katzenbach et al., 2000). Therefore, the 75 mm and 150 mm tolerable settlement criteria were adopted to determine the corresponding load for each MPR with a different number of micropiles evenly distributed across the raft.

Table 7.4 summarizes the tolerable bearing pressure, q, values for different MPR systems in clay, as well as the average percentage increase in tolerable bearing pressure (PIBP) of the MPR with different micropile spacings compared to that of the raft without micropiles.

Table 7.4. Tolerable bearing pressure for different MPR systems in clay (all q in MPa).

δ	0.075 m						0.15 m						
t_r (m)	0.3		0.6		1.2		0.3		0.6		1.2		Avg. PIBP %
S/D_{mp}	q	PIBP %	q	PIBP %	q	PIBP %	q	PIBP %	q	PIBP %	q	PIBP %	
0	0.10	0	0.10	0	0.11	0	0.11	0	0.11	0	0.11	0	0
5	0.18	72	0.18	76	0.20	88	0.24	120	0.25	124	0.26	129	101
8	0.14	38	0.15	44	0.16	54	0.19	71	0.20	78	0.21	85	62
10	0.13	32	0.14	38	0.16	47	0.17	50	0.18	60	0.18	65	49
16	0.11	6	0.12	12	0.13	18	0.14	29	0.15	33	0.15	35	22
20	0.10	2	0.11	4%	0.12	12	0.12	12	0.13	16	0.14	21	11

Figure 7.8 shows the average percentage increases in tolerable bearing pressure (PIBP) of the MPR with different micropile spacings compared to the raft without micropiles for firm clay (s_u = 30 kPa). The results in Figure 7.8 and Table 7.4 clearly demonstrate that the MPR concept resulted in a significant increase in tolerable bearing pressure compared to the raft case, especially for S/D_{mp} = 5 to 10. As S/D_{mp} decreased, i.e. the number of micropiles increased, the average PIBP increased up to 101% for micropiles distributed at S/D_{mp} = 5. This increase in tolerable bearing pressure is attributed to the part of the load transmitted to deeper soil by the micropiles and decreases in stress concentration under the raft, which allowed the MPR to sustain a higher load before reaching the tolerable settlement. From Table 7.4, it is noted that the PIBP for MPR at δ = 0.15 m is much is higher than the PIBP at δ = 0.075 m. This is because the tolerable bearing pressure (BP) for the isolated raft reaches its failure load at displacement of 0.075 m; therefore the tolerable bearing pressure (BP) of isolated raft was the same at both tolerable settlement values. By adding the micropiles in the MPR, the BP increased as the tolerable settlement increased which resulted in higher PIBP at δ = 0.15 m. Curve fitting the results of the PIBP for firm clay (s_u= 30 kP), the following equation is obtained:

$$\text{PIBP (\%)} = -0.64 \ln \left(S/D_{mp} \right) + 1.97 \qquad \text{For } s_u = 30 \text{ kPa} \qquad (7.7)$$

It is important to note that by increasing the raft thickness from 0.3 m to 1.2 m, the average increase in tolerable bearing pressure for the same micropile spacing was only 8%, which is not as significant as increasing the number of micropiles. However, the raft

thickness has a major impact in controlling the differential settlement, which will be discussed later.
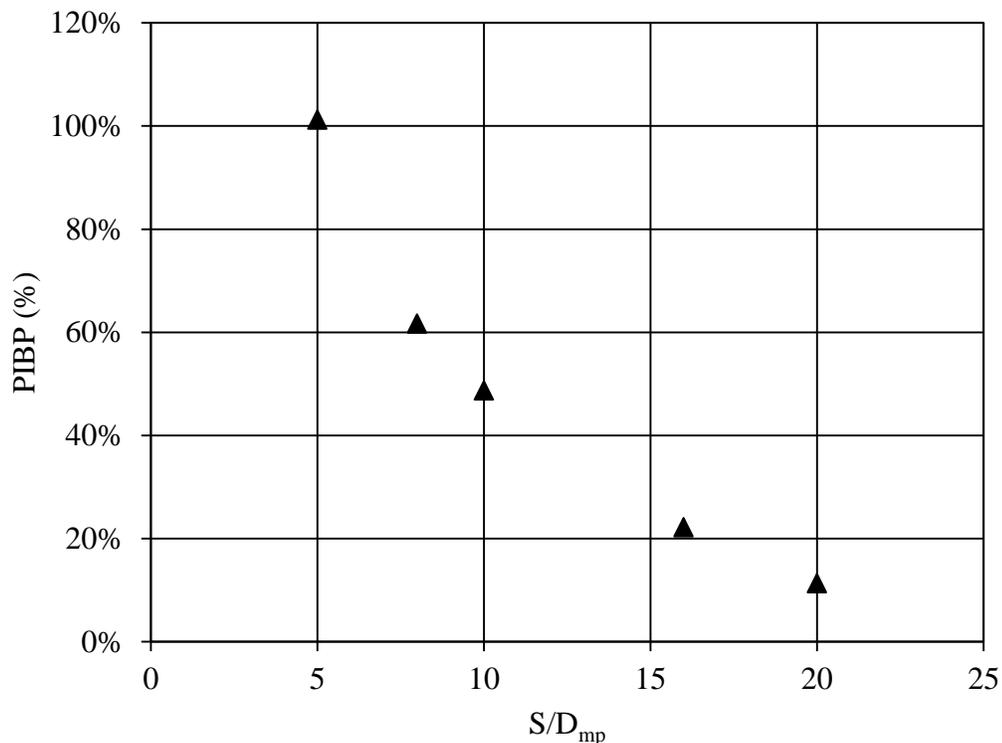
Figure 7.8. PIBP of MPR at different S/D_{mp} for firm clay (s_u= 30 kP).

7.3.3. Axial Stiffness of the MPRs

The axial stiffness of MPR, k_{mpr}, is evaluated from the load displacement curve for each case and the results are presented in Figure 7.9. It is noted from Figure 7.9 that the raft thickness has a slight impact on k_{mpr}, especially for the relatively flexible rafts (t_r = 0.3 m and 0.6 m) as k_{mpr} increased by only 12% as t_r increased from 0.3 m to 0.6 m. On the other hand, as t_r increased to 1.2 m, k_{mpr} increased by approximately 34%. This is because a relatively rigid raft (t_r = 1.2 m) tends to transfer the pressure to the soil more evenly due to the small differential settlement compared to the flexible raft (t_r = 0.3 m

and 0.6 m), which reduces stress concentration in the soil, and consequently increased k_{mpr}.

Spacing (S/D$_{mp}$)
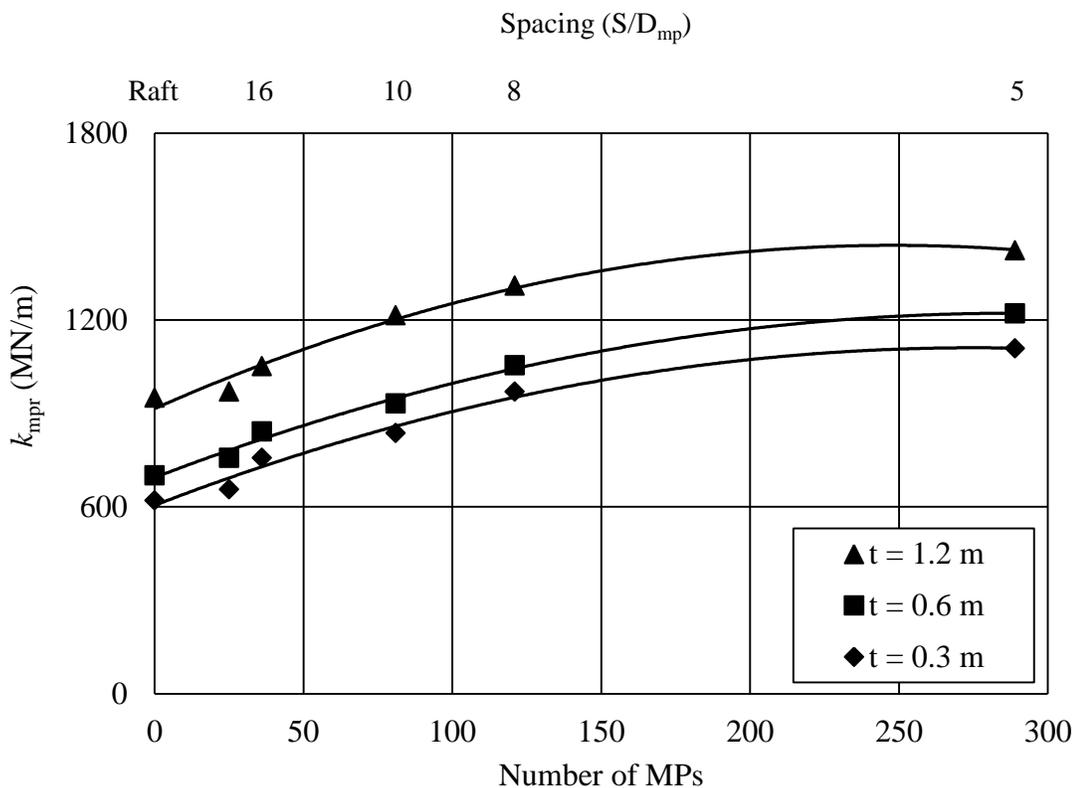
Figure 7.9. k_{mpr} for different numbers of micropiles and raft thickness

To examine the effect of the number of micropiles on the MPR axial stiffness, 25, 36, 81, 121 and 289 uniformly distributed micropiles were considered, which corresponded to S/D_{mp} = 20, 16, 10, 8 and 5, respectively. As expected, an increase in the number of micropiles resulted in a higher k_{mpr} value for all cases. This is attributed to the stiffening action of the micropiles and their transfer of some load to deeper soil with higher undrained shear strength and undrained modulus of elasticity; consequently, the displacement decreased and k_{mpr} increased. Interestingly, the rate of increase of k_{mpr} was not constant with decrease in S/D_{mp}. For up to $S/D_{mp} \approx 8$, the average rate of increase

between two successive spacings was approximately 16%; however, beyond $S/D_{mp} \approx 8$, the rate of increase was only 7% (see Figure 7.9). This is because reducing the micropile spacing results in overlapping in shear stress within the adjacent soil. Therefore, the number of micropiles should be optimized to achieve most efficient design.

7.3.4. Estimating Axial Stiffness of the MPR using the PDR Method

Poulos (2001) introduced the simplified Poulos-Davis-Randolph (PDR) method in order to estimate the axial stiffness of a piled raft foundation. This method consists of the analytical methods proposed by Poulos and Davis (1974) and Randolph (1994), which were developed for the analysis of piled rafts. In this method, the axial stiffness of a piled raft is evaluated considering the pile group stiffness and the raft axial stiffness (Randolph, 1994), i.e.,

$$K_{pr} = \frac{K_{PG} + (1 - 2a_{rp})K_r}{1 - \left(a_{rp}^2 \left(\frac{K_r}{K_{PG}}\right)\right)} \tag{7.8}$$

In Eq. 7.8, K_{PG} is the stiffness of the pile group and is calculated using the following equation:

$$K_{PG} = n_p^{1-e_f} K_p \tag{7.9}$$

Where n_p is the number of piles within the group, e_f is an exponent and K_p is the stiffness of a single pile. The e_f value varies between 0.3 and 0.5 for frictional piles, and up to 0.6 for end-bearing piles (Fleming et al, 2009). This exponent is primarily affected by the pile slenderness ratio (L/D_{mp}), spacing between the piles and soil Poisson's ratio. The e_f

values used in this study are 0.47, 0.42, 0.38, 0.33 and 0.32 for S/D_{mp} equal to 5, 8, 10, 16 and 20, respectively.

The vertical stiffness for a rectangular raft foundation is calculated according to Poulos and Davis (1974) i.e.,

$$K_r = I\sqrt{BL_r}\left(\frac{2G_{sr}}{(1-\nu_s)}\right) \text{ (kN/m)} \tag{7.10}$$

Where: K_r = axial stiffness for the raft foundation; L_r and B_r = length and width of the raft foundation; G_{sr} = shear modulus at depth = 2B/3; ν_s = soil Poisson's ratio =0.3; and I = influence factor which is a function of the raft aspect ratio = 1.03 for square raft.

The stiffness of a single pile, can be calculated using the equation proposed by Wood (2004) to evaluate the initial axial stiffness for micropiles in clay a, i.e.

$$k_{mp} = \frac{\pi r_0^2 E_p \eta \ (1+(\xi \tanh \eta L)}{(\xi + \tanh \eta L)} \tag{7.11}$$

Where: $\eta = \frac{1}{r_o}\sqrt{\frac{G}{2E_p}}$; r_o are pile length and radius; E_p = Young's modulus; G = average soil shear modulus; $\xi = \frac{(1-\nu_b)\pi r_o^2 E_p \eta}{4r_b G_b}$; G_b and ν_b are Poisson's ratio for soil beneath the pile. Similarly, Randolph (1994) proposed to evaluate the pile stiffness as (Fleming et al., 2009):

$$K_p = G_{sl} * D_p * \frac{\frac{2\eta}{(1-\nu)\xi}+\frac{2\pi\rho}{\zeta}*\frac{\tanh(\mu L)}{\mu L}*\frac{L_p}{D_p}}{1+\left[\frac{8\eta}{\pi\lambda(1-\nu_p)\xi}*\frac{\tanh(\mu L_p)}{\mu L_p}*\frac{L_p}{D_p}\right]} \tag{7.12}$$

Where: r_o = pile radius; D_p = pile diameter; $\zeta = \ln(r_m/r_o)$; $r_m=2.5\rho(1-\nu)L_p$; $\xi = E_{sl}/E_{sb}$; $\rho=E_{sav}/E_{sl}$; $\mu L= (2/(\zeta\lambda))^{0.5}*(L/r_o)$; $\lambda=E_p/G_{sl}$; $\eta=r_b/r_o$; L_p= pile length; E_{sl} = soil Young's

modulus at the pile toe level; E_{sb} = soil Young's modulus below pile toe; E_{sav} = average soil Young's modulus along pile shaft; ν_s = soil Poisson's ratio; G_{sl} = soil shear modulus at the pile toe level; and E_p = pile material Young's modulus (Fleming et al., 2009). Finally, a_{rp} is the raft pile interaction factor, which can be given by:

$$a_{rp} = 1 - \{\ln(r_c/r_o)/\zeta\} \tag{7.13}$$

The suitability of these analyses for the case of a MPR needs to be evaluated considering the relatively small axial stiffness of the micropile compared to that of the larger diameter piles. The PDR method was employed to estimate k_{mpr} for all MPR cases with different S/D_{mp} in medium-stiff clay. It was found that Eq. 7.11 yields a more accurate MPR axial stiffness in clay soil. The results presented in Table 7.5 revealed that the PDR method has the capability to estimate k_{mpr} for a MPR with a rigid raft within 3% error of the calibrated numerical model results. However, as the raft thickness decreased the error in estimating k_{mpr} using the PDR method increased to 18% and 26% for raft thicknesses of 0.6 m and 0.3 m, respectively. This is because Eqs. 7.8 and 7.10 do not account for the effect of the raft flexibility, influenced primarily by its thickness. Therefore, an adjustment factor (ω_{PR}) should be applied to the axial stiffness of the MPR in order to account for the raft flexibility in the PDR method. Using the adjustment factor (ω_{PR}), Eq. 7.8 can be rewritten to account for the raft flexibility, i.e.,

$$k_{mpr} = \omega_{PR} \frac{K_{PG} + (1 - 2a_{rp})K_r}{1 - \left(a_{rp}^2\left(\frac{K_r}{K_{PG}}\right)\right)} \tag{7.14}$$

The adjustment factor (ω_{PR}) was evaluated by comparing the axial stiffness obtained from the results of the calibrated model for the different MPR configurations.

Table 7.5. k_{mpr} (MN/m) obtained from both PDR method and FEA.

		s_u= 30 kPa					
		Raft Thickness (m)					
		1.2		0.6		0.3	
S/D_{mp}	k_{mpr} (PDR)	k_{mpr} (FEA)	Error	k_{mpr} (FEA)	Error	k_{mpr} (FEA)	Error
5	1360	1423.59	5%	1221	10%	1108	19%
8	1260	1309.31	4%	1054	16%	969	23%
10	1192	1214.64	2%	932	22%	837	30%
16	1060	1050.92	1%	842	21%	757	29%
20	950	935.48	2%	757	20%	656	31%
		Average	3%	Average	18%	Average	26%

In order to more appropriately evaluate ω_{PR} considering the effect of raft flexibility, it is correlated with the raft relative flexibility coefficient (K_f) proposed by Horikoshi and Randolph (1997). They proposed an equation to evaluate the raft flexibility considering an earlier definition of the raft-soil stiffness ratio for a circular raft proposed by Brown (1969). The flexibility of a rectangular raft is given by (Horikoshi and Randolph, 1997):

$$K_f = 5.57 \frac{E_r}{E_s} \frac{(1-\nu_s^2)}{(1-\nu_r^2)} \left(\frac{B_r}{L_r}\right)^{\alpha_o} \left(\frac{t_r}{L_r}\right)^3 \qquad (7.15)$$

Where: E_r = the raft Young's modulus; ν_r = raft Poisson's ratio = 0.2; t_r = raft thickness; and ν_s = soil Poisson's ratio =0.5; = average soil elastic modulus; and α_o = optimal value = 0.5.

Although Eq. 7.15 is for a raft foundation, it is used for the MPR in this study but the micropile spacing is used instead of the raft width, B_r, and length, L_r, i.e.,

$$K_f = 5.57 \frac{E_r}{E_s} \frac{(1-\nu_s^2)}{(1-\nu_r^2)} \left(\frac{S_B}{S_L}\right)^{\alpha_o} \left(\frac{t_r}{S_L}\right)^3 \qquad (7.16)$$

Where S_L and S_B= spacing between micropiles along the length and width of the MPR.

This is justified because the micropile spacings represent the unsupported span of the raft. As the pile spacing decreases, the deflections at locations between the micropiles and at the center of the raft decreases. Thus, it is considered more representative of the MPR width for the purpose of evaluating its flexibility (Alnuaim et al., 2013).

By curve fitting the relationship between ω_{PR} and K_f, the following equation is obtained for firm clay:

$$\omega_{PR} = 0.055 \ln(K_f) + 0.6 \qquad \text{For } s_u = 30 \text{ kPa} \qquad (7.17)$$

Table 7.6 summarizes k_{mpr} (MN/m) obtained from both the revised PDR method and the FEA results for different S/D_{mp} in clay soil with $s_u = 30$ kPa. As can be noted from Table 7.6, the error in evaluating the MPR axial stiffness using Eqs. 7.14 and 7.17 vary between 1% and 9% with an average of 3%.

Table 7.6. k_{mpr} (MN/m) obtained from both revised PDR method and FEA.

		s_u= 30 kPa								
		Raft Thickness (m)								
		1.2			0.6			0.3		
S/D_{mp}	k_{mpr} - PDR	k_{mpr} - FEA	k_{mpr} - Eq.7.14	Error	k_{mpr} - FEA	k_{mpr} - Eq.7.14	Error	k_{mpr} - FEA	k_{mpr} - Eq.7.14	Error
5	1360	1424	1472	3%	1221	1288	5%	1108	1146	3%
8	1260	1309	1255	4%	1054	1116	6%	969	964	1%
10	1192	1215	1144	6%	932	1005	8%	837	868	4%
16	1060	1051	958	9%	842	811	4%	757	700	8%
20	950	935	852	9%	757	692	9%	656	606	8%
		Average		3%	Average		2%	Average		3%

7.3.5. Differential Settlement

It is equally important to control the differential settlement in a MPR foundation as excessive differential settlement can cause serious damage to the superstructure in terms of serviceability and safety. A widely adopted criterion for limiting the differential settlement is specified in terms of angular distortion (θ), which is defined as the difference in the settlement of two points or adjacent columns divided by the distance between the points or columns. The specified value of θ typically ranges between 1/300 and 1/500 to ensure safe design (Tan and Chow, 2004). The effect of the micropile spacing and the raft thickness on θ for MPR installed in firm clay under uniform and concentrated loading conditions. Two methods were adopted to perform this analysis. First, the differential settlement of the MPR with different S/D_{mp} was compared to the differential settlement of an isolated raft (with same raft thickness) at loads corresponding to isolated raft maximum settlements of 75 mm and 150 mm. Second, angular distortion for all cases at $\delta = 75$ mm and 150 mm.

Table 7.7 and 7.8 present the angular distortion for different MPR cases normalized by the angular distortion for the raft alone case (θ/θ_r) under same loading conditions. For MPR subjected to concentrated loads, a negative effect of micropiles on differential settlement was observed as θ increased up to 3 and 7 times θ_r for raft thickness of 1.2 m and 0.6 m, respectively. This is because the micropiles close to the edge column reduced the settlement more than the micropiles at the center column, which carries higher loads. However, as the load increased, θ/θ_r decreased to 1.35. This significant reduction in θ/θ_r is because the micropiles were fully mobilized and the raft edge experienced excessive settlement. A similar observation was made by Poulos (2001). This is a disadvantage of

distributing the micropiles uniformly. Although the increase in the angular distortion seems high, it is still within the acceptable level, as average θ equals to 1/1450 and 1/390 for t_r 1.2 m and 0.6 m, respectively. The most optimal way is to distribute the micropiles uniformly to achieve the desired tolerable bearing pressure and strategically locate a number of micropiles with small spacing where high loads are located. For example, more micropiles should have been located at the center columns in the current case to reduce the differential settlement between the center and edge columns.

Table 7.7. θ/θ_r for different MPR cases under concentrated loading.

t_r (m)	1.2				0.6			
q(kPa)	102		112		100		111	
S/D_{mp}	θ	θ/θ_r	θ	θ/θ_r	θ	θ/θ_r	θ	θ/θ_r
Raft	0.0002	1.0	0.0005	1.0	0.0003	1.0	0.0022	1.00
16	0.00054	2.3	0.0005	1.0	0.0029	8.8	0.0032	1.45
10	0.0008	3.3	0.0008	1.6	0.0026	7.9	0.0031	1.38
5	0.0009	3.7	0.0009	1.8	0.0018	5.4	0.0023	1.03

For uniformly distributed load, the angular distortion for MPR in firm clay was about 1.5 and 3.5 times θ_r for raft thickness of 1.2 m and 0.6 m, respectively. This shows the significant influence of raft thickness in controlling the deferential settlement. By comparing θ for t_r = 1.2 m and 0.6 m, there is approximately 50% reduction in angular distortion. However, as the micropiles at the raft edge were fully mobilized, the average θ/θ_r became 0.7 for both cases (MPR with t_r= 1.2 m and 0.6 m, respectively). In case of very flexible raft (t_r =0.3 m), which performed poorly in resisting the differential settlement, the addition of micropiles reduces the θ by about 75%. Increasing t_r to 1.2 m for the MPR has decreased differential settlement significantly, with θ = 1/1700, which is well below 1/300. Figure 7.10 shows the angular distortion (θ) values for all cases under

a total settlement, $\delta = 75$ mm and 150 mm. For different MPR with $t_r = 1.2$ m, θ was significantly lower than the limit of 1/1500. This indicates the substantial influence of raft thickness in controlling the differential settlement. The MPR with $t_r = 0.6$ m performed quite well and the angular distortion was within the limits. Moreover, θ and θ_r for $t_r = 0.3$ exceed the allowable angular distortion in all cases.

Table 7.8. θ/θ_r for different MPR cases under uniform loading.

t_r (m)	1.2				0.6				0.3			
q(kPa)	103		112		103		112		104		111	
S/D_{mp}	θ	θ/θ_r	θ	θ/θ_r	θ	θ/θ_r	θ	θ/θ_r	θ	θ/θ_r	θ	θ/θ_r
Raft	0.0004	1.0	0.0007	1.0	0.0006	1.0	0.0037	1.0	0.0068	1.0	0.0255	1.0
5	0.0007	1.9	0.0006	0.9	0.0016	2.9	0.0018	0.5	0.0018	0.3	0.0020	0.1
8	0.0007	1.8	0.0006	0.9	0.0020	3.6	0.0022	0.6	0.0024	0.4	0.0027	0.1
10	0.0006	1.4	0.0005	0.8	0.0021	3.8	0.0024	0.7	0.0032	0.5	0.0037	0.1
16	0.0006	1.3	0.0003	0.5	0.0021	3.7	0.0025	0.7	0.0037	0.5	0.0044	0.2
20	0.0003	0.7	0.0000	0.1	0.0020	3.5	0.0017	0.5	0.0018	0.3	0.0015	0.1
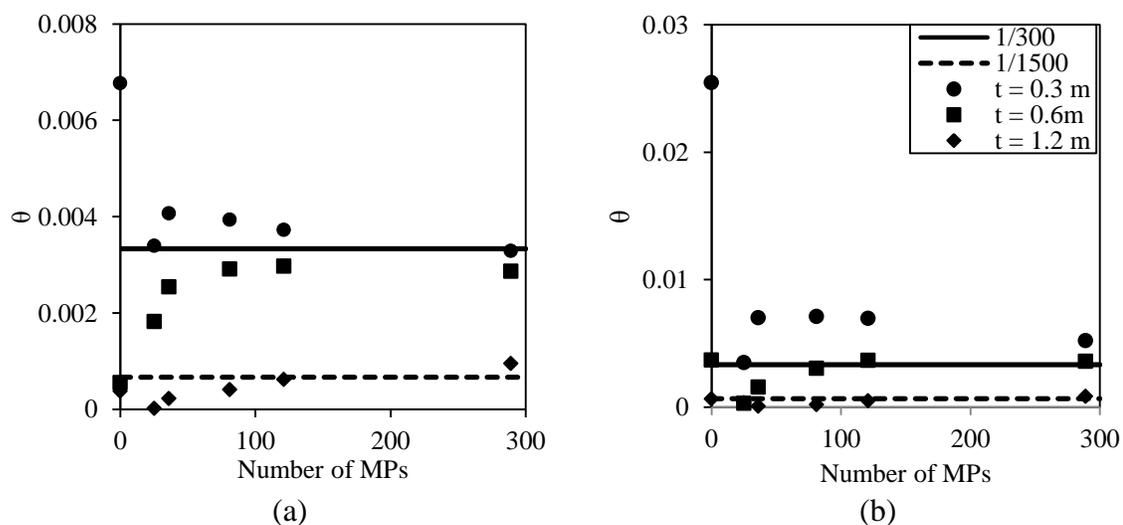
Figure 7.10 θ for: (a) MPR at δ=75 mm; (b) MPR at δ=150 mm.

7.3.6. Load Sharing

The raft flexibility, which is determined primarily by the micropile spacing and the raft thickness as demonstrated by Eq. 7.16, has major role in controlling the load transmitted by the raft and the micropiles. Figure 7.11 presents the percentage of the load carried by the raft with different values of micropile spacing and raft thickness for MPR in clay with $s_u = 30$ kPa. The effect of S/D_{mp} is substantial because as the spacing increased, the MPR became more flexible and as a result, the load carried by the raft increased by up to 94% for micropile spacing of $20D_{mp}$. A similar observation was described by Katzenbach et al. (2000) and Fleming et al. (2009) for piled rafts. Fleming et al. (2009) estimated the load carried by raft to exceed 80% in some cases; moreover, Horikoshi and Randolph (1996) evaluated the load carried by raft as a member of a piled raft foundation with spacing of $8D_p$ using centrifuge tests in clay soils to be about 86%. Reducing the raft thickness had a slight effect on the load transmitted by the raft. As t_r decreases from 1.2 m to 0.3 m, the load carried by the raft increased by about 10%; a comparable remark was reported by Poulos (2001). The percentage of the load carried by the raft can be evaluated as a function of the micropile spacing using the following equation:

$$R_{raft} (\%) = \left(0.55 \, ln \left(S/D_{mp} \right) - 0.69 \right) * 100 \qquad For \; s_u = 30 \; kPa \qquad (7.18)$$
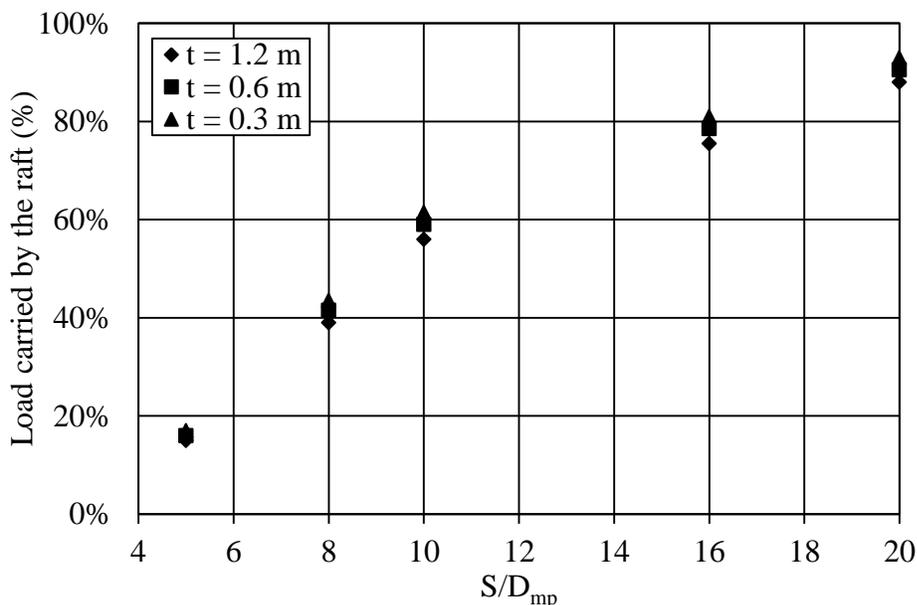
Figure 7.11. Load carried by the raft for the MPR in firm clay

7.3.7. Bending Moment

Assessing the bending moment for the raft component is essential for the design of raft reinforcement. Therefore, the bending moment for different MPR configurations is evaluated for both uniform and concentrated loads. In general, the maximum bending moment occurred at the central area of the raft for the uniform loading case, and beneath the core columns for the concentrated loading case.

Table 7.9 shows the bending moment (M_u) due to an applied uniform pressure, q, that resulted in tolerable settlement, $\delta = 0.075$ m and 0.15 m. The normalized moments (M_u/Q), where $Q = qB_rL_r$ is the total applied load, are also presented in Table 6.10. The normalized moment is deemed to be more representative of the MPR performance as the loads required to achieve specified settlement varied between different MPR configurations.

Table 7.9 demonstrates that as the stiffness of the MPR system increased (i.e. smaller S/D_{mp}), the load applied to reach the tolerable settlement level increased and hence the bending moment (M_u) increased. However, M_u/Q decreased, indicating better performance. This means a flexible MPR would experience a higher bending moment if it is subjected to the same load level. For example, at $Q = 57$ MN for a MPR with $t_r = 0.3$ m, $M_u = 0.1$ MN.m/m and 0.5 MN.m/m for $S/D_{mp} = 5$ and 20, respectively. However, for MPR with raft thickness of 1.2 m, M_u/Q increased as S/D_{mp} decreased due to the increase in differential settlement. Moreover, as the load increased for MPR with $t_r = 1.2$m, the maximum bending moment decreased due the decrease in the differential settlement as discussed in Section 7.3.5.

Table 7.9. Bending moment (M_u) for different MPR cases under uniform loading (moment unit is MN.m/m).

t_r (m)	1.2				0.6				0.3			
δ (m)	0.075		0.15		0.075		0.15		0.075		0.15	
S/D_{mp}	M_u	M_u/Q	M_u	M_u/Q	M_u	M_u/Q	M_u	M_u/Q	M_u	M_u/Q	M_u	M_u/Q
5	0.9	0.01	0.95	0.008	0.32	0.004	0.39	0.004	0.1	0.001	0.12	0.001
8	0.8	0.011	0.64	0.007	0.31	0.005	0.34	0.004	0.09	0.001	0.12	0.001
10	0.6	0.009	0.41	0.005	0.30	0.005	0.33	0.004	0.09	0.002	0.12	0.002
16	0.4	0.007	0.29	0.004	0.26	0.005	0.27	0.004	0.08	0.002	0.11	0.002
20	0.3	0.005	0.30	0.005	0.20	0.004	0.28	0.005	0.08	0.002	0.09	0.002
Raft	0.12	0.003	0.38	0.008	0.11	0.001	0.37	0.01	0.1	0.020	0.32	0.01

Table 7.10 presents the maximum bending moment beneath the core columns (M_{cl}) for different MPR cases. As expected, due to the concentrated loads, the moment was significantly higher than the moment for the uniform loading case. The ratio between the moments under concentrated loads and uniform loads (M_{cl}/M_u) is 2.5 and 5.5 for MPR with $t_r = 1.2$ m and 0.6 m, respectively. The MPR with a flexible raft ($t_r = 0.6$ m) experienced higher bending moment compared to the case of uniformly distributed load,

which is about 50% M_{cl}/M_u higher than the MPR with the relatively rigid raft (t_r = 1.2 m).
However, the area of maximum bending moment is approximately 8 times the column
dimensions. The rest of the raft area experienced bending moment of magnitudes similar
to the uniform loading case. These findings should be used for the reinforcement design.

Table 7.10. Bending moment (M_{cl}) for different MPR cases under concentrated loading
(moment unit is MN.m/m).

t_r (m)	1.2				0.6			
δ (m)	0.075		0.15		0.075		0.15	
S/D_{mp}	M_{cl}	M_{cl}/Q	M_{cl}	M_{cl}/Q	M_{cl}	M_{cl}/Q	M_{cl}	M_{cl}/Q
5	2.35	0.027	2.8	0.025	1.6	0.022	2.2	0.022
10	1.6	0.026	1.84	0.023	1.24	0.022	1.7	0.022
16	1.30	0.024	1.3	0.02	1.13	0.023	1.4	0.022
Raft	0.63	0.014	0.49	0.01	0.78	0.018	0.64	0.013

7.3.8. Micropile Skin Friction

The micropile skin friction was evaluated by integrating the stresses in the interface
elements along the micropile shaft. Table 7.11 presents the average skin friction along the
micropiles for different cases. All results are based on δ = 0.075 m and 0.15 m. As the
micropiles-soil interface approached its plastic condition at δ = 0.075 m, the micropile
shaft capacity was about 22 kPa for all cases except for cases with S/D_{mp} = 16 and 20 as
the axial load was relatively low. However, at δ = 0.15 m, the micropiles' ultimate
capacity was fully mobilized and the micropile soil interface reached the plastic condition
and the average skin friction was approximately 24 kPa.

Table 7.11 shows that the average skin friction was 24 kPa for most of the cases as the micropiles capacity was mobilized. The skin friction obtained from the FEA was less than the range of skin friction reported by the Federal Highway Administration (FHWA) (2005) for Type B micropiles. According to FHWA (2005), the ultimate bond strengths for soft to medium plastic silt and clay with some sand is 35-95 kPa. This is expected as for the actual construction of the Type B micropiles, the pressurized grout penetrates through the soil, which improves the grout-ground strength and hence, increases the shaft friction. This additional increase in strength was not simulated in the current study. Although the average skin friction was 24 kPa, at the lower section of the micropile, the skin friction was approximately 32 kPa. The skin friction for the clay was within the theoretical values (25 kPa) using the α method, which is suitable for estimating the skin friction for undrained conditions, i.e. (Terzaghi et al., 1996):

$$f_s = \alpha s_u \tag{7.19}$$

Where: α = Coefficient is a function of undrained shear strength = 0.9 (Tomlinson, 1957).

As the number of micropiles in the MPR decreased ($S/D_{mp} > 5$), the micropile load decreased as the total load transmitted by micropiles decreased. In addition, the percentage of the axial load carried by the micropile toe was reduced and most of load was transferred through the micropile shaft. The total at the micropile top (P_t) was calculated as:

$$P_t = \sigma_{zt} A_{mp} \tag{7.20}$$

Where: σ_{zt} = axial stress at top of micropile; and A_{mp} = cross-sectional area of micropile.

In addition, the axial forces carried by the micropiles' shafts were estimated by integrating the skin friction obtained from interface elements along the micropile, i.e.

$$P_s = \sum_{i=1}^{n_s} f_{si} C_{mp} h_{si} \tag{7.21}$$

Where: i = segment number; n_s = total number of segments which is 20; F_{si} = skin friction corresponding for each segment; C_{mp} = circumference of micropile; and h_{si} = height of each segment (which was 0.5 m).

Table 7.11. Micropile skin friction for different cases.

δ (m)		0.075			0.15		
n	S/D_{mp}	F_s(kPa)	P_s/P_t	P_t (MN)	F_s(kPa)	P_s/P_t	P_t (MN)
289	5	22	59%	0.29	24	60%	0.31
121	8	22	54%	0.32	24	57%	0.33
81	10	22	58%	0.30	24	59%	0.31
36	16	21	70%	0.24	23	72%	0.25
25	20	21	90%	0.18	23	93%	0.19

[*] F_s =skin Friction; P_s = axial force carried by shaft of micropile;
and P_t =total applied axial load at the top of micropile.

7.4. CONCLUSIONS

Finite element analyses were carried out to investigate the performance of MPRs installed in firm clay (s_u = 30kPa). The 3D finite element model employed in the analysis was calibrated and verified using centrifuge testing results. The performance of the MPR was evaluated in terms of tolerable bearing pressure, axial stiffness, differential settlement, load sharing, bending moment and micropile skin friction. The factors that were considered in the analysis are micropile spacing, raft thickness and load type. The main findings and observations from the numerical study are listed below:

1. The tolerable bearing pressure and axial stiffness of the MPR increased significantly (up to 100%) compared to an isolated raft. As the number of

micropiles decreased (or S/D_{mp} increased), the rate of increase declined, especially for $S/D_{mp} > 10$.

2. The PDR method can be employed to estimate k_{mpr} for MPR with a very stiff raft with 3% error margin in comparison with values obtained from finite element analysis. However, for more flexible rafts the error margin in predictions of PDR method increased to 26%.

3. An adjustment factor (ω_{PR}) is proposed to account for the raft flexibility when evaluating the axial stiffness employing the PDR method for an MPR with flexible raft.

4. The differential settlement of an MPR could be higher than that of a raft if the micropiles are distributed uniformly. To control differential settlement of MPRs, the micropiles should be located strategically (close to loaded areas) to minimize differential settlement.

5. For MPRs subjected to uniformly distributed loads, the effect of micropiles is more prominent for MPRs with flexible rafts. The average angular distortion decreased by as high as 90% for MPRs with $t_r = 0.3$ m, compared to a reduction in the differential settlement of 30% to 40% for MPRs with thicker rafts at a settlement level of 0.15 m.

6. As S/D_{mp} increases, the MPRs become more flexible, and as a result, the load carried by the rafts increases. For example, the raft load increased to 91% for an MPR with $S/D_{mp} = 20$.

7. The raft bending moment under concentrated loads could be 3 to 5 times higher than the raft bending moment under uniform loading. The maximum bending moment for

the case of concentrated loads occurs over a tributary area around the core column

with dimensions of 8 times the column dimensions.

REFERENCES

Abd Elaziz, A. and El Naggar, M. (2014a). Geotechnical Capacity of Hollow Bar Micropiles in Cohesive Soils. Canadian Geotechnical Journal, **51**(10): 1123-1138.

Abd Elaziz, A. and El Naggar, M. H. (2014b). Group Behaviour of Hollow Bar Micropiles in Cohesive Soils. Canadian Geotechnical Journal, **51**(10): 1139-1150.

Alnuaim, A. M., El Naggar, H. and El Naggar, M. (2013). Performance of Piled-Raft System under Axial Load. *In* Proceedings of the 18th International Conference on Soil Mechanics and Geotechnical Engineering, Paris, pp. 2663-2666.

Brown, P. T. (1969). Numerical Analyses of Uniformly Loaded Circular Rafts on Deep Elastic Foundations. Géotechnique, **19**(3): 399-404.

Bruce, D. A., DiMillio, A. F. and Juran, I. (1995). Introduction to Micropiles: An International Perspective. Foundation Upgrading and Repair for Infrastructure Improvement, ASCE, Geotechnical Special Publication No. 50, pp.1-26.

Cho, J., Lee, J. H., Jeong, S. and Lee, J. (2012). The Settlement Behaviour of Piled Raft in Clay Soils. Ocean Engineering, **53**(1): 153-163.

Clancy, P. and Randolph, M. F. (1993). An Approximate Analysis Procedure for Piled Raft Foundations. International Journal for Numerical and Analytical Methods in Geomechanics, **17**(12): 849-869.

Clancy, P. and Randolph, M. F. (1996). Simple Design Tools for Piled Raft Foundations. Géotechnique, **46**(2): 313-328.

Drbe, O. and El Naggar, M. H. (2014). Axial Monotonic and Cyclic Compression Behaviour of Hollow Bar Micropiles. Canadian Geotechnical Journal, Accepted for publication.

El Naggar, M. and Sakr, M. (2000). Evaluation of Axial Performance of Tapered Piles from Centrifuge Tests. Canadian Geotechnical Journal, **37**(6): 1295-1308.

FHWA. (2005). Micropile Design and Construction Guidelines, Implementation Manual. National Highway Institute.

Fleming, K., Weltman, A., Randolph, M. and Elson, K. (2009). Piling Engineering. 3rd edition. New York, Taylor and Francis group.

Han, J. and Ye, S. (2006). A Field Study on the Behaviour of A Foundation Underpinned by Micropiles. Canadian Geotechnical Journal, **43**(1): 30-42.

Horikoshi, K. and Randolph, M. F. (1996). Centrifuge Modelling of Piled Raft Foundations on Clay. Géotechnique, **46**(4): 741 –752.

Horikoshi, K. and Randolph, M. (1997). On The Definition of Raft-Soil Stiffness Ratio for Rectangular Rafts. Géotechnique, **47**(5): 1055-1061.

Horikoshi, K. and Randolph, M. F. (1998). A Contribution to Optimum Design of Piled Rafts. Géotechnique, **48**(3): 301-317.

Horikoshi, K., Matsumoto, T., Hashizume, Y., Watanabe, T. and Fukuyama, H. (2003a). Performance of Piled Raft Foundations Subjected to Static Horizontal Loads. International Journal of Physical Modelling in Geotechnics, **3**(2): 37-50.

Horikoshi, K., Matsumoto, T., Hashizume, Y. and Watanabe, T. (2003b). Performance of Piled Raft Foundations Subjected to Dynamic Loading. International Journal of Physical Modelling in Geotechnics, **3**(2): 51-62.

Horikoshi, K., Watanabe, T., Fukuyama, H. and Matsumoto, T. (2002). Behaviour of Piled Raft Foundations Subjected to Horizontal Loads. *In* Proceeding of the International Conference on Physical Modelling in Geotechnics. St John's, Newfoundland, Canada: Taylor & Francis.

Jaimolkowski, M., Lancellotta, R., Pasqualini, E., Marchetti, S. and Nova, R. (1979). Design Parameters for Soft Clays. General Report. *In* Proceedings of the 7th European Conference on Soil Mechanics and Foundation Engineering. n. 5, pp. 27–57.

Juran, I., Benslimane, A. and Hanna, S. (2001). Engineering Analysis of Dynamic Behaviour of Micropile Systems. Transportation Research Record: Journal of the Transportation Research Board, **1772**(1): 91-106.

Katzenbach, R., Arslan, U. and Moormann, C. (2000). Piled Raft Foundation Projects in Germany. In J. A. Hemsley (Ed.), Design Applications of Raft Foundation. London: Thomas Telford.

Katzenbach, R., Schmitt, A. and Turek, J. (2005). Assessing Settlement of High-Rise Structures by 3D Simulations. Computer-Aided Civil and Infrastructure Engineering, **20**(3): 221-229.

Khan, M.K., El Naggar, M.H. and Elkasabgy, M. (2008). Compression Testing of Drilled Concrete Tapered Piles in Cohesive-Frictional Soil. Canadian Geotechnical Journal, **45**(3): 377-392.

Kulhawy, F. H., Duncan, J. M., and Seed, H. B. (1962). Finite Element Analysis of Stresses and Movement in Embankments during Construction. University of California, Berkeley, College of Engineering. Under contract with US Army Engineers Waterways Experiment Station, Vicksburg, MI.

Lee, J., Kim, Y. and Jeong, S. (2010). Three-Dimensional Analysis of Bearing Behaviour of Piled Raft on Soft Clay. Computers and Geotechnics, **37**(1): 103-114.

Lin, L. (1995). Strength Characteristics of a Modelling Silty Clay. M.Eng. Thesis, Memorial University of Newfoundland. St. John' s, Newfoundland. Canada.

Lizzi, F. (1982). The Static Restoration of Monuments: Basic Criteria-Case Histories, Strengthening of Buildings Damaged by Earthquakes. Genova: Sagep Editrice.

Long, J., Maniaci, M., Menezes, G. and Ball, R. (2004). Results of Lateral Load Tests on Micropiles. *In* Proceedings of sessions of the GeoSupport Conference: Innovation and Cooperation in the Geo-Industry, Orlando, Florida: Geo-Institute of the American Society of Civil Engineers, pp. 122-133.

Maharaj, D. K. and Gandhi, S. R. (2004). Non-Linear Finite Element Analysis of Piled-Raft Foundations. ICE- Geotechnical Engineering, **157**(3):107-113.

Mayne, P. W. and Kulhawy, F. H. (1982). Ko - OCR Relationships in Soil. Journal of the Geotechnical Engineering Division, **108**(6): 851-872.

National Building Code of Canada (NBC). (2010). Ottawa: National Research Council Canada (NRC).

PLAXIS BV. (2013). PLAXIS 3D 2013 Reference Manual. Delft: PLAXIS BV.

Poulos, H. G. (2000). Practical Design Procedures for Piled Raft Foundations in Germany. In J. A. Hemsley (Ed.), Design applications of raft foundation. London: Thomas Telford.

Poulos, H. G. (2001). Piled Raft Foundations: Design and Applications. Géotechnique, **51**(2): 95-113.

Poulos, H. G. and Davis, E. H. (1974). Elastic Solutions for Soil and Rock Mechanics. New York: John Wiley and Sons. Inc.

Randolph, M. F. (1994). Design Methods for Piled Groups and Piled Rafts. Proc. 13th ICSMFE, New Delhi, India, pp. 61-82.

Reul, O. and Randolph, M. F. (2003). Piled rafts in Overconsolidated Clay: Comparison of in Situ Measurements and Numerical Analyses. Géotechnique, **53**(3): 301–315.

Richards, T. D. and Rothbauer, M. J. (2004). Lateral Loads on Pin Piles (Micropiles). *In* Proceedings of sessions of the GeoSupport Conference: Innovation and Cooperation in the Geo-Industry. Orlando, Florida: Geo-Institute of the American Society of Civil Engineers.

Roberts, L., Fick, D. and Misra, A. (2011). Performance-Based Design of Drilled Shaft Bridge Foundations. Journal of Bridge Engineering, **16**:(Special issue): 749-758.

Rose, A. V., Taylor, R. N. and El Naggar, M. (2013). Numerical Modelling of Perimeter Pile Groups in Clay. Canadian Geotechnical Journal, **50**(3): 250-258.

Sadek, M. and Shahrour, I. (2004). Three-Dimensional Finite Element Analysis of the Seismic Behaviour of Inclined Micropiles. Soil Dynamics and Earthquake Engineering, **24**(6): 473-485.

Shahrour, I. and Ata, N. (2002). Analysis of the Consolidation of Laterally Loaded Micropiles. Ground Improvement, **6**(1): 39-46.

Shahrour, I., Sadek, M. and Ousta, R. (2001). Seismic Behaviour of Micropiles: Used as Foundation Support Elements: Three-Dimensional Finite Element Analysis. Transportation Research Record: Journal of the Transportation Research Board, **1772**(1): 84-90.

Stewart, D. and Randolph, M. (1994). T-Bar Penetration Testing in Soft Clay. ASCE Journal of Geotechnical Engineering, **120**(12): 2230-2235.

Tan, Y. C. and Chow, C. M. (2004). Design of Piled Raft Foundation on Soft Ground. *In* GSM-IEM Forum: The roles of engineering geology and geotechnical engineering in construction works.

Teerawut, J. (2002). Effect of Diameter on the Behaviour of Laterally Loaded Piles in Weakly Cemented Sand. Ph.D. Dissertation, University of California, San Diego.

Terzaghi, K., Peck, R. and Mesri, G. (1996). Soil Mechanics in Engineering Practice. New York: Wiley-Interscience.

Tomlinson, M. J. (1957). The Adhesion of Piles Driven in Clay Soils. *In* Proceedings of the 4th International Conference on Soil Mechanics and Foundation Engineering, London, Vol. 2, pp. 66-71.

Wood, D. M. (2004). Geotechnical Modelling (Applied Geotechnics). 1st edition. London and New York: Spon Press.

CHAPTER 8: SUMMARY, CONCLUSIONS AND RECOMMENDATIONS

A research program was conducted to investigate the performance of micropiled rafts (MPR) installed in sand and in clay soils. The research program comprised of a centrifuge testing program and a comprehensive numerical study. The main aspects of the research program are summarized and the main findings and conclusions are presented herein. In addition, some recommendations for future research are also suggested.

8.1. SUMMARY

Micropiles are used to retrofit existing buildings and to support new construction. In these applications, the overall behaviour of a MPR foundation system is similar to a piled raft foundation, where the load is transferred to the soil through both the raft and the micropiles. In addition, using the micropiled raft (MPR) is a new highly efficient foundation system that combines the advantages of the piled raft system and the efficient installation of micropiles and associated ground improvement. However, there is no guidance available regarding the performance of MPR foundations. This study investigated the performance of the MPR foundations installed in both cohesionless and cohesive soils.

The research program comprised three main phases. In the first phase, a series of geotechnical centrifuge tests was conducted on MPR foundations as well as single micropile and isolated rafts installed in sand and clay soils. In addition, a number of element tests on soil samples retrieved from the soil bed used in the centrifuge testing program were performed to determine the necessary parameters for the finite element

model (FEM). In the second phase, a 3D FEM was established employing the computer program PAXIS (PLAXIS BV., 2013) and was calibrated and verified using the test results from the experimental studies of Phase 1. Finally, the verified FEM was then used to perform a comprehensive parametric study to further evaluate the behaviour of MPR foundations in sand and clay soils.

Four MPR centrifuge tests were conducted: three tests in sandy soil and one test in clay soil. Furthermore, a single micropile and isolated raft foundation centrifuge tests were carried out in both sand and clay. The MPR, isolated raft, and single micropile used in the centrifuge tests were instrumented in order to investigate the performance of MPRs in terms of their axial stiffness, bearing capacity, differential settlement, contact pressure and raft bending moment compared to an isolated raft. Also, the effect of the raft flexibility on load sharing between micropiles and the raft was examined in cohesionless soil with a view to develop a simplified approach to evaluate the axial stiffness of MPR foundations.

The results of the centrifuge tests were used to calibrate and verify the non-linear, three-dimensional, finite element models for the MPR installed in both sand and clay, which was subsequently employed to conduct the parametric study. The parametric study investigated the effects of number and spacing of micropiles, flexibility of the raft and type of loading on the axial stiffness, tolerable bearing pressure and total and differential settlements of the MPR as well as the bending moment of the raft. The physical dimensions of structural components and parameters considered in the parametric study were within the range considered in the current practice. The results of the centrifuge

tests and numerical study were analyzed to establish some design guidelines for applications of micropiled rafts in foundation engineering.

Based on the findings of this thesis, equations were proposed to evaluate the percentage increase in tolerable bearing pressure (PIBP) for MPRs installed in different types of soils considering the spacing between the micropiles. The observations from the current study demonstrated that the Poulos-Davis-Randolph (PDR) method could be used to evaluate the performance of a MPR system with relatively stiff rafts in both sand and clay with an error margin of up to 3%. However, the error margin increased to 15% and 26% for MPRs installed in sand and clay soils, respectively. An adjustment factor was proposed to account for the raft flexibility in the PDR method.

8.2. CONCLUSIONS

The main observations and findings of this research program are presented in terms of characteristics of the soil used as a test bed, centrifuge modeling of MPRs, and numerical modeling of MPRs.

8.2.1. Kaolin-Silt Clay

The use of kaolin clay to simulate the behaviour of natural clay in geotechnical physical modeling has been adopted and used in many research studies due to its ability to simulate different stress histories with different undrained shear strength values to model the soil under consideration. The characterization of the K-S clay involved UU and CU triaxial tests using specimens retrieved from the soil bed after the conclusion of the centrifuge testing program. Based on the results of the triaxial tests, an equation is

proposed relating the undrained shear strength to the mean effective stress for 50% kaolin and 50% silt mixture, i.e.

$$s_u = 0.31 \, \sigma'_m \, (OCR)^{0.51} \qquad (8.1)$$

The undrained shear strength, s_u, calculate from Equation 8.1 was found to be in good agreement with the values obtained from the in-flight T-bar test. It was also found that the undrained modulus of elasticity, E_u, is approximately 155 times the mean effective stress.

8.2.2. Centrifuge modeling of MPRs

The behaviour of MPR in sand and clay were evaluated utilizing the geotechnical centrifuge technology. The influence of flexibility of the raft on the MPR axial stiffness, differential stiffness, and micropiles skin friction were examined in the sand. The major findings related to the behaviour of MPR in both the sand and clay soils as gleaned from testing program are presented here.

8.2.2.1. MPRs in sand

The results of the centrifuge testing program for MPR in sand show that the raft thickness has a significant effect on its axial stiffness. For instance, the MPR axial stiffness increased by 90% and 20% as the raft thickness increased from 0.30 m to 0.45 m then to 0.60 m. The PDR method was shown to be suitable for estimating the axial stiffness for the MPR with a relatively stiff raft. Nonetheless, for flexible micropiled rafts, the PDR method can grossly overestimate the axial stiffness. An adjustment factor (ω_{PR}) was proposed in order to accurately estimate the axial stiffness of flexible raft using PDR method. Due the increase in the confining pressure as results of the high contact

pressure of the raft, the skin friction for the MPR with a flexible raft was 3.5 times higher than the MPR with rigid raft only at the upper section of the micropiles. The load carried by the raft was 41%, 49%, and 58% of the total load applied to the MPR with a raft thickness of 0.30 m, 0.45 m, and 0.60 m, respectively. Using micropiles as differential and total settlement reducers by strategically locating the micropile beneath the load directly was proven by a centrifuge test to be a valid option as reductions of 31.4% and 33.3% reduction in the differential and total settlements, respectively.

8.2.2.2. MPRs in clay

The kaolin-silt clay bed was reconstituted from slurry deposition with a 1:1 kaolin to silt ratio; the slurry was consolidated to 300 kPa vertical effective stress to achieve the targeted undrained shear strength of 30 kPa. Three geotechnical centrifuge tests were conducted at 50g in order to investigate the behaviour of the MPR foundations in clay under concentrated vertical load. It was established that the micropiles in the MPR increased the axial stiffness by 207% in comparison to the raft alone and 35% comparing to a group of 4 micropiles. Moreover, the skin friction along the micropile shaft was not affected due to the interaction with the raft, which was manifested in terms of almost equal unit skin friction of single micropile and the micropile as a component of the MPR. The load carried by the MPR components reached a plateau and became almost constant at approximately 52% and 48% for the MPs and the raft, respectively

8.2.3. Numerical Modeling of MPRs

The results of the centrifuge tests were used to calibrate and verify the finite element models for MPR in sand and clay. The calibrated models were used to perform

comprehensive parametric studies. The size of the structural components and parameters considered in the parametric study were within the range considered in the current practice (i.e. terms of micropile spacing, raft thickness, soil properties, load type, and load magnitude) to provide meaningful observations to contribute in the design process. The results of the numerical parametric study were analyzed to establish design guidelines for applications of MPRs in foundation engineering.

8.2.3.1. FEM of MPRs in sand

The findings of the 3D FEM were analyzed in order to establish some design criteria for MPRs constructed in sandy soil. It was found that the tolerable bearing pressure and axial stiffness of MPRs increased significantly compared to an isolated raft as the micropile spacing decreased in addition, the percentage increase in tolerable bearing pressure for MPR with $S/D_{mp} = 5$ compared to an isolated raft foundation was 160%, 180%, and 190% for sand with $D_r = 70\%$, 50% and 25%, respectively. A set of equations were proposed in order to estimate the increase in tolerable bearing pressure of MPRs, which depends on the micropile spacing and sand relative density. The PDR method was shown to have the ability to estimate k_{mpr} for a MPR with a rigid raft with an error of up to 3%. However, to use the PDR method for the MPR with flexible raft, an adjustment factor (ω_{PR}) should be used to evaluate the axial stiffness in order to account for raft flexibility, which can be calculated using the following equation:

$$\omega_{PR} = \kappa \ln(K_f) + \mu \tag{8.2}$$

Where: $\kappa = 0.01 \ln(D_r) + 0.04$ and $\mu = -0.14 \ln(D_r) + 0.66$

The differential settlement would decrease by 20% to 40% for MPRs with micropile spacings less than 10 D_{mp} and subjected to concentrated loads; however, for $S/D_{mp} > 10$, micropiles may increase the differential settlement for MPRs constructed in dense sand ($Dr = 70\%$) as θ increased by about 17%. This is because the micropiles close to the edge column reduce the settlement more than micropiles at the center column. It is recommended to use thicker rafts in the case of concentrated loads (e.g. columns loads). For the uniformly distributed load cases, the effect of micropiles is more noticeable for MPRs with flexible rafts ($t_r = 0.3$ m and 0.6 m), as angular distortion reduced by 35% for MPRs with spacing less than 10 D_{mp}. The raft bending moment under column loads is 3.4 to 7.5 times higher than the raft bending moment under uniform loading for MPRs with t_r = 1.2 m and 0.6 m, respectively. The maximum bending moment for the case of concentrated loads occurs over a tributary area around the core column with dimensions 6 times the column dimensions.

8.2.3.2. MPRs in clay

The parametric study provided useful insights of the performance characteristics and some criteria for the design of MPRs. The results from the parametric study suggested that the MPR capacity could increase by 101% for $S/D_{mp} = 5$ compared to an isolated raft foundation with the same dimensions and supporting soil. The PDR method was shown to be suitable for predicting k_{mpr} for MPRs with very stiff rafts with an error of 3% of the calibrated FEA results. However, for more flexible raft, the error in predictions using the PDR method increased up to 26% for MPRs with t_r = 0. 3 m. Hence, the adjustment factor (ω_{PR}) should be used to evaluate the axial stiffness according to the PDR method to

account for raft flexibility for MPRs in medium-stiff clay (s_u = 30 kPa), which can be calculated using the following equation:

$$\omega_{PR} = 0.055 \ln(K_f) + 0.6 \qquad (8.3)$$

The MPR has the ability to reduce the differential settlement by about 90% for MPR with flexible raft. The raft bending moment under column loads is 3.5 to 5.1 times higher than the raft bending moment under uniform loading for MPRs with t_r = 1.2 m and 0.6 m, respectively. In addition, the maximum bending moment for the case of concentrated loads occurs over a tributary area around the core column with dimensions approximately eight times the column dimensions.

8.3. RECOMMENDATIONS

This section offers some recommendation for future studies to better understand the behaviour of MPR foundations and optimize their design. The recommendations are divided into two parts: (i) further centrifuge testing and (ii) numerical modeling.

8.3.1. MPR Centrifuge Testing

It is recommended to perform another series of geotechnical centrifuge tests on MPR in both sand and clay. The following points should be considered as research objectives:

- Employ different raft aspect ratios (B_r/L_r) in MPRs in order to validate and generalize the modified PDR method.
- To optimize the MPR in terms of reducing differential settlement at high bearing capacity; it is suggested to evaluate the efficiency of using uniform micropile spacings in addition to central micropiles beneath the loading (i.e. at the center of the raft)

- Study the behaviour of MPRs in both cohesionless and cohesive soils under lateral loading utilizing both reinforced micropiles with an outer steel case and unreinforced micropiles.

- Perform centrifuge tests on MPRs under dynamic loading with different time histories and amplitudes to investigate the seismic performance of MPRs.

8.3.2. Numerical Modeling of MPRs

It is recommended to utilize the available calibrated FEM from this study to evaluate different optimization methods to control differential settlement without compromising the MPR bearing capacity. In addition, calibrated finite element models should be used to evaluate the lateral performance of MPR foundations.

REFERENCES

PLAXIS BV. (2013). PLAXIS 3D 2013 Reference Manual. Delft: PLAXIS BV.

CURRICULUM VITA

Ahmed Mohamed Alnuaim

- ## Education:

  - Ph.D. Candidate in Civil and Environmental Engineering **2010 - 2014**
    Western University, London, Ontario

  - Master of Engineering Science in Civil Engineering **2008 - 2010**
    Western University, London, Ontario

  - Bachelor of Science in Civil Engineering **2001 - 2006**
    King Saud University, Riyadh, Saudi Arabia

- ## Honours and Awards

  - King Saud University Scholarship **2007 – Present**

  - Saudi Arabian Cultural Bureau Excellence Awards (PhD) **2010 and 2011**

  - Western Graduate Research Scholarships (WGRS) **2010**

  - Saudi Arabian Cultural Bureau Excellence Awards (MESc) **2008 and 2009**

- ## Related Works

  - Visiting Researcher **2013**
    C-CORE, Memorial University, St. John's, NL

  - Research Assistant **2008 - Present**
    Western University, London, Ontario

  - Teaching Assistant **2006- 2007**
    King Saud University, Riyadh, Saudi Arabia

- ## Publications

  - Journals

    1. **Alnuaim, A. M.**, El Naggar, H. and El Naggar, M. H. (2014). Performance of Micropiled Raft in Sand Subjected to Vertical Concentrated Load: Centrifuge Modeling. **Canadian Geotechnical Journal**, Accepted.

2. **Alnuaim, A. M.**, El Naggar, H. and El Naggar, M. H. (2014). Performance of Micropiled Raft in Clay Subjected to Vertical Concentrated Load: Centrifuge Modeling. **Canadian Geotechnical Journal**, Accepted.

3. **Alnuaim, A. M.**, El Naggar, H. and El Naggar, M. H. (2014). Evaluation of Piled Raft Performance Using a Verified 3D Nonlinear Numerical Model**. Soils and Foundations,** under review.

4. **Alnuaim, Ahmed M.** and M. H. El Naggar. (2014) "Performance of Foundations in Sabkha Soil: Numerical Investigation." **Geotechnical and Geological Engineering**, 32 (3): 637-656.

- Conferences

5. **Alnuaim, A.**, El Naggar, H. and El Naggar, M. H. (2014). Using micropile as settlement reducer: centrifuge and numerical investigations. In **the 67th Canadian Geotechnical Conference (GeoRegina)**, Regina, Saskatchewan, Canada, September 28 to October 1, 2013, (Paper ID: 160).

6. **Alnuaim, A.** and El Naggar, M. H. (2013). Performance of Deep Foundation in Sabkha Soil. In **the 66th Canadian Geotechnical Conference (GeoMontreal)**, Montreal, Québec, September 29 to October 3, 2013, (Paper ID: 161).

7. **Alnuaim, A.**, El Naggar, H. and El Naggar, M. H. (2013). Contact Pressure and Stress Distribution in Piled Raft Foundation Subjected to Vertical Loading. In **the 66th Canadian Geotechnical Conference (GeoMontreal)**, Montreal, Québec, September 29 to October 3, 2013, (Paper ID: 173).

8. **Alnuaim, A.** and El Naggar, M. H. (2013). Performance of Shallow Foundation on Sabkha Soil. In **the 3rd Specialty Conference on Material Engineering & Applied Mechanics** part of CSCE annual conference (Montreal 2013), Montréal, Québec, May 29 to June 1, 2013, (Paper ID: MEC - 29).

9. **Alnuaim, A.**, El Naggar, H. and El Naggar, M. H. (2013). 3D Modeling of Piled Raft Foundation Subjected To Vertical Loading. In **the 3rd Specialty Conference on Material Engineering & Applied Mechanics** part of CSCE annual conference (Montreal 2013), Montréal, Québec, May 29 to June 1, 2013, (Paper ID: MEC - 7).

10. **Alnuaim, A.**, El Naggar, H. and El Naggar, M. H. (2013). Performance of piled-raft system under axial load. In Proceedings of the **18th International Conference on Soil Mechanics and Geotechnical Engineering,** Paris, France, September2-6, 2013, pp. 2663-2666.